

**Effects of Oil Dispersants on the Transport of Oil Contaminants and  
Photolysis/Photocatalysis of Oil-Related PAHs**

by

Zhengqing Cai

A dissertation submitted to the Graduate Faculty of  
Auburn University  
in partial fulfillment of the  
requirements for the Degree of  
Doctor of Philosophy

Auburn, Alabama  
August 6, 2016

Keywords: Oil dispersants, Marine sediment particles, Sedimentation,  
PAHs, Photodegradation, Photocatalysis

Copyright 2016 by Zhengqing Cai

Approved by

Dongye Zhao, Chair, Elton Z. And Loid G. Endowed Professor of Environmental Engineering  
German Mills, Professor of Chemistry

Kenneth M. Halanych, Stewart Schneller Endowed Chair and Alumni Professor of Biology

Mark O. Barnett, Malcolm Pirnie Professor of Environmental Engineering

T. Prabhakar Clement, Harold Vince Groome Jr. Endowed Professor of Environmental  
Engineering

## **Abstract**

Petroleum is the largest energy source consumed in the US today. Routine oil exploration, transportation, refining, and consumption process result in the release of a large amount of oil into marine environments. Oil spills also frequently occur due to accidental well blow-outs or tanker spills, and oil dispersants are used as common countermeasures for mitigating such oil spills. Unfortunately, there is no quick and low-cost way to measure dispersant concentration in seawater; the effects of oil dispersants on the sediment-associated transport of oil in marine environments are also not well known. Furthermore, the effects and mechanisms of dispersants on the photolysis of oil contaminants still need to be studied. In addition to accidental spills, a large amount of oil-contaminated wastewater has been produced by the petroleum industry, which are highly toxic, and these wastes should be properly treated.

In the first part of this study (Chapter 2), a new method based on surface tension measurement was developed to determine the Corexit EC9500A concentration in seawater. The method can accurately analyze Corexit EC9500A in the concentration range of 0.5–23.5 mg/L. Minor variations in solution salinity, pH, and dissolved organic matter had negligible effects on the measurements. This simple, fast, economical method offers a convenient analytical method for quantifying complex oil dispersants dissolved in seawater.

In the second part of this study (Chapter 3), the effects of three model oil dispersants (Corexit EC9527A, Corexit EC9500A and SPC1000) on the settling of fine sediment particles, as well as particle-facilitated distribution and transport of oil components in sediment-seawater systems were investigated. All three dispersants enhanced the settling of sediment particles (the nonionic surfactants, Tween 80 and Tween 85, play key roles in promoting particle aggregation). Yet, the effects varied with environmental factors (pH, salinity, dissolved organic matter, and temperature). Notably, total petroleum hydrocarbons, PAHs and alkanes in the sediment phase were dramatically increased in the presence of Corexit EC9527A.

In the third part of this study (Chapter 4), the effects of oil dispersants on the photodegradation of anthracene and 9,10-DMA were studied under simulated solar light. All three tested dispersants promoted the photodegradation rate of tested PAHs. Kerosene, span 80 and tween 85 are the key dispersant components that promote the photodegradation rate. The dissolved oxygen plays different roles in the photodegradation of anthracene and 9,10-DMA. The photodegradation pathway of anthracene and 9,10-DMA showed no difference in the presence or absence of a dispersant. The dispersant components undergo photodegradation under solar light.

In the fourth part of this study (Chapter 5), a new class of platinum-deposited anatase/hexa-titanate nanotubes (TNTs) were prepared, and the effects of Pt form, i.e., reduced state of Pt(0) and oxidized state of Pt(IV), on photocatalytic activity were compared. The materials showed higher phenanthrene degradation rate than TiO<sub>2</sub> (P25). Both mechanisms of the enhanced photocatalytic activity were studied. Furthermore, the nanotubes can be separated through gravity-

sedimentation, and reused in multiple cycles of operations without loss in the photocatalytic activity.

## **Acknowledgments**

I would like to express my sincere appreciation to my advisor, Dr. Dongye Zhao, for his supervision, guidance, support, and patience throughout my Ph.D. Studies. The experience of working with him over the last five years in Auburn has left me wonderful memories to appreciate for the rest of my life.

I want to thank my committee members, Dr. German Mills, Dr. Kenneth M. Halanych, Dr. Mark Barnett, Dr. Prabhakar Clement and my dissertation outside reader Dr. Edward Davis for providing unconditional support and valuable suggestions during the studies. I feel fortunate that I met them and had a chance to work with them. I would like to thank Jinling Zhuang for the analytical and technical assistance. Special thanks are extended to Dr. Wen Liu, Dr. Jie Fu, and my fellow students in the Environmental Engineering Program at Auburn for their friendship, help, research advice and for creating a supportive environment.

I would also like to express my love and gratitude to my wife for her endurance, infinite support, and loving care. I wish to thank my daughter for bringing me happiness and joy in the past two years. Finally, I wish to thank my parents for their support. It is their constant encouragement that made this dissertation possible.

## Table of Contents

<b>Abstract</b> .....	<b>ii</b>
<b>Acknowledgments</b> .....	<b>v</b>
<b>List of Tables</b> .....	<b>viii</b>
<b>List of Figures</b> .....	<b>ix</b>
<b>Chapter 1. General Introduction</b> .....	<b>1</b>
1.1. Introduction of oil spill and wastewater from oil industry .....	1
1.2. Application of oil dispersants .....	6
1.3. Dispersant analysis.....	8
1.4. Effect of dispersant on the transport of spilled oil .....	9
1.5. Photodegradation of oil components and the effects of dispersants .....	12
1.6. Photocatalytic degradation of PAHs .....	14
1.7. Objectives.....	17
1.8. Organizations .....	18
<b>Chapter 2. A Surface Tension Based Method for Measuring Oil Dispersant Concentration in Seawater</b> .....	<b>20</b>
2.1. Introduction .....	20
2.2. Experimental methods.....	26
2.2.1. Materials.....	26
2.2.2. Effects of environmental factors .....	27
2.2.3. Analytical methods.....	28
2.3. Results and discussion .....	29
2.3.1. Analysis of dispersant samples .....	29
2.3.2. Effects of environmental factors on surface tension analysis .....	33
2.3.3. Accuracy of the method .....	38
2.4. Conclusions .....	40
<b>Chapter 3. Effects of Oil Dispersants on Settling of Marine Sediment Particles and Particle-associated Transport of Oil Components</b> .....	<b>42</b>
3.1. Introduction .....	42
3.2. Materials and methods .....	45
3.2.1. Materials.....	45
3.2.2. Effects of dispersants on sediment settling .....	48
3.2.3. Particle size distribution and settling velocity distribution curve of suspended sediment .....	50
3.2.4. Effects of environmental factors, WAO and DWAO on settling of sediment particles .....	50
3.2.5. Effects of dispersant on sorption and transport of oil and PAHs .....	51
3.2.6. Analytical methods.....	52
3.3. Results and discussion .....	54

3.3.1. Effect of dispersants on sediment settling.....	54
3.3.2. Effects of dispersant under various environmental conditions .....	65
3.3.3. Effect of dispersant on sediment-facilitated distribution and transport of oil components.....	70
3.4. Conclusions.....	78
<b>Chapter 4. Effects of Dispersants on Photodegradation of PAHs in Seawater .....</b>	<b>80</b>
4.1. Introduction.....	80
4.2. Materials and methods .....	83
4.2.1. Materials.....	83
4.2.2. Experimental apparatus .....	83
4.2.3. Effects of dispersants on the photodegradation of PAHs.....	87
4.2.4. Roles of dissolved oxygen and radicals for the photodegradation of PAHs .....	88
4.2.5. Analytical methods.....	89
4.3. Results and discussion .....	89
4.3.1. Effects of dispersants on the PAHs photolysis.....	90
4.3.2. Effect of dispersant components on the PAHs photolysis .....	94
4.3.3. Mechanism of the PAHs photolysis in the presence of dispersants .....	101
4.3.4. Photodegradation pathway of anthracene and 9,10-DMA .....	109
4.3.5. Photochemical stability of dispersant under solar irradiation .....	111
4.4. Conclusions.....	113
<b>Chapter 5. Platinum-Deposited Anatase/Hexa-Titanate Nanotubes with Enhanced Photocatalytic Activity for Phenanthrene Degradation under Solar Light .....</b>	<b>115</b>
5.1. Introduction.....	115
5.2. Materials and methods .....	118
5.2.1. Chemicals .....	118
5.2.2. Synthesis of Pt-doped TNTs .....	119
5.2.3. Photocatalytic degradation .....	120
5.2.4. Hydroxyl radicals ( $\bullet\text{OH}$ ) and hydrogen peroxide ( $\text{H}_2\text{O}_2$ ) measurement .....	122
5.2.5. Material characterizations .....	122
5.3. Results and discussion .....	124
5.3.1. Photocatalytic activity of Pt-deposited TNTs under different synthesis conditions 124	
5.3.2. Morphology, crystal phases and compositions of Pt-deposited TNTs.....	127
5.3.3. Photocatalytic degradation of phenanthrene by various Ti-based materials .....	133
5.3.4. Mechanisms for enhanced photocatalytic activity of Pt-deposited TNTs.....	135
5.3.5. Reusability of Pt doped TNTs .....	143
5.4. Conclusions.....	147
<b>Chapter 6. Conclusions and Recommendations for Future Research .....</b>	<b>149</b>
6.1. Summary and conclusions .....	149
6.2. Contribution and limitations .....	152
6.3. Recommendations for future work .....	153
<b>Appendix.....</b>	<b>155</b>
<b>References.....</b>	<b>191</b>

## List of Tables

Table 2-1. Characteristics of surfactant compositions in the oil dispersant Corexit EC9500A (Gong et al. 2014b, USEPA 2011). .....	22
Table 2-2. Salient physical and chemical properties of marine sediments used in this work.....	26
Table 2-3. Comparison of Corexit EC9500A concentrations in seawater measured by TOC analysis and by the surface tension based method. Number of replicate measurements = 5. ....	39
Table 3-1. Physicochemical characteristics of the sediment samples.....	48
Table 4-1. Output spectrum distribution of simulated solar irradiation (data were provided by the Newport Corporation).....	86
Table 4-2. Photodegradation rate constants of anthracene and 9,10-DMA under solar irradiation. ....	93
Table 5-1. Parameters of first-order kinetic models for photocatalytic degradation of phenanthrene by Pt(0)-deposited TNTs synthesized under different conditions.....	126
Table 5-2. Element weight percentage of Pt(0)-TNTs-600 and Pt(IV)-TNTs-600. ....	133
Table 5-3. Parameters of zero- and first-order kinetic models for photocatalytic degradation of phenanthrene by various Pt-based nanomaterials.....	135
Table 5-4. Apparent rate constant ( $k_1$ ) and phenanthrene removal efficiency by Pt(0)-TNTs-600 over 6 cycles of consecutive runs. ....	146
Table 5-5. Materials costs of Ti-based nanomaterials. ....	146



## List of Figures

Figure 1-1. Fate of spilled oil in the marine system. ....	11
Figure 2-1. Three regions of a typical surface tension vs ln[surfactant] plot. ....	25
Figure 2-2. Correlation of equilibrium surface tension vs. ln[Corexit EC9500A] in seawater... ..	30
Figure 2-3. Equilibrium surface tension vs. ln [Corexit EC9500A] at various levels of salinities. .....	34
Figure 2-4. Equilibrium surface tension vs. ln[Corexit EC9500A] at pH 6.0, 7.0, 7.9 and 9.0.. .	35
Figure 2-5. Equilibrium surface tension vs. ln[Corexit EC9500A] at various DOM levels.....	36
Figure 2-6. Equilibrium surface tension vs. ln[Corexit EC9500A] in seawater.....	38
Figure 3-1. Effects of three commercial oil dispersants on the settling kinetics of marine sediments: GB at 4 g/L (a), OS at 12 g/L (b), and EIWR at 14 g/L (c).....	55
Figure 3-2. Effects of three commercial oil dispersants on the particle size distribution of three marine sediments .....	57
Figure 3-3. Settling kinetics of OS sediment particles in the presence of various concentrations of Corexit EC9527A (a), and zeta potential of the sediment suspension (b).....	59
Figure 3-4. Particle size distribution (a) and settling velocity distribution curve (b) of suspended sediment particles (OS) in the presence of dispersant Corexit EC9527A .....	59
Figure 3-5. Settling kinetics of OS sediment in presence of individual key dispersant components, and effects of individual dispersant components on zeta potential of sediment suspension (b).....	61
Figure 3-6. Average hydrodynamic particle size of suspended particles in the presence of various key dispersant components. ....	62
Figure 3-7. Influence of pH on settling kinetics of OS sediment: .....	65
Figure 3-8. Settling kinetics of OS sediment particles at various NaCl concentrations .....	67
Figure 3-9. Settling kinetics of OS sediment particles with humic acid.....	68
Figure 3-10. Settling kinetics of sediment particles at 4 °C (a), and 25 °C (b). ....	69
Figure 3-11. Effects of WAO and DWAO on settling of OS sediment particles. ....	70
Figure 3-12. Sorption kinetics of phenanthrene and pyrene in the presence or absence of dispersant (Corexit EC9527A). ....	71
Figure 3-13. TPH distributions on seawater surface, in seawater column or sediment in various systems.....	72
Figure 3-14. Total PAHs distributions on seawater surface, in seawater column or sediment in various systems: seawater and oil (a), seawater, oil and sediment without dispersant (b), and seawater, oil and sediment with dispersant (c).....	73
Figure 3-15. Total alkanes distributions on seawater surface, in seawater column or sediment in various systems: seawater and oil (a), seawater, oil and sediment without dispersant (b), and seawater, oil and sediment with dispersant (c).....	74

Figure 3-16. Mass distribution of various PAHs on seawater surface (a), in seawater column (b) or sediment (c) in various systems: seawater and oil; seawater, oil and sediment without dispersant; and seawater, oil and sediment with dispersant, and mass distribution of various PAHs in the crude oil (d). .....	77
Figure 4-1. Experimental set-up of PAHs photodegradation. Simulated solar light system (a), photo-reactor (b). .....	85
Figure 4-2. UV-vis absorbance spectrum of the UV cut-off filter.....	87
Figure 4-3. Effects of Corexit EC9500A on photodegradation of anthracene (a), and 9,10-DMA (b) in seawater.....	91
Figure 4-4. UV-Vis absorption spectra of anthracene (a), and 9,10-DMA (b) in seawater and Corexit EC9500A solution. Spectra were corrected by subtracting the absorption spectrum of seawater.. .....	100
Figure 4-5. First-order photodegradation kinetic plots of anthracene (a) and 9,10-DMA (b) under solar irradiation.....	93
Figure 4-6. Effects of various dispersants on photodegradation of 9,10-DMA in seawater (a), and their first-order kinetic plots (b).. .....	94
Figure 4-7. Effects of various dispersant components on the photodegradation of 9,10-DMA in seawater. ....	95
Figure 4-8. UV-Vis absorption spectra of 9,10-DMA, Tween 85, and Corexit EC9500A in seawater.. .....	96
Figure 4-9. 9,10-DMA concentration at different depth in the photo-reactor in the presence of Corexit EC9500A or individual components.. .....	98
Figure 4-10. Contributions of visible irradiation in the solar light to the photolysis of anthracene (a) and 9,10-DMA (b) in the absence/presence of Corexit EC9500A.....	101
Figure 4-11. Effects of DO on the photodegradation of anthracene (a) and 9,10-DMA (b) in the presence or absence of Corexit EC9500A.....	103
Figure 4-12. Contributions of radicals $\bullet\text{OH}$ , $^1\text{O}_2$ , $\bullet\text{O}_2^-$ to the photolysis of anthracene in the absence (a) and presence (b) of Corexit EC9500A; to the photolysis of 9,10-DMA in the absence (c) and presence (d) of Corexit EC9500A.....	107
Figure 4-13. Fluorescence spectra of anthracene (a) and 9,10-DMA (b) in the absence/presence of Corexit EC9500A.....	109
Figure 4-14. Proposed photodegradation pathway of anthracene (a) and 9,10-dimethylanthracene (b) in seawater by simulated sunlight. ....	111
Figure 4-15. Peak area of detected dispersants compounds before and after solar irradiation... ..	112
Figure 5-1. Photocatalytic degradation of phenanthrene by various Pt(0)-deposited TNTs synthesized at different Pt loadings (a) and calcination temperatures (b). .....	125
Figure 5-2. TEM images of $\text{TiO}_2$ (P25) (a), TNTs (b), Pt(0)-TNTs-600 (c), and EDS spectra (d) of Pt(0)-TNTs-600. ....	128
Figure 5-3. XRD patterns of various Ti-based materials.....	130
Figure 5-4. FTIR spectra of various Ti-based materials.....	131
Figure 5-5. XPS survey spectra (a) and high resolution of Pt 4f (b) for Pt(0)-TNTs-600 and Pt(IV)-TNTs-600. ....	132

Figure 5-6. Photocatalytic degradation of phenanthrene by various Ti-based materials (a), and linear first-order model fitting for different materials (b). .....	134
Figure 5-7. DRS UV-vis spectra of TNTs, Pt(0)-TNTs-600 and Pt(IV)-TNTs-600. ....	136
Figure 5-8. Contribution of UV and visible irradiation for photocatalytic degradation of phenanthrene by different materials.. .....	137
Figure 5-9. PL spectra of various Ti-based materials under solar irradiation.. .....	139
Figure 5-10. Formation of H <sub>2</sub> O <sub>2</sub> in various nanomaterial suspension under solar irradiation. ..	140
Figure 5-11. Schematic illustration of enhanced photocatalytic activity of Pt(0)-TNTs-600 (a) and Pt(IV)-TNTs-600 (b).....	143
Figure 5-12. Comparison on sedimentation kinetics of TiO <sub>2</sub> , TNTs and Pt(0)-TNTs-600.. .....	144
Figure 5-13. Reuse of Pt(0)-TNTs-600 in 6 consecutive runs for photocatalytic degradation of phenanthrene.....	145

## **Chapter 1. General Introduction**

### **1.1. Introduction of oil spill and wastewater from oil industry**

Petroleum is the largest energy source consumed in the US, making up approximately 40% of the total energy consumption. The petroleum production and refining industry in the US mainly resides in the Gulf Coast region (Apergis and Payne 2010). During the exploration, transportation, refining, consumption, or waste management, oil may be released into water from routine or accidental releases (Gong et al. 2014a). In history, huge amounts of oil have been accidentally released into the environment, especially the marine environment. For example, the *Tsesis* (1977), *Ixtoc 1* (1979), *Antonio Gramsci* (1979), *Exxon Valdez* (1989), *Nakhodka* (1997), *Hebei Spirit* (2007) and *Deepwater Horizon (DwH)* oil spill (2010) are the most known oil spills (Gesteira and Dauvin 2000, Jung et al. 2015). The wastewater from oil industry, such as oil field wastewater and refinery wastewater, are rich in oil components, which can cause severe pollution if discharged into the environment without proper treatment (Asatekin and Mayes 2009, McCormack et al. 2001).

#### **1.1.1. Oil spill**

The oil spills frequently happen due to well blow-outs (e.g. *Ixtoc 1*, *DwH* oil spill) or tanker spills (e.g. *Exxon Valdez*, *Hebei Spirit*, *Prestige*, and *Torey Canyon* oil spill). The spilled oil can spread expansively depending on tide, wind, and current when they occur offshore, and cause

widespread damage to the marine environment. The most notable oil spill accidents are reviewed in this part.

The *Ixtoc 1* oil spill in June of 1979 released ca. 475,000 tons of crude oil into the Gulf of Mexico. After the blowout of the offshore oil rig, oil continued to be released into the open ocean for 9 months. The spilled oil was dispersed by current and wind and formed a brown and orange water-in-oil emulsion near the well head (Patton et al. 1981). This accident had been considered as the largest offshore oil spill until the *DwH* oil spill.

In April 2010, the *DwH* oil platform exploded and sank about 41 miles off the Louisiana coast, and approximately 655,000 tons of crude oil were released into the Gulf of Mexico within 87 days, which is the worst marine oil spill in the US history (McNutt et al. 2012). The crude oil was released from the Macondo well-head (1500 m depth), and the long travel distance to the surface greatly enhanced the partitioning of hydrocarbons into the aqueous phase (Reddy et al. 2012). Together with the application of dispersant, the amount of spilled oil in the water column was greatly increased. After the *DwH* oil spill, the progression of spilled oil along with the effectiveness and toxicity of oil dispersant were extensively studied (Cornwall 2015, Kleindienst et al. 2015a).

In March 1967, the tanker *Torrey Canyon* ran aground on a reef and spilled approximately 60,000 tons of crude oil in the ocean near the England coast (O'Sullivan and Richardson 1967). Large quantities of detergent were used to emulsify the spilled oil; this is considered as the first time a large amount of “dispersant” was used to disintegrate spilled oil. However, the toxic detergent led to widespread environmental damage and motivated researchers to develop new dispersants with lower toxicity (Lessard and Demarco 2000).

In March 1989, the *Exxon Valdez* oil spill released ca. 34,000 tons of Alaska North Slope crude oil into the Prince William Sound, which affected ca. 2000 miles of coastline (Malakoff and Pegau 2014). It was considered as the largest oil spill in the US at that time (Incardona et al. 2013). The relatively low water temperature and short travel distance to water surface eliminated a portion of dissolved crude oil in seawater, which was beneficial for the following clean-up operation. Bioremediation was extensively used to naturally degrade the oil residual and mitigate the negative ecological impact on the intertidal communities (Bragg et al. 1994).

In November 2002, the tanker *Prestige* broke in two and released approximately 77,000 tons of heavy fuel-oil into the ocean off the Galicia coast (NW Spain). The wind and sea-current moved ca. 60,000 tons of emulsified oil to the NW Spanish coast, and polluted more than 800 km of the coastline (González et al. 2006). Researchers found that the spilled oil had undergone a low degree of natural weathering even 1 year after the spill, indicating that the heavy oil is relatively persistent in the environment (Díez et al. 2007).

In December 2007, the *Hebei Spirit* oil spill released approximately 10,900 tons of Middle East crude oils off the west coast of the Republic of Korea, which polluted ca. 375 km of coast. The wide geographic spread of crude oil extensively damaged the mariculture resources and fishery industries in the polluted area (Kim et al. 2013b). This spill reveals the importance of interwoven physical, chemical and biological processes in regulating the fate and transport of crude oil through the ocean environment (Reddy et al. 2012).

### **1.1.2. Oil contaminated wastewater from industry**

For the oil industry, the production of 1 tons of gasoline will consume 2.8–6.6 tons of water in the US; for over 55% of the oil from Canadian Oil Sands, 5.2 tons of water will be consumed for producing one ton of gasoline (Kujawski 2009). Therefore, a huge amount of wastewater is produced by the oil industry. Among the different stages of oil refinement, the oil drilling and refinery processes produces the most wastewater.

The oil drilling operation generates a large amount of wastewater. An example of this would be the drilling and fracturing of a well which consumes approximately 19,000 tons of water. Accordingly, huge amounts of wastewater are produced, which generally contains oil or gas, throughout the productive lifetime of the well (Hickenbottom et al. 2013). An average refinery consumes 2.5 tons of water for processing one ton of crude oil (Stepnowski et al. 2002). Data from the literature shows that the globally produced wastewater from the oil and gas industry amounts to around 30 million tons per day, which is approximately 3 times the amount of oil produced (9.5 million tons/day), and the volume of generated wastewater is still increasing (Ahmadun et al. 2009).

The produced wastewater is a mixture of dissolved and dispersed oil compounds, minerals, and other solids. The oil contaminants in the wastewater include benzene, toluene, ethylbenzene, and xylenes (BTEX), aliphatic fraction (e.g. branched and cycloalkanes and saturated hydrocarbons), and polycyclic aromatic hydrocarbons (PAHs). The oil components, especially PAHs, are of acute toxicity and high persistence, which makes the wastewater difficult to be treated by biological methods (Stepnowski et al. 2002).

### **1.1.3. Oil components and toxicity**

Crude oil is a mixture of hydrocarbons, metals, and polar compounds (Simanzhenkov and Idem 2003). Hydrocarbons including saturated compounds (i.e. paraffins, isoparaffins, and cycloparaffins), aromatics (i.e. monocyclic aromatic hydrocarbons and PAHs), and olefins are predominant in crude oil. PAHs are aromatic compounds with two to eight conjugated benzene rings, which constitute 0.5 to 3 percent of the weight of the oil (Harvey 1991). PAHs are known as environmental persistent contaminants with toxic, carcinogenic, and mutagenic properties. Sixteen of the parent PAHs are listed as priority pollutants by United States Environmental Protection Agency (US EPA) (US EPA 2014). The abundance of alkylated PAHs is much higher than their parent PAHs in crude oil, which amount to 80-90% of the total PAHs) (Liu et al. 2012a, Wu et al. 2012), and they are even more toxic than their parent PAHs (Turcotte et al. 2011). However, most studies have only focused on the 16 parent PAHs specified in the priority pollutants list, and neglected the alkylated PAHs.

Crude oil in marine environments is harmful to the aquatic species due to the toxicity of the oil components, e.g. PAHs, and the suffocation effects of the viscous oil (Lin and Mendelssohn 2012). The toxicity of crude oil to fish and other organisms has been found to depend on the composition of the mixture of hydrocarbons. Low molecular weight (LMW) oil components, e.g. naphthalene, C1-C10 aliphatic are acutely toxic to fish by narcosis but contribute little to chronic toxicity since they are highly volatile and easy to dilute in water (Skadsheim et al. 2000). The medium molecular weight (MMW) oil components are responsible for the chronic toxicity of crude oil to aquatic species (Skadsheim et al. 2000). For instance, alkylated PAHs with three or four



rings were implicated as the primary compounds of oil toxicity to the development of fish embryos and may be related to the recruitment failure of fish where the spawning is found to be affected by an oil spill (Carls et al. 1999). High molecular weight (HMW) oil components, e.g. asphaltenes, waxes, and resins, have too low solubility to be taken by fish or microorganisms to reach toxic concentrations (Wu et al. 2012).

Dispersion of oil into droplets can increase the surface area of oil exposed to water, thereby, promoting the partitioning of oil components into the water phase. The application of chemical dispersant will greatly diffuse oil into droplets and increase the dissolved oil components in the water phase, thereby increase the toxicity of oil to the aquatic species (Kleindienst et al. 2015a). Wu et al. (2012) studied the chronic toxicity of four types of crude oils to the embryos of fish; the chemically dispersed crude oils were found to dramatically increased the toxicity, by 35 to 300 fold or greater.

## **1.2. Application of oil dispersants**

Dispersants are a mixture of nonionic and anionic surfactants as well as organic solvents (Place et al. 2010). Take Corexit EC9500A as an example: the major nonionic surfactants of this dispersant include ethoxylated sorbitan mono- and trioleates and sorbitan monooleate (commercially known as Tween 80, Tween 85, and Span 80), and the major anionic surfactant is sodium dioctylsulfosuccinate (DOSS). The solvents are a mixture of n-alkanes ranging from nonane to hexadecane, including Di(Propylene Glycol) Butyl Ether (DPnB), Propylene Glycol, 2-butoxyethanol etc. (Mill et al. 1981, Place et al. 2010).

Oil dispersants have been widely applied to disintegrate spilled oil slicks into fine droplets, thereby facilitating dispersion of oil into water column and accelerating the natural attenuation processes (Griffiths 2012, Lessard and Demarco 2000, Prince et al. 2016). When applied, oil dispersants embed themselves at the interfaces between oil and water due to the amphiphilic nature of the surfactant molecules, which lowers the interfacial tension and facilitates the formation and entrainment of small (<100  $\mu\text{m}$ ) oil-surfactant droplets into the water column (Clayton 1993, Singer et al. 1996).

Oil dispersants have been employed in several major oil spill accidents, and over the years, this approach has evolved into a major countermeasure to mitigate the adverse effects of oil spills (Griffiths 2012, Lessard and Demarco 2000). The appearance of low toxicity and high-efficiency dispersant formulations makes the application of dispersants a major countermeasure to mitigate the adverse effects of oil spills (Griffiths 2012). Application of modern dispersants began in the *Torrey Canyon* oil spill in 1967, where 1000 tons of dispersants (primarily BP1002) were applied to treat the spilled Kuwait crude oil (Southward 1978). Since then, application of dispersants has evolved to be a common countermeasure for mitigating oil spills while the search for more effective and less toxic oil dispersants remains active (Lessard and Demarco 2000). In 1996, 12 tons of Corexit EC9500A was applied during the *Sea Empress* spill in the UK (Lessard and Demarco 2000), representing the first field application of this popular oil dispersant. In 1997, 10 tons of Corexit EC9500A was used in the *Captain* Spill in the North Sea to disperse 650 tons of spilled crude oil. In 1998, ~11.5 tons of Corexit EC9527A was sprayed in the offshore pipeline spill in Texas (Lessard and Demarco 2000). During the *DwH* oil spill, BP applied approximately

8000 tons of Corexit EC9500A and EC9527A to the surface (5100 tons) and wellhead (2900 tons) (Kujawinski et al. 2011), representing the single largest application of oil dispersants in history. The wide application of the dispersants, especially since the 2010 *DwH* oil spill, has triggered extensive investigations into their effectiveness, toxicity, environmental fate and transport (Anderson 2011, Goodbody-Gringley et al. 2013, Moles et al. 2002).

### **1.3. Dispersant analysis**

Since the dispersants have been extensively applied and investigated, it has been challenging to quantitatively analyze oil dispersants conveniently and economically. This is not only due to the complex nature of the mixture of a variety of dispersants and solvents, but also due to proprietary and incomplete information on the type and quantity of the dispersant components. For instance, the most common practice for analyzing Corexit EC9500A in water has been to analyze just one or possibly a few of the key dispersant components that can be quantified following the standard methods (Kujawinski et al. 2011). According to the EPA methods for detecting dispersants in water (USEPA 2010), DOSS and DPnB are analyzed by LC/MS/MS (Liquid Chromatography with Tandem-Mass Spectrometry) (detection limits = 20 and 125  $\mu\text{g/L}$ , respectively), and the other solvent components, such as Propylene Glycol and 2-Ethylhexanol, are solvent-extracted and then determined by GC/MS (Gas Chromatography-Mass Spectrometry) (detection limits = 10 and 500  $\mu\text{g/L}$ , respectively). Researchers have also reported methods for the analysis of nonionic surfactants. For example, Tween 80 can be analyzed by using HPLC-MS (detection limit = 0.01  $\mu\text{g/L}$ ) (Christiansen et al. 2011, Im et al. 2008). Scelfo and Tjeerdema (1991) proposed a method to measure the ethoxylated sorbitan esters (anionic surfactants in

Corexit EC9527A) concentration by incorporating ion-pair formation with bis (ethylenediamine) copper (II), then extracting and analyzing by flame atomic absorption spectroscopy. Similarly, Kasahara et al. (1995) developed a spectrophotometric method by using a trifluoromethyl derivative as a counter ion for extraction and quantification of anionic surfactants in seawater. However, these methods bear the following drawbacks: 1) They are quite costly, and/or time- and labor-consuming, especially for the LC/MS/MS method; 2) The results for individual components may not reflect the integrity of the dispersant as a whole; 3) The undisclosed components in a dispersant are neglected.

To quantify the concentration of Corexit EC9527A and Corexit EC9500A in aqueous solutions, Mitchell and Holdway (2000) applied a UV-Vis spectroscopic method, where the concentration is measured at a wavelength of 230 nm. The mean measured concentration ranged from 0 to 280 mg/L for Corexit EC9527A and 0 to 450 mg/L for Corexit EC9500A. However, the effects of water chemistry and environmental conditions on the viability of the methods were not addressed, though such factors are known to alter the UV-Vis spectra. Consequently, more rapid and economical analytical methods have been desired by the oil spill research community and relevant industries.

#### **1.4. Effect of dispersant on the transport of spilled oil**

Once the oil is released into the ocean, it will undergo complex physical, chemical and biological processes, including photooxidation, volatilization, biodegradation, sedimentation, etc. (as shown in **Figure 1-1**) (Joye 2015). The light fractions of crude oil, with a boiling point below

250 °C, can be volatilized quickly after the oil reaches the air-water interface (Kiruri et al. 2013). Photodegradation is a vehicle for transforming the oil components to acidic and phenolic compounds or even CO<sub>2</sub> (Board and Board 2003b), however, some intermediates produced by the photolysis process can be more toxic than the original oil (Board and Board 2003b). Biodegradation processes are important for the weathering of crude oil and are also considered as a remediation methods for spilled oil. However, the emulsification of spilled oil will make it less likely to be bioavailable (Prince et al. 2003). Formation of oil-sediment aggregates (OSAs) and tar balls during the oil weathering process involved in the adsorption of PAHs and other oil components (Kiruri et al. 2013), and the settling process of OSAs can transport oil components to the bottom of the ocean.

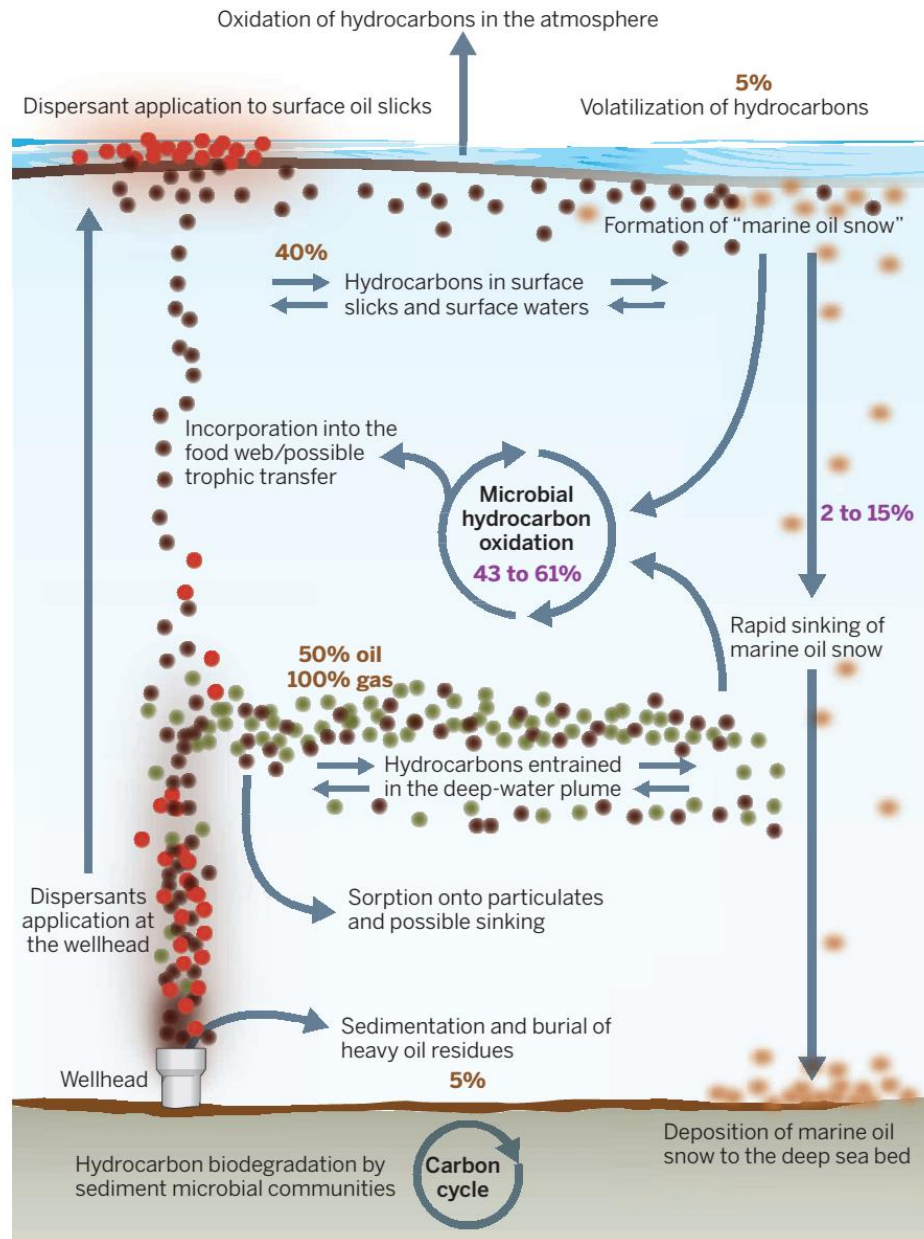


**Figure 1-1.** Fate of spilled oil in the marine system (Joye 2015). The number in brown color reflect the contribution of gas (green circles) and crude oil (brown circles) during the *DwH* oil spill (MacDonald 2010). The red circles refer to the applied dispersants.

Application of oil dispersant reduces the risk of oil slicks reaching the coastal areas and physical contamination (Almeda et al. 2014), but results in elevated oil droplet concentrations in the water column. For example, the volatile aromatic hydrocarbons in an oil plume during the *DWH* oil spill reached 139  $\mu\text{g/L}$  (Hazen et al. 2010). The high oil droplet concentration is favorable for the formation of oil sediment aggregates (OSAs) (Gong et al. 2014a), which can not only alter the settling behavior, but also alter the distribution and transport of important oil compounds that are associated with the aggregates. Guyomarch et al. (1999) found that the presence of the chemical dispersant, Inipol IP90, enhanced the formation of OSAs. Their wave tank experiment showed that approximately 80% of oil was entrained in the OSAs, which subsequently settled to the bottom of the tank. Our recent work also showed that the Corexit EC9500A promoted the formation of marine oil snow (MOS) and the partitioning of oil components into MOS (Fu et al. 2014b). Large quantities of crude oil will eventually reach the sediment of the ocean via participate in OSAs, MOS formation, or adsorption on the suspended particulate matters (SPMs), and would be followed by a settling process (Board and Board 2003a, Fu et al. 2014a, Luo et al. 2008, Mackay and Hickie 2000). Therefore, the settling process can be important for the fate of crude oil. However, little is known about effects of dispersants or dispersed oil on the transport of fine sediment particles, and how such particle-facilitate oil transport affects the fluxes and fate of oil components (Allan et al. 2012).

### **1.5. Photodegradation of oil components and the effects of dispersants**

Photodegradation is considered as a major abiotic process affecting spilled oil attenuation (Fu et al. 2014a, Nicodem et al. 2001). Under solar light, the chromophores compounds in oil absorb

solar radiation which initiates the photochemical reactions, resulting in the chemical transformation or even mineralization of oil components (D'Auria et al. 2008). The primary action spectrum for the photooxidation reaction is ultraviolet (UV) light ( $\lambda < 400$  nm) (Shankar et al. 2015), but which only takes up approximately 5% of the total solar light energy. Some crude oil compounds can absorb visible light (400–700 nm) and undergo photodegradation (Mallakin et al. 2000).

The photolysis of oil components, e.g. PAHs, involves both direct photolysis and indirect photolysis (Shankar et al. 2015). For direct photolysis, the pollutants absorb solar radiation and undergo chemical reaction, but it is limited by the amount of light screening of the aquatic system (Glover et al. 2014, Zepp and Cline 1977). Indirect photolysis of PAHs involves the excitation of photosensitizers, e.g. chromophoric dissolved organic matter (CDOM) or nitrate ( $\text{NO}_3^-$ ), resulting in the production of reactive intermediates, e.g. hydroxyl radical ( $\bullet\text{OH}$ ), singlet oxygen ( $^1\text{O}_2$ ), superoxide ( $\bullet\text{O}_2^-$ ), triplet excited CDOM ( $^3\text{CDOM}\bullet$ ) (Lam et al. 2003), which react with pollutants. CDOM is the primary photosensitizer to produce  $^1\text{O}_2$  and  $^3\text{CDOM}\bullet$  in surface water, and is usually the main source of  $\bullet\text{OH}$  (Latch and McNeill 2006; Takeda et al. 2004; Vione et al. 2006).

The extent of photodegradation depends on the spectrum, incident light intensity, optical properties of water, the presence of photosensitizers and oil contaminants themselves (Coleman et al. 2002). In a marine environment, the natural substances are found to either accelerate or decelerate the photolysis rate of oil components. For instance, some humic substances can absorb solar irradiation and be excited into their triplet states, which transfer energy to  $\text{O}_2$  to produce  $^1\text{O}_2$  (Minella et al. 2013). The low molecular weight humic acid is found to be more effective at



producing  $^1\text{O}_2$  under light irradiation (Minella et al. 2013). PAHs are known as good sensitizers for the production of  $^1\text{O}_2$ . The transformation of ground triplet state oxygen into the reactive singlet state ( $^1\text{O}_2$ ) needs more than 94 kJ/mol, and the excited PAHs, in both singlet and triplet state, at the sufficient energy level for exciting oxygen (Murov and Carmichael 1993). Dong et al. (2012) studied the photochemical formation of  $\bullet\text{OH}$  from effluent organic matter in treated wastewater, and found that the nitrate and dissolved organic matter in the water phase are potential sources of  $\bullet\text{OH}$  during the photolysis process.

The presence of surfactants or dispersants in the aqueous phase are reported to alter the photooxidation rate of oil components. An (2001) studied the photodegradation of phenanthrene and pyrene under UV light in the presence of surfactants (LiFOS), and found the monomeric surfactants enhanced the photolysis of PAHs, but he did not reveal the mechanism for the accelerated PAHs photolysis. Gong et al. (2015) studied the effects of oil dispersant (Corexit EC9500A) on the photodegradation of pyrene in seawater, where the presence of dispersant increased the photolysis rate of pyrene. However, the key dispersant components were not studied, and their roles on promoting the photolysis rate should be investigated deeper. Meanwhile, the effects of dispersants on the photolysis of alkylated PAHs are still lacking.

## **1.6. Photocatalytic degradation of PAHs**

The oil industry produced a huge amount of wastewater. This PAHs contaminated water can be of acute toxicity and persistent, which makes the wastewater difficult to be treated by traditional biological methods (Stepnowski et al. 2002). Many methods, e.g. chemical oxidation,

electrochemical methods, activated carbon adsorption, and solvent extraction, have been applied to removal PAHs in water (Abdelwahab et al. 2009). However, these methods are always associated with problems such as low efficiency, high investment, high energy or material consumption, etc. (Abdelwahab et al. 2009). The photocatalytic degradation of PAHs, especially under solar light, is considered as a promising route for the removal of PAHs from water (Hoffmann et al. 1995).

Many photocatalysts, e.g.  $\text{TiO}_2$ ,  $\text{ZnO}$ ,  $\text{BiVO}_4$ , have been investigated for photocatalytic degradation of PAHs in water (Kohtani et al. 2005, Vela et al. 2012). Ireland et al. (1995) applied  $\text{TiO}_2$  to photocatalytically degrade 16 PAHs in water by UV light and found the degradation rates of PAHs were relatively slow. Pal and Sharon (2000) supported porous  $\text{TiO}_2$  particles on glass substrates to promote the photocatalytic activity, which showed elevated degradation efficiency for naphthalene and anthracene removal in the water phase. Vela et al. (2012) compared the effectiveness of  $\text{ZnO}$  and  $\text{TiO}_2$  for photocatalytically degrading a mixture of 5 PAHs in groundwater under natural sunlight, and found 7–15 min and 18–76 min, respectively, are required for  $\text{ZnO}$  and  $\text{TiO}_2$  to remove 90% of the PAHs. Kohtani et al. (2005) compared the effects of pure and Ag-loaded  $\text{BiVO}_4$  on the photocatalytic degradation of 9 PAHs under visible light irradiation and found that both catalysts enhanced the photodegradation efficiency, and the loading of Ag accelerated the  $\bullet\text{OH}$  production.

$\text{TiO}_2$  is the most popular heterogeneous photocatalyst for organic pollutant removal; it has the advantages of low cost, nontoxicity, as well as excellent activities and stabilities. Since Fujishima and Honda (1972) discovered the photocatalytic splitting of water on  $\text{TiO}_2$  in 1972, interest in

application of TiO<sub>2</sub> as a photocatalyst has significantly increased, and it has become the most widely used photocatalyst for environmental application (Sires and Brillas 2012, Theron et al. 2008). Generally, the photocatalytic efficiency of TiO<sub>2</sub> is affected by two inherent limitations: 1) easy recombination of photo-generated holes and electrons (Malato et al. 2009), and 2) low visible/solar energy utilization efficiency (Liu et al. 2015a, Veldurthi et al. 2015). The large intrinsic band gaps of TiO<sub>2</sub> (3.2 eV for anatase and 3.0 eV for rutile) restricts the light-harvesting as the useful UV radiation only accounts for about 5% of sunlight irradiation, and the visible light includes 45% of the energy (Afzal et al. 2013, Shankar et al. 2015, Shannon et al. 2008). Therefore, efforts have been devoted to retard the recombination of electron-hole pairs, and enhance the photocatalytic activity of Ti-based catalysts under visible light (Doong et al. 2013, Sung-Suh et al. 2004, Veldurthi et al. 2015, Zhao et al. 2016). Noble metal ions (e.g. Pt, Au, Ag, etc.) doping/depositing is widely applied to facilitate the electron-hole separation and promote the production of reactive oxygen species (ROS) (Malato et al. 2009, Pan et al. 2016). Meanwhile, it also facilitates the absorption of visible light by narrowing the absorption band gaps (Burgeth and Kisch 2002). Among the commonly used noble metals, Pt is one of the most used dopants for modifying TiO<sub>2</sub> and titanate (Liu et al. 2011). It can provide the highest Schottky Barrier among the metal types that facilitate electron capture and produce longer electron-hole pair separation life time (Li and Li 2002). Meanwhile, the incorporation of Pt<sup>3+</sup> into TiO<sub>2</sub> can create a defect energy level, which extend visible light absorption (Li and Li 2002). Previous studies reveal that the Pt metal deposited TiO<sub>2</sub> induced a faster photocatalytic oxidation rate of o-cresol than TiO<sub>2</sub> (P25) (Chen et al. 2007), and Pt(IV) modified TiO<sub>2</sub> is found to be more active than TiO<sub>2</sub> (P25) upon UV irradiation for 4-chlorophenol degradation (Burgeth and Kisch 2002). However, to the best of our

knowledge, the effects of Pt forms (reduction state of Pt(0) and oxidation state of Pt(IV)) on modifying TiO<sub>2</sub> or other TiO<sub>2</sub> based materials are not well investigated in previous studies.

### **1.7. Objectives**

The key research objectives were to: 1) establish a quick and low-cost method to measure dispersant concentration in seawater; 2) investigate effects of oil dispersants (Corexit EC9500A, Corexit EC9527A, and SPC 1000) on the settling performance of suspended sediment particles and sediment-associated transport of oil components, and on the enhanced photolysis of PAHs and alkylated PAHs; and 3) synthesize and test a new class of photocatalyst for PAHs degradation.

The specific objectives were to:

- Propose and test a new method to determine dispersant concentration in seawater;
- Test the accuracy of the new method under various environmental conditions, e.g. pH, salinity, DOM concentration;
- Test the effects of three model dispersants on the settling velocity of suspended sediment particles, find the most effective ingredients for enhancing the settling performance and elucidate the mechanism;
- Evaluate the effects of dispersants on the transport of sediment-associated oil components;
- Evaluate the effects of oil dispersants and the dispersant components on the photolysis of anthracene and its alkylated homolog (9,10-dimethylanthracene) under simulated solar light;

- Elucidate the mechanisms of anthracene and 9,10-dimethylanthracene photodegradation in the presence/absence of dispersant;
- Synthesize a new class of platinum-titanate nanotube for catalytically degrading phenanthrene in the aqueous phase, and find the optimal synthesis condition;
- Characterize the new material and elucidate the mechanism on enhancing photocatalytic activity, and test the separation property and reusability of the new catalyst.

## 1.8. Organizations

This dissertation includes six chapters and the appendix part, each chapter is formatted as a standalone paper in the style of *Water Research* except for Chapter 1 (General Introduction) and Chapter 6 (Conclusions and Suggestions for Future Research). **Chapter 1** gives a general introduction of the background and outlines the objectives of this dissertation. **Chapter 2** describes a new method that determines the Corexit EC9500A concentration in seawater by measuring the surface tension of the solution. **Chapter 3** investigates the effects of oil dispersants on the settling behavior of suspended sediment particles as well as on the distribution and transportation of oil and key oil components in sediment-seawater systems, and explores the effects of dispersants under various environmental conditions. **Chapter 4** investigates the effects of oil dispersants on the photodegradation of anthracene and 9,10-dimethylanthracene in the marine environment. The photodegradation mechanisms and pathways are elucidated. **Chapter 5** investigates the photocatalytic degradation of phenanthrene by a new class of Pt-deposited titanate nanotubes under simulated solar light, the mechanisms are investigated and reusability of this material is evaluated. **Chapter 6** gives a summary of the key conclusions of all the research and suggestions

for future work. The **appendix part** describes the feasibility and efficiency of the carboxyl methyl cellulose stabilized zero-valent iron (ZVI) nanoparticles for reductive removal of nitrobenzene in aqueous and soil phase. The mechanisms of nitrobenzene reduction are studied, and effects of environmental parameters on the reduction rates were evaluated.

## **Chapter 2. A Surface Tension Based Method for Measuring Oil Dispersant Concentration in Seawater**

Many methods have been applied for determining the dispersant concentration in the aqueous phase, e.g. LC/MS/MS, GC/MS, HPLC-MS. However, these methods bear the drawbacks of high cost, the results for individual components don't always reflect the integrity of the dispersant as a whole, the undisclosed components in a dispersant are often neglected, and/or excessive time- and labor-consumption. In this section, a convenient and economical analytical method is proposed to measure the dispersant concentration in seawater.

### **2.1. Introduction**

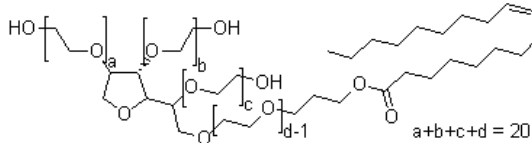
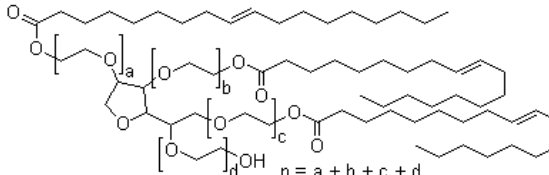
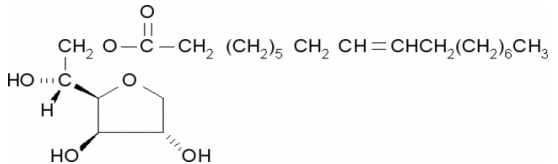
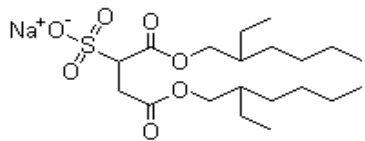
Oil dispersants have been widely employed to mitigate environmental impacts of spilled oil (Prince et al. 2016, Rahsepar et al. 2016). The application of modern dispersants began in the *Torrey Canyon* oil spill in 1967, where 1000 tons of dispersants (primarily BP1002) were applied to mitigate the spilled Kuwait crude oil (Southward 1978). Since then, application of dispersants has evolved to be a common countermeasure for mitigating oil spills, while the search for more effective and less toxic oil dispersants remains active (Lessard and Demarco 2000). In 1996, 12 tons of Corexit EC9500A was applied during the *Sea Empress* spill in the UK, representing the

first field application of this popular oil dispersant (Lessard and Demarco 2000). In 1997, 10 tons of Corexit EC9500A was used in the *Captain* Spill in the North Sea to disperse 650 tons of spilled crude oil. In 1998, ~11.5 tons of Corexit EC9527A was sprayed in the offshore pipeline spill in Texas (Lessard and Demarco 2000). During the Deepwater Horizon (DwH) oil spill in the Gulf of Mexico in 2010, BP applied approximately 8000 tons of Corexit EC9500A and EC9527A (Kujawinski et al. 2011), representing the single largest application of oil dispersants in the history.

Corexit EC9500A is a mixture of nonionic and anionic surfactants as well as organic solvents (Place et al. 2010). The major nonionic surfactants include ethoxylated sorbitan mono- and trioleates and sorbitan monooleate (commercially known as Tween 80, Tween 85, and Span 80), and the major anionic surfactant is sodium dioctylsulfosuccinate (DOSS). **Table 2-1** gives detailed information on the compositions of Corexit EC9500A. The solvents are a mixture of n-alkanes ranging from nonane to hexadecane, including Di(Propylene Glycol) Butyl Ether (DPnB), Propylene Glycol, and 2-butoxyethanol (Mill et al. 1981, Place et al. 2010). The wide application of the dispersant, especially since the 2010 *DwH* oil spill, has triggered extensive investigations into its effectiveness, toxicity, and environmental fate and transport (Anderson 2011, Goodbody-Gringley et al. 2013, Moles et al. 2002).



**Table 2-1.** Characteristics of surfactant compositions in the oil dispersant Corexit EC9500A (Gong et al. 2014b, USEPA 2011).

Surfactants	Ionic property	Molecular formula	Molecular weight (g/mol)	Critical micelle concentration (CMC) (mg/L)	Chemical structure
Polyoxyethylene (20) sorbitan monooleate (Tween 80)	Neutral	$C_{64}H_{124}O_{26}$	1310	14 (Yeom et al. 1995)	
Polyoxyethylene(20) sorbitan trioleate (Tween 85)	Neutral	$C_{60}H_{108}O_{8'}(C_2H_4O)_n$		23 (Wan and Lee 1974)	
Sorbitan monooleate (Span 80)	Neutral	$C_{24}H_{44}O_6$	428.60	35000 (Ross and Olivier 1959)	
Sodium dioctyl sulfosuccinate (SDSS or DOSS)	Anionic	$C_{20}H_{37}NaO_7S$	444.56	578 (Yehia 1992b)	

Yet, it has been challenging to quantitatively analyze oil dispersants conveniently and economically. This is not only due to the complex nature of the mixture of a variety of dispersants and solvents, but also proprietary and incomplete information on the type and quantity of the dispersant components. For instance, the most common practice for analyzing Corexit EC9500A in water has been to analyze one or some of the key dispersant components that can be quantified following the standard methods (Kujawinski et al. 2011). According to the EPA methods for detecting dispersants in water (USEPA 2010), DOSS and DPnB are analyzed by LC/MS/MS (Liquid Chromatography with Tandem-Mass Spectrometry) (detection limits = 20 and 125  $\mu\text{g/L}$ , respectively); and the other solvent components, such as Propylene Glycol and 2-Ethylhexanol, are solvent-extracted and then determined by GC/MS (Gas Chromatography-Mass Spectrometry) (detection limits = 10 and 500  $\mu\text{g/L}$ , respectively). Researchers have also reported methods for the analysis of nonionic surfactants. For instance, Tween 80 can be analyzed by using HPLC-MS (detection limit = 0.01  $\mu\text{g/L}$ ) (Christiansen et al. 2011, Im et al. 2008). Scelfo and Tjeerdema (1991) developed a method to monitor the anionic surfactant (ethoxylated sorbitan esters) of Corexit EC9527A by incorporating ion-pair formation with bis(ethylenediamine) copper (II), then extracting and analyzing the complex by flame atomic absorption spectroscopy. Similarly, Kasahara et al. (1995) developed a spectrophotometric method by using a trifluoromethyl derivative as a counter ion for extraction and quantification of anionic surfactants in seawater. However, these methods bear the following drawbacks: 1) they are quite costly, and/or time- and labor-consuming, especially for the LC/MS/MS method, 2) the results for individual components

may not reflect the integrity of the dispersant as a whole, and 3) the undisclosed components in a dispersant are neglected.

To quantify the concentration of Corexit EC9527A and Corexit EC9500A in aqueous solutions, Mitchell and Holdway (2000) applied a UV-Vis spectroscopic method, where the concentration is measured at a wavelength of 230 nm. The mean concentration ranged from 0 to 280 mg/L for Corexit EC9527A and 0 to 450 mg/L for Corexit EC9500A. However, the effects of water chemistry and environmental conditions on the viability of the methods were not addressed, though such factors are known to alter the UV-Vis spectra. Consequently, more rapid and economical analytical methods have been desired by the oil spill research community and relevant industries.

It has been observed that surface tension ( $\gamma$ ) is correlated with the concentration of a surfactant (Fu et al. 2015, Menger et al. 2009, Myers 1999). Specifically, Menger et al. (2009) observed that when  $\gamma$  is plotted against  $\ln[\textit{surfactant}]$ , the curve can be divided into three distinct regions (**Figure 2-1**): Region A:  $\gamma$  slightly decreases with increasing surfactant concentration; Region B:  $\gamma$  decreases sharply and almost linearly with increasing surfactant concentration; and Region C: the slope abruptly levels off (i.e.,  $\gamma$  remains nearly constant) at the surfactant concentration above the CMC value. Conventionally, it is assumed that the surfactant is saturated at the air/water interface throughout Region A (Perez et al. 1998, Vader 1960), which allows the calculation of the area-per-molecule via the classic Gibbs equation (Menger et al., 2009). In an effort to determine the CMC value of oil dispersants, Gong et al. (2014b) observed that the Corexit EC9500A concentration is linearly correlated to  $\gamma$  of solution. Hence, the concentration of the dispersant may

be measured by indirectly measuring the combined effect of the dispersant components, i.e., by gauging the surface tension of a dispersant solution.

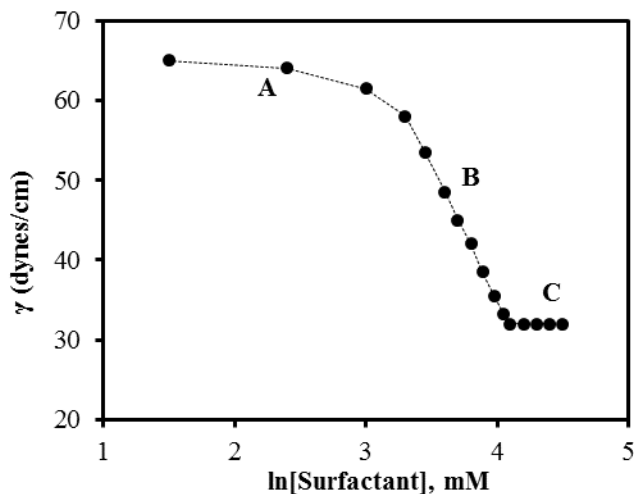


**Figure 2-1.** Three regions of a typical surface tension vs  $\ln[\text{surfactant}]$  plot (Menger et al. 2009).

Based on the linear correlation between  $\gamma$  and dispersant concentration (region B), the goal of this study was to develop and validate a new analytical method for simple and rapid quantification of oil dispersants in seawater. To illustrate the concept, Corexit EC9500A was used as the model dispersant and Gulf coast seawater as the prototype solution matrix. The specific objectives were to: 1) establish the linear correlation between  $\gamma$  and  $\ln$  [dispersant concentration], 2) assess the effects of environmental factors, such as salinity, pH, and dissolved organic matter (DOM) on the correlation, and 3) identify the applicable conditions as well as constraints of the method. The new method is expected to provide a convenient and economical analytical tool for researchers and practitioners in the field of oil spill and marine pollution.

## 2.2. Experimental methods

### 2.2.1. Materials

Seawater sample was collected at the Grand Bay area, AL, USA in the Gulf of Mexico (N30.37873, W88.30679). It was stored in sealed containers at 4 °C and filtered through 0.22 µm membrane to remove suspended solids before use. Marine sediment was collected from the Ocean Springs National Seashore Park, MS, USA (N30.39772, W88.79175). The sediment was classified as loamy sand sediment and the organic matter content is 1.6% (sediment analysis was performed by the Soil Testing Laboratory at Auburn University, more physicochemical characteristics of sediment are shown in **Table 2-2**).

**Table 2-2.** Salient physical and chemical properties of marine sediment used in this work.

pH <sup>a</sup>	SOM <sup>b</sup> %	Cation Exchange Capacity Meq/100g			Taxonomy <sup>c</sup>	Sand <sup>d</sup> %	Silt <sup>d</sup> %	Clay <sup>d</sup> %	
6.4	1.6	6.6			Loamy sand	81.6	15.3	3.1	
Ca	K	Mg	P	Al	B	Zn	Mn	Na	Fe
pm	ppm	ppm	ppm	ppm	ppm	ppm	ppm	ppm	ppm
441.9	182.7	314.5	9.1	87.7	3.23	5.2	3.9	4118.4	73.1

<sup>a</sup> Sediment pH was measured on a 1:1 sediment:water mixture via the Reference Soil Test Methods (UGA 1983).

<sup>b</sup> SOM (soil organic matter) was obtained by thermogravimetric method (Davies 1974).

<sup>c</sup> Sediment texture was conducted following the hydrometer method (Bouyoucos 1962).

<sup>d</sup> Categorized based on USDA-definition.

Note: Metal contents were measured per EPA method 3050B. Soil calcium, magnesium, potassium, and sodium were first extracted per the Mehlich 1 procedure, filtered through a #1 qualitative filter paper, and then determined by ICP using a Varian Vista-MPX Radial Spectrometer.

All chemicals used in this study were of analytical or higher grade, and were used as received, including humic acid (Fluka Chemie, Switzerland), sodium hydroxide (NaOH, Fisher Scientific, Fair Lawn, NJ, USA), and hydrochloric acid (HCl, 36.5-38.0%, Mallinckrodt Chemical, St. Louis, MO, USA). Corexit EC9500A was acquired per courtesy of Nalco Company (Naperville, IL, USA). A Corexit EC9500A stock solution was prepared at 1 g/L by mixing Corexit EC9500A and seawater in a glass flask under magnetic stirring for 1 h, and then the desired working solutions (up to 200 mg/L) were obtained by diluting the stock solution with seawater. Serial dilution was avoided to reduce cumulative error (Scelfo and Tjeerdema 1991).

### **2.2.2. Effects of environmental factors**

Effects of environmental factors on the viability of the surface-tension based method were assessed at various solution salinities, pH and DOM concentrations. The pH of the seawater was adjusted using HCl (0.5 M) or NaOH (0.5 M) solution from the initial 7.9 to the final value of 6.0, 7.0 or 9.0. Different DOM concentrations were achieved by diluting a DOM stock solution (550 mg/L as TOC), which was obtained by dissolving the standard humic acid into seawater. The salinity effects were tested using artificially prepared seawater at various salinity levels (0, 1%,

2%, and 4% (expressed as wt.% of salt) following the method by Kester et al. (1967). The effects of the environmental factors on the surface tension measurement as well as on the  $\gamma - \ln[C]$  ( $C$  is the dispersant concentration) correlations were evaluated by measuring the  $\gamma - \ln[C]$  curves under various pH, salinity and DOM levels.

In marine oil spill studies, mixed sediment-seawater systems are often encountered (Zhao et al. 2015). To determine the effects of possible sediment exudates, surface tension was also measured using sediment amended seawater. The sediment amended seawater was prepared as follows: first, mix seawater with the sediment at a sediment/seawater ratio of 16 g/40 mL on a rotator at 50 rpm for 48 h; then separate the solid and liquid by centrifugation ( $1359 \times g$  for 5 min) and collect the supernatant. The sediment amended seawater (i.e., the supernatant) had a salinity of 3.5 wt.%, pH 7.0, a DOM concentration of 1.3 mg/L as TOC.

### **2.2.3. Analytical methods**

A Du Noüy Tensiometer (CSC scientific 70535 series, Fairfax, VA, USA) was used to determine the surface tension of the dispersant solutions. The Du Noüy ring method (Tuckermann 2007) has been commonly used to measure the surface tension of solutions. The details on the measuring principle and procedure can be found elsewhere (Lunkenheimer and Wantke 1981, Noüy 1925). Briefly, a platinum ring, which is linked with a balance arm, is slowly lifted from the surface of a liquid, then the force required to break the surface (overcome the surface tension) is measured. To this end, each 20 mL of a dispersant solution was added in  $60 \times 15$  mm glass Petri dishes. The samples were kept still in the dishes for 30 min to assure the system equilibrium was

achieved, i.e., the chemical potential at the interface is equal to that of the bulk solution (Eastoe and Dalton 2000). The tensiometer was calibrated on a daily basis, and all measurements were performed in duplicate and at  $25 \pm 1$  °C. A Dohrmann Phoenix 8000 TOC Analyzer (Tekmar Dohrmann, Cincinnati, OH, USA) was used to analyze DOM and Corexit EC9500A as total organic carbon (TOC).

## 2.3. Results and discussion

### 2.3.1. Analysis of dispersant samples

**Figure 2-2** shows the change of surface tension as a function of  $\ln[\text{dispersant}]$ . The general trend was similar to the correlation of surface tension vs dispersant concentration as in **Figure 2-1**. When the dispersant concentration is lower than 0.2 mg/L (or  $\ln C < -1.6$ ) (Region A), the dispersant had little effect on surface tension; however, in Region B where the dispersant is  $>0.2$  mg/L but  $< \text{CMC}$  (23.5 mg/L), the surface tension decreased sharply and linearly with increasing dispersant concentration with a slope ( $k$ ) of -7.8; the linear correlation remains in region C (dispersant  $> \text{CMC}$ ) but with a much lower slope ( $k = -2.0$ ).



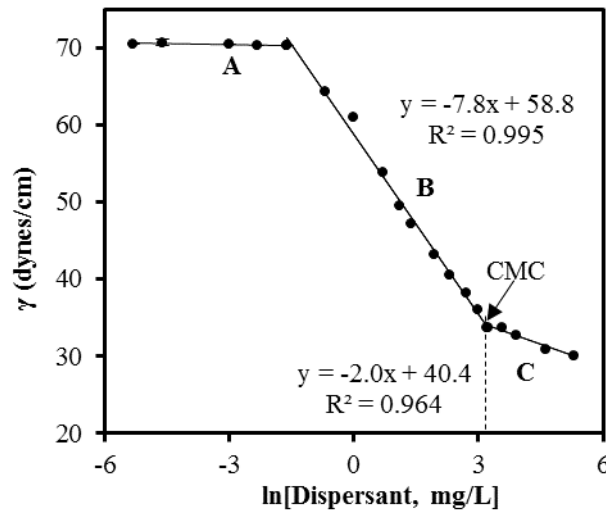


**Figure 2-2.** Correlation of equilibrium surface tension vs.  $\ln[\text{Corexit EC9500A}]$  in seawater. Experimental conditions: temperature =  $25 \pm 1$  °C; pH = 7.9; salinity = 3.15 %; DOM = 0.2 mg/L.

The resulting correlation equations are as follows:

$$\gamma = -7.8 \cdot \ln(C) + 58.8, R^2 = 0.995, p < 0.001 \quad (0.2 \text{ mg/L} < C < 23.5 \text{ mg/L}) \quad \text{(Eq. 2-1)}$$

$$\gamma = -2.0 \cdot \ln(C) + 40.4, R^2 = 0.964, p = 0.003 \quad (C > 23.5 \text{ mg/L}) \quad \text{(Eq. 2-2)}$$

where  $C$  is the dispersant concentration (mg/L) and  $R^2$  is the coefficient of determination. The low  $p$  values indicate that changes in the predictor variable ( $C$ ) are strongly associated with changes in the response variable ( $\gamma$ ).

According to the Gibbs equation (Adamson 2001, Li et al. 2013), the change in the surface tension with surfactant activity is described by

$$-d\gamma = RT \sum_i \Gamma_i d(\ln a_i) \quad (\text{Eq. 2-3})$$

where  $\Gamma_i$  is the surface excess of component  $i$ ,  $a_i$  is the activity of the component in the aqueous phase,  $R$  is the universal gas constant, and  $T$  is temperature (K).

When the concentration is below the CMC value, the activity can be approximated with the concentration for nonionic surfactants (Li et al. 2013). Thus, the Gibbs equation can be written as

$$\frac{d\gamma}{d(\ln C_i)} = -RT \sum_i \Gamma_i \quad (\text{Eq. 2-4})$$

where  $C_i$  is the surfactant concentration,  $d\gamma/d(\ln C_i)$  is the slope of the  $\gamma$ - $\ln C_i$  curves.

In accord with the Gibb's equation, **Figure 2-2** indicates that there exist three distinct levels of surface excess of the dispersant with three different slopes that correspond to the three regions. The observation agrees with the reported correlations in various surfactant systems (Lopez-Cervantes et al. 2013, Reichert and Walker 2013, Simister et al. 1992).

The observed  $\gamma$ - $\ln[C]$  curve mimics an S-shaped adsorption isotherm (Gong et al., (2014b)). In the low concentration range (Region A), the dispersant components prefer to partition into the solution phase more than the interface, which can be attributed to the enhanced dissolution effect of the mixed surfactants and co-solvents. As a result, a very flat slope was evident. In Region B, aggregates of the surfactants are formed (Gong et al. 2014b) and the partition becomes increasingly more favorable toward the interface, resulting in the sharp change of  $d\gamma/\ln[C]$ . At dispersant concentrations near or above the CMC (Region C), micelles (mainly the neutral surfactants) are

formed, and the surfactants prefer to partition into the micelles than accumulate on the interface (Li et al. 2013, Menger et al. 2009). Consequently, the slope of the  $d\gamma - \ln[C]$  line is abruptly changed. It is also noteworthy that the CMC value (578 mg/L) for the anionic surfactant (DOSS) (Yehia 1992a) is much higher than those for the non-ionic surfactants (e.g., 23 mg/L for Tween 85 and 14 mg/L for Tween 80). Namely, no micelles of the anionic surfactants are likely formed under the experimental conditions. Therefore, the much-reduced slope in Region C than in Region B is attributed to the formation of micelles of the non-ionic surfactants.

The findings indicate that despite being a complex mixture of surfactants and solvents, Corexit EC9500A behaves like a lumped or combined “surfactant”. While the lumped CMC value reflects the collective effect of the surfactants and co-solvents, the mixture CMC for the dispersant was nearly the same as that (23 mg/L) of Tween 85, slightly higher than that (14 mg/L) of Tween 80, but much lower than that (578 mg/L) of DOSS (Gong et al. 2014b), suggesting that Tween 85 plays a predominant role in the mixed micelles (Ahn et al. 2010), which can be attributed to its much large size, special molecular structure and possibly high fraction in the dispersant.

The correlation curve (**Eq. 2-1**) can be used to conveniently determine the concentration of Corexit EC9500A in the concentration range from  $>0.5$  to  $<23$  mg/L by simply measuring the surface tension using a simple and low-cost interfacial Tensiometer. The detection limit may be lowered if the correlation line in Region A is determined accurately, which may need a more sophisticated Tensiometer. When the dispersant concentration is above the CMC, **Eq. 2-2** can be used, or alternatively, the solution can be diluted to the concentration window that is suitable for **Eq. 2-1**.

The  $\gamma - \ln[C]$  correlation in Region B was highly reproducible; experimental results showed that the relative standard deviation was within 3% from 5 replicate measurements. Based on 10 replicate measurements of blank and Corexit EC9500A samples (Harris 2010), the detection limit with **Eq. 2-1** was determined at 0.5 mg/L.

### **2.3.2. Effects of environmental factors on surface tension analysis**

#### *2.3.2.1. Salinity*

**Figure 2-3** shows that the solution salinity can significantly decrease surface tension of the dispersant solution. The effect is more significant when the salinity was increased from 0 to 1%. This phenomenon can be interpreted by the increased surfactant adsorption onto the air/water interface with the increase of electrolyte concentration (Xu et al. 2013), known as the “salting out” effect (Prosser and Franses 2001). Similar findings were also reported by Persson et al. (2003), who studied the correlation between surface tension-concentration of surfactant sodium dodecyl sulfate (SDS) at various NaCl concentrations. Therefore, proper standard curves will need to be developed to assure the consistent salinity between samples and the standards. It is noteworthy that despite the different levels of surface tension at different salinities, the correlation lines appear parallel to each other, i.e., they have nearly the same slope. Therefore, the same standard curve may be scaled for measuring  $\gamma$  at various salinities by correcting the difference in the intercept.

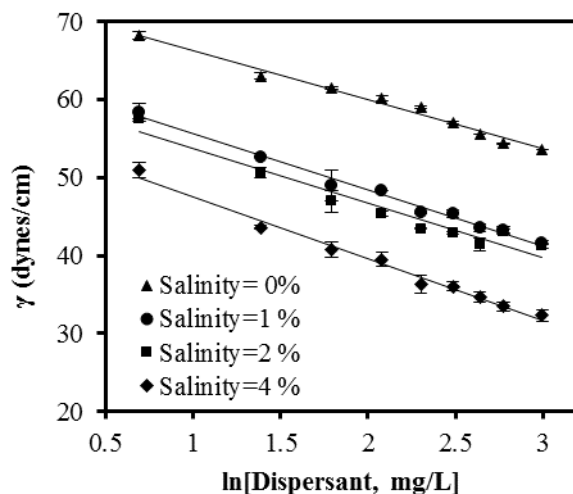


**Figure 2-3.** Equilibrium surface tension vs.  $\ln$  [Corexit EC9500A] at various levels of salinities. Experimental conditions: Corexit EC9500A concentration = 2 to 20 mg/L in seawater; temperature =  $25 \pm 1$  °C. Data were plotted as mean of duplicates, and error bars indicate standard error range.

#### 2.3.2.2. Effects of pH

**Figure 2-4** shows that the  $\gamma$ -  $\ln[C]$  correlation remained statistically unchanged ( $p > 0.05$ ) when the solution pH was raised from 7.9 to 9.0; however, the surface tension dropped significantly as the pH was lowered from 7.9 to 6.0.

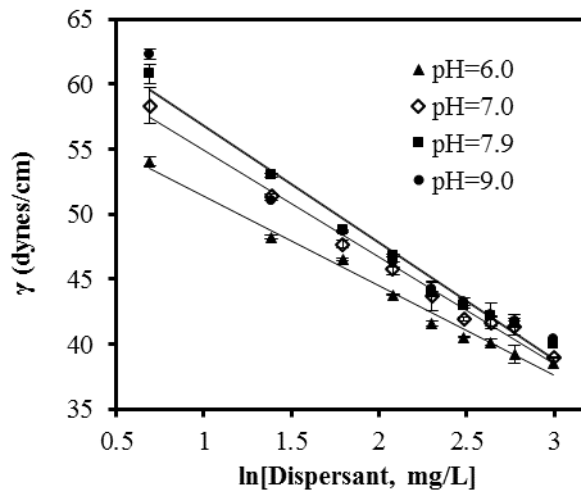


**Figure 2-4.** Equilibrium surface tension vs.  $\ln[\text{Corexit EC9500A}]$  at pH 6.0, 7.0, 7.9 and 9.0. Experimental conditions: Corexit EC9500A concentration = 2 to 20 mg/L in seawater; temperature =  $25 \pm 1$  °C; salinity = 3.15 %; DOM = 0.2 mg/L.

The anionic surfactant, i.e., DOSS, of Corexit EC9500A undergoes increasing protonation as pH decreases (Underberg and Lingeman 1983). While fully deprotonated DOSS is rather hydrophilic (Yates and von Wandruszka 1999), the protonation at lower pH renders the hydrophilic heads of DOSS less polar. As a result, more surfactant molecules migrate to the surface, resulting in decreased surface tension at lower pH. **Figure 2-4** also indicates that the pH effect is more profound at lower dispersant concentrations.

#### 2.3.2.3. Effects of DOM

**Figure 2-5** shows that the presence of DOM at 5 mg/L (as TOC) significantly decreased the surface tension, and the effect was more evident at lower dispersant concentrations ( $<2$  mg/L).

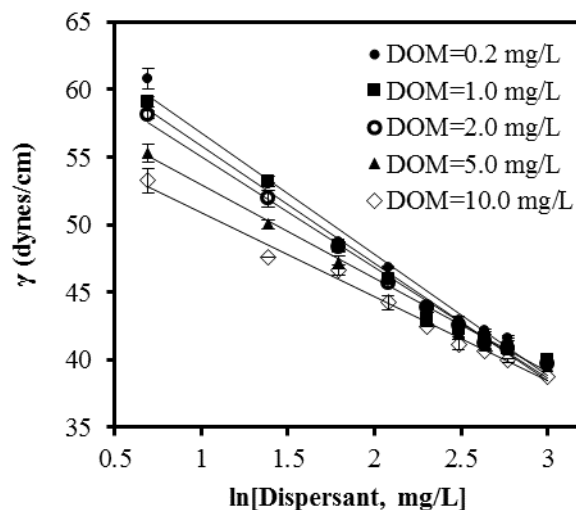


**Figure 2-5.** Equilibrium surface tension vs.  $\ln[\text{Corexit EC9500A}]$  at various DOM levels (measured as TOC). Experimental conditions: Corexit EC9500A concentration = 2 to 20 mg/L in seawater; temperature =  $25 \pm 1$  °C; pH =  $7.9 \pm 0.5$ ; salinity = 3.15 %.

Due to the amphiphilic characteristics of some components in DOM, such as humic acid, DOM can affect both the surfactant activity and the surface excess (Yates and von Wandruszka 1999). The Szyskowski equation (Aumann et al. 2010, von Szyszkowski 1908) is often used to describe the effects of organic compounds, such as carboxylic acids, alcohols and esters, on the surface tension of aqueous solutions.

$$\gamma = \gamma_0 - \Gamma_{\max} RT \ln \left( 1 + \frac{c}{\beta} \right) \quad (\text{Eq. 2-5})$$

where  $\gamma$  and  $\gamma_0$  are surface tension for solution and pure water, respectively,  $\Gamma_{\max}$  is the maximum surface excess,  $c$  is the solute (DOM) concentration, and  $\beta$  is the inverse Langmuir adsorption coefficient. This equation predicts that increasing DOM decreases surface tension of a solution.

Lee and Hildemann (2013) measured the surface tension of humic acid solutions at 20 °C, and obtained the  $\Gamma_{\max}$  and  $\beta$  values by fitting the experimental surface tension data over a range of solute concentrations, where  $\Gamma_{\max} = 2.93 \pm 0.35 \times 10^{-6}$  mol/m<sup>2</sup>,  $\beta = 966 \pm 267 \times 10^{-3}$  g/kg. At low DOM concentrations, DOM affects the surface tension mainly by altering the surface excess of surfactants, while at elevated DOM concentrations, DOM may reduce both surface excess and the activity of surfactants, resulting in a lower  $\gamma$ .

#### *2.3.2.4. Effects of soluble components from marine sediment*

In sediment-water systems, it has been challenging to measure dispersant concentration due to interference from the soluble components from the sediment. **Figure 2-6** shows effects of sediment extracts on the surface tension. Compared with the seawater, the salinity of sediment amended seawater increased from 3.15 to 3.50 ‰, DOM increased from 0.2 mg/L to 1.3 mg/L, but pH decreased from 7.9 to about 7.0. It is evident from **Figure 2-6** that the effect of the sediment extracts on the surface tension measurement was statistically insignificant ( $p > 0.05$ ) despite the variations of the water chemistry conditions.



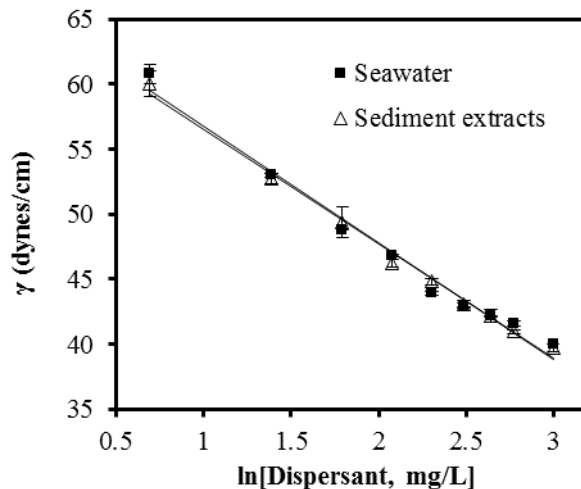


**Figure 2-6.** Equilibrium surface tension vs.  $\ln[\text{Corexit EC9500A}]$  in seawater and sediment extracts. Experimental conditions: Corexit EC9500A concentration = 2 to 20 mg/L; temperature =  $25 \pm 1$  °C; pH =  $7.9 \pm 0.5$ ; salinity = 3.15 %.

Taken together the results, the surface tension measurements will not be affected when the changes in salinity, DOM and pH are within the following limits: salinity change  $<0.3$  %, DOM  $<1.3$  mg/L as TOC, and  $7.0 \leq \text{pH} \leq 9.0$ . Separate  $\gamma - \ln[C]$  correlation equations will need to be established or corrected when changes in the water quality parameters exceed these criteria.

### 2.3.3. Accuracy of the method

To confirm the accuracy of this surface tension based method, the same Corexit EC9500A solutions at the dispersant concentrations of 1, 5, 10, 15, and 20 mg/L were analyzed by this method and by direct TOC analysis. **Table 2-3** gives the resulting dispersant concentration obtained independently with the two methods. The results show that the differences in the mean concentrations obtained by the two methods are statistically insignificant ( $p < 0.05$ ) except for the

case of 1 mg/L, and in all cases, the measurement errors were within 3.5% from the true values. Between the two methods, the relative standard deviation of the surface tension based method ranged from 2% to 5%, compared to from 4% to 53% for the TOC-based method, indicating that the new the method is of higher precision. At 1 mg/L, the TOC method is not accurate, while the surface tension method remained robust. The fluctuation of the results measured by the TOC method can be attributed to: 1) accumulation of the dispersant components at the water-air interface, which affects the consistency in sampling of the water for TOC analysis but not for the surface tension measurement, 2) adsorption of the surfactants on the sampling devices and TOC analyzer, and 3) incomplete catalytic conversion of the organic carbon by the UV/persulfate based TOC analyzer. Indeed, we observed long and gradual tails of the TOC evolution curve, suggesting that some the components in Corexit EC9500A are persistent to the UV-persulfate oxidation.

**Table 2-3.** Comparison of Corexit EC9500A concentrations in seawater measured by TOC analysis and by the surface tension based method. Number of replicate measurements = 5.

<b>Corexit concentration (mg/L)</b>	<b>EC9500A</b>	<b>1</b>	<b>5</b>	<b>10</b>	<b>15</b>	<b>20</b>
Measured by surface tension (mg/L)		0.98±0.05	5.16±0.14	9.65±0.15	15.40±0.24	20.06±0.39
Relative standard deviation (%)		5	3	2	2	2
Measured by TOC (mg/L)		0.81±0.43	5.42±0.55	9.14±0.92	15.09±0.55	20.51±2.12
Relative standard deviation (%)		53	10	10	4	10

## 2.4. Conclusions

Oil dispersants are a mixture of numerous known and unknown surfactants and solvents. Although highly desired, it has been challenging to quantify dispersant concentration in seawater and under various water chemistry and environmental conditions. This work proposed and tested a new method to determine the Corexit EC9500A concentration in seawater by measuring the surface tension of the dispersant solutions and by utilizing the linear correlation between surface tension and  $\ln[\text{dispersant concentration}]$ . Compared to conventional methods, which often target a fraction of the dispersant components, this method is not only simple, fast, economical and viable, but also measures the collective effect of the dispersant as a whole. The most suitable dispersant concentration range is 0.5 to 23.5 mg/L. However, dispersant of lower or higher concentrations than the optimum window may be accommodated by use of separate standard  $\gamma - \ln[C]$  lines and/or through proper concentration or dilution of the samples. Small changes in solution salinity (<0.3%), pH (7.0–9.0), and DOM (<1.5 mg/L as TOC) had negligible effects on the surface tension measurements, and thus, the correlation equations. While the method is most sensitive to salinity changes, the correlation lines appear parallel to each other at various salinity levels, and so, the correlation equation at one salinity level can be scaled to others by correcting the Y-axis intercept. In case of radical changes in water chemistry and environmental conditions, separate correlation curves can be readily constructed in accordance with the target sample conditions. Effects of extracts from typical marine sediments were negligible, thus, the method may be directly applied to seawater-sediment systems. The method accuracy was confirmed by comparing with the TOC analysis. Although the method was demonstrated using Corexit EC9500A as the prototype oil

dispersant, the method may be extended to other oil dispersants and surfactants. Given the ongoing active research activities in the field, this new analytical method provides a convenient and useful alternative means for researchers and practitioners for quantitative analysis of complex oil dispersants and surfactants in aquatic systems.

## **Chapter 3. Effects of Oil Dispersants on Settling of Marine Sediment Particles and Particle-Associated Transport of Oil Components**

This chapter investigates the effects and mechanisms of oil dispersants on the settling of fine marine sediment particles. Moreover, the effects of dispersant-facilitated particle sedimentation on the transport of important oil components in the water column are evaluated.

### **3.1. Introduction**

Oil dispersants are a mixture of surfactants and hydrocarbon-based solvents. Dispersants have been widely used to disintegrate spilled oil slicks into fine droplets, thereby facilitating dispersion of oil into water column and accelerating the natural attenuation processes (Griffiths 2012, Lessard and Demarco 2000). Oil dispersants have been employed in several major oil spill accidents, and over years, this approach has evolved into a major countermeasure to mitigate the adverse effects of oil spills (Griffiths 2012, Lessard and Demarco 2000). For examples, approximately 12 tons of Corexit EC9500A was applied in the *Sea Empress* spill in the UK in 1996 (Lessard and Demarco 2000); and approximately 11.5 tons of Corexit EC9527A was sprayed in the pipeline spill offshore in Texas in 1998 (Lessard and Demarco 2000). The single-largest application was carried out during the *Deepwater Horizon (DwH)* oil spill, where approximately 7800 tons of Corexit

EC9500A and EC9527A were applied on the surface (~5000 tons) and deepwater (~2800 tons) (Gong et al. 2014a, Kujawinski et al. 2011).

Researchers have studied the adsorption of surfactants on minerals (Fuerstenau 2002), but very few have addressed effects of oil dispersants on the settling behaviors of suspended particulate matter (SPM) or fine sediment particles in marine systems. Adsorption of dispersant components, e.g. surfactants, on the sediment particles may alter the surface potential of the particles. This can destabilize and coagulate the particles via inducing their aggregation, which can also enhance particle settling (Paria and Khilar 2004).

Application of oil dispersant results in elevated concentrations of oil droplets in the water column, for example, the volatile aromatic hydrocarbons in an oil plume during the *DwH* oil spill reached 139  $\mu\text{g/L}$  (Hazen et al. 2010). The high oil droplet concentration is favorable for the formation of oil sediment aggregates (OSAs) (Gong et al. 2014a), which can not only alter the settling behavior, but also facilitate distribution and transport of important oil compounds that are associated with the aggregates. Guyomarch et al. (1999) found that the presence of the chemical dispersant, Inipol IP90, enhanced the formation of OSAs, and approximately 80% of oil was entrained in the OSAs, which subsequently settled down to the bottom of the tank during wave tank experiments. Recent work also showed that the presence of Corexit EC9500A promotes the formation of marine oil snow (MOS) and sorption of oil components onto MOS (Fu et al. 2014b).

The *DwH* oil spill gushed approximately 655,000 tons of crude oil into the Gulf of Mexico ecosystems (Allan et al. 2012), of which 25,500 tons of polycyclic aromatic hydrocarbons (PAHs) were released (Reddy et al. 2012). During the spill, the concentration of PAHs near the wellhead

reached as high as 0.189 mg/L (Allan et al. 2012, Diercks et al. 2010). As PAHs can strongly interact with suspended sediment particles, a large portion of PAHs can be adsorbed on, or incorporated in the OSAs. Consequently, the formation of OSAs and subsequent particle settling/transport in the marine environment can alter the distribution, transport and environmental fate of PAHs and other important oil components (Bouloubassi et al. 2006, Zuijdghest and Huettel 2012). For instance, adsorption of PAHs onto sediment particles may mitigate the peak concentration of PAHs in the water column by transferring significant amounts of PAHs into the sediment phase; on the other hand, the particle-facilitated transport process can facilitate transport of PAHs to the sea bottom, surface or nearshore areas. In addition, as PAHs persist much longer in the sediment phase than at the sea surface (Harayama et al. 1999), sediment adsorption may prolong the life time of PAHs in the ecosystems. While a wealth of information on the adsorption of oil components onto sediments has been reported (Guo et al. 2007, Tremblay et al. 2005, Zhao et al. 2015), little is known about effects of dispersants or dispersed oil on the transport of fine sediment particles and how such particle-facilitated oil transport affects the fluxes and fate of oil components (Allan et al. 2012). As oil spills often occur in, or can reach, nearshore and estuarine zones, where the concentration of suspended sediment particles is usually high (NRC 2005), the oil-particle interactions may play even more profound roles in these more ecologically sensitive areas.

Environmental conditions, such as pH, salinity, temperature, and DOM are known to affect settling of suspended particles. Kretzschmar et al. (1998) investigated the influence of pH and humic acid on the coagulation of kaolinite by the dynamic light scattering technique, and observed

that at pH <5.8 the interparticle attractive forces predominate in suspension systems, resulting in a destabilization of the particles. Humic acid was reported to render a suspension system more stable due to the combination of electrostatic and steric stabilization effects (Heil and Sposito 1993a, b, Kretzschmar et al. 1993). However, knowledge has been lacking on the effects of such environmental parameters in the presence of oil dispersants, especially, how oil dispersants affect the settling properties of suspended particles under various environmental conditions.

The overall goal of this study was to systematically investigate effects of three model oil dispersants (Corexit EC9527A, Corexit EC9500A, and SPC1000) on the settling behaviors of sediment particles and how such dispersant-particle interactions affect distribution and transport of key oil components. The specific objectives were to: 1) determine the settling kinetics of representative sediment particles in the presence of the model dispersants; 2) elucidate the mechanisms underlying the particle-dispersant interactions; 3) test the dispersant effects under various environmental conditions, such as pH, salinity, DOM, and temperature; and 4) explore how dispersant-facilitated particle sedimentation affects distribution and transport of important oil components in sediment-water systems.

## **3.2. Materials and methods**

### **3.2.1. Materials**

The following chemicals (analytical grade or higher) were used as received: humic acid (Fluka Chemie, Switzerland), sodium hydroxide (NaOH) and NaN<sub>3</sub> (Fisher Scientific, Fair lawn, NJ, USA), hydrochloric acid (HCl, 36.5–38.0%, Mallinckrodt Chemical, St. Louis, MO, USA),



phenanthrene and pyrene (98%, Alfa Aesar). The dispersants Corexit EC9500A and Corexit EC9527A were obtained per courtesy of Nalco Company (Naperville, IL, USA), and SPC1000 was purchased from US Polychemical Corporate (Chestnut Ridge, NY, USA). The key compositions of the Corexit dispersants, such as Tween 85, Tween 80, Dioctyl sulfosuccinate sodium salt (DOSS) and 2-butoxyethanol, were purchased from VWR Corporate (Radnor, PA, USA). A standard reagent of 16 EPA listed PAHs, and a standard of *n*-alkanes mixtures (C9-C40), Pristane and Phytane, and two internal standards (fluorine-*d*<sub>10</sub> for PAHs and 5  $\alpha$ -androstne for *n*-alkanes) were purchased from Supelco (Bellefonte, PA, USA).

A surrogate Louisiana Sweet Crude (LSC) oil was acquired by courtesy of BP (Houston, TX, USA). This oil is considered physically, chemically, and toxicologically similar to the Macondo Well crude oil in the Mississippi Canyon Block 252. Artificially weathered oil was prepared according to the evaporation method by Sorial et al. (2004). Briefly, air was bubbled from the bottom of a graduated cylinder filled with 1.0 L of crude oil at a constant flow rate of ~2 L/min. The volume and weight of crude oil remaining in the cylinder were recorded as a function of time. After 10 days of the weathering process, the oil mass diminished from 807 to 608.5 g (by 24.6 wt.%), and the density of the oil increased from 0.807 to 0.834 g/cm<sup>3</sup>.

Water accommodated oil (WAO) and dispersed WAO (DWAO) were prepared according to the established methods (Singer et al. 2000). In brief, 3,000 mL glass aspirator bottles with hose bibs at the base fitted with silicone tubing and hose clamps were filled with 2,000 mL seawater. One mL of the weathered oil was added into the seawater surface, then sealed and magnetically stirred for 18 hours. The stirring intensity was controlled to yield a 25% vortex. The mixture was

then gravity-settled for 6 hours, and then the WAO fraction was carefully collected through the bottom bib and stored in amber bottles without headspace. DWAO was prepared in a similar manner except a dispersant was added in the seawater at a dispersant-to-oil ratio (DOR) of 1:20 after the 25% vortex was established.

Seawater was collected from the Grand Bay area, AL (N30.37873, W88.30679). The seawater sample was filtered with 0.22  $\mu\text{m}$  pore size membrane and preserved at 4 °C with  $\text{NaN}_3$  of 200 mg/L to inhibit microbial activities. The salient features of the seawater were as follows: pH = 7.9, DOM = 0.77 mg/L (as total organic carbon (TOC)), and salinity = 3.15 wt.%. The PAHs in the seawater were not detected. Three model sediments, referred to as GB, OS and EIWR were collected, respectively, from the Grand Bay, AL (N30.37873, W88.30679), the Ocean Springs National Seashore Park, MS (N30.39772, W88.79175), and the Elmer's Island Wildlife Refuge (EIWR), LA (N29.17764, W90.07401). The sediment samples were collected at the depth of 0-60 cm, thoroughly mixed and wet-sieved through 2 mm openings to remove the plant debris and large objects, and then air-dried for 1 week. The dried aggregates were then crushed using ceramic mortar and pestle, and sieved through 0.84 mm openings, and the subsamples (i.e. particles of  $\leq 0.84$  mm) were oven-dried for 6 h at 80 °C, which also inactivated the sediment microorganisms. The salient physical and chemical properties of the sediments were tested by the Soil Testing Laboratory at Auburn University, the details on the analytical methods have been described elsewhere (Gong et al. 2012).

**Table 3-1** gives the physicochemical characteristics of the sediment samples.

**Table 3-1.** Physicochemical characteristics of the sediment samples.

<b>Sample name</b>	<b>pH</b>	<b>SOM</b> %	<b>CEC</b> Meq/100g	<b>Taxonomy</b>	<b>Sand</b> %	<b>Silt</b> %	<b>Clay</b> %
<b>GB</b>	6.0	3.1	19.6	Sandy Loam	56.5	33.5	10.0
<b>OS</b>	6.4	1.6	6.6	Loamy Sand	81.6	15.3	3.2
<b>EIWR</b>	7.9	0.8	8.9	Sand	87.2	11.5	1.3

<b>Sample name</b>	<b>Ca</b> mg/kg	<b>K</b> mg/kg	<b>Mg</b> mg/kg	<b>Na</b> mg/kg	<b>Al</b> mg/kg	<b>Zn</b> mg/kg	<b>Fe</b> mg/kg	<b>Mn</b> mg/kg	<b>B</b> mg/kg	<b>P</b> mg/kg
<b>GB</b>	767.6	646.6	1209.3	16701.5	204.0	17.2	191.7	18.6	9.2	15.7
<b>OS</b>	441.9	182.7	314.5	4118.4	87.7	5.2	73.1	3.9	3.23	9.1
<b>EIWR</b>	1140.6	247.5	309.2	3894.0	54.0	3.4	232.0	34.0	2.9	61.5

Note: SOM = organic matter, CEC = cation exchange capacity.

### 3.2.2. Effects of dispersants on sediment settling

The settling rate of the sediment particles was tested in 480-mL amber bottles with PTFE lined caps. First, each bottle was filled with 300 mL seawater, and then a known mass (1.2 to 4.2 g, depending on the sediment type) of a sediment was added into the seawater (the sediment mass was adjusted to achieve an equal initial turbidity of  $180 \pm 24$  NTU for the suspensions). The sediment-seawater suspensions were then thoroughly mixed by hand shaking. Upon addition of a known concentration (up to 20 mg/L) of a dispersant, the bottles were placed on an orbital shaker (Excella E5 Platform Shaker, New Brunswick scientific, NJ, USA) operated at 200 rpm for 12

hours, and then at 50 rpm for 10 minutes to allow complete contacts between the dispersant molecules and sediment particles. The fully mixed suspensions were then allowed to stand still to initiate quiescent gravity settling of the particles. At predetermined times, samples (4 mL each) were taken from the center (6 cm from the surface) of the suspensions, and then measured for the turbidity change over time. It should be noted that it took about 15 seconds to obtain a stable turbidity reading. In addition to the three dispersants, the effects of key individual dispersant components, including three surfactants (Tween 80, Tween 85, DOSS) and one solvent (2-butoxyethanol) were also tested to assess their individual effects on the settling performance. In all cases, control tests were carried out without dispersant but under otherwise identical conditions. To assure data quality, all experiments were conducted in duplicate. In all figures, data were plotted as mean of duplicates and error bars were calculated as standard deviation to indicate data reproducibility.

Gordon (1970) showed that the suspended particles are numerically most abundant at the size (diameter) of  $<7 \mu\text{m}$  in the ocean. For the sediment particles involved, it takes  $\sim 40$  min for the  $7\text{-}\mu\text{m}$  particles to settle from surface to below the sampling point ( $\sim 6$  cm) (See Section 3.2.3). Therefore, the 40-min sedimentation efficiency ( $R_{40}$ ) was used to compare settling rates of particles under various conditions.

$$R_{40} = \frac{\text{Turbidity at 40 min } (T_{40})}{\text{Initial Turbidity } (T_0)} \quad \text{(Eq. 3-1)}$$

### 3.2.3. Particle size distribution and settling velocity distribution curve of suspended sediment

Assuming the density of all suspended particles is uniform and does not change, the particle size was calculated according to Stokes' law:

$$V = \frac{2(\rho_p - \rho_f)}{9\mu} gR^2 \quad (\text{Eq. 3-1})$$

where  $V$  is the settling velocity of sediment particle (m/s),  $g$  is the gravitational acceleration ( $9.8 \text{ m/s}^2$ ),  $\rho_p$  is the density of the particles ( $2380 \text{ kg/m}^3$ ),  $\rho_f$  is the density of the seawater ( $1024 \text{ kg/m}^3$ ), and  $\mu$  is the dynamic viscosity ( $9.594 \times 10^{-4} \text{ kg/m}\cdot\text{s}$ ).  $R$  is the radius of the sediment particle (m).

From the calculation, the particles with diameter larger than  $82 \mu\text{m}$  will settle from the surface layer to below the sampling point (depth of 6 cm) within 15 seconds.

### 3.2.4. Effects of environmental factors, WAO and DWAO on settling of sediment particles

The effect of pH was evaluated by comparing the particle settling rates in the pH range of 4 to 9.2, where pH was adjusted using dilute (0.5 M) NaOH or HCl solutions. The effect of salinity was tested by using synthetic solutions containing 0 to 3.5 wt.% NaCl (in this case deionized water was used). To test the effect of DOM, a commercial humic acid was added to the seawater to achieve a DOM concentration of 10 mg/L as TOC. The effect of temperature was tested at  $4 \text{ }^\circ\text{C}$  simulating the deepwater temperature and  $25 \text{ }^\circ\text{C}$  for surface water temperature (Liu et al., 2012). All the experiments were carried out in the presence or absence of a dispersant (Corexit EC9527A). To assess effects of WAO and DWAO on sediment settling, the batch settling experiments were also conducted using 300 mL of the WAO or DWAO solution.

### 3.2.5. Effects of dispersant on sorption and transport of oil and PAHs

Adsorption kinetic tests of two model PAHs (phenanthrene and pyrene) by sediment was carried out to evaluate the adsorption rate and sediment-facilitated transport of oil compounds. The tests were carried out using 480-mL amber glass bottles capped with Teflon-lined septa. First, 3.6 g of sediment (OS) were mixed with 300 mL seawater in each bottle, and then an aliquot of the Corexit EC9527A solution was added to reach a dispersant concentration of 10 mg/L. Then, the sorption was initiated by adding an aliquot of the PAH stock solutions into the sediment-seawater suspensions, which resulted in an initial phenanthrene concentration of 600 µg/L or pyrene concentration of 40 µg/L. The bottles were mixed on an orbital shaker operated at 200 rpm. At predetermine times, samples (3 mL each) were withdrawn from the bottles and centrifuged at 3000 rpm (1359 ×g) for 5 minutes to separate the solids from the solution. The supernatant was then mixed with methanol (v/v = 1:1), and the mixture was filtered through a 0.2 µm Anopore syringe filter (Whatman® Anotop 10, Germany). The filtrate was analyzed for the PAHs. The addition of methanol prevents PAHs sorption on the filter. For comparison, the same tests were also carried out without dispersant.

The effects of oil dispersants on the sediment-facilitated transport of crude oil and PAHs from water column to bottom sediment were tested through the same batch settling test procedure. Briefly, 60 µL of the oil sample was added to 300 mL sediment-seawater mixture in 480 mL-amber glass bottles. Then, an aliquot of the Corexit EC9527A stock solution was added to achieve a dispersant concentration of 10 mg/L, or a dispersant-to-oil ratio (DOR) of 1:20. Then the bottles were mixed on an orbital shaker for 12 hours and settled for 8 hours. The remaining surface oil,

settled sediment, and the water column were separated as follows: first ~90% water was pipette-sampled from the water column; then, the mixture was frozen, which allowed the surface oil phase to be collected with dichloromethane; the remaining sediment phase was then obtained upon thawing the mixture. The water column and sediment samples were extracted three times using dichloromethane (Zhang et al. 2010), and the total petroleum hydrocarbons (TPHs), PAHs and *n*-alkanes in the extracts were determined using gas chromatography-flame ionization detector (GC-FID) or gas chromatography-mass spectrometry (GC-MS) (Section 3.2.6). Control tests indicated that the liquid-liquid extraction recovered >95% of the oil compounds in water, and >90% in the sediment phase.

### **3.2.6. Analytical methods**

The turbidity of the sediment suspensions was measured using a HACH 2100N Turbidimeter (Hach Company, Colorado, USA), with a detection limit of 0.5 NTU. The hydrodynamic diameter and zeta potential of suspended particles were determined by dynamic light scattering (DLS) (Zetasizer Nano ZS, Malvern Instruments Ltd, Malvern, Southborough, MA, USA) at 25 °C. TOC was measured by a Tekmar Dohrmann Pheonix 8000 UV-Persulfate TOC analyzer (Mason, OH, USA) with a detection limit of 0.2 mg/L. TPHs were analyzed on an Agilent 6890 GC-FID (Agilent Technologies Inc., Santa Clara, CA, USA) with an Agilent 7683 autosampler and a 30 m×0.25 mm i.d. (0.25 µm film) HP-5MS capillary column. Helium was used as the carrier gas. The injector and detector temperatures were 290 and 300 °C, respectively. The oven temperature was programmed as follows: hold at 50 °C for 3 min; ramp to 300 °C at 6 °C/min and hold for 16 min. Each 1.0 µL sample was injected in the splitless mode with 1 min purge off. Oil *n*-alkanes (C9-

C40) and 16 EPA listed PAHs were analyzed following a modified GC-MS method (Fu et al. 2014b, Liu et al. 2012b) using an Agilent 7890A GC coupled with the 5975C Series MS, with a DB-EUPAH column (30 m×0.18 mm×0.14 mm). Helium was used as the carrier gas at a flow rate of 0.9 mL/min. Each 2.0 µL sample was injected with 3 min solvent delay. The oven temperature was programmed as follows: 2 min hold at 40 °C; ramp to 300 °C at 8 °C/min; and hold for 10 min. The detection was conducted by a mass selective detector (MSD) with electron impact ionization (EI) in the selected ion monitoring (SIM) mode. Individual *n*-alkanes and PAHs were identified based on the mass to charge ratio (*m/z*) and retention times. External calibration was performed based on a five-point calibration curve for individual components.

Phenanthrene and pyrene in seawater were quantified using an HPLC system (HP series 1100, Hewlett Packard, CA, USA) with a Zorbax SB-C18 column. The mobile phase consisted of a mixture of acetonitrile and DI-water (70:30 v/v) with 0.5 wt.% phosphoric acid, the flow rate was set at 1 mL/min, and the sample injection volume was 80 µL. The UV detector wavelength was 250 nm for phenanthrene and 240 nm for pyrene, and the method afforded a detection limit of 2 µg/L for both PAHs.



### 3.3. Results and discussion

#### 3.3.1. Effect of dispersants on sediment settling

**Figure 3-1** presents the settling kinetics of the three sediments in the presence of the three model dispersants. **Figure 3-1a** and **b** show that all three dispersants accelerated the settling rates of GB and OS sediments significantly ( $p < 0.05$ ). For GB, the effects for the three dispersants were nearly equal, where the  $R_{40}$  increased from 77.4% to ca. 88.3% in the presence of dispersants (**Figure 3-1a**). However, the effects of dispersants on OS varied slightly, although the steady state turbidity levels were about the same (**Figure 3-1b**). The presence of Corexit EC9500A, Corexit EC9527A and SPC 1000 increased the  $R_{40}$  from 66.2% (as control) to 83.3%, 88.5%, and 84.7%, respectively. Corexit EC9527A appeared to be most effective on enhancing the settling velocity of the particles, followed by Corexit EC9500A (a sister product). However, **Figure 3-1c** shows that the effect of Corexit EC9500A was more profound than Corexit EC9527A and SPC1000 on enhancing the settling rate of EIWR sediment particles. Among the three sediments, the EIWR sediment displayed the fastest settling rate than the other sediments in the absence of dispersant (the  $R_{40}$  values are 77.4%, 66.2%, 81.6% for GB, OS, EIWR sediments, respectively).

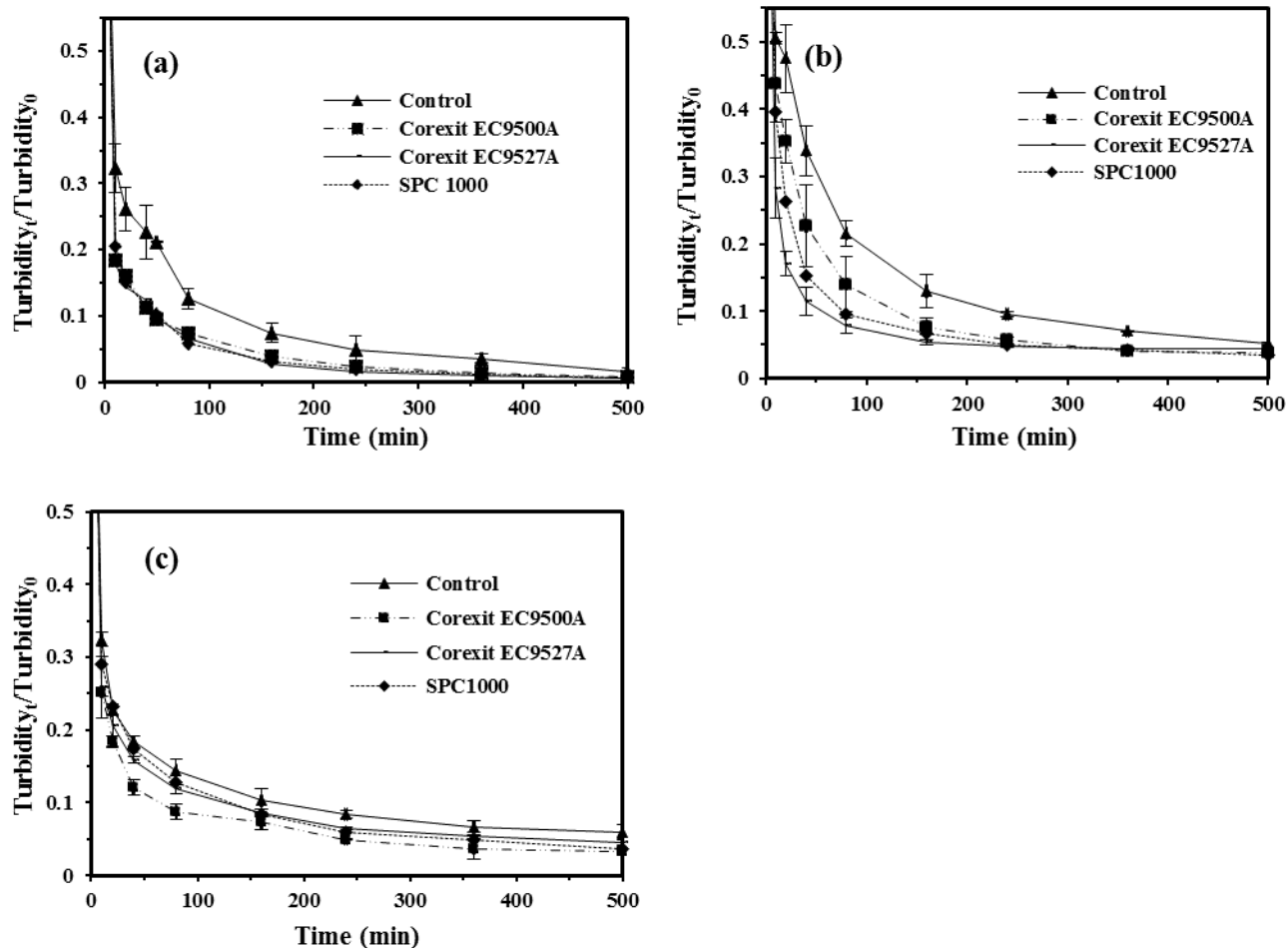


Figure 3-1. Effects of three commercial oil dispersants on the settling kinetics of three marine sediments: GB at 4 g/L (a), OS at 12 g/L (b), and EIWR at 14 g/L (c). Experimental conditions: initial turbidity =  $180 \pm 24$  NTU in all cases, Corexit EC9527A = 5 mg/L, pH =  $7.0 \pm 0.5$ , temperature =  $25 \pm 1$  °C.

**Table 3-1** shows that GB is classified as sandy loam, OS as loamy sand, EIWR as sand. The SOM, silt and clay contents in sediments follow the sequence of: GB > OS > EIWR, which agree

with the notion that the initial turbidity of sediments is primarily due to suspended silt and clay particles.

Surfactants (the major dispersant components) can be adsorbed on sediment particles through hydrophobic interactions between the surfactant tail and SOM or through electrostatic interactions between the surfactant heads and the mineral functional groups of sediments. The adsorption is more favored with smaller particles or larger surface area and/or higher sediment SOM content (Jones-Hughes and Turner 2005). Based on particle size, GB and OS are expected to take up more dispersants than EIWR; on the other hand, based on the SOM content and the actual sediment dosage in the mixtures, the total SOM in the OS system was the highest (0.192 g/L), followed by GB (0.124 g/L) and then EIWR (0.112 g/L). The fact that the dispersants showed the most effect on the settling of OS and least on EIWR indicates that SOM content is the most critical parameter governing the dispersant effect.

The settling velocity distribution of suspended sediment at various dispersant concentrations was calculated based on the sampling depth (6 cm) and settling time, and the corresponding size distribution of suspended sediment particles was calculated according to Stokes' law (**Eq. 3-2**), and is shown in **Figure 3-2**. The results indicate that the addition of the dispersant enhanced aggregation of the fine particles, e.g. the percentage of particles with  $r < 2.9 \mu\text{m}$  decreased from 22.6% to 12.4% for GB sediment, 33.8% to 11.5% for OS sediment, 18.4% to 15.9% for EIWR sediment in the presence of Corexit EC9527A at 5 mg/L.

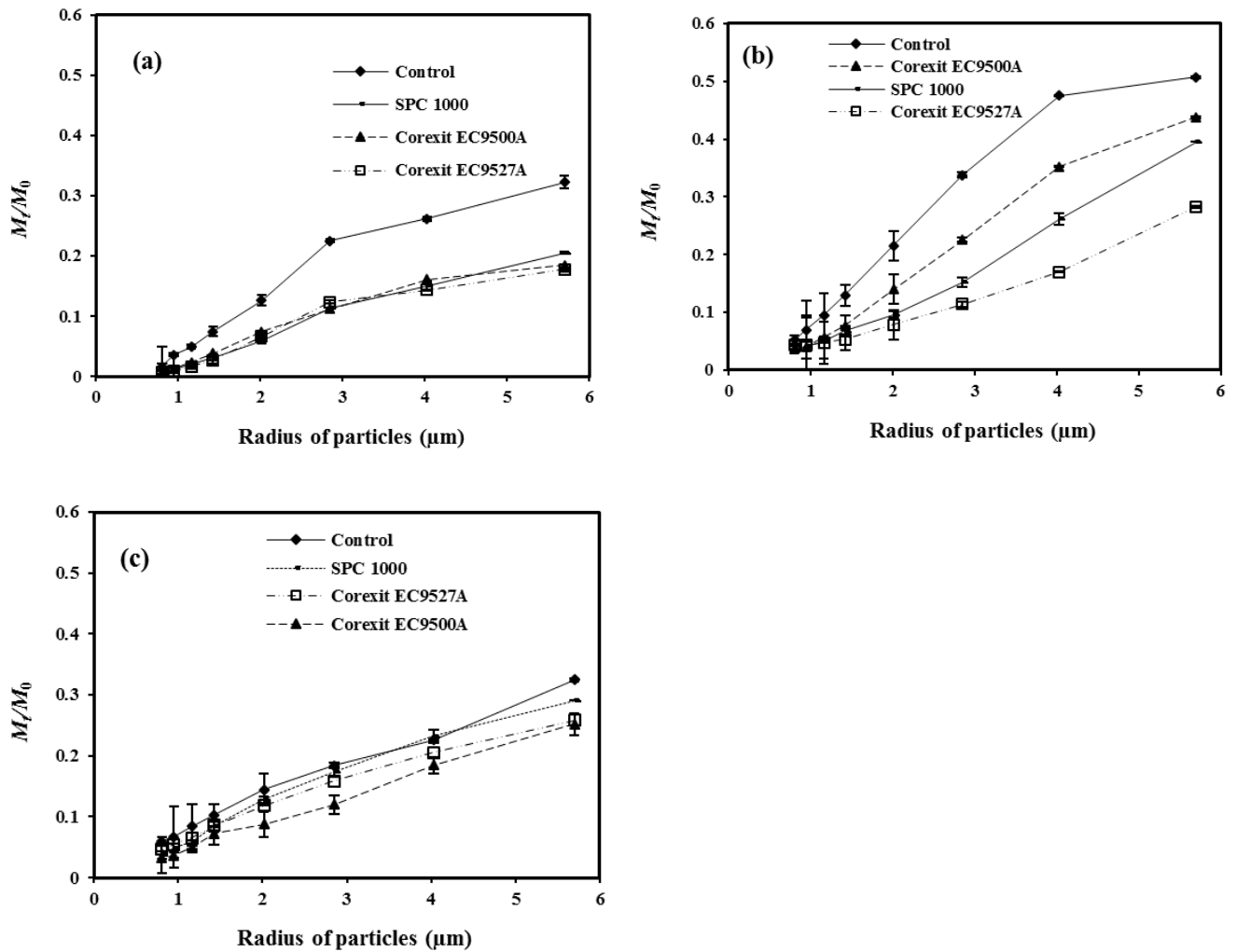


**Figure 3-2.** Effects of three commercial oil dispersants on the particle size distribution of three marine sediments: GB at 4 g/L (a), OS at 12 g/L (b), and EIWR at 14 g/L (c).  $M_0$  is the total mass of all particles, and  $M_i$  refers to the mass of particles with radius less than the corresponding x-axis value.

As the most salient dispersant effects were observed for the OS sediment with Corexit EC9527A, more detailed investigation was carried out with OS and Corexit EC9527A

subsequently to further explore the mechanisms on the dispersant-accelerated settling of suspended sediment particles.

**Figure 3-3** shows effects of various levels of Corexit EC9527A on the settling of the sediment particles. The presence of 2 and 5 mg/L of the dispersant increased  $R_{40}$  from 66.2% to 72.1% and 82.8%, respectively. However, further increasing the dispersant concentration to 20 mg/L showed insignificant additional effect. The observation indicates that the 10 mg/L dispersant concentration represents a saturation level showing the maximum effect. **Figure 3-3b** shows that increasing the dispersant concentration from 0 to 20 mg/L modestly suppressed the zeta potential of the particles from -15.5 to -13.5 mV ( $p < 0.05$ ), indicating that the decrease in the surface potential, and thus, decreased in the electrostatic stability, played a minor but significant role (Hunter 2013). **Figure 3-4** shows the size and settling velocity distributions of suspended particles as a function of the dispersant concentration, and the data indicate that increasing the dispersant concentration up to 10 mg/L progressively enhanced aggregation of the fine particles, e.g., in the presence of 2 and 10 mg/L of Corexit EC9527A, the percentage of particles with  $r < 2.9 \mu\text{m}$  decreased from 33.8% to 27.9% and 13.0%, and that for particles with  $v < 0.00005 \text{ m/s}$  decreased from 47.5% to 37.1% and 20.0%, respectively.

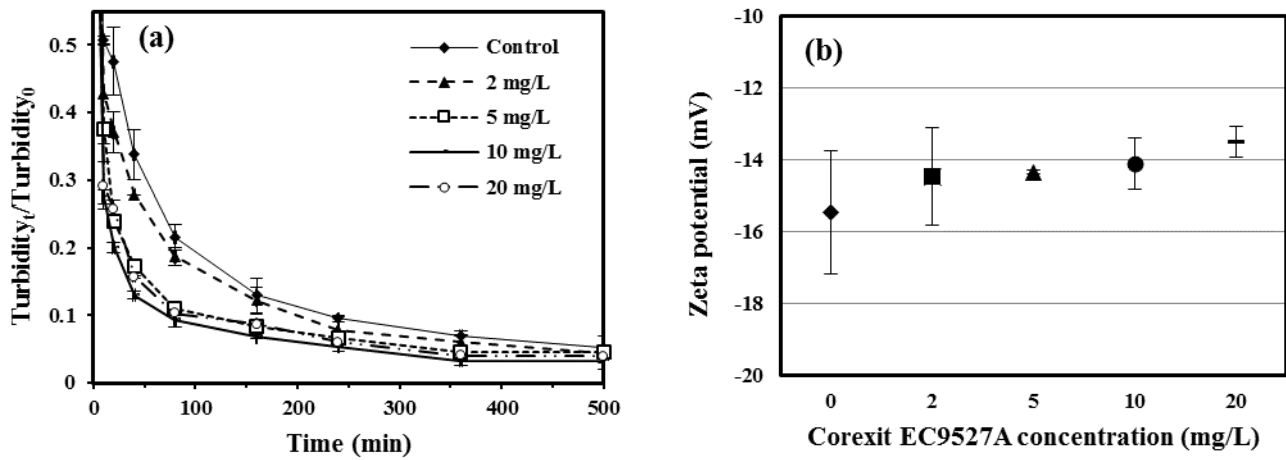


**Figure 3-3.** Settling kinetics of OS sediment particles in the presence of various concentrations of Corexit EC9527A (a), and zeta potential of the sediment suspension (b). Experimental conditions: OS sediment = 12 g/L, seawater volume = 300 mL, pH = 7.3 ± 0.3.

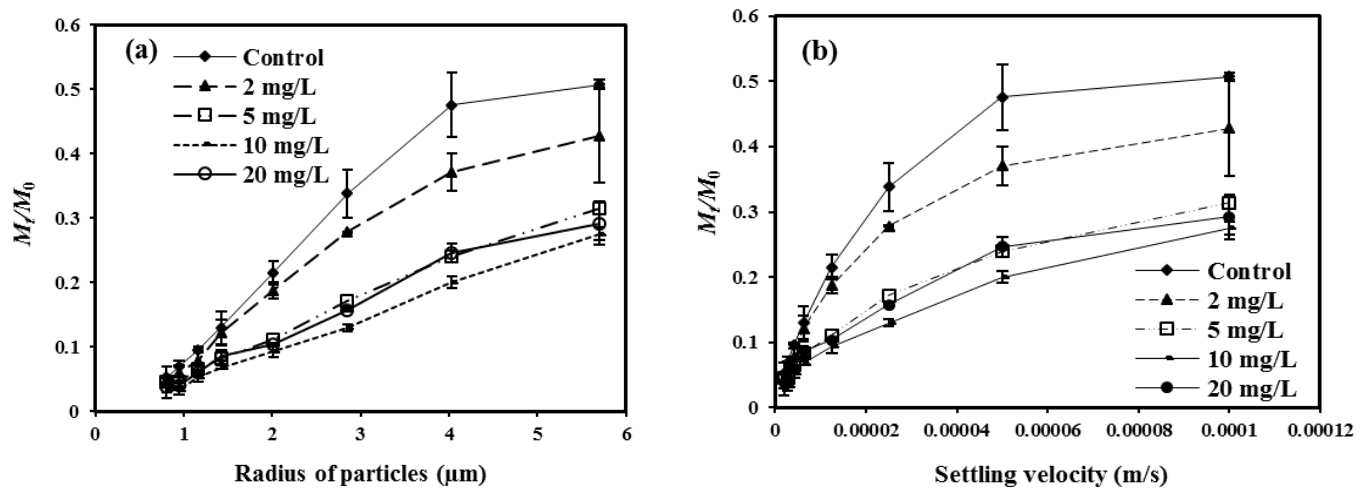


**Figure 3-4.** Particle size distribution (a) and settling velocity distribution curve (b) of suspended sediment particles (OS) in the presence of dispersant Corexit EC9527A at 0–20 mg/L.  $M_0$  is the

total mass of all particles, and  $M_i$  refers to the mass of particles with radius or settling velocity less than the corresponding x-axis value.

Corexit EC9527A is a mixture of both anionic (35%) and nonionic (48%) surfactants in solvent (Bruheim et al. 1999). It contains the same surfactants as Corexit EC9500A, and a solvent 2-butoxyethanol, which is not an ingredient in Corexit EC9500A (Gong et al. 2014b, Zhao et al. 2015). **Figure 3-5a** shows the individual effects of the three key surfactants (Tween 80, Tween 85, and DOSS) of the Corexit dispersants and the solvent (2-butoxyethanol) on the settling performance of the sediment particles. The nonionic surfactants, i.e. Tween 85 and Tween 80, displayed the most prominent enhancement of the settleability, while the anionic surfactant DOSS had negligible effect. Between the two nonionic surfactants, Tween 85 has three hydrophobic tails (three C18 tails) per molecule, while Tween 80 has only one hydrophobic tail per molecule with the same chain length (C18) (Cirin et al. 2012, Mahdi et al. 2011). Consequently, Tween 85 offers higher affinity for SOM, and thus, was found more effective in enhancing the particle aggregation. 2-butoxyethanol was also able to accelerate the settling velocity, though to a lesser extent than the non-ionic surfactants, which partially explains the greater effect of EC9527A over EC9500A. **Figure 3-5b** shows that the presence of the two nonionic surfactants suppressed the zeta potential by ~5 mV, while DOSS exhibited a negligible effect.

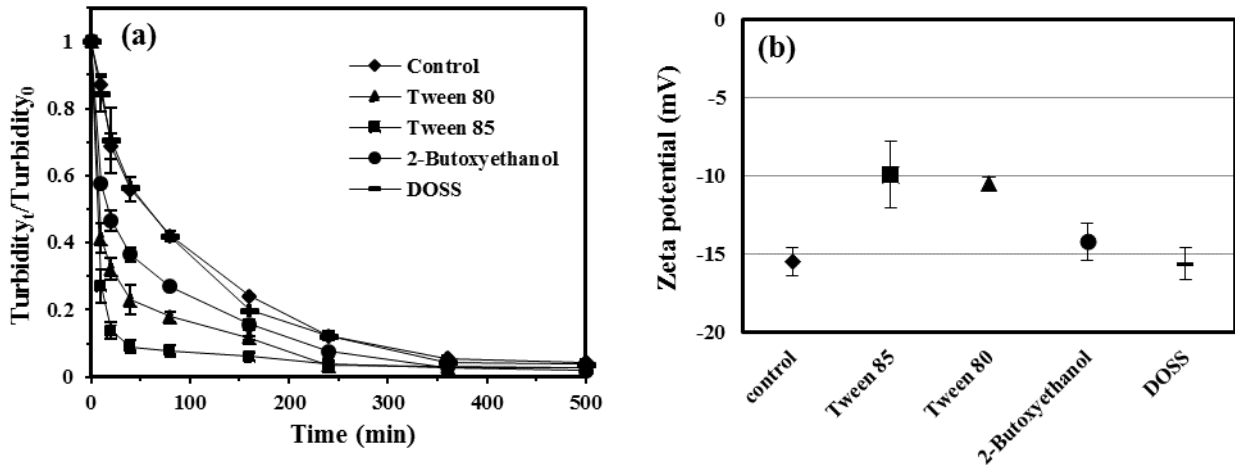


**Figure 3-5.** Settling kinetics of OS sediment in the presence of individual key dispersant components (a), and effects of individual dispersant components on zeta potential of sediment suspension (b). Experimental conditions: sediment dosage = 15 g/L, dispersant components = 10 mg/L, pH = 7.3 ± 0.2.

Both Tween 80 and Tween 85 contain hydrophilic ethylene glycol heads and hydrophobic alkyl tails. These amphiphilic molecules can bind with sediment minerals and SOM through electrostatic and hydrophobic interactions (Joshi et al. 2008, Shen et al. 2011, Zhou et al. 2011), and can act as a bridging agent to facilitate flocculation of fine particles. In addition, the adsorbed nonionic surfactant layer on charged particles may shield the surface electrical potential and thus diminish the electrostatic repulsion between the particles, both being conducive to particle aggregation. Rufier et al. (2011) studied the effect of surfactants on hydrophobically end-capped poly(ethylene oxide) self-assembled aggregates by using small-angle neutron scattering (SANS), and found that the addition of a nonionic surfactant increased the aggregation. 2-butoxyethanol ( $\text{CH}_3(\text{CH}_2)_3\text{O}(\text{CH}_2)_2\text{OH}$ ) behaves as an alcohol that lowers the surface tension and reduces the



surface charge of particles (Kline and Kaler 1994). It was reported that increasing 2-butoxyethanol concentration could convert the strong interparticle repulsive force to hard sphere attractive force (Kline and Kaler 1994). The observation indicates that the enhanced settling by the Corexit dispersants is primarily attributed to the effects of the nonionic surfactants along with the solvent, whereas the anionic surfactant DOSS tends to maintain the same surface potential due to its negative heads.

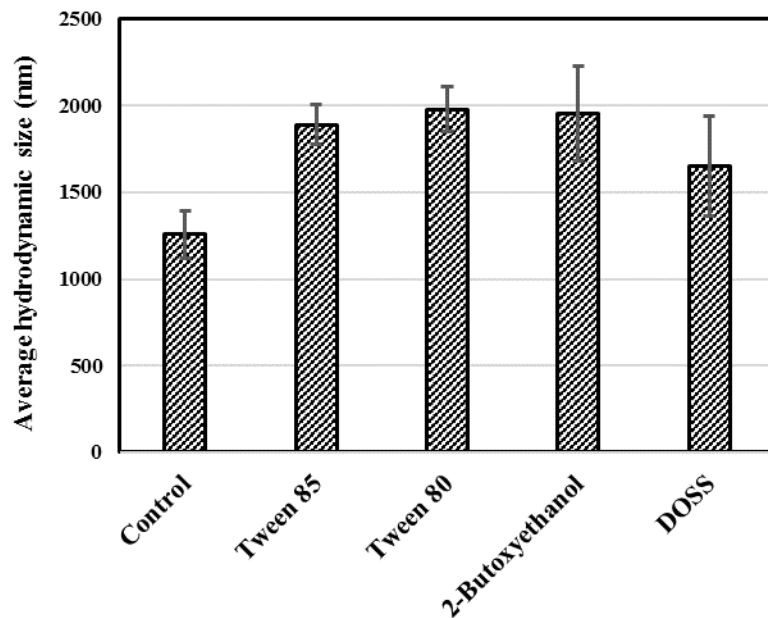


**Figure 3-6.** Average hydrodynamic particle size of suspended particles in the presence of various key dispersant components. Dispersant components concentration was 10 mg/L. Experimental condition:  $\text{pH} = 7.3 \pm 0.3$ .

To test effects of the dispersant components on aggregation of the finer sediment particles, the hydrodynamic size of the suspended particles of  $<10 \mu\text{m}$  was monitored using the Malvern

Zetasizer. The suspended particles were obtained by taking the supernatant from a sediment-seawater mixture after 80 min of gravity settling (initial OS = 15 g/L). **Figure 3-6** shows the effects of various dispersant components (10 mg/L) on the hydrodynamic diameter of the particles when the particles were mixed with the dispersant components for 12 h.

**Figure 3-6** shows that the presence of Tween 85, Tween 80, and 2-butoxyethanol increased the average hydrodynamic particle size from 1.26 (control) to 1.89, 1.98, and 1.96  $\mu\text{m}$ , respectively, which is consistent with the zeta potential profile (**Figure 3-5**). However, although DOSS had little effect on the zeta potential (**Figure 3-5**), it also increased the average hydrodynamic size of the sediment particles, though to a lesser extent. This can be due to the opposing effects of the tail and head of DOSS: while the surfactant chain tends to bridge the fine particles (Gupta et al. 2014), the charged head tends to resist the aggregation of the particles. The comparison of **Figure 3-5** and **Figure 3-6** reveals that despite the modestly increased hydrodynamic particle size, DOSS did not significantly promote the settling rate, suggesting that the aggregates associated with DOSS are more loose and fluffy. Likewise, although the presence 2-butoxyethanol increased the hydrodynamic size to that comparable to Tween 85 or Tween 80, the settleability enhancement was not as significant as by the surfactants (**Figure 3-5a**). In fact, the solvent barely altered the zeta potential (**Figure 3-5b**). This observation indicates that the hydrodynamic size alone may not reflect the settleability, other factors such as the density and shapes of the aggregates should also be taken into account.

The settling velocity ( $v$ ) of fine sediment particles is dependent on the balance between the drag and gravitational forces on the particles as depicted by **Eq. 3-3** (Khelifa and Hill 2006).

$$v = \left( \frac{4}{3} \theta \cdot g \cdot C_d^{-1} \cdot \frac{\Delta \rho}{\rho_w} \cdot D \right)^{0.5} \quad (\text{Eq. 3-3})$$

where  $\theta$  is the dimensionless particle-shape factor,  $g$  is the gravitational acceleration ( $\text{m/s}^2$ ),  $C_d$  is the dimensionless drag coefficient,  $\Delta \rho$  is the effective density of the particle, or excess density ( $\rho_p - \rho_w$ ) with  $\rho_p$  and  $\rho_w$  being the densities of the particle and solution ( $\text{kg/m}^3$ ), respectively, and  $D$  is the equivalent spherical diameter of the particle (m).  $C_d$  can be determined by the empirical correlation equation:

$$C_d = \frac{24}{Re} (1 + 0.15 Re^{0.687}) \quad (\text{Eq. 3-4})$$

where  $Re$  is the Reynolds number.

**Eq. 3-3** and **Eq. 3-4** are in accord with the classic Stokes law, where the size and density of particles govern the settling velocity (Khelifa and Hill 2006). The dispersant components may not increase the density of the particles, rather, they can promote the aggregation of small particles through interparticle bridging and/or by lowering the interparticle repulsive electrical double-layer forces. Given the rather negative zeta potential and coating of the bulky surfactant molecules on the particle surface, the particle aggregation falls into the unfavorable collision domain, i.e., the aggregation is due to the secondary energy minimum according to the DLVO theory (Redman et al. 2004, Shen et al. 2007). Therefore, formation of the dispersant-associated aggregates is likely to be reversible.

### 3.3.2. Effects of dispersant under various environmental conditions

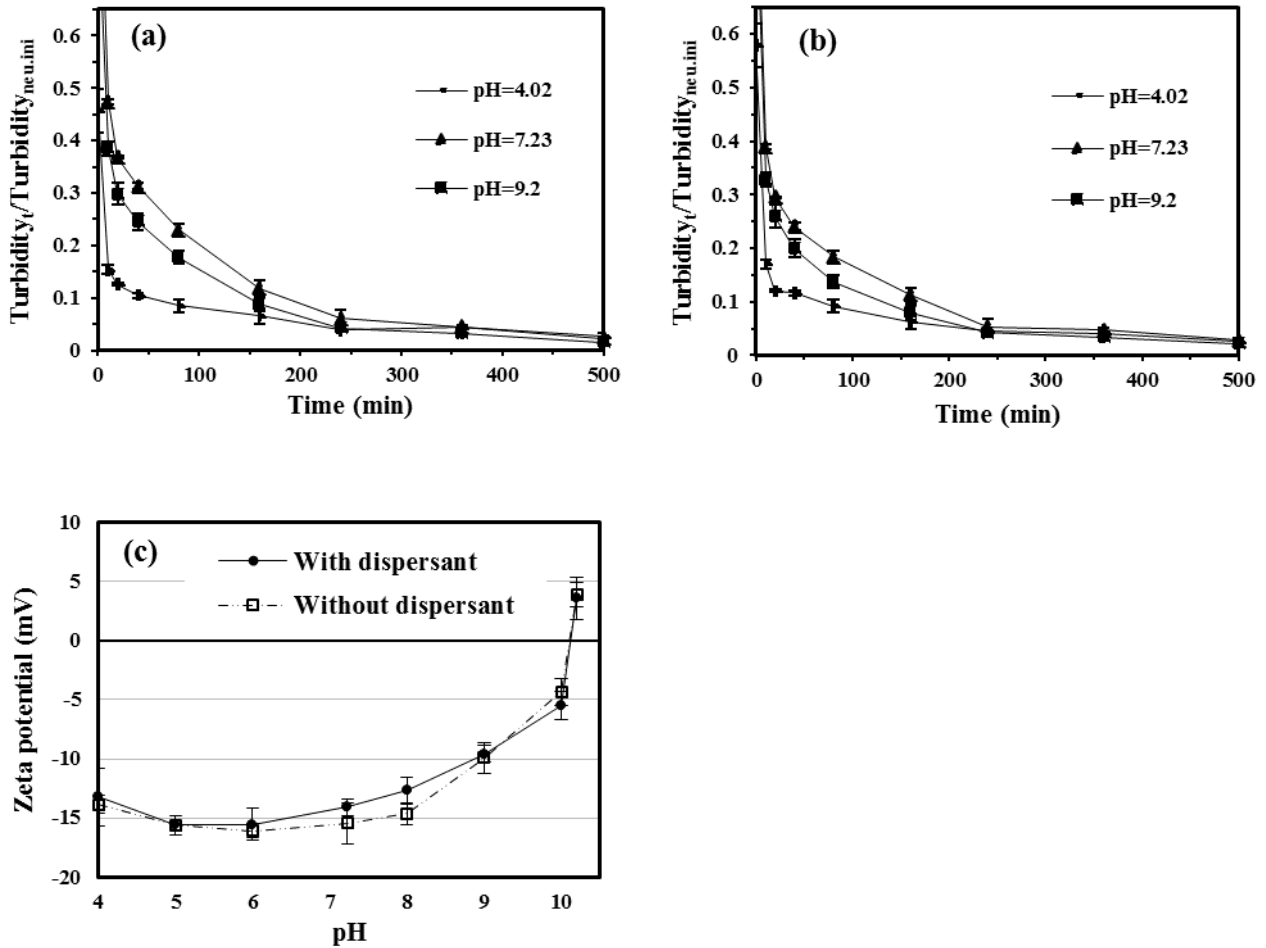


**Figure 3-7.** Influence of pH on settling kinetics of OS sediment: without dispersant (a), with Corexit EC9527A (b), and zeta potential of the sediment particles as a function of pH (c). Experimental conditions: Corexit EC9527A = 10 mg/L, sediment (OS) = 12 g/L.

**Figure 3-7** shows the settling kinetics and zeta potential of sediment particles as a function of pH with or without dispersant. The results show that regardless of the dispersant, the fastest particle settling was observed at the acidic pH 4.02 ( $R_{40} = 88.4\%$  with dispersant and  $89.5\%$

without dispersant), whereas the slowest settling was at pH 7.23 ( $R_{40} = 75.9\%$  and  $68.8\%$ , respectively). The dispersant increased  $R_{40}$  from  $68.7\%$  to  $75.9\%$  at pH 7.23 and from  $75.5\%$  to  $80.0\%$  at pH 9.2, but had little effect at pH 4.02. **Figure 3-7c** shows that the dispersant had negligible effect on the zeta potential in the broad pH range except at pH 7 and 8, indicating that the zeta potential is important to the settling performance of sediment at neutral pH, but not the only factor that alters the aggregation and settling performance of sediment particles.

The seawater and sediment contain high concentrations of metal ions, e.g.  $Mg^{2+}$  and  $Ca^{2+}$  concentration are  $1250$  and  $360$  mg/L in the seawater,  $314.5$  and  $441.9$  mg/kg in the OS sediment. As pH rises, more precipitates of metal hydroxides and carbonates will form, resulting in lowered zeta potential. For instance, based on the Visual MINTEQ (version 3.1) calculation,  $Mg^{2+}$  becomes oversaturated at pH  $>10$ , where brucite  $Mg(OH)_2$  is formed. The dramatic drop in soluble metal concentrations at pH  $>10$  was confirmed by directly analyzing the soluble metal concentrations. Consequently, the unusually high pH of the point of zero charge ( $pH_{pzc}$ ) shown in **Figure 3-7c** may not indicate the true value for the sediment (Yukselen and Kaya 2003). The high metal concentrations can also be responsible for the weakened effect of the dispersant on the zeta potential.

**Figure 3-8** confirms the conventional notion that increasing electrolyte (NaCl) concentration greatly accelerates particle aggregation and increases the settling velocity of suspended solids in the absence of dispersant ( $R_{40} = 56.6\%$ ,  $64.4\%$  and  $66.8\%$  at 0, 1.0, and 3.5 wt.% of NaCl, respectively). However, the electrolyte effects differed notably in the presence of the dispersant: First, the presence of NaCl and the dispersant synergistically enhanced the settling and increased

$R_{40}$  to 79.0% even at 1.0 wt.% of NaCl, which is in accord with the double-layer theory; Second, further increasing the salt to 3.5 wt.% showed negligible further effect, indicating that the dispersant molecules shielded some of the negative sites on the sediment particles from interacting with counter ions in the solution, i.e., the dispersant may alleviate the ionic strength effect.

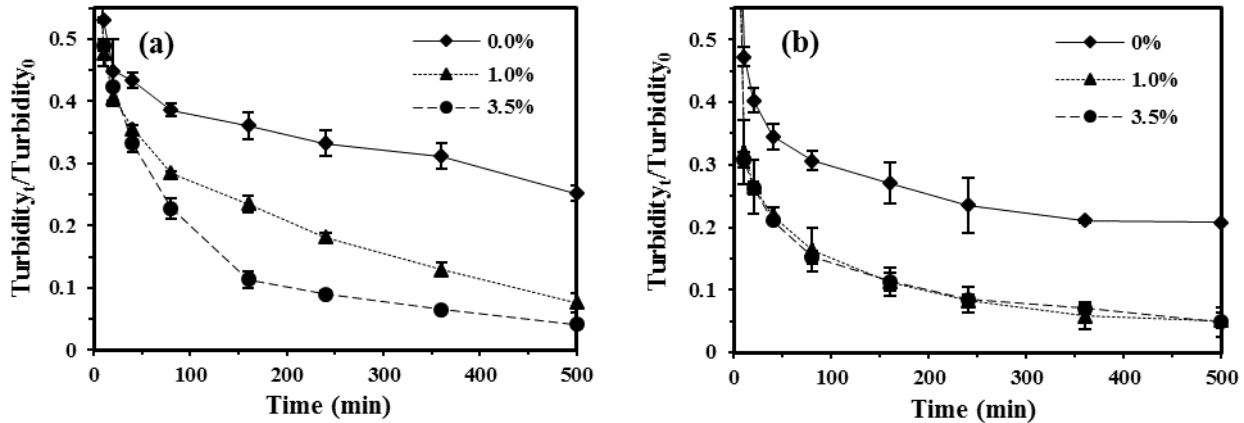


**Figure 3-8.** Settling kinetics of OS sediment particles at various NaCl concentrations in the absence (a) or presence (b) of dispersant Corexit EC9527A. Experimental conditions: OS sediment = 12 g/L, Corexit EC9527A = 10 mg/L, pH = 7.3 ± 0.2.

**Figure 3-9** shows that the presence of humic acid decreased the settling rate ( $R_{40}$ ) from 71.7% to 66.6%. However, the presence of humic acid accelerated the  $R_{40}$  from 78.6% to 83.1% in the presence of dispersant. Humic acid has strong affinity to the surface of clay and metal oxide particles (Tombacz et al. 2004), the sorption of humic acid renders a more negatively charged particle surface, and thus stronger repulsive forces and greater particle stability (Furukawa et al. 2009, Kretzschmar et al. 1997). However, the presence of dispersant and humic acid synergistically accelerated the settling rate, which can be due to the increased uptake of dispersant

on sediment with sorbed humic acid (Alila et al. 2007). The elevated dispersant on sediment in turn masked the electrical potential from the dissociated organic acid functional groups, resulting in elevated aggregation of the sediment particles.

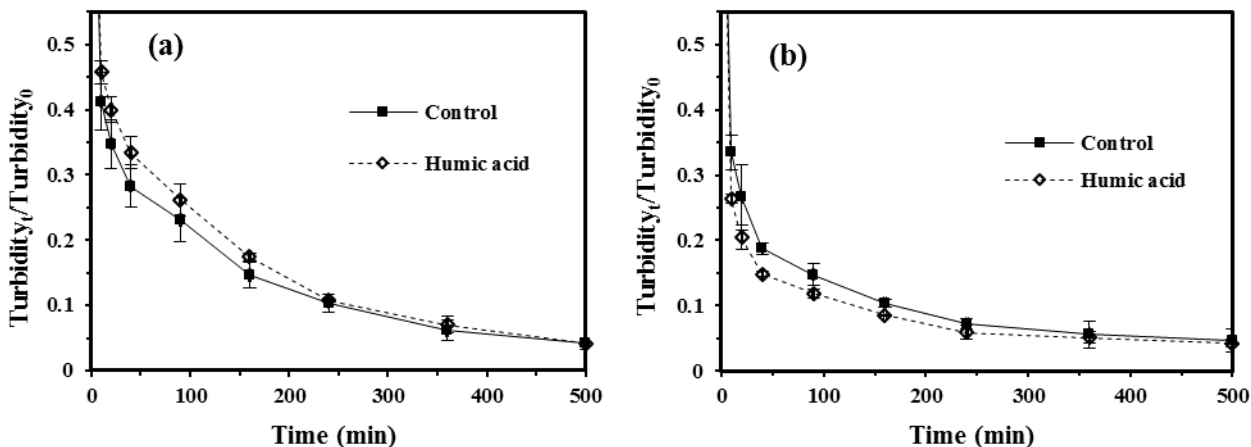


**Figure 3-9.** Settling kinetics of OS sediment particles with humic acid in the absence (a) or presence (b) of dispersant Corexit EC9527A. Experimental conditions: OS sediment = 12 g/L, Corexit EC9527A = 10 mg/L, pH =  $7.3 \pm 0.2$ , temperature =  $25 \pm 1$  °C.

Seawater temperature varies widely from surface to bottom. **Figure 3-10** compares the dispersant effects at 4 and 25 °C, representing bottom and surface seawater temperatures. The dispersant shows negligible effect on altering settling of the sediment at 4 °C, but increased  $R_{40}$  from 73.6% to 83.4% at 25 °C. The hindered dispersant effects at 4 °C can be primarily attributed to the reduced adsorption of non-ionic surfactants by sediment. Increasing temperature increasingly desolvates the head group, rendering it less hydrophilic and more compact, and thus increases the surface activity and saturation adsorption values (Paria and Khilar 2004). Zhao et al. (2015)

reported that the adsorption of dispersant (Corexit EC9500A) by marine sediment at 4 °C was much lower than at 21 °C.

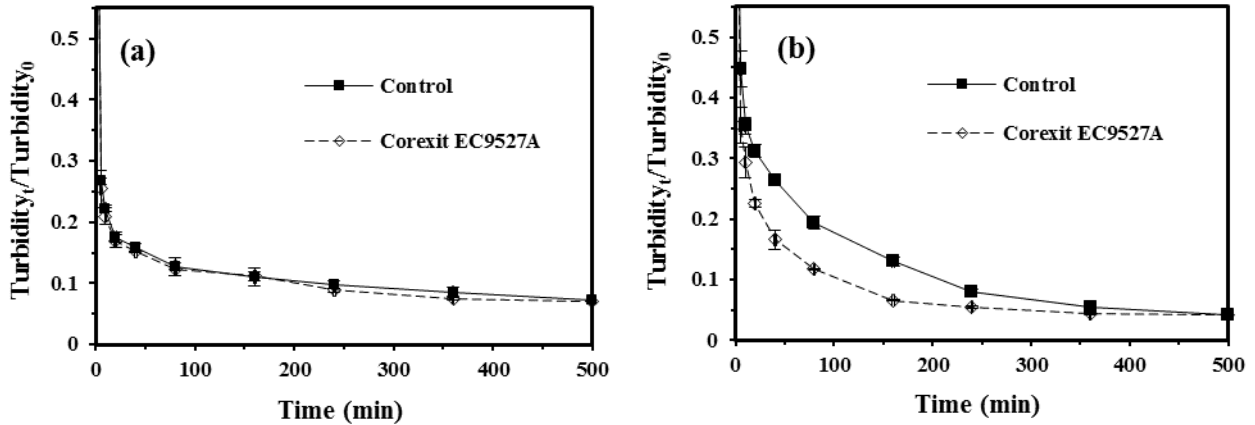


**Figure 3-10.** Settling kinetics of sediment particles at 4 °C (a), and 25 °C (b) with or without dispersant. Experimental conditions: sediment (OS) = 12 g/L, Corexit EC9527A = 10 mg/L, pH  $7.3 \pm 0.2$ .

**Figure 3-11** shows effects of WAO and DWAO on the settleability of the sediment particles. The presence of WAO increased  $R_{40}$  from 70.0% to 74.1%, and the addition of DWAO increased  $R_{40}$  from 70.0% to 81.0%. The very subtle effect of WAO is associated with the very limited solubility of oil (<2 mg/L), whereas the much pronounced impact of DWAO is attributed to: 1) with the dispersant, much more oil was dispersed, and thus much more oil was adsorbed on the particles, and 2) DWAO and elevated oil uptake can facilitate the formation of OSAs (Wang et al. 2013). The final turbidity for the suspension with DWAO appeared slightly higher, which can be attributed to the distributed oil droplets and some oiled-particles that are lighter and less settable. Fu et al. (2014b) studied the effects of oil and dispersant Corexit EC9500A on formation of MOS,



and found that both the dispersant and oil promoted the formation of MOS. The researchers also observed that dispersant may facilitate sorption of oil components onto MOS (Xue et al. 2015), which in turn promotes further aggregation and facilitates transport of the oil components.

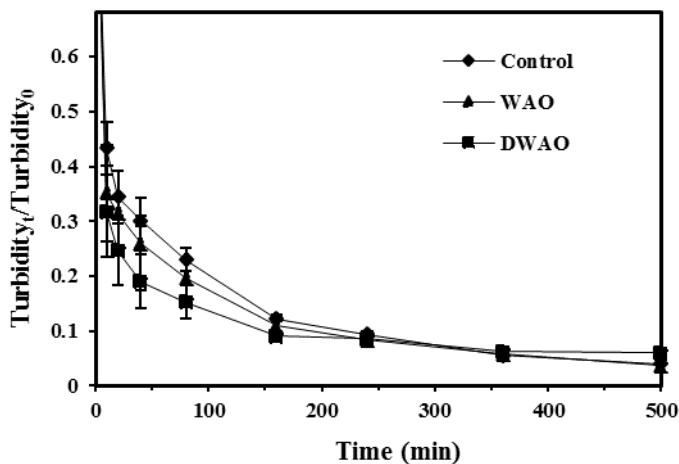


**Figure 3-11.** Effects of WAO and DWAO on settling of OS sediment particles. Experimental conditions: sediment (OS) = 12 g/L, pH =  $7.3 \pm 0.2$ , temperature =  $25 \pm 1$  °C.

### 3.3.3. Effect of dispersant on sediment-facilitated distribution and transport of oil components

PAHs and other oil components are subject to sorption to sediment particles. For instance, **Figure 3-12** shows that the OS sediment particles can rapidly adsorb both phenanthrene and pyrene. Given that the dispersant enhances settling of suspended particles, the dispersant would also facilitate the vertical transport of sediment-associated oil components to the seafloor.

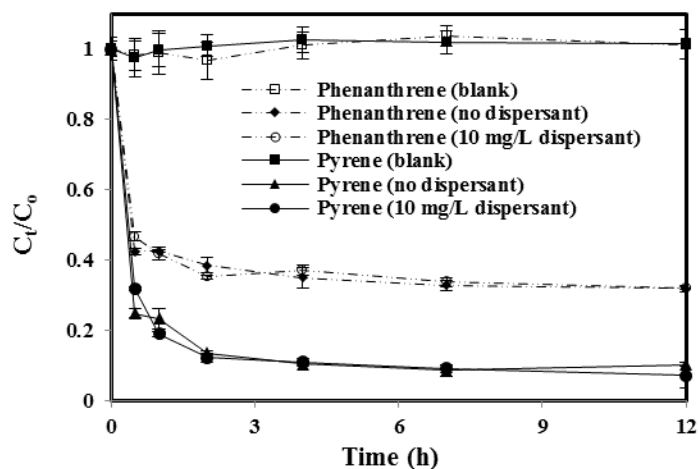


**Figure 3-12.** Sorption kinetics of phenanthrene and pyrene in the presence or absence of dispersant (Corexit EC9527A). Experimental conditions: initial phenanthrene = 600  $\mu\text{g/L}$ , initial pyrene = 40  $\mu\text{g/L}$ , sediment (OS) = 12 g/L, pH = 7.0-7.5, temperature =  $25\pm 1$   $^{\circ}\text{C}$ . Control tests were carried out without sediment.

**Figure 3-13** shows the equilibrium distributions of oil (as TPHs). In the presence of the dispersant, oil in the sediment phase was increased from 6.9% (no dispersant) to 90.1%, which reveals that oil dispersion can dramatically promote partitioning of oil into the sediment phase. The sediment-facilitated transport of dispersed oil may partially account for the oil in the bottom sediment observed following the *DwH* oil spill (White et al. 2012). Interestingly, the oil content in the water column was increased only modestly from 3.7% to 5.4%, compared with 2.8% without dispersant and sediment. This observation clearly reveals that when sufficient sediment is present, the primary role of the dispersant is to facilitate transferring oil from the water surface to the sediment phase rather than in the water column. Furthermore, it might be conceived that in some

circumstances dispersants and selected sediment particles may be applied simultaneously as a rapid and emergency approach to mitigate impacts of oil spill.

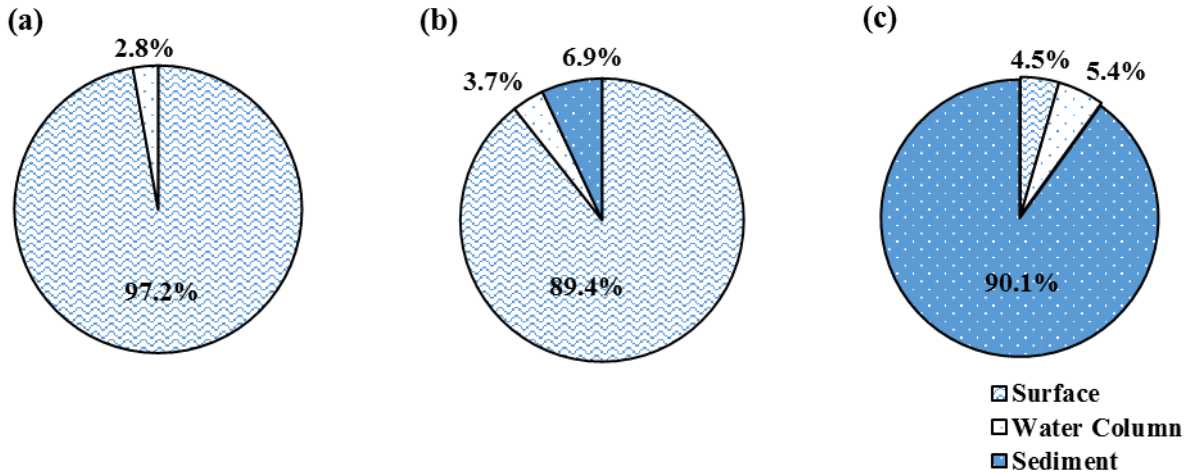


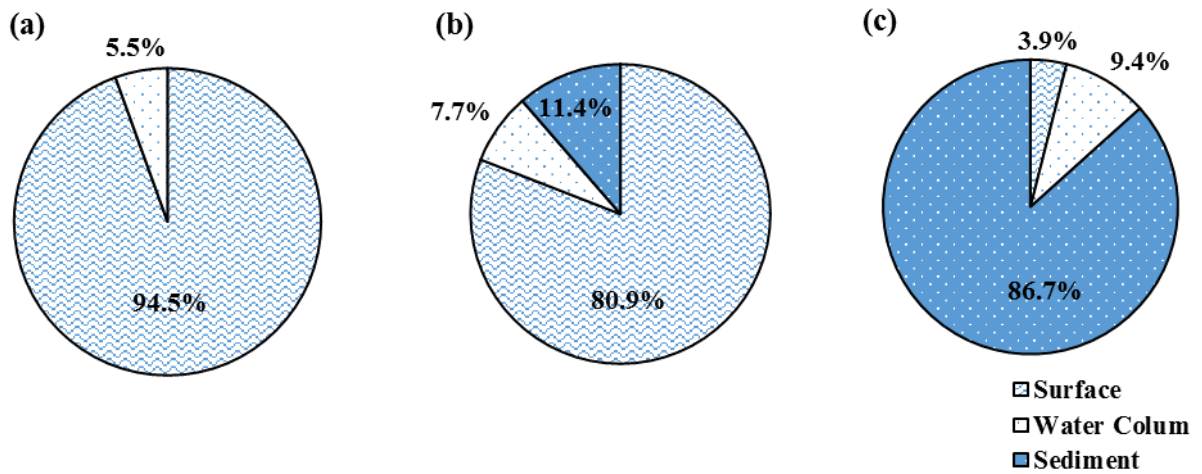
**Figure 3-13.** TPH distributions on seawater surface, in seawater column or sediment in various systems: seawater and oil (a), seawater, oil and sediment without dispersant (b), and seawater, oil and sediment with dispersant (c). Experimental conditions: sediment (OS) = 12 g/L, Corexit EC9527A = 10 mg/L, pH = 7.3 ± 0.2, oil dosage = 60 µL oil in 300 mL seawater for all the cases.

Oil dispersants are known to facilitate formation of small oil-surfactant aggregates, thereby dispersing more oil into the water column (Paris et al. 2012). Gong et al. (2014b) reported that dispersant not only enhances dissolution, but also promotes sediment uptake of oil components. Payne et al. (1989) proposed an equation to characterize the loss rate of free oil droplets due to collision and adherence to SPM.

$$dC/dt = -1.3\alpha[\epsilon/\nu]^{1/2}CS \quad (\text{Eq. 3-5})$$

where  $C$  = concentration of oil droplets (mg/L),  $S$  = concentration of SPM (mg/L),  $\alpha$  = SPM “shape, size, and sticking” coefficient,  $\varepsilon$  = the energy dissipation rate (per mass of fluid), and  $\nu$  = the kinematic viscosity of the water.

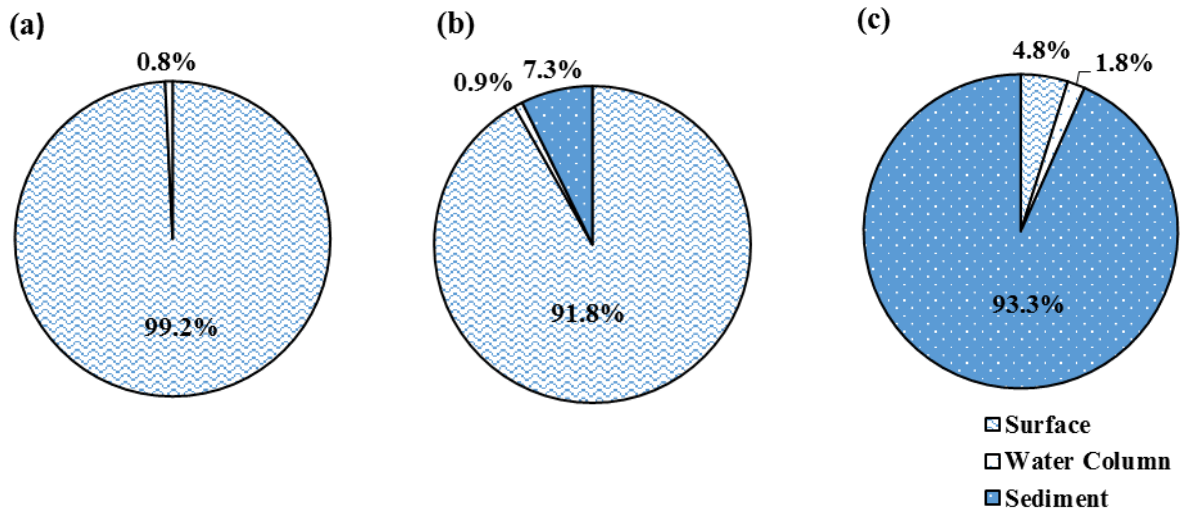
From **Eq. 3-5**, the removal of the dispersed oil droplets from the water column by sediment is primarily attributed to the high sediment concentration (12 g/L). Furthermore, taking into account the dynamic particle aggregation, the initially sorbed oil droplets and dispersant molecules create an even more favorable condition for attracting more oil from the water column, resulting in the formation of even larger oil-sediment aggregates (Bandara et al. 2011).



**Figure 3-14.** Total PAHs distributions on seawater surface, in seawater column or sediment in various systems: seawater and oil (a), seawater, oil and sediment without dispersant (b), and seawater, oil and sediment with dispersant (c). Experimental conditions: sediment (OS)

concentration = 12 g/L, Corexit EC9527A = 10 mg/L, pH = 7.3 ± 0.2, oil dosage = 60 µL oil in 300 mL seawater for all the cases.

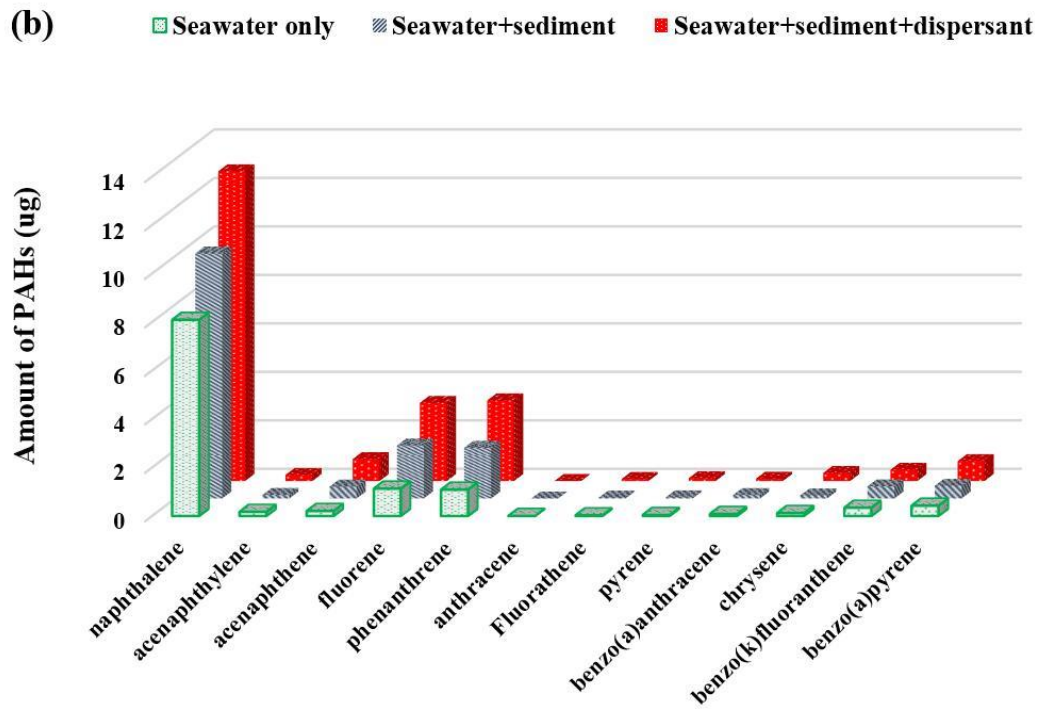
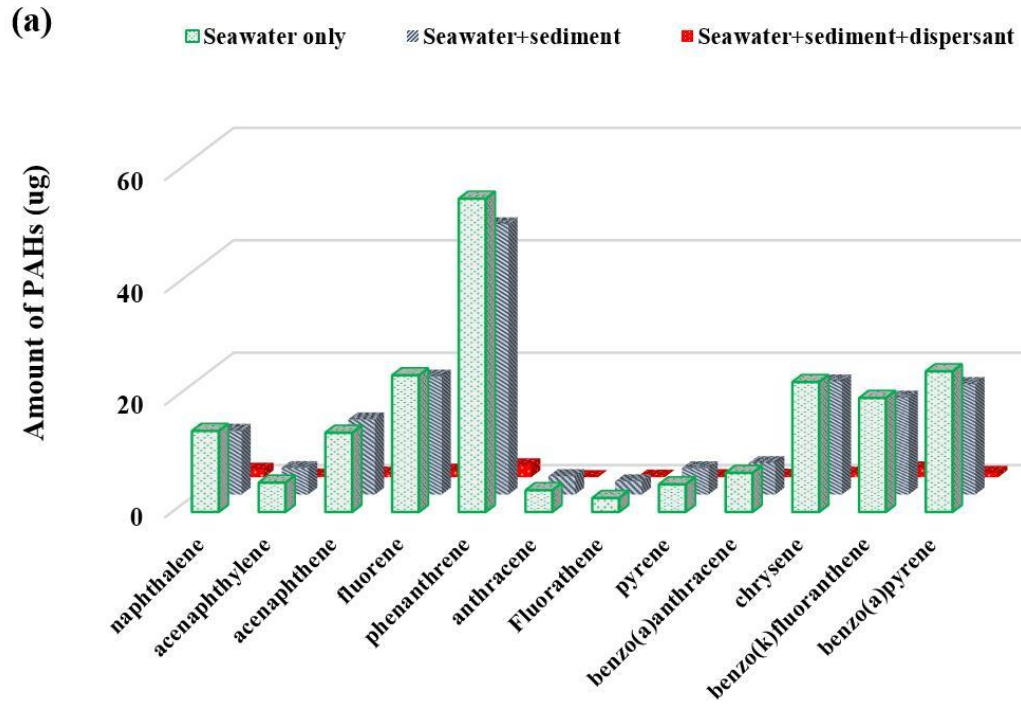
**Figure 3-14** shows that the presence of dispersant increased the total PAHs content in the sediment phase from 11.4% to 86.7%, and the PAHs concentration in the water column from 7.7% to 9.4%, which is consistent with the distributions of TPHs. Similar dispersant-facilitated sediment uptake was also observed for the oil alkanes. **Figure 3-15** shows that the presence of the dispersant increased alkanes in the sediment phase from 7.3% to 93.3%. In light of the extremely low solubility of alkanes, the dispersant-facilitated formation of fine oil droplets is critical for the substantial sediment uptake of alkanes.



**Figure 3-15.** Total alkanes distributions on seawater surface, in seawater column or sediment in various systems: seawater and oil (a), seawater, oil and sediment without dispersant (b), and seawater, oil and sediment with dispersant (c). Experimental conditions: sediment (OS)

concentration = 12 g/L, Corexit EC9527A = 10 mg/L, pH =  $7.3 \pm 0.2$ , oil dosage = 60  $\mu$ L oil in 300 mL seawater for all the cases.

**Figure 3-16** shows the mass distributions of 12 PAHs of the oil in the three phases (surface oil, water column and sediment). Evidently, the surface oil phase was nearly depleted in the presence of the dispersant and sediment (**Figure 3-16a**). In the water column, naphthalene stood out as the most dominant PAH (**Figure 3-16b**), which can be attributed to its higher solubility (or weaker interactions with the sediment and dispersant); in addition, significant amounts of fluorene and phenanthrene were also detected in the water column, which can be attributed to their relatively lower adsorbability and higher concentrations in the crude oil. In the sediment phase, only small amounts of PAHs (mainly naphthalene, fluorene, and phenanthrene) were detected in the absence of dispersant, while the sediment uptake was dramatically increased for all PAHs in proportion to the distribution of PAHs in the crude oil. The experimental results reveal the following findings: 1) in the absence of the dispersant, most oil PAHs prefers to stay in the surface oil phase; 2) the presence of the dispersant splits the PAHs from the bulk oil phase and PAHs in the dispersed oil droplets are more prone to sediment adsorption (Kim et al. 2013a); and 3) the dispersant-facilitated adsorption is likely more effectively for the larger and more hydrophobic PAHs, which are inherently lipophilic.



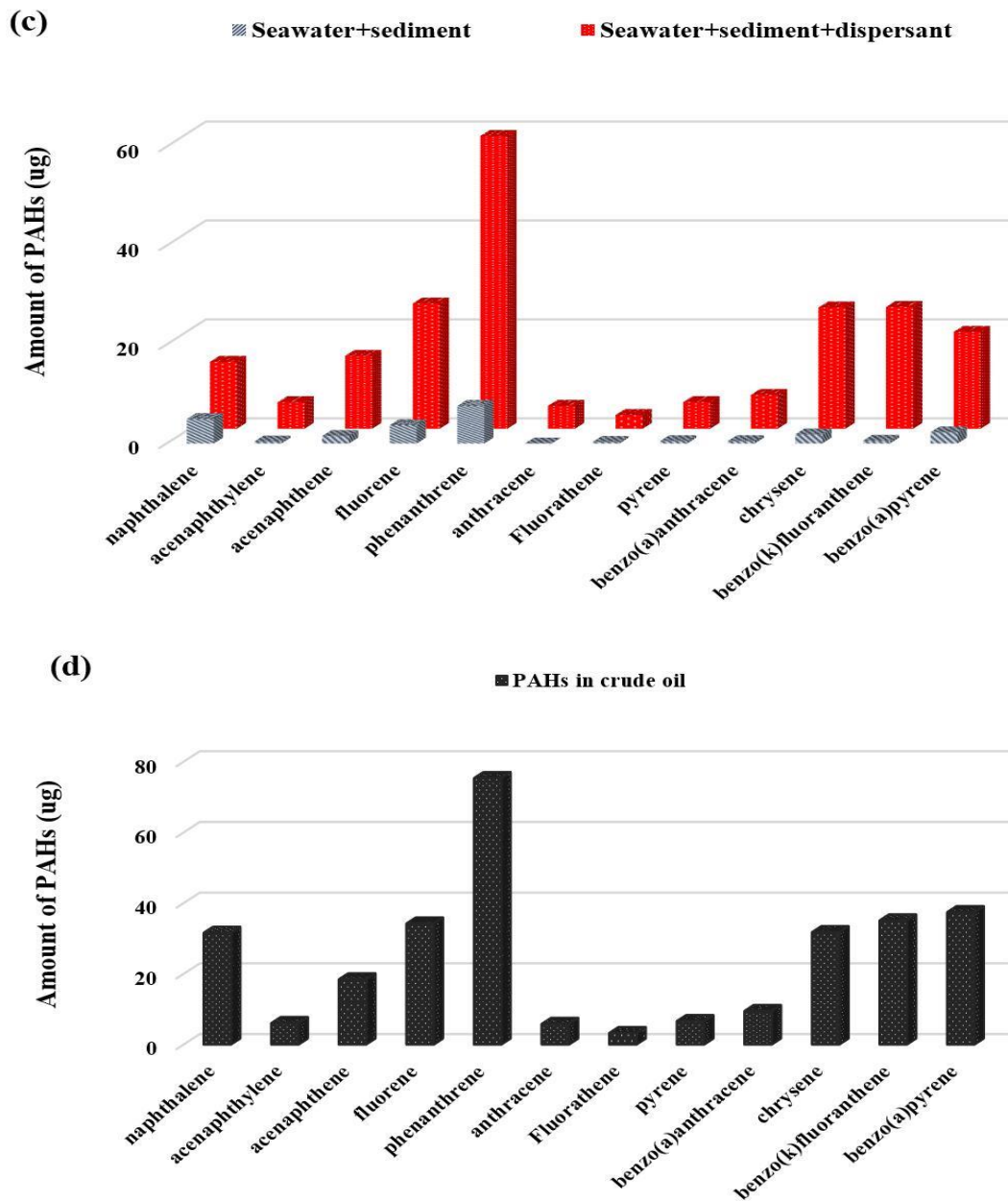


**Figure 3-16.** Mass distribution of various PAHs on seawater surface (a), in seawater column (b) or sediment (c) in various systems: seawater and oil; seawater, oil and sediment without dispersant; and seawater, oil and sediment with dispersant, and mass distribution of various PAHs in the crude



oil (**d**). Experimental conditions: sediment (OS) concentration = 12 g/L, Corexit EC9527A = 10 mg/L, pH =  $7.3 \pm 0.2$ , oil dosage = 60  $\mu$ L oil in 300 mL seawater for all the cases.

### 3.4. Conclusions

This study investigated the effects of oil dispersants on the settling behavior of suspended sediment particles as well as on the distribution and transport of oil components in sediment-seawater systems, and explored the effects of dispersants under various environmental conditions. Major findings are summarized as follows:

(1) All three model dispersants were able to accelerate the settling velocity of suspended sediment particles, with the Corexit dispersants being more effective than the SPC1000 dispersant. The nonionic surfactants (Tween 80 and Tween 85) in the dispersants are the most effective ingredients for enhancing aggregation and settling of sediment particles. The dispersant effects are profound for sediment particles of higher SOM content and smaller size.

(2) The dispersant enhanced the particle settling more profoundly at alkaline or neutral pH, but had little effect at pH 4.02. The dispersant-enhanced particle settling was further boosted in the presence of electrolytes. While humic acid alone decreased the sediment settling rate, combining the dispersant with humic acid showed synergistic acceleration of the settling velocity. The dispersant effect on sediment settling was insignificant at the simulated deepwater temperature (4 °C). The presence of WAO and DWAO increased  $R_{40}$  from 70.0% to 74.1% and 81.0%, respectively.

(3) The presence of oil dispersant in sediment-seawater systems greatly increased the formation of oil-mineral aggregates and facilitated transferring of oil slicks to the sediment phase. In the presence of 10 mg/L of Corexit EC9527A, the TPHs mass percentage in the sediment phase was increased from 6.9% (without dispersant) to 90.1%, and that increased from 11.4% to 86.7% for PAHs.

The findings may aid our understanding of the role of oil dispersants in the formation of oil-sediment aggregates and in the sediment-facilitated transport of oil and PAHs in the marine environment.

## **Chapter 4. Effects of Dispersants on Photodegradation of Polycyclic Aromatic Hydrocarbons in Seawater**

This chapter studied the effects of three model oil dispersants on photodegradation of anthracene and 9,10-dimethylanthracene in seawater. To reveal the mechanism of enhanced PAHs degradation rate, the effects of individual components of dispersant were compared, and the roles of dissolved oxygen and radicals on the photolysis of PAHs were investigated. Moreover, the photolysis pathway of anthracene and 9,10-dimethylanthracene were studied.

### **4.1. Introduction**

Oil dispersants are a mixture of surfactants and solvents. Oil dispersants can lower the oil-water interfacial tension (Prince et al. 2016), break oil slicks into fine oil droplets in the water column, and accelerate the natural attenuation of spilled oil (Griffiths 2012, Prince et al. 2016). Dispersants have been routinely employed in oil spill accidents since the 1960s (Lessard and Demarco 2000). With the development of low-toxicity and high-efficiency dispersant formulations, the application of dispersants has evolved as a major countermeasure to mitigate the adverse effects of oil spills (Griffiths 2012). During the *Sea Empress* spill in the U.K. in 1996, ~12 tons of Corexit EC9500A were used to disperse the oil (Lessard and Demarco 2000). In a pipeline spill offshore in Texas in 1998, ~11.5 tons of Corexit EC9527A were applied (Lessard and

Demarco 2000). The largest dispersant application took place during the Deepwater Horizon (*DwH*) oil spill in 2010 (Kleindienst et al. 2015b), where ~7800 tons of oil dispersants, including Corexit EC9500A and EC9527A, were applied to the surface (~5000 tons) and deepwater (~2800 tons) (Gong et al. 2014a, Kujawinski et al. 2011). While the pros and cons of large-scale application of dispersants remain under intensive researches (Kleindienst et al. 2015b, Prince et al. 2016), it is generally believed that oil dispersants may accelerate the natural weathering processes (Griffiths 2012). However, quantitative information remains limited on the effects of oil dispersants on photochemical weathering of oil components in the marine environment.

The Macondo well oil contains ca. 3.9% of PAHs (by weight), and the *DwH* oil spill released ca. 21000 tons of PAHs into the Gulf of Mexico (Reddy et al. 2012). PAHs are known to be toxic, carcinogenic, and mutagenic. Sixteen of the parent PAHs have been listed as priority pollutants by the United States Environmental Protection Agency (EPA) (US EPA 2014).

Typically, crude oil contains much more alkylated PAHs than the parent PAHs (Liu et al. 2012a). More-alkylated PAHs are more likely to accumulate in plant and animal systems (Brandt et al. 2002), and show stronger carcinogenic potency (Slaga et al. 1980). However, less information on the degradation of alkylated PAHs is available than for the parent PAHs. Therefore, it is of great significance to evaluate the weathering of both parent and alkylated PAHs in the marine environment. Anthracene and the alkylated derivative, 9,10-dimethylanthracene (9,0-DMA), are of high abundance in crude oil and have been commonly detected in the oil affected ecosystems (Allan et al. 2012).

Photodegradation is a major abiotic process affecting spill oil attenuation, and has significant implications to redox cycling, transport, and degradation of oil components (Fu et al. 2014a, Nicodem et al. 2001, Saeed et al. 2011). While a significant body of knowledge exists on the photochemical degradation of PAHs in natural waters, information has been lacking on the photodegradation rate and mechanisms of dispersed PAHs (Fasnacht and Blough 2002). Oil dispersants are known to alter the physico-chemical properties of PAHs, such as distribution of PAHs in the water column, size of the oil droplets, light absorbance, quantum yield, and production of reactive oxygen species (ROS) (Gong et al. 2015). While these changes are likely to impact photolysis of PAHs, there has been no information available on the effects of oil dispersants on the photodegradation of PAHs and alkylated PAHs by solar light and on the underlying mechanisms.

The overall goal of this study was to examine the effects of oil dispersants on the photodegradation of PAHs (anthracene and 9,10-DMA) in seawater under simulated solar light. The specific objectives were to: 1) investigate the effects of three model dispersants, i.e. Corexit EC9500A, Corexit EC9527A and SPC 1000, on photodegradation of the two model PAHs; 2) identify the key dispersant components that affect the photodegradation rate of PAHs; 3) evaluate effect of DO on the photolysis of PAHs and identify the key reactive oxygen species in the presence of oil dispersants; 4) elucidate the photodegradation mechanisms in the presence of oil dispersants; and 5) determine the photochemical stability of oil dispersants.

The findings of this research will aid in our understanding of photochemical attenuation of oil components in the presence of chemical dispersants in the Gulf of Mexico's ecosystem.

## 4.2. Materials and methods

### 4.2.1. Materials

The following chemicals (analytical grade or higher) were used as received: anthracene, 9,10-DMA, *tert*-butanol, superoxide dismutase, methanol (Alfa Aesar, Ward Hill, MA, USA), humic acid (Fluka Chemie, Switzerland), NaN<sub>3</sub>, NaOH and NaCl (Fisher Scientific, Fair lawn, NJ, USA). Corexit EC9500A and Corexit EC9527A were acquired per courtesy of Nalco Company (Naperville, IL, USA), and SPC1000 was obtained from US Polychemical Corporation (Chestnut Ridge, NY, USA). The Corexit dispersant components (Tween 85, Span 80, kerosene, and 2-butoxyethanol) and the SPC 1000 components (polyethylene glycol monooleate (Ethox T09A), dipropylene glycol monomethyl ether (DPM), and cocamide DEA) were obtained from either Fisher Scientific (Fair lawn, NJ, USA) or Sigma-Aldrich (St. Louis, MO, USA).

Seawater was collected from the top 30 cm of the water column at the Grand Bay area, AL, USA. (N30.37873, W88.30679). The seawater sample was preserved at 4 °C, and filtered through 0.22 µm pore-size membrane before use. The key physicochemical properties of the seawater were as follows: pH = 7.9, salinity = 3.15 wt.%, dissolved organic matter (DOM) = 0.77 mg/L (as total organic carbon (TOC)).

### 4.2.2. Experimental apparatus

**Figure 4-1** shows the photodegradation setup. The solar irradiation was provided by a Newport 84041A solar simulator (Newport Corp., Irvine, CA, USA) equipped with a 450 W xenon-ozone free short arc lamp and an air mass 1.5 global filter to remove the infrared irradiation in the visible

region. **Table 4-1** gives the output spectrum distribution of simulated solar irradiation. The light intensity was set at  $85 \pm 0.5 \text{ mW/cm}^2$ , which was measured by an 818-UV/DB photodetector (Newport Corporation, Irvine, CA, USA). A sealed glass photo-reactor with a working volume of 250 mL was used in the experiments, including a quartz cover to allow the vertical transport of the solar light, and a water circulating coating to keep the reactor at constant temperature (25 °C).

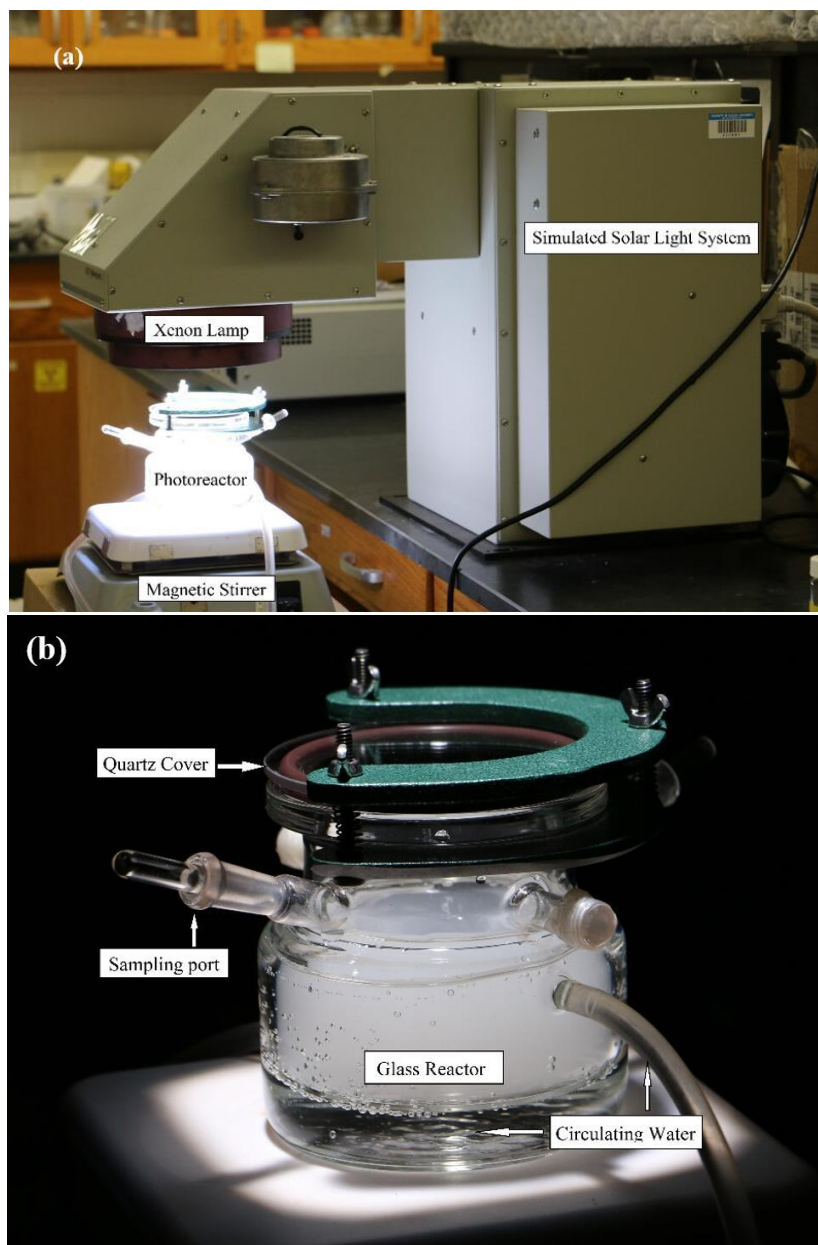


**Figure 4-1.** Experimental set-up of PAHs photodegradation. Simulated solar light system (a), photo-reactor (b).



**Table 4-1.** Output spectrum distribution of simulated solar irradiation (data were provided by the Newport Corporation).

	Range (nm)	% of 200-2500 nm
UVC	<280	0
UVB	280-320	0.1
UVA	320-400	5.3
Visible	400-450	7.3
	450-500	10.5
	500-550	9.8
	550-600	10
	600-650	9
	650-700	8.1
Infrared	700-800	11.3
	800-900	7.3
	900-1000	4.7
	1000-1100	2.2
	1100-1500	7
	1500-2000	5.3
	2000-2500	2.2

To evaluate the contribution of visible irradiation on the total removal of PAHs by photodegradation, an UV cut-off filter (Institute of Electric Light Source, Beijing, China) was attached to the photo-reactor to remove the irradiation with wavelength <420 nm. The UV-vis absorbance spectrum of the UV cut-off filter is shown in **Figure 4-2**.

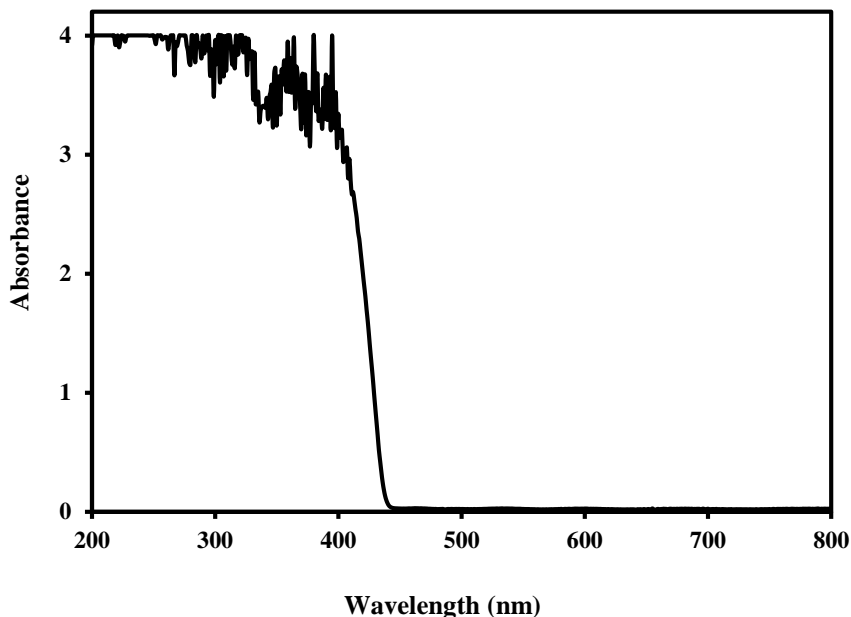


**Figure 4-2.** UV-vis absorbance spectrum of the UV cut-off filter.

#### **4.2.3. Effects of dispersants on photodegradation of PAHs**

Batch photodegradation kinetic tests were carried out to evaluate the effects of dispersants. Stock solution of anthracene and 9,10-DMA (each at 0.3 g/L) were prepared separately by dissolving a known amount of a PAH in methanol. In each batch test, 250 mL of filtered seawater was added in the photo-reactor, followed by adding an aliquot of the PAH stock solution and a dispersant (or dispersant components), which gave an initial PAH concentration of 30  $\mu\text{g/L}$  and

dispersant (or dispersant components) concentration of 18 mg/L. The solution was mixed for 30 min by magnetic stirring in a sealed photo-reactor. Then, the photodegradation was initiated by irradiating the reactor with the simulated solar light. At predetermined time intervals, samples were withdrawn for determining the PAHs remaining in the solution or reaction intermediates. Control experiments were conducted in dark but under otherwise identical conditions.

To investigate effects of oil dispersants on the vertical distribution of PAHs in the water column, a 250 mL anthracene solution of 30  $\mu\text{g/L}$  was mixed with a dispersant or dispersant component in the photo-reactor for 30 min in the dark. Then, each 1 mL samples were withdrawn at various depths and mixed with methanol for analysis of the PAHs concentration.

To evaluate the contribution of visible irradiation on the photolysis of PAHs, a UV cut-off filter was applied on the photo-reactor to selectively remove the UV part (wavelength  $<420$  nm) of solar irradiation. All other experimental conditions were identical to those with dispersant.

#### **4.2.4. Roles of dissolved oxygen and radicals for photodegradation of PAHs**

To investigate the effects of dissolved oxygen (DO), the photodegradation tests were also carried out with seawater that was purged with nitrogen for 1 h.

The roles of radicals, i.e.  $^1\text{O}_2$ , superoxide ( $\text{O}_2^{\cdot-}$ ), and hydroxyl ( $\cdot\text{OH}$ ) radicals, in PAH photodegradation were evaluated by using selective radical scavengers. Specifically, *tert*-butanol at 221 mg/L was used for quenching  $\cdot\text{OH}$ , sodium azide at 200 mg/L for  $^1\text{O}_2$  and  $\text{O}_2^{\cdot-}$  (Gong et al. 2015), superoxide dismutase at 14 mg/L for  $\text{O}_2^{\cdot-}$  (Diaz et al. 2004, Ryu and Choi 2004).

#### 4.2.5. Analytical methods

Anthracene and 9,10-DMA in seawater were quantified using an Agilent 1260 Infinity high performance liquid chromatography (HPLC) system equipped with a Poroshell 120 EC-C18 column ( $50 \times 4.6$  mm,  $2.7 \mu\text{m}$ ). The column temperature was  $30 \text{ }^\circ\text{C}$ , and the mobile phase consisted of a mixture of acetonitrile and water (70:30 v/v) with 0.5 wt.% phosphoric acid, and the flow rate was set at 1 mL/min. The sample injection volume was  $80 \mu\text{L}$ , and the eluate was analyzed by an UV detector at the wavelength of 254 nm, which afforded a detection limit of  $0.5 \mu\text{g/L}$  for both PAHs.

To determine the photodegradation intermediates, each 100 mL of solution samples were withdrawn from the photo-reactor at various reaction times, and extracted using 5 mL dichloromethane consecutively for 3 times, then the extracts were dried by sodium sulfate anhydrous ( $\text{Na}_2\text{SO}_4$ ) and concentrated to 0.5 mL under a gentle stream of  $\text{N}_2$  gas. The concentrated extracts were then analyzed by an Agilent 7890A Gas Chromatography coupled with a 5975C Series Mass Spectrometry (GC-MS). A HP-5MS 5% phenyl methyl siloxane capillary column was used with helium as the carrier gas at a flow rate of 0.9 mL/min. The sample injection volume was  $2 \mu\text{L}$ , and the inlet temperature was  $250 \text{ }^\circ\text{C}$ . The oven temperature was programmed as follows: hold at  $40 \text{ }^\circ\text{C}$  for 1 min, ramp from  $70 \text{ }^\circ\text{C}$  to  $280 \text{ }^\circ\text{C}$  at  $10 \text{ }^\circ\text{C}/\text{min}$ , and then hold at  $280 \text{ }^\circ\text{C}$  for 6 min. The scan range was from 35 to 550 m/z (mass to charge ratio).

UV-Vis absorption spectra and fluorescence analysis of the PAH solutions were obtained using a SpectraMax M2 plate reader (Molecular Devices, Sunnyvale, California, USA) with a 1-cm path quartz cuvette. The excitation wavelengths of anthracene and 9,10-DMA were 366 and 375 nm,

respectively, and the emissions were recorded in the range of 360 to 550 nm for the fluorescence analyses.

### **4.3. Results and discussion**

#### **4.3.1. Effects of dispersants on PAHs photolysis**

**Figure 4-3** shows effects of Corexit EC9500A on photodegradation of anthracene and 9,10-DMA under simulated sunlight. The control tests indicate that the loss of anthracene or 9,10-DMA was <4% without light, and the dispersant does not react with the PAHs. The presence of Corexit EC9500A remarkably promoted photodegradation of both PAHs. The presence of 18 mg/L of the dispersant shortened the complete removal time from 300 to 120 min for anthracene and from 80 to 15 min for 9,10-DMA. Between the two PAHs, the alkylated counterpart (9,10-DMA) was more vulnerable to photolysis than its parent PAH. This observation is consistent with other studies where increasing alkyl-substitution of PAHs gives faster photooxidation rates (Lima et al. 2005), and it can be attributed to the benzyl hydrogen activation of 9,10-DMA where the alkyl group acts as the electron donating group (Radding et al. 1976). The results also indicate that the dispersant enhanced the photodegradation of the alkylated PAH more effectively than the parent PAH. More details on the mechanisms of dispersant facilitated photodegradation will be discussed in Section 4.3.3.

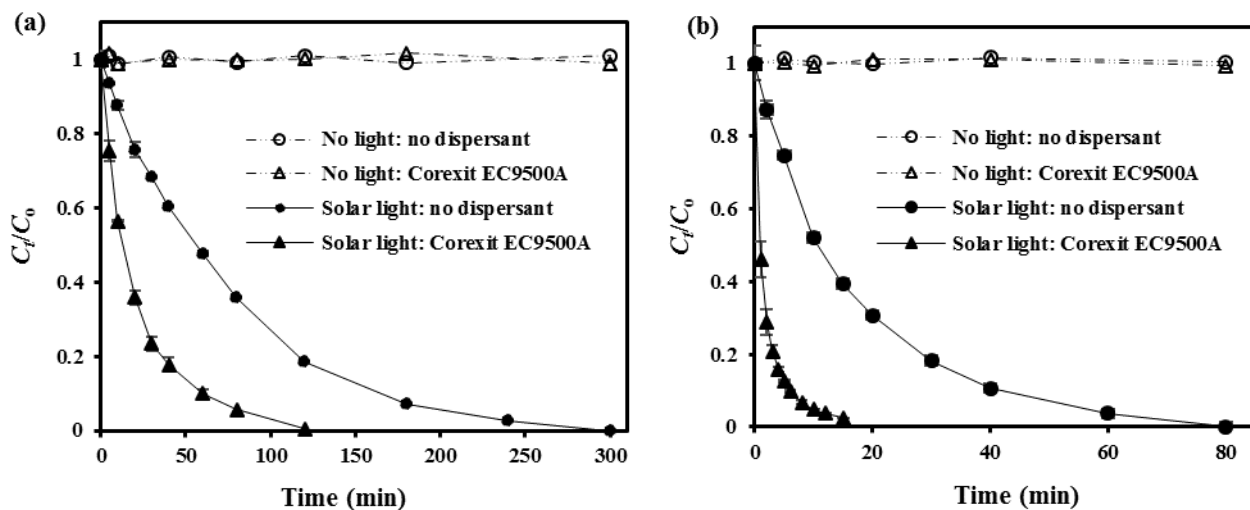


**Figure 4-3.** Effects of Corexit EC9500A on photodegradation of anthracene (a), and 9,10-DMA (b) in seawater. Experimental conditions: Corexit EC9500A = 18 mg/L, initial anthracene or 9,10-DMA = 30  $\mu\text{g/L}$ , pH =  $7.8 \pm 0.2$ , temperature =  $25 \pm 0.2$  °C.

The first-order kinetic model is employed to interpret the kinetic data (Gong et al. 2015):

$$\ln(C_t / C_0) = -k \cdot t \quad (\text{Eq. 4-1})$$

where  $C_0$  and  $C_t$  ( $\mu\text{g/L}$ ) are the PAH concentrations at reaction time 0 and  $t$  (min), respectively, and  $k$  is the first-order reaction rate constant ( $\text{min}^{-1}$ ).

**Figure 4-4** shows the linearized plots of the kinetic data in accord with the rate model. For both PAHs, the first-order kinetic model was able to adequately ( $R^2 > 0.99$ ) describe photolysis rates when no dispersant was present. However, the presence of the dispersant (18 mg/L) induced a two-stage degradation kinetic profile for both PAHs, i.e. a faster initial degradation rate (with a steeper slope) followed by a later slower rate. Nonetheless, the first-order model was able to

separately fit the kinetic data over the two stages. **Table 4-2** gives the best fitted  $k$  values. It is noteworthy that the presence of Corexit EC9500A increased the  $k$  values by a factor of 3.8 and 9.1, respectively, for anthracene and 9,10-DMA in the initial stage, and by 2.2 and 3.0 in the second stage. Similar two-stage profiles have been observed by Gong et al. (2015). The photodegradation rate of pyrene under UV light was 7.9 times faster at the initial stage (first 10 min) than that at second stage (10-360 min). They claimed that the two stage degradation kinetics are due to the more prevalent role of direct photolysis in the initial stages, and dominant role of electron transfer from excited pyrene species to oxygen in the second stages (Gong et al. 2015). However, the two-stage degradation kinetics of PAHs can also be attributed to: 1) some photodegradation byproducts are produced and act as internal light absorbers, thus weakening the light intensity that is available for the target PAHs, or act as quenchers for the radicals (Chu and Kwan 2002); 2) the effective dispersant components that accelerating PAHs degradation may be photodegraded in the initial stages.

Considering that 77% of anthracene and 84% of 9,10-DMA were degraded in the initial stage, the  $k$  values of the initial stage were used to compare the enhanced photolysis rates hereafter in this paper.

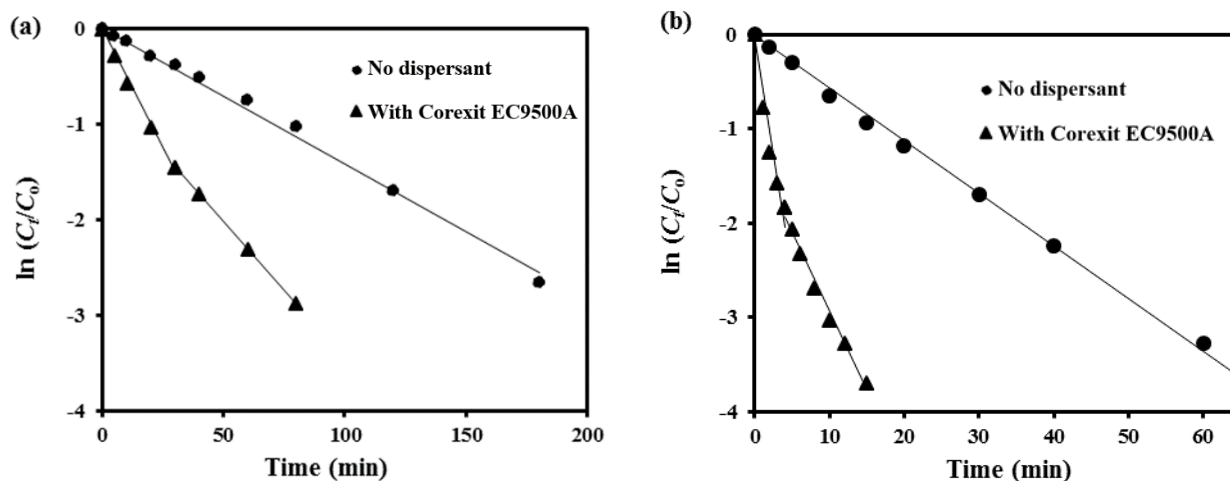


**Figure 4-4.** Fitting the first-order kinetic model to the experimental rate data of: anthracene (a) and 9,10-DMA (b), in the absence or presence of 18 mg/L of Corexit EC9500A.

**Table 4-2.** The first-order photodegradation rate constants ( $k$ ) of anthracene and 9,10-DMA under solar irradiation.

PAHs	No dispersant		With Corexit EC9500A (18 mg/L)			
	$k$ (min <sup>-1</sup> )	$R^2$	Initial stage		Second stage	
	$k$ (min <sup>-1</sup> )	$R^2$	$k$ (min <sup>-1</sup> )	$R^2$	$k$ (min <sup>-1</sup> )	$R^2$
<b>Anthracene</b>	0.013	0.99	0.050	0.99	0.029	1.00
<b>9,10-DMA</b>	0.056	1.00	0.511	0.92	0.167	0.99

Using 9,10-DMA as a model PAH, the effects of two other dispersants, i.e. Corexit EC9527A and SPC 1000, on the photodegradation rate were further studied. **Figure 4-5** compares the effects of the three oil dispersants. Evidently, all three dispersants accelerated the photodegradation rate



of 9,10-DMA, and the effectiveness follows the order of: Corexit EC9500A >> Corexit EC9527A > SPC 1000. Like Corexit EC9500A, Corexit EC9527A showed a higher initial photolysis rate ( $k_1 = 0.122 \text{ min}^{-1}$ ) and a lower rate ( $k_2 = 0.057 \text{ min}^{-1}$ ) in the second stage (after 12 min), and the  $k_2$  is comparable to the photolysis rate without dispersant ( $0.056 \text{ min}^{-1}$ ); for SPC 1000, however, a straight constant rate ( $0.062 \text{ min}^{-1}$ ) was observed. The different behaviors of the three dispersants are attributed to their different formulas and effective compositions (See Section 4.3.2 below).

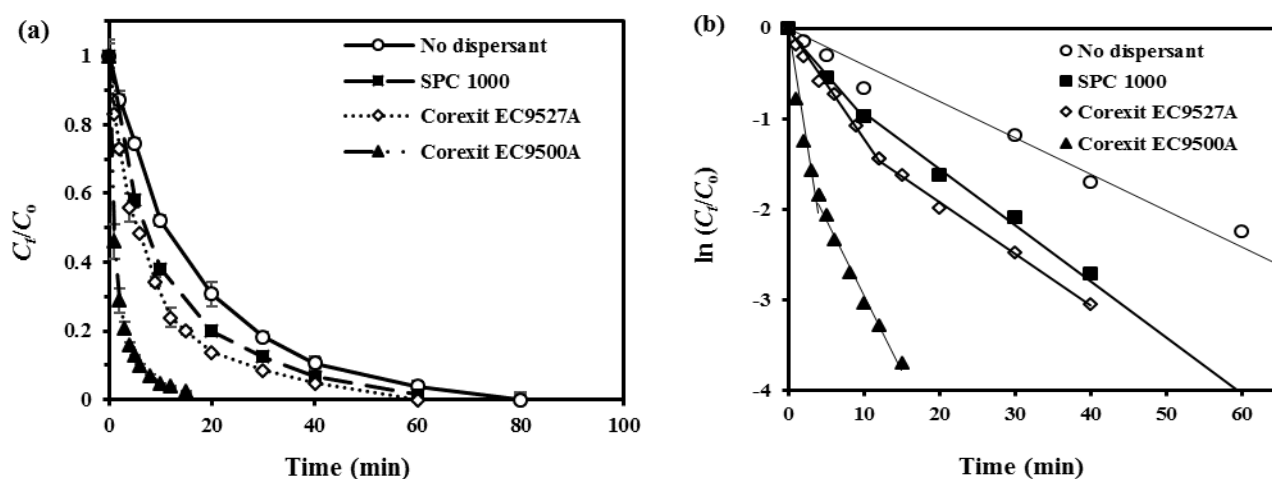


**Figure 4-5.** Effects of three model oil dispersants on photodegradation of 9,10-DMA in seawater (a), and the linearized first-order kinetic plots (b). Experimental conditions: dispersant dosage = 18 mg/L, initial 9,10-DMA = 30  $\mu\text{g/L}$ , pH =  $7.8 \pm 0.2$ , temperature =  $25 \pm 0.2 \text{ }^\circ\text{C}$ .

#### 4.3.2. Effects of dispersant components on PAH photolysis

Oil dispersant contains various surfactants and organic solvents (Fu et al. 2015, Hayworth and Clement 2012). Therefore, it is important to understand the effects of key individual dispersant components on the photochemical reactions. Again, using 9,10-DMA as a model PAH, the effects of individual components of Corexit dispersants on the degradation rate were studied as follows.

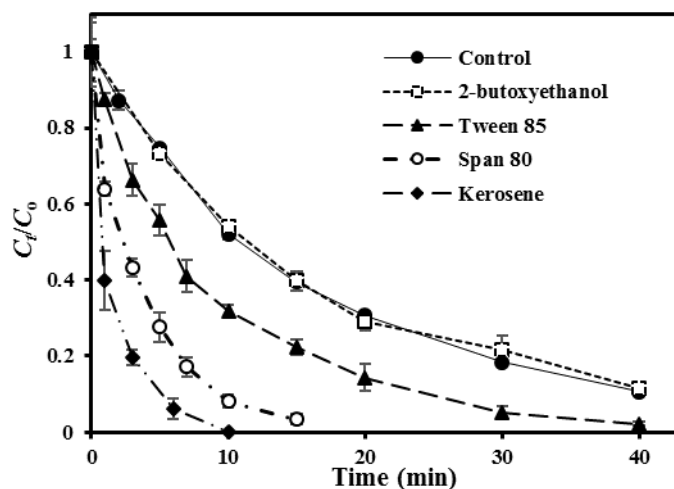


**Figure 4-6.** Effects of key components of Corexit dispersants on photodegradation of 9,10-DMA in seawater. Experimental conditions: dispersant component concentration = 18 mg/L, initial 9,10-DMA = 30  $\mu\text{g/L}$ , pH =  $7.8 \pm 0.2$ , temperature =  $25 \pm 0.2$  °C.

**Table 4-3.** Photodegradation rate constants ( $k$ ) of anthracene in the presence of individual dispersant components under solar irradiation.

	Control	2-butoxyethanol	Tween 85	Span 80	Kerosene
$k$ ( $\text{min}^{-1}$ )	0.056	0.055	0.098	0.239	0.493
$R^2$	1.00	0.98	0.99	0.97	0.95

**Figure 4-6** shows the photodegradation rates of 9,10-DMA in the presence of 5 key Corexit dispersant components, including Tween 85, Span 80, kerosene and 2-butoxyethanol (each at 18 mg/L). **Table 4-3** gives the best-fitted  $k$  values in the initial stage. Tween 85, Span 80 and kerosene all accelerated the photolysis rate by a factor of 1.8, 4.3 and 8.8, respectively, while 2-

butoxyethanol showed negligible effect on the photodegradation rate. As the nonionic surfactants (Tweens and Span 80) account for nearly 50% of the dispersant (Bruheim et al. 1999), Tween 85 and Span 80 can be the critical contributors to the enhanced photolysis rate.

**Figure 4-7** shows that Tween 85 exhibited a strong peak in the UVC range (<260 nm), much stronger than that for the dispersant as a whole, which can be attributed to the abundance of electron-rich double bonds in the molecular structure of Tween 85 (Erdem et al. 2014). The absorbed solar energy on Tween 85 may lead to the formation of primary and secondary reactive species, e.g.  $^1\text{O}_2$  (Wenk et al. 2011), and/or transfer energy to PAHs, and thus induce the photosensitized degradation.

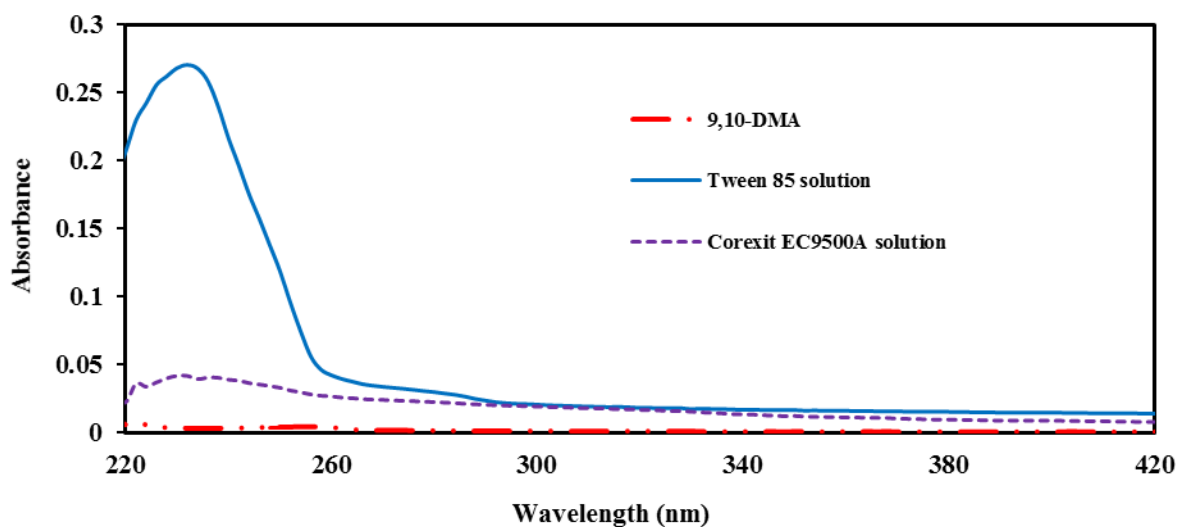


**Figure 4-7.** UV-Vis absorption spectra of 9,10-DMA, Tween 85, and Corexit EC9500A in seawater. Spectra were corrected by subtracting the absorption spectrum of seawater. Experimental conditions: Corexit EC9500A or Tween 85 = 18 mg/L, 9,10-DMA = 30  $\mu\text{g/L}$ .

Span 80 is a nonionic surfactant with low hydrophilic-lipophilic balance (HLB) value (4.3) (Ruckmani et al. 2000), which can only be partially dissolved or dispersed in water (Barbetta and Cameron 2004). 9,10-DMA is highly hydrophobic ( $\log K_{ow} = 5.69$ ) and it can favorably partition and accumulate in the hydrophobic phase of Span 80. Furthermore, the density of Span 80 (0.99 g/mL) is lower than that of the seawater (1.03 g/mL). Consequently, Span 80 may stratify in the water column with more surfactant in the upper part, namely, Span 80 may entrain and enrich more 9,10-DMA in the upper layer of the solution, which is favorable for absorbing light. Likewise, kerosene is also hydrophobic solvent ( $\log K_{ow} = 3.7-8.0$ ), with an even lower density (0.80 g/mL), and thus, kerosene will pose even greater floating effect than Span 80 on the 9,10-DMA enrichment despite its small fraction in the dispersant.

**Figure 4-8** shows the vertical distribution of 9,10-DMA in the photo-reactor water column in the presence of the dispersant (18 mg/L) or with the same concentration of each individual components. Evidently, kerosene displayed the strongest floating effect on the PAH, which enriched the PAH concentration in the top layer by ~20% compared to that in the control (plain seawater). Span 80 alone caused slightly more PAH stratification than the dispersant as a whole, enriched the surface PAH concentration by ~5.4% and ~4.8%, respectively. Therefore, the surface enrichment of PAHs facilitated by the light hydrophobic components is partially responsible for the dispersant-enhanced photodegradation. It should be noted, though, that the enrichment effect was less significant for the dispersant than the individual components, which is because the dispersant was formulated in a way to achieve maximal water dispersibility of the hydrophobic compounds.

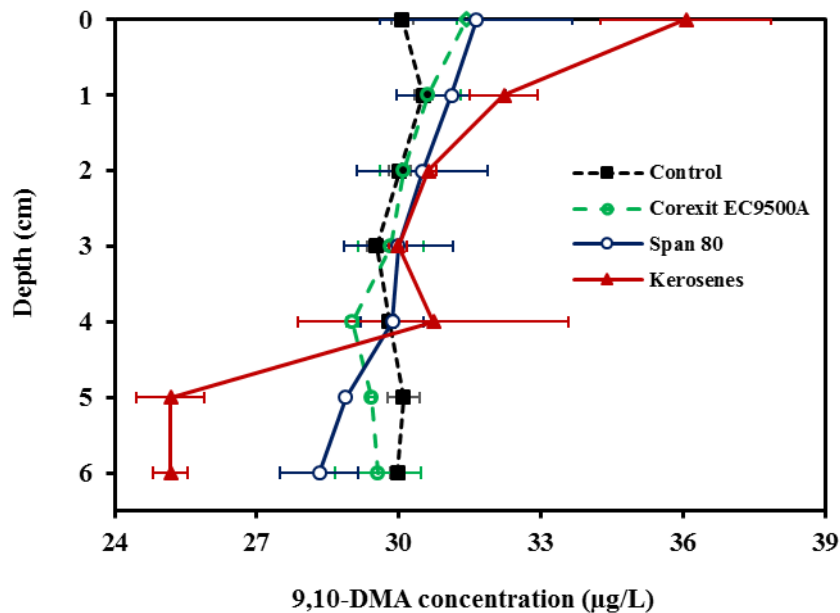


**Figure 4-8.** Vertical distribution of 9,10-DMA concentration in the photo-reactor in the absence or presence of Corexit EC9500A or individual Corexit dispersant components. Experimental conditions: Corexit EC9500A or dispersant components = 18 mg/L, 9,10-DMA = 30 µg/L.

The dispersant components of Corexit EC9527A are similar to Corexit EC9500A but with a unique organic solvent (2-butoxyethanol). The 2-butoxyethanol had negligible effect on the photolysis of 9,10-DMA (as shown in **Figure 4-6**), which may partially interpret the weaker effect of Corexit EC9527A than Corexit EC9500A on enhancing the photolysis rate of 9,10-DMA.

For comparison, the effects of three most abundant SPC 1000 components, i.e. polyethylene glycol monooleate, DPM and cocamide DEA, on the photodegradation of 9,10-DMA were tested at the identical conditions. The polyethylene glycol monooleate did not affect the photolysis rate of 9,10-DMA; dipropylene glycol monomethyl ether (DBE) and cocamide DEA (Ninol 4OCO) changed the photolysis rate ( $k_1$ ) from 0.056 to 0.044 and 0.094 min<sup>-1</sup>, respectively. DBE and Ninol

4OCO only amount to <19% of the total SPC 1000 content (Jacob et al. 2001), but the polyethylene glycol monooleate and water comprise ca. 36% and 20% of total SPC 1000 content (Jacob et al. 2001). Therefore, the SPC 1000 is less effective than Corexit dispersants on accelerating the photolysis of PAHs.

#### **4.3.3. Mechanism of dispersant-enhanced PAH photolysis**

**Figure 4-9** shows the corrected UV-Vis absorbance spectra of anthracene and 9,10-DMA in plain seawater or in Corexit EC9500A seawater solution. The maximum absorbance for anthracene and 9,10-DMA occurred at 248 nm and 255 nm, respectively, in seawater. The presence of the dispersant dramatically enhanced the absorbance of solar irradiation, especially in the UV region (<400 nm). Although UV light only accounts for a small fraction (~5%) of sunlight, UV irradiation is much more energetic than visible light. Therefore, enhanced UV absorbance contributes in part to the accelerated photodegradation rate.

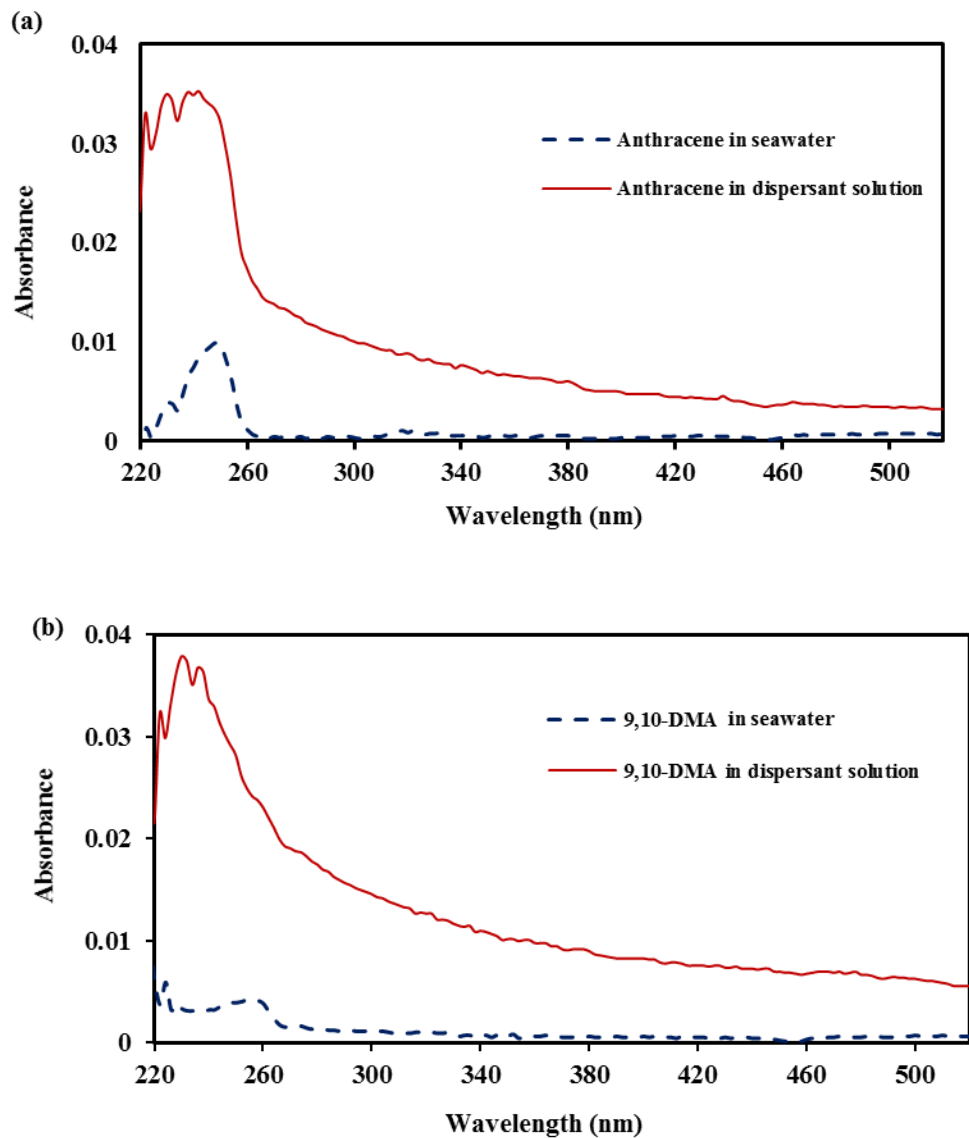


**Figure 4-9.** UV-Vis absorption spectra of anthracene (a), and 9,10-DMA (b) in plain seawater and Corexit EC9500A seawater solution. Spectra were corrected by subtracting the absorbance spectra of seawater. Experimental conditions: anthracene or 9,10-DMA = 30  $\mu\text{g/L}$ , Corexit EC9500A = 18 mg/L.

**Figure 4-10** compared the photodegradation rates of anthracene and 9,10-DMA under solar and visible light irradiation. The presence of Corexit EC9500A accelerated the photolysis rate constants ( $k$ ) of anthracene from 0.013 to 0.050  $\text{min}^{-1}$  under solar light, and from 0.004 to 0.012  $\text{min}^{-1}$  under visible light. Similarly, the presence of Corexit EC9500A increased the photolysis rate constants ( $k$ ) of 9,10-DMA from 0.056 to 0.511  $\text{min}^{-1}$  under solar light, and from 0.013 to 0.183  $\text{min}^{-1}$  under visible light. The results showed that the UV irradiation contributed to more than 2/3 of the total photolysis of PAHs in the absence of dispersant. The increased photolysis rate of PAHs is primarily due to the enhanced utilization efficiency of UV irradiation in the presence of Corexit EC9500A, which in agree with the enhanced UV absorbance by dispersant (as shown in **Figure 4-9**).

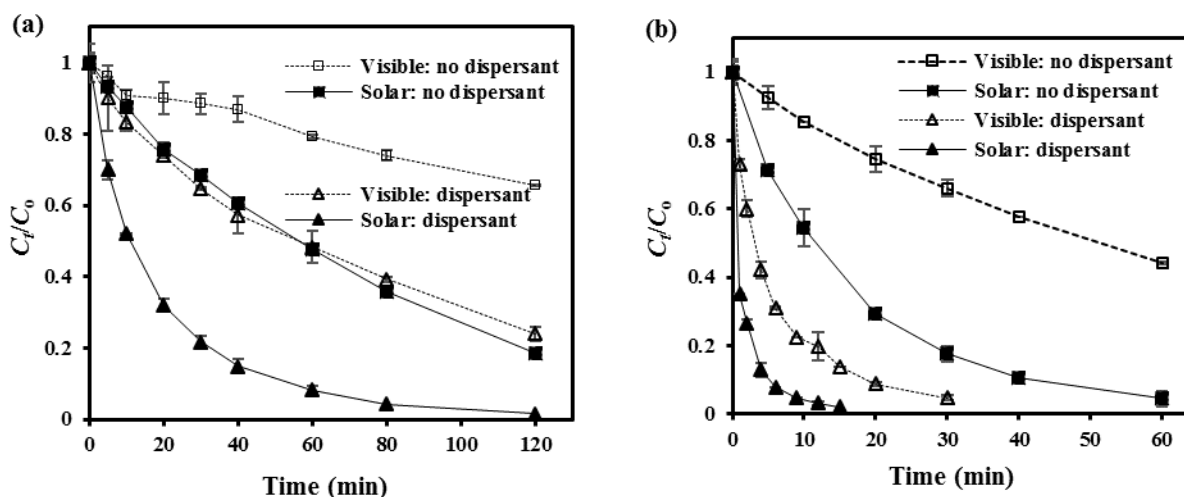


**Figure 4-10.** Contributions of solar and visible irradiation on the photolysis of anthracene (a) and 9,10-DMA (b) in the absence/presence of Corexit EC9500A. Experimental conditions: Corexit EC9500A = 18 mg/L, initial anthracene or 9,10-DMA = 30  $\mu\text{g/L}$ , pH = 8.0  $\pm$  0.3, temperature = 25  $\pm$  0.2  $^{\circ}\text{C}$ .



In addition to the enhanced light absorbance, the dispersant may chemically enhance the photodegradation rate of PAHs. As is well known, photochemical change may involve both direct and indirect (sensitized) photolysis. In direct photolysis, a substrate absorbs the solar quanta “directly”, followed by degradation of the excited state (Zepp 1979). Organic chemicals that are structurally composed of chromophoric moieties, e.g. aromatics, conjugated C=C, or ketones, can absorb light at wavelengths present in solar irradiation, and are susceptible to direct photolysis (Schwarzenbach et al. 2003). Direct photolysis has been known to be the dominant pathway for PAHs photodegradation in natural waters (Fasnacht and Blough 2002, Miller and Olejnik 2001). Indirect photolysis of PAHs involves the excitation of photosensitizers, e.g. colored DOM or nitrate, resulting in production of reactive species, e.g. free radicals and triplet excited DOM ( $^3\text{DOM}\bullet$ ) (Lam et al. 2003). To investigate the underlying photodegradation mechanisms in the presence of Corexit EC9500A, a series of tests were carried out to examine the roles of various radicals in the photolysis of the PAHs.

DO plays an important part in photodegradation of PAHs as DO can react with excited PAHs or produce reactive oxygen species (ROS), leading to indirect photolysis of PAHs (Miller and Olejnik 2001); on the other hand, molecular oxygen can also act as a quencher for the singlet and triplet states, leading to inhibited photolysis (Lehto et al. 2000).

**Figure 4-11** profiles the effects of DO on the photodegradation of anthracene and 9,10-DMA under solar light, and **Table 4-4** presents the photodegradation rate constants. For anthracene, the depletion of DO (<0.1 mg/L) remarkably increased the photodegradation rate regardless of the dispersant. For instance, it increased the  $k$  value from 0.013 to 0.034  $\text{min}^{-1}$  in the absence of Corexit

EC9500A, and from  $0.050$  to  $0.070 \text{ min}^{-1}$  in the presence of Corexit EC9500A, indicating that the inhibitive effect of DO is much mitigated in the presence of the dispersant. In contrast, DO showed the opposite effects on the photolysis of 9,10-DMA. In the absence of Corexit EC9500A, the removal of DO did not significantly alter the photolysis rate of 9,10-DMA; the removal of DO decreased the  $k$  value from  $0.511$  to  $0.144 \text{ min}^{-1}$  in the presence of Corexit EC9500A.

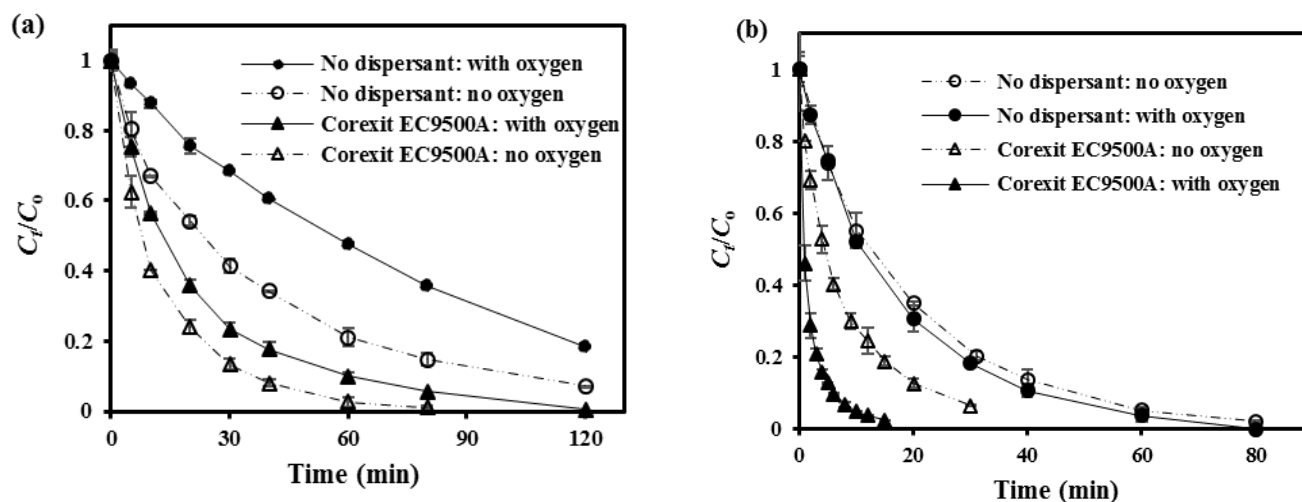


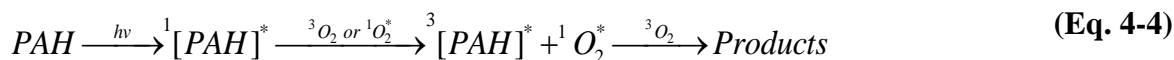
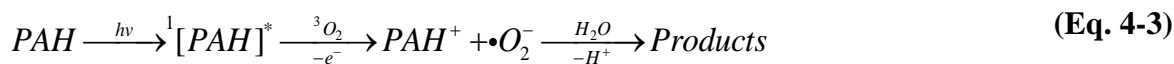
**Figure 4-11.** Effects of DO on photodegradation of anthracene (a) and 9,10-DMA (b) in the presence or absence of Corexit EC9500A. Experimental conditions: Corexit EC9500A = 18 mg/L, initial anthracene or 9,10-DMA =  $30 \mu\text{g/L}$ , pH =  $8.0 \pm 0.3$ , temperature =  $25 \pm 0.2 \text{ }^\circ\text{C}$ .

**Table 4-4.** First-order rate constants for the initial stage of anthracene and 9,10-DMA photodegradation with/without DO.

PAHs		With DO		Without DO	
		<i>k</i> (min <sup>-1</sup> )	<i>R</i> <sup>2</sup>	<i>k</i> (min <sup>-1</sup> )	<i>R</i> <sup>2</sup>
<b>Anthracene</b>	No dispersant	0.013	0.99	0.023	0.97
	With dispersant	0.050	0.99	0.070	0.97
<b>9,10-DMA</b>	No dispersant	0.056	1.00	0.049	1.00
	With dispersant	0.511	0.92	0.144	0.97

The opposite effects of DO on the photodegradation of the parent and alkylated PAHs indicate that different degradation mechanisms are operative and the dispersant plays different roles in the two reaction systems (Kahan and Donaldson 2007). Photolysis of PAHs in the aqueous phase can take place through: 1) direct photochemical ionization at the initial reaction step followed by oxidation of the formed PAH radical cations (**Eq. 4-2**) (Fasnacht and Blough 2003), 2) formation of PAH radical cations via electron transfer to oxygen due to quenching of excited singlet PAH (<sup>1</sup>[PAH]<sup>\*</sup>), followed by photooxidation of PAHs radical cations (**Eq. 4-3**) (Fasnacht and Blough 2003), and/or 3) formation of excited singlet and triplet PAH (<sup>3</sup>[PAH]<sup>\*</sup>), followed by the reaction of excited triplet state PAH with oxygen by transferring energy to molecular oxygen (**Eq. 4-4**) (Fasnacht and Blough 2003, Kahan and Donaldson 2007). In the absence of DO, the photolysis of anthracene and 9,10-DMA undergoes direct ionization.





In the presence of DO, the molecular oxygen quenches the singlet and triplet states, and thus contributes to the decay of any excited state that has a long lifetime (Lehto et al. 2000). The life time of triplet PAHs is exceedingly long (>100  $\mu$ s) (Dabestani and Ivanov 1999) and the quenching rate of triplet PAHs, e.g. phenanthrene, anthracene, chrysene, by oxygen is quite high ( $\geq 10^{10}$  M<sup>-1</sup>s<sup>-1</sup>) (Abdel-Shafi and Wilkinson 2000). For anthracene, deoxygenation greatly increased the photolysis rate (**Fig. 4-11a**), indicating that the excited triplet state anthracene during direct ionization was vulnerable to quenching by molecular oxygen. The presence of Corexit EC9500A mitigated the quenching effect, which may due to the consumption of DO by reacting with the dispersant components (Andrews et al. 2000).

The roles of various free radicals were further investigated by applying three selective radical scavengers, i.e. *tert*-butanol for quenching  $\bullet$ OH, azide for  ${}^1O_2$  and  $\bullet$ OH, and superoxide dismutase for  $\bullet O_2^-$ . **Figure 4-12** presents the photodegradation rates of anthracene and 9,10-DMA in the presence of each of the radical scavengers. Evidently, the quenching of  ${}^1O_2$ ,  $\bullet$ OH, and  $\bullet O_2^-$  radicals did not alter the photolysis rate of anthracene regardless of the dispersant, indicating that these radicals had negligible contribution to the photodegradation process. For 9,10-DMA, the presence of *tert*-butanol and superoxide dismutase did not significantly change the photolysis rate regardless of Corexit EC9500A; however, the presence of azide decreased the rate constant from 0.511 and

0.278 min<sup>-1</sup> in the presence of Corexit EC9500A, but had no effect in the absence of Corexit EC9500A. This observation indicated that the radicals •OH and •O<sub>2</sub><sup>-</sup> played negligible roles in the photodegradation of 9,10-DMA in all cases, but the <sup>1</sup>O<sub>2</sub> radical played an important role in the photolysis process in the presence of the dispersant. The results reveal that Corexit EC9500A boosted the formation of <sup>1</sup>O<sub>2</sub>, which enhanced photodegradation of 9,10-DMA.

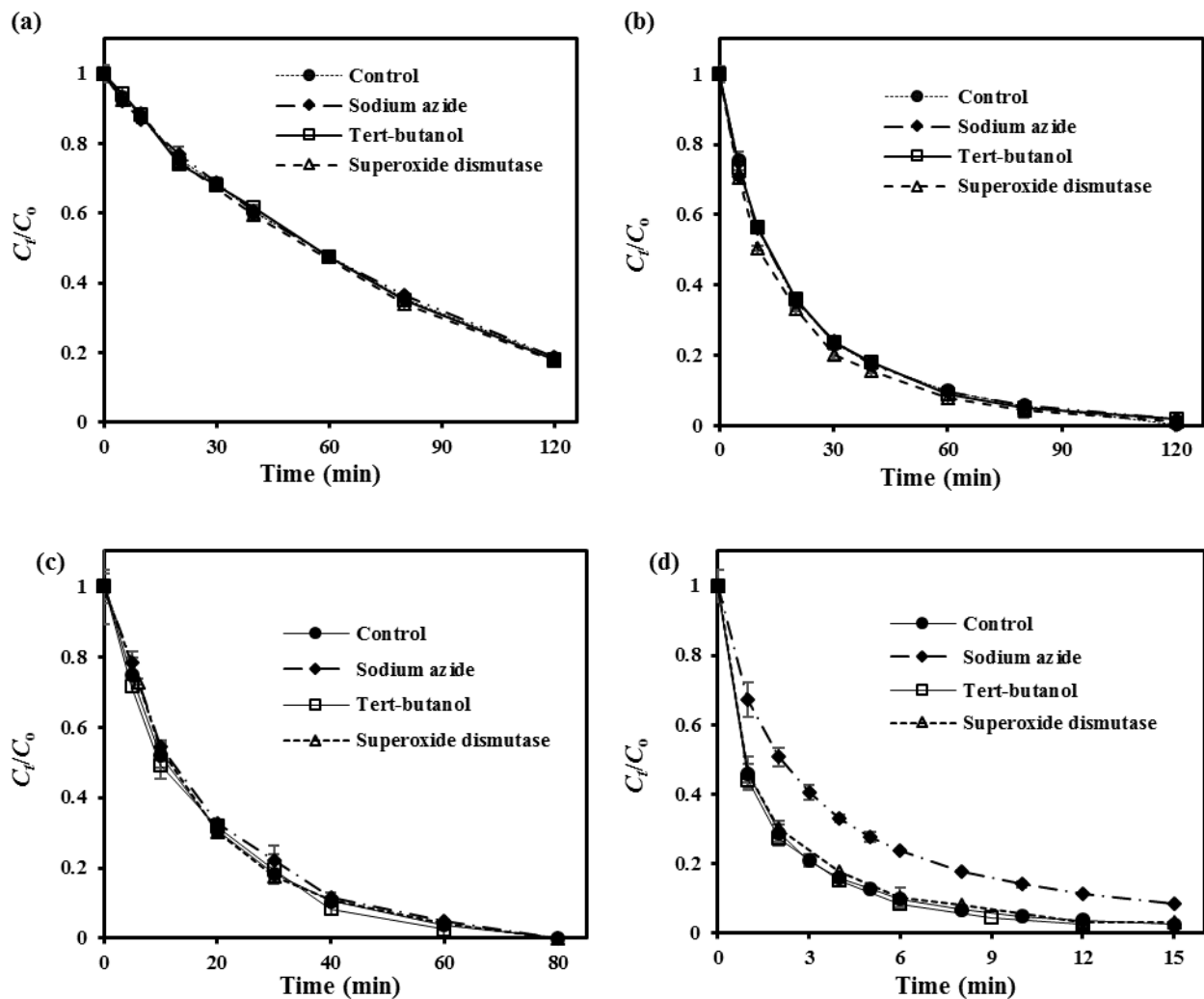


**Figure 4-12.** Effects of various radical scavengers on photolysis of anthracene in the absence (a) or presence (b) of Corexit EC9500A; and on photolysis of 9,10-DMA in the absence (c) or presence (d) of Corexit EC9500A. Experimental conditions: Corexit EC9500A = 18 mg/L, initial 9,10-DMA or anthracene = 30  $\mu\text{g/L}$ , pH =  $8.0 \pm 0.3$ , temperature =  $25 \pm 0.2$  °C.

In the aqueous phase, PAHs can perform as sensitizers for the formation of  $^1\text{O}_2$  (Braun et al. 1991). **Figure 4-12** shows that  $^1\text{O}_2$  did not significantly contribute to the PAH degradation in the

absence of the dispersant. Therefore, it is more likely that the dispersant components themselves act as the photosensitizers. Energy is transferred from the excited sensitizers to the ground state oxygen and raises its energy status, resulting in the production of  $^1\text{O}_2$  (Foote and Wexler 1964). The alkyl bond of 9,10-DMA can act as electron donating group, which made the 9,10-DMA be more prone to reaction with  $^1\text{O}_2$  than anthracene (Gandra et al. 2009, Radding et al. 1976), the elevated  $^1\text{O}_2$  concentration had a more profound effect on the photolysis of 9,10-DMA than anthracene.



Due to the relatively low radical production rate and the sinks of photochemically generated radicals, i.e.  $\bullet\text{OH}$ ,  $^1\text{O}_2$ , and  $\bullet\text{O}_2^-$ , in natural waters (Fasnacht and Blough, 2002), the contribution of indirect PAHs photolysis is lower than direct photolysis even in the presence of dispersant.

The fluorescence of PAHs can be quenched when PAHs are associated with DOM, and thus, measuring fluorescence spectra can distinguish the DOM-associated PAHs and freely dissolved PAHs (Gauthier et al. 1986, Raber et al. 1998). **Figure 4-13** profiles the fluorescence spectra of anthracene and 9,10-DMA in the absence or presence of Corexit EC9500A. Evidently, the dispersant dramatically quenched the fluorescence intensity of anthracene (peaked at the emission wavelength of 430 nm), but showed negligible effect on 9,10-DMA, indicating that more

anthracene is associated with the dispersant than 9,10-DMA. Therefore, the energy captured by the dispersant molecules may directly transfer to anthracene and accelerate its photolysis process, while for the case of 9,10-DMA, it is more likely transferred to oxygen to form  $^1\text{O}_2$ , which also explains the different roles of DO in the photodegradation of anthracene and 9,10-DMA.

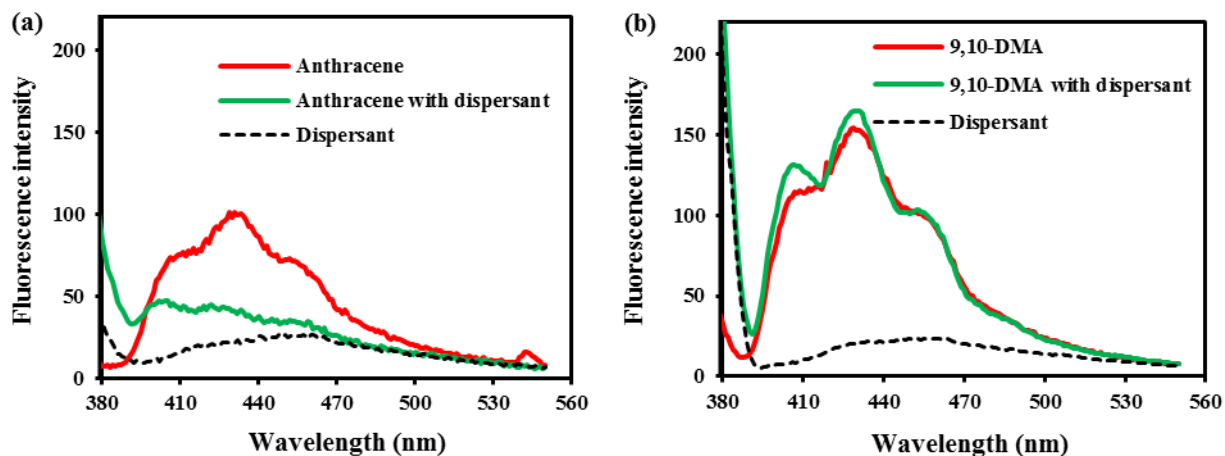


**Figure 4-13.** Fluorescence spectra of anthracene (a) and 9,10-DMA (b) in the absence/presence of Corexit EC9500A. Experimental conditions: Corexit EC9500A = 18 mg/L, initial anthracene or 9,10-DMA = 30  $\mu\text{g/L}$ , pH =  $8.0 \pm 0.3$ , temperature =  $25 \pm 0.2$   $^{\circ}\text{C}$ .

#### 4.3.4. Photodegradation pathway of anthracene and 9,10-DMA

9,10-anthraquinone, 1-hydroxy-9,10-anthraquinone, phthalic acid and trace amount of anthrone were detected by GC/MS during the photolysis of anthracene, but only an anthrone derivative was found during the photolysis of 9,10-DMA. Based on the mechanistic studies and intermediates identified by GC/MS, **Figure 4-14** depicts the proposed photolysis pathways of anthracene and 9,10-DMA. The photo-excited anthracene underwent the photolysis process to form 9,10-anthraquinone, which is a major intermediate and can act as photosensitizer to accelerate



the photolysis process. The 9,10-anthraquinone involved in further degradation to form 1-hydroxy-9,10-anthraquinone or anthrone. The formation of anthrone from 9,10-anthraquinone is a reversible reaction (Theurich et al. 1997); anthrone will finally be degraded via converting to 9,10-anthraquinone. The photooxidation of 1-hydroxy-9,10-anthraquinone resulted in the formation phthalic acid, and further produce the final products ( $H_2O$ ,  $CO_2$ ). For the photolysis of 9,10-DMA, the solar irradiation induced the excitation of 9,10-DMA, which resulted in the formation of  $^1O_2$  in the presence of dispersant (as found in this experiment). The  $^1O_2$  attacked 9,10-DMA to form the endoperoxides, which further converted to an anthrone derivative, then involved in further photodegradation/mineralization (Mill et al. 1981). Our study showed that the photolysis of anthracene and 9,10-DMA can undergo without DO (**Figure 4-11**), the oxygen in the observed intermediates may come from water, probably via a cation radical intermediate (**Eq. 4-2**) (Mill et al. 1981).

For the experiments conducted in the presence or absence of Corexit EC9500A, no new intermediates were detected by GC/MS. Therefore, the presence of dispersant only increased the photolysis rate but did not change the photodegradation pathway.

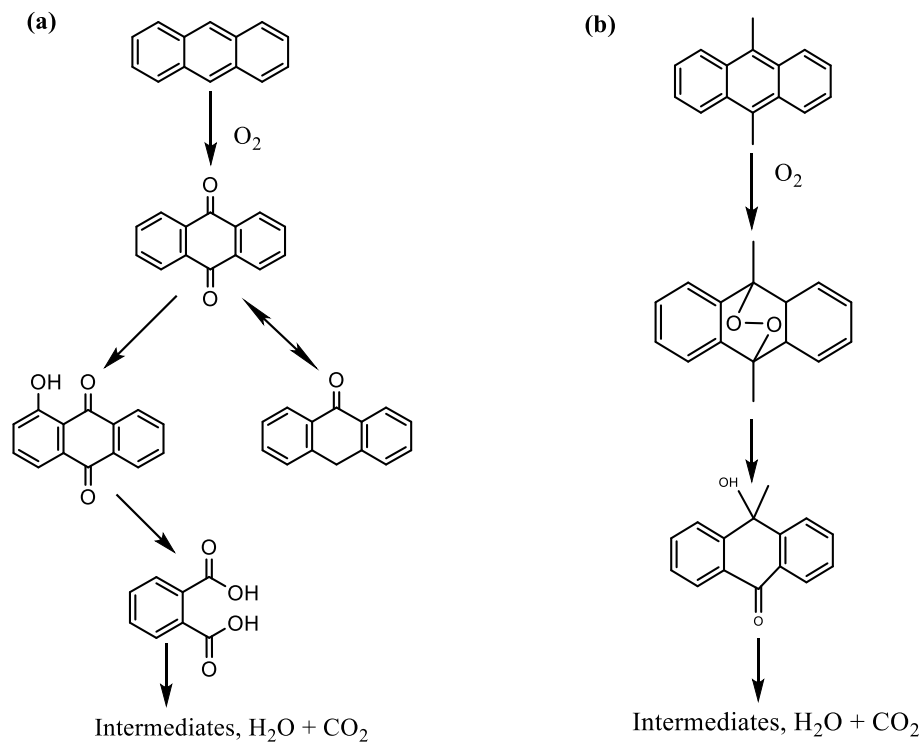


**Figure 4-14.** Proposed photodegradation pathway of anthracene (a) and 9,10-dimethylantracene (b) in seawater by simulated sunlight.

#### 4.3.5. Photochemical stability of dispersant under solar irradiation

Together with oil components, dispersants may undergo the photolysis process under solar irradiation. However, investigations only studied the photochemical stability of a few oil dispersant components in the marine environment (Batchu et al. 2014, Kover et al. 2014). In this study, the degradation of various dispersant components was monitored by GC/MS, and the depletion of detectable dispersant components was shown in **Figure 4-15**.

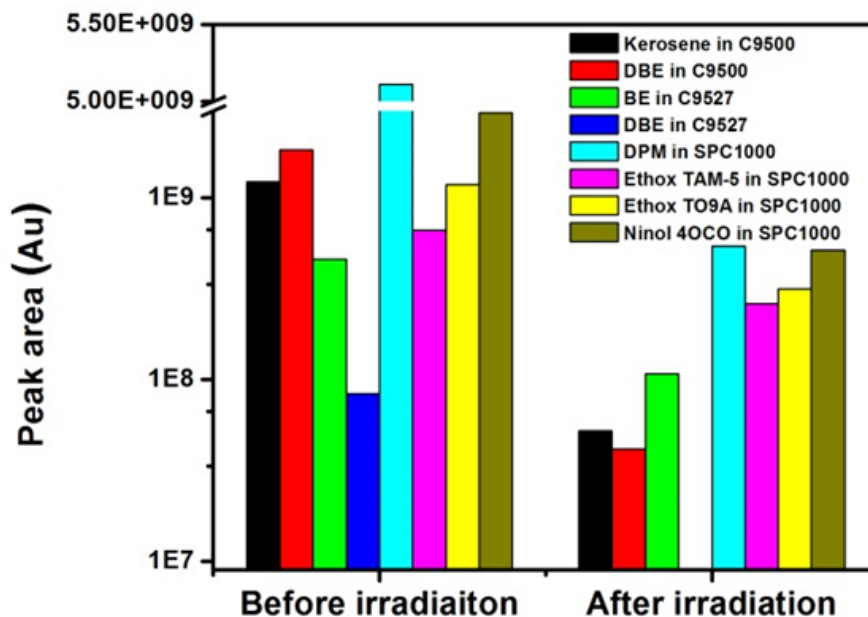


**Figure 4-15.** Peak area of detected dispersants compounds before and after solar irradiation. Experimental conditions: initial dispersant concentration = 18 mg/L, pH =  $7.8 \pm 0.2$ , temperature =  $25 \pm 0.2$  °C, reaction time = 6 h.

All the detected dispersant components underwent the photolysis under solar irradiation, including kerosene and DBE in Corexit EC9500A; 2-butoxyethanol (BE) and DBE in Corexit EC9527A; DPM, polyoxyethylene tallow amine (Ethox TAM-5), Ethox TO9A, and Ninol 4OCO in SPC 1000. Among them, the Corexit EC9500 showed lowest photochemical stability with an average degradation of 96.7%, while SPC1000 was relatively more stable with a degradation of 76.5% under solar irradiating for 6 h. The results indicated that the dispersants were diminished by the photolysis, together with the biodegradation (Zhuang et al. 2016) and dilution (Kujawinski

et al. 2011). Therefore, the photolysis promoting effects of dispersants on oil components are not long-lasting in marine environment.

#### 4.4. Conclusions

This work studied the effects of model oil dispersants on the photodegradation of two model PAHs (anthracene and 9,10-DMA) in seawater. The key findings are summarized as follows:

- (1) The tested dispersants, i.e. Corexit EC9500A, Corexit EC9527A and SPC 1000, markedly promoted the photolysis rate of the PAHs. The accelerating effects follow the order of: Corexit EC9500A > Corexit EC9527A > SPC 1000.
- (2) In the presence of dispersant, the photodegradation rate follows a two-stage, first-order kinetic law, with a faster initial photolysis rate; while in the absence of dispersant, the photolysis rate obeys the classic first-order rate law with one constant rate constant. Corexit EC9500A increased the photolysis rate ( $k$ ) of anthracene and 9,10-DMA by a factor of 3.8 and 9.1, respectively.
- (3) The dispersant components, i.e. Tween 85, Span 80 and kerosene, were found to be the critical dispersant components that promote the photolysis rate of the PAHs. Tween 85 enhanced the UV absorbance, while kerosene and span 80 enriched the surface PAH concentration, which are favorable for the photolysis of PAH.
- (4) Chemically, dissolved oxygen acts as a quencher for the excited states of the organics, thus hindering the photolysis of anthracene. Conversely, DO is involved in the formation ROS (e.g.  $^1\text{O}_2$ ) in the presence of oil dispersants, which is beneficial to the photolysis of 9,10-DMA.

More anthracene is found to be associated with dispersant than 9,10-DMA, which is favorable for directly transferring energy to anthracene; while in case of 9,10-DMA, the energy is more likely transferred to oxygen to form  $^1\text{O}_2$ .

(5) Oil dispersants accelerate the photolysis rates of anthracene and 9,10-DMA but do not change their degradation pathways.

(6) Oil dispersants are subject to photochemical weathering.

The results provide useful information for understanding the roles of oil dispersants on the environmental weathering of persistent oil components in the marine environment.

## **Chapter 5. Platinum-Deposited Anatase/Hexa-Titanate Nanotubes for Enhanced Photocatalytic Activity for Phenanthrene Degradation Under Solar Light**

This chapter describes the synthesis of a new class of Pt-deposited titanate nanotubes (TNTs) as photocatalysts. The mechanisms of enhanced photocatalytic reactivity of the new photocatalysts were studied by characterizing the materials, measuring the produced radicals and the extended visible irradiation utilization efficiency. Meanwhile, the settling performance and reusability of the materials were evaluated.

### **5.1. Introduction**

The oil industry produced a huge amount of wastewater (Ahmadun et al. 2009, Kujawski 2009); these PAHs contaminated water can be of acute toxicity and persistent, which makes the wastewater difficult to be treated by traditional biological methods (Stepnowski et al. 2002). Many other methods, e.g. chemical oxidation, electrochemical methods, activated carbon adsorption, and solvent extraction, have been applied to removal PAHs in water (Abdelwahab et al. 2009). However, these methods are always associated with limits such as low efficiency, high investment, high energy or materials consumption (Abdelwahab et al. 2009). Owing to the low cost and high efficiency, the photocatalytic degradation of PAHs under solar light is considered a promising route for the removal of PAHs from water (Hoffmann et al. 1995).

Many photocatalysts, e.g.  $\text{TiO}_2$ ,  $\text{ZnO}$ ,  $\text{BiVO}_4$ , have been investigated for photocatalytic degradation of PAHs in water (Kohtani et al. 2005, Vela et al. 2012). Ireland et al. (1995) applied  $\text{TiO}_2$  to photocatalytically degrade 16 PAHs in water by UV light, and found the degradation rates of PAHs were relatively low. Pal and Sharon (2000) supported the porous  $\text{TiO}_2$  particles on glass substrate to promote the photocatalytic activity, which showed elevated degradation efficiency for naphthalene and anthracene removal from water. Vela et al. (2012) compared the effectiveness of  $\text{ZnO}$  and  $\text{TiO}_2$  for photocatalytic degradation of a mixture of 5 PAHs in groundwater under natural sunlight and found that 7–15 min and 18–76 min are required for  $\text{ZnO}$  and  $\text{TiO}_2$  to remove 90% of the PAHs. Kohtani et al. (2005) compared the pure and Ag-loaded  $\text{BiVO}_4$  for the photocatalytic degradation of 9 PAHs under visible light irradiation. They found that both catalysts enhanced the photodegradation efficiency, and that loading of Ag accelerated the  $\bullet\text{OH}$  production.

$\text{TiO}_2$  has been most commonly employed for its cost effectiveness, non-toxicity, excellent activity and stability. Since Fujishima and Honda discovered the photocatalytic splitting of water on  $\text{TiO}_2$  in 1972 (Fujishima and Honda 1972), interest in the application of  $\text{TiO}_2$  as photocatalyst has significantly increased, and it has become the most widely used photocatalyst for environmental application nowadays (Sires and Brillas 2012, Theron et al. 2008). In recent years, titanate with layered or tubular structures has emerged as a modified version of  $\text{TiO}_2$  with promising photocatalytic activity for decomposition of various organic compounds (Rodriguez-Gonzalez et al. 2009).

To enhance the photocatalytic activity, a myriad of efforts have been devoted to developing nanoscale or nano-structured materials. When the size of a catalyst is comparable to the de-Broglie

wavelength of the charge carriers, e.g. 5–25 nm for TiO<sub>2</sub>, the diffusion process is negligible for the wave function of the charge carriers to spread over the entire particles and to react with the surface species, thereby increasing the quantum yield (Antony et al. 2012). In addition to the nano-effects, the much higher specific surface area (up to 300 m<sup>2</sup>/g) for these nano-materials provides more reactive sites (Zhang et al. 2000). More recently, titanate nanotubes (TNTs), a one-dimensional (1-D) nano-composite material, have been synthesized through various approaches, such as hydrothermal treatment of TiO<sub>2</sub>, template assisted chemical deposition, and anodic oxidation (Antony et al. 2012, Bavykin et al. 2006, Huang and Chien 2013, Ou and Lo 2007a). Owing to the strong mechanical strength, high specific surface area, large cation adsorption capacity, and high photocatalytic activity, TNTs attracted increasing attention as promising photocatalysts (Bavykin et al. 2006, Ou and Lo 2007a, Zhuang et al. 2007).

Generally, the photocatalytic efficiency of TiO<sub>2</sub> or titanate is constrained by two inherent processes: 1) recombination of photo-generated holes and electrons within the catalysts (Malato et al. 2009), and 2) poor photosensitivity under visible/solar irradiation (Liu et al. 2015a, Veldurthi et al. 2015). Moreover, due to the rather broad intrinsic band gaps of TiO<sub>2</sub> (3.2 eV for anatase and 3.0 eV for rutile), the catalysts only absorb UV radiation (wavelength <400 nm), which accounts for only ~5% of the sunlight (Afzal et al. 2013, Shankar et al. 2015, Shannon et al. 2008). Therefore, researchers have been consistently attempting to modify Ti-based photocatalysts through retarding the recombination of electron-hole pairs and narrowing down the band gaps (Doong et al. 2013, Liu et al. 2015a, Sung-Suh et al. 2004, Veldurthi et al. 2015, Zhao et al. 2016). To this end, various noble metal, e.g. Pt, Au and Ag, had been used as dopants, facilitating



production of reactive oxygen species (ROS) and absorption of visible light (Malato et al. 2009, Pan et al. 2016, Burgeth and Kisch 2002). Pt is one of the most used dopants for modifying TiO<sub>2</sub> and titanate (Liu et al. 2011). Pt can provide the highest Schottky Barrier among the metal species facilitating the electron capture, and produce longer electron-hole pair separation life time (Li and Li 2002). Meanwhile, the incorporation of Pt<sup>3+</sup> into TiO<sub>2</sub> can create a defect energy level, which extends visible light absorption (Li and Li 2002). Previous studies revealed that Pt(0)-doped TiO<sub>2</sub> displayed faster photocatalytic oxidation rate of o-cresol than TiO<sub>2</sub> (P25) under UV irradiation (Chen et al. 2007), and Pt(IV)-modified TiO<sub>2</sub> was more active than TiO<sub>2</sub> (P25) for photodegradation of 4-chlorophenol (Burgeth and Kisch 2002). However, the effects of Pt(0) or Pt(VI) on titanate nanotubes have not been reported.

The overall goal of this research was to develop and evaluate a new type of platinum-deposited TNTs (Pt-TNTs) for photocatalytic degradation of PAHs under solar irradiation. The specific objectives were to: 1) synthesize the desired Pt-TNTs nanomaterial and optimize the preparation conditions, 2) characterize the new composite material, 3) evaluate the effectiveness of the photocatalysts by testing the photodegradation of phenanthrene (as a model PAH), and 4) elucidate the underlying mechanisms and roles of Pt based on the material characterization, contribution of visible irradiation to the reactivity, and production of ROS.

## **5.2. Materials and methods**

### **5.2.1. Chemicals**

All chemicals are of analytical grade or higher, and were used as received. TiO<sub>2</sub> (P25) was purchased from Degussa Corporation (Dusseldorf, Germany), H<sub>2</sub>PtCl<sub>6</sub>·xH<sub>2</sub>O (40% Pt), NaOH, and methanol were acquired from Acros Organics (Fair Lawn, NJ, USA). H<sub>2</sub>O<sub>2</sub> was from BDH (West Chester, PA, USA); phenanthrene, terephthalic acid, and KI from Alfa Aesar (Ward Hill, MA, USA). A stock solution (2 g/L) of phenanthrene was first prepared by dissolving phenanthrene in methanol. Deionized (DI) water (18.2 MΩ·cm) was used in preparing all aqueous solutions.

### 5.2.2. Synthesis of Pt-doped TNTs

Pt-deposited TNTs were synthesized through a two-step method, i.e., hydrothermal conversion of TiO<sub>2</sub> to TNTs and subsequent Pt deposition. Briefly, 1.2 g TiO<sub>2</sub> powder was dispersed in 20 mL DI water, magnetically stirred for 20 min, and then sonicated for another 20 min (solution A). Meanwhile, a 15 M NaOH solution was prepared by dissolving 29 g NaOH in 47 mL DI water (solution B). Then, solutions A and B were mixed and sonicated for 60 min, and the mixture was then transferred into a Teflon reactor with stainless steel coating and heated at 130 °C for 72 h. The resulting white precipitates (TNTs) were washed with DI water until pH ≈ 10, then dispersed in 10 mL ethanol and oven-dried at 80 °C for 4 h. Pt was then deposited on TNTs by mixing 1 g of TNTs with 40 mL of a H<sub>2</sub>PtCl<sub>6</sub> solution at various Pt concentrations (12.5, 25, 125 and 250 mg/L as Pt). The mixture was shaken at pH 3 for 4 h, when Pt(IV) was completely adsorbed on TNTs, the mixture was then purged with N<sub>2</sub> for 20 min to remove dissolved oxygen, and subsequently, 10 mL of a fresh NaBH<sub>4</sub> solution (0.8 g/L) was added into the flask dropwise under vacuum and shaking (200 rpm) on a flat-top shaker. The resulting materials (gray to black depending on Pt dosage) were then washed with DI water and methanol consecutively (3 times

each), and oven-dried at 80 °C for 4 h. The catalyst is denoted by Pt(0)-TNTs for typographical convenience. For comparison, Pt(IV) loaded TNTs, i.e., Pt(IV)-TNTs, were prepared following the same procedure except for the NaBH<sub>4</sub> reduction step. The materials were then calcined at 400, 600 or 800 °C, respectively, for 2 h in a muffle furnace, and the resulting materials were referred to as Pt(0)-TNTs-xxx or Pt(IV)-TNTs-xxx (where xxx indicates the calcination temperature). For comparison, neat TNTs (without Pt) were prepared under the same conditions and calcined at 600 °C.

### 5.2.3. Photocatalytic degradation

The photocatalytic activity of the new catalysts was tested for the photodegradation of phenanthrene under simulated solar light. **Figure 4-1** shows the experimental setup, which includes a sealed glass photo-reactor (250 mL) with a quartz cover and a water circulating system, and a Newport 84041A solar simulator (Newport Corp., Irvine, CA USA) equipped with a 450 W xenon-ozone free short arc lamp and an air mass 1.5 global filter. The solar intensity in the reactor was determined to be  $85 \pm 0.5$  mW/cm<sup>2</sup>.

Photocatalytic kinetic tests were conducted under the following conditions: solution volume = 200 mL, initial phenanthrene = 200 µg/L, catalyst dosage = 0.04 g. The solution pH was adjusted to ~7.0 using dilute HCl or NaOH solutions. The mixture was first stirred in dark for 2 h to allow for phenanthrene adsorption equilibrium. Subsequently, photodegradation was initiated by exposing the reactor to the simulated solar light. At predetermined time intervals, a 1 mL sample was taken, and then centrifuged at 6000 rpm (5434 ×g force) for 3 min to remove the solids, and

the supernatant was then mixed with methanol (1:1 v/v) and filtered through a 0.22  $\mu\text{m}$  PTFE syringe filter (Millipore, Bedford, MA, USA) (addition of methanol minimizes retention of phenanthrene by the filter). The filtrate was then analyzed for phenanthrene by an Agilent 1260 series high-performance liquid chromatography (HPLC, Santa Clara, CA, USA) equipped with a Poroshell 120 EC-C18 column ( $50 \times 4.6$  mm) and a UV detector using an injection volume of 80  $\mu\text{L}$ . The mobile phase consisted of 70% acetonitrile, 30% water, and 0.1% phosphoric acid (by volume), flow rate was set at 1 mL/min, the column temperature was 30  $^{\circ}\text{C}$ , and the detection wavelength was 250 nm, which afforded a detection limit of 1.0  $\mu\text{g/L}$  for phenanthrene. Control tests were carried out without catalyst but under otherwise identical conditions.

To evaluate the photocatalytic activity of Pt(0)-TNTs-600 and Pt(IV)-TNTs-600 under only visible light, a UV cut-off filter (Institute of Electric Light Source, Beijing, China) was applied on top of the photo-reactor to remove irradiation with wavelength  $<420$  nm. **Figure 4-2** shows the UV-vis absorption spectra of the UV cut-off filter.

The procedures for testing reusability were identical to the described photocatalytic kinetic tests for the first cycle. After the phenanthrene was completely degraded, the catalyst in suspension was recovered by filtering through a 0.22  $\mu\text{m}$  PTFE membrane and naturally air-dried, and then reused by repeating the procedure for phenanthrene photodegradation. Separate tests showed that the air-drying of catalysts did not alter its photocatalytic activity.

#### 5.2.4. Measuring Hydroxyl Radicals and H<sub>2</sub>O<sub>2</sub> Production

The formation of hydroxyl radicals ( $\bullet\text{OH}$ ) with various Ti-based materials was measured by the photoluminescence (PL) method using terephthalic acid as a probe molecule, which reacts with  $\bullet\text{OH}$  to form a highly fluorescent product, 2-hydroxyterephthalic acid. The fluorescence intensity is proportional to the  $\bullet\text{OH}$  concentration (Yu et al. 2009). To this end, 0.2 g/L of a catalyst was dispersed in 200 mL of a solution containing 0.5 mM terephthalic acid and 2 mM NaOH. After 1 h irradiation under simulated solar light, the samples were filtered using a 0.22  $\mu\text{m}$  PTFE syringe filter, and the PL spectra were obtained using a SpectraMax M2 plate reader (Molecular Devices, Sunnyvale, CA, USA) with a 1-cm path quartz cell at an excitation wavelength of 425 nm (Yu et al. 2009, Zhao et al. 2016).

The production of H<sub>2</sub>O<sub>2</sub> was determined by the Ghormley triiodide (I<sub>3</sub><sup>-</sup>) method, which is based on measuring I<sub>3</sub><sup>-</sup> formed by reaction of I<sup>-</sup> with photo-catalytically produced H<sub>2</sub>O<sub>2</sub> (Klassen et al. 1994). Briefly, a solution was prepared by diluting 6.6 g KI, 0.2 g NaOH, and 0.02 ammonium molybdate tetrahydrate in 100 mL DI water; and buffer solution was prepared by dissolving 2 g KHP in 100 mL DI water. For measuring H<sub>2</sub>O<sub>2</sub>, each 1 mL of the solutions were premixed, and then 1 mL sample was added and mixed for 5 min. UV absorbance was then measured at 351 nm by the SpectraMax M2 plate reader. The detection limit for H<sub>2</sub>O<sub>2</sub> was 1  $\mu\text{M}$ .

#### 5.2.5. Material characterizations

The morphology of the new materials was analyzed using Tecnai30 FEG transmission electron microscopy (TEM, FEI, Eindhoven, Netherlands) operated at 300 kV, and energy-dispersive X-

ray spectroscopy (EDS) of the samples were obtained at the same time. The crystalline structure of nanomaterials was determined by a Dmax/2400 XRD (Rigaku, Japan) using Cu  $K\alpha$  radiation ( $\lambda = 1.5418 \text{ \AA}$ ) at a scanning speed ( $2\theta$ ) of  $4^\circ/\text{min}$ . The elemental compositions and oxidation states were determined by an AXIS-Ultra X-ray photoelectron spectroscopy (XPS, Kratos, Manchester, UK). The spectra were excited by Al  $K\alpha$  as the X-ray source run at 15 kV and 15 mA. The standard C1s peak (Binding energy,  $E_b = 284.80 \text{ eV}$ ) was used to eliminate static charge effects. The diffuse reflectance UV/Vis absorption spectra (UV-DRS) of the nanomaterials were recorded at 298K using a UV-2400 spectrophotometer (Shimadzu, Japan). BaSO<sub>4</sub> powder was used as the reference material at all energies (100% reflectance), and the reflectance measurements were converted to absorption spectra. Fourier transform infrared (FTIR) spectroscopy analysis was carried out on a Tensor 27 FT-IR spectrometer (Bruker, Germany).

The SpectraMax M2 plate reader with a 1-cm path quartz cell was used to quantify the gravitational sedimentation rate of the particles in aqueous suspensions (Zhao et al. 2016). Briefly, 0.02 g of a material was first dispersed in 100 mL of DI water and mixed on a shaker at 30 rpm for 24 h, and then the UV absorbance of the suspension was measured as a function of time (Liu et al. 2013b).

### 5.3. Results and discussion

#### 5.3.1. Photocatalytic activity of Pt-TNTs prepared under various conditions

The photocatalytic activity of Pt(0)-TNTs prepared with different Pt loadings (0.05–1.0 wt.%, with a fixed calcination temperature of 600 °C) and calcination temperatures (400, 600 and 800 °C, with a fixed Pt loading of 0.1 wt.%) were evaluated in terms of the phenanthrene degradation under simulated solar light. The first-order kinetic model was used to interpret the phenanthrene degradation kinetic data:

$$\ln(C_0 / C_t) = k_1 t \quad (\text{Eq. 5-1})$$

where  $C_0$  and  $C_t$  are the phenanthrene concentration ( $\mu\text{g/L}$ ) at time zero and  $t$  (h), and  $k_1$  is the first-order rate constants ( $\text{h}^{-1}$ ), respectively.

**Figure 5-1** shows the photodegradation kinetic, and **Table 5-1** lists the best-fitted parameters according to the first-order kinetic models. The first-order model was able to well interpret the kinetic data ( $R^2 > 0.98$ ). Increasing the Pt dosage from 0.05 to 0.1 wt.% increased the apparent rate constant ( $k_1$ ) from 0.10 to 0.12  $\text{h}^{-1}$  (**Figure 5-1, Table 5-1**). However, further increasing Pt dosage to 0.5 and 1.0 wt.% decreased the  $k_1$  to 0.10 and 0.08  $\text{h}^{-1}$ . Consequently, the optimum Pt loading was set at 0.1 wt.%. Generally, Pt at lower dosages acts as an electron trap to inhibit the recombination of photo-induced electron-hole pairs; however, too much Pt on the TNTs may act as a recombination center for electron-hole pairs or block the active sites (Ou and Lo 2007b).

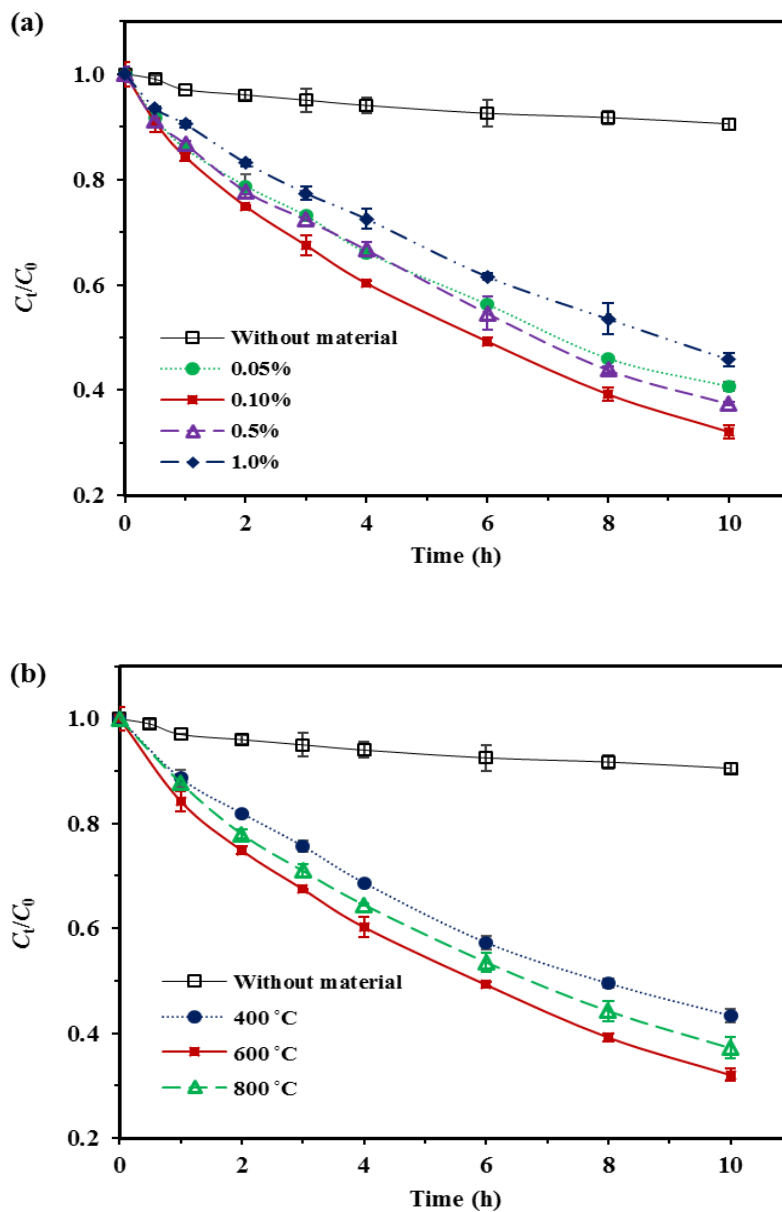


**Figure 5-1.** Photocatalytic degradation of phenanthrene by various Pt(0)-TNTs synthesized at different Pt loadings (a) and calcination temperatures (b). Experimental conditions: phenanthrene = 200  $\mu\text{g/L}$ , material dosage = 0.2 g/L, pH =  $7.0 \pm 0.2$ , temperature =  $25 \pm 0.2$  °C.



**Table 5-1.** Best-fitted first-order kinetic model parameters for photocatalytic degradation of phenanthrene by Pt(0)-deposited TNTs synthesized under various conditions.

Parameters	Deposited Pt (wt.%)				Calcination temperature (°C)		
	0.05	0.10	0.50	1.0	400	600	800
$k_1$ (h <sup>-1</sup> )	0.10	0.12	0.10	0.08	0.09	0.12	0.10
$R^2$	0.98	0.99	0.99	0.10	0.99	0.99	0.99

**Figure 5-1b** shows that increasing the calcination temperature from 400 to 600 °C increased the  $k_1$  value from 0.09 to 0.12 h<sup>-1</sup>; however, further increasing the calcination temperature to 800 °C lowered the rate constant to 0.10 h<sup>-1</sup>. Calcination temperature can affect the morphology and structure of TNTs (Lee et al. 2007a). There are two types of dehydration: 1) dehydration of intralayered –OH groups, which occurs at lower calcination temperature and has little effect on the nanotube length; and 2) dehydration of interlayered –OH groups, which occurs at higher temperature and will induce the change of the crystalline form and damage of the tubular structure (Lee et al. 2007b). Increasing the calcination temperature leads to stronger crystallization of anatase, which exhibits much higher photocatalytic activity than non-calcined TNTs (Lee et al. 2007b, Yu et al. 2006b). However, too high of a temperature (>700 °C) decreases the specific surface area of TNTs and convert anatase into rutile, which is a less efficient photocatalyst than anatase (Lee et al. 2007b, Yu et al. 2006b). Consequently, the optimum calcination temperature was set at 600 °C, which is consistent with the finding by Lee et al. (2007b). Based on the observations, Pt(0)-TNTs-600 prepared with a Pt dosage of 0.1 wt.% and calcination temperature of 600 °C was further characterized and tested.

### 5.3.2. Morphology, crystal phases and compositions of Pt-TNTs

**Figure 5-2** presents TEM images Pt(0)-TNTs-600 and the precursor materials. TiO<sub>2</sub> (P25) was observed as agglomerated particles with a mean size of 20–50 nm (**Figure 5-2a**), and TNTs obtained from the hydrothermal treatment compose of multilayered (4–5 layers) nanotubes with an inner diameter of ~4.5 nm and outer diameter of ~9 nm (Xiong et al. 2010). The interlayer distance of pristine TNTs ~0.75 nm, which is assigned to the crystal plane of tri-titanate (020) (**Figure 5-2b**) (Chen et al. 2002). Upon calcination at 600 °C, the tubular structure was partially broken into shorter nanotubes as well as nanoparticles/nanorods (**Figure 5-2c**), with a slightly reduced interlayer distance of ~0.7 nm, which is assigned to crystal plane (020) of hexa-titanate (confirmed later by XRD) (Liu et al. 2015b, Yang et al. 2011). However, the facets of titanate (020) reveals that part of the TNTs survived in the calcination process (Zhao et al. 2016). The formation of nanoparticles/nanorods with a crystal distance of 0.35 nm attributed to the facets of anatase (101) suggests that TNTs also partially converted to TiO<sub>2</sub> (anatase) (**Figure 5-2c**) (Cai et al. 2015). **Figure 5-2c** reveals some dark dots with a diameter of ~2 nm on Pt(0)-TNTs-600, which are ascribed to Pt(0) based on the EDS scan for the materials in the red box (**Figure 5-2d**). Moreover, the EDS spectra also reveal that the main elements of Pt(0)-TNTs-600 are Na, O, Ti and Pt, which indicate the Pt is successfully deposited on TNT, which was further confirmed by XRD and XPS analyses.

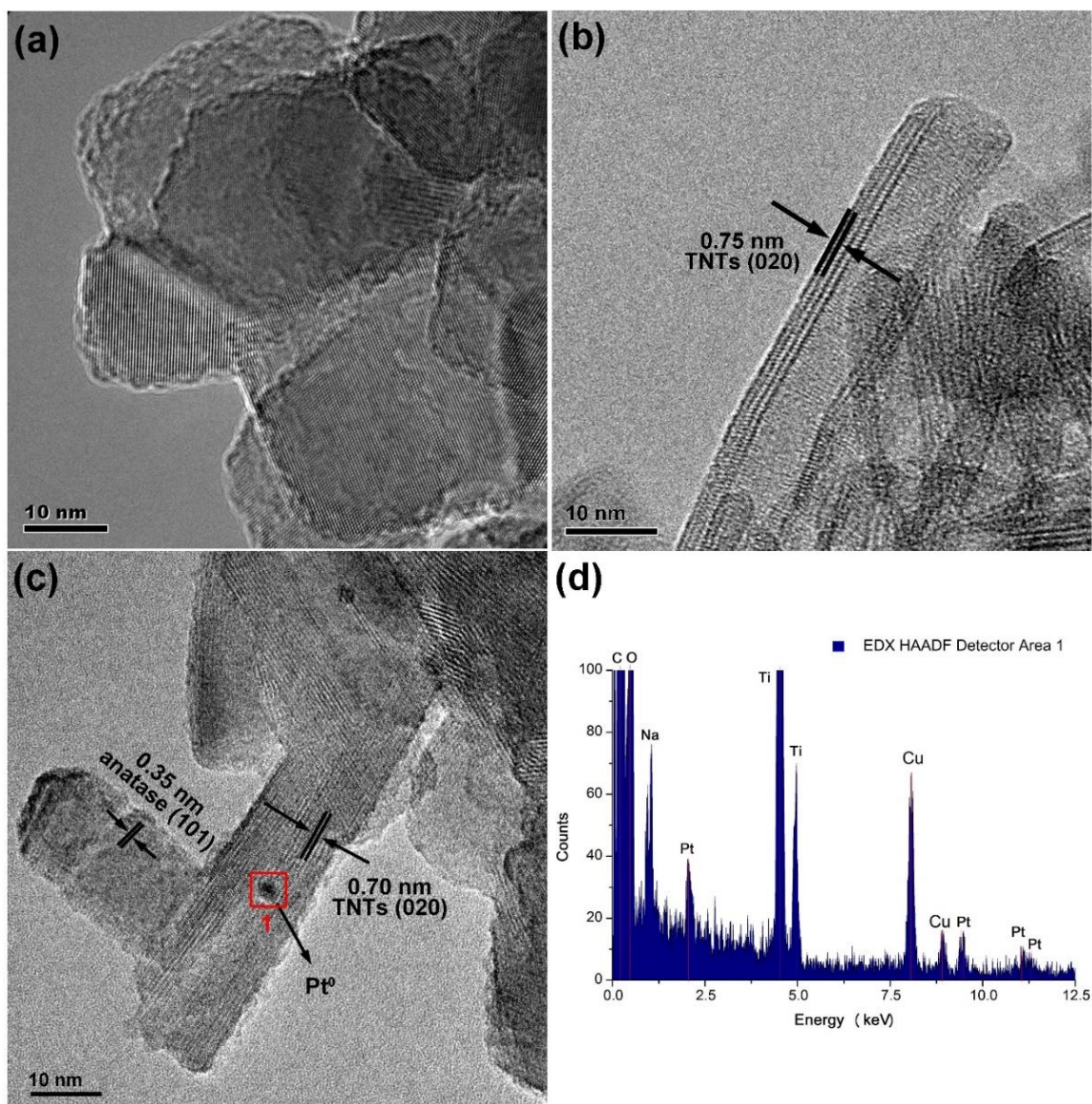


**Figure 5-2.** TEM images of TiO<sub>2</sub> (P25) (a), TNTs (b), Pt(0)-TNTs-600 (c), and EDS spectra (d) of Pt(0)-TNTs-600.

**Figure 5-3** presents XRD patterns for various Ti-based nanomaterials. The hydrothermal treatment completely converted TiO<sub>2</sub> (P25, a mixture of anatase and rutile) into titanate (TNTs), which is evidenced by the diffraction peaks at ca. 10°, 24°, 28°, 48° and 62° (Liu et al. 2013c, Sun

and Li 2003). Moreover, the obtained titanate is a sodium tri-titanate composed of the edge-sharing triple  $[\text{TiO}_6]$  octahedrons with  $\text{H}^+/\text{Na}^+$  located in the interlayers, and the chemical formula  $\text{Na}_x\text{H}_{2-x}\text{Ti}_3\text{O}_7$  ( $x$  depends on the sodium content) (Liu et al. 2013a, Liu et al. 2013c, Xiong et al. 2011, Zhao et al. 2016). The peak at  $10^\circ$  represents the interlayer distance of TNTs (0.75 nm as shown in **Figure 5-2b**) (Liu et al. 2013c, Sun and Li 2003). Evidently, both Pt(0)-TNTs-600 and Pt(IV)-TNTs-600 show good crystallinity but different crystalline phases than neat TNTs. While both materials showed a sodium hexa-titanate ( $\text{Na}_2\text{Ti}_6\text{O}_{13}$ ) crystalline phase, only Pt(0)-TNTs-600 displayed the anatase crystal structure. The hexa-titanate is represented by the enclosing tunnel structures formed by corner- and edge- shared  $[\text{TiO}_6]$  octahedra, while the tri-titanate ( $\text{Na}_2\text{Ti}_3\text{O}_7$ ) is formed with the zigzag ribbon structures consisting of edge-shared  $[\text{TiO}_6]$  octahedral (Inoue et al. 1991). During calcination of TNTs, tri-titanate with high sodium content tend to be converted to hexa-titanate, while decreasing the sodium content favors conversion to anatase (Lee et al. 2007b). During the synthesis of Pt(0)-TNTs-600, the washing step after the reduction of Pt(IV) to Pt(0) removed part of the  $\text{Na}^+$  that sorbed on TNTs (9.6 wt.% for Pt(0)-TNTs-600 and 13.1 wt.% for Pt(IV)-TNTs-600 measured by XPS shown in **Table 5-2**). The lower sodium content of Pt(0)-TNTs-600 resulted in formation of anatase, while the high sodium content in Pt(IV)-TNTs-600 just led to the conversion of tri-titanate to hexa-titanate. In addition, the Pt(111) peak, which belongs to Pt(0), was observed for Pt(0)-TNTs-600, although very weak due to the low Pt loading (0.1 wt.%). The interlayer peaks ( $2\theta \approx 10^\circ$ ) of tri-titanate (020) were greatly diminished for both Pt(0)-TNTs-600 and Pt(IV)-TNTs-600, indicating calcination greatly altered the interlayers of TNTs.

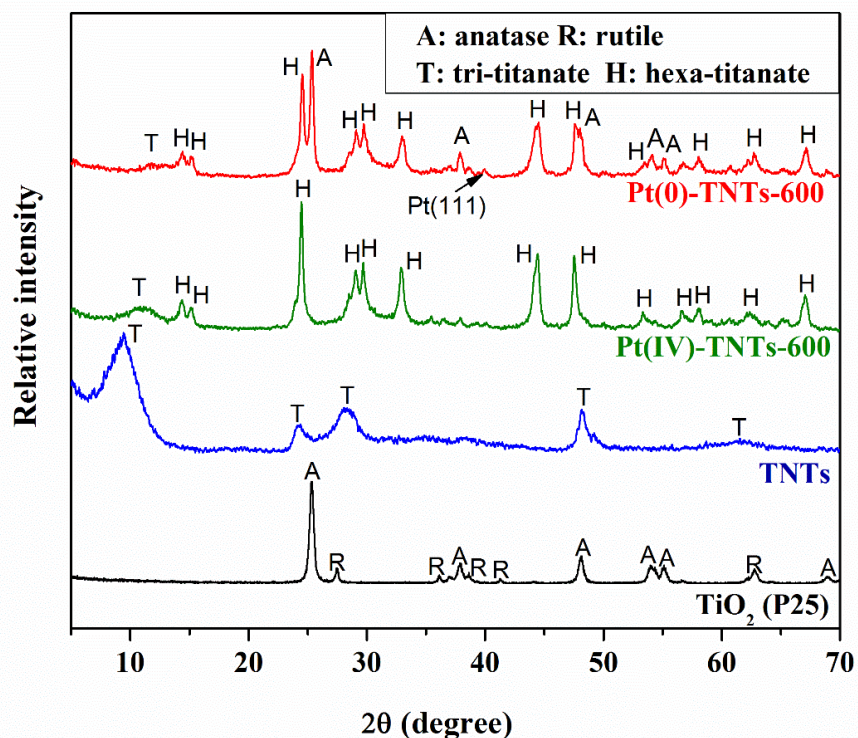


**Figure 5-3.** XRD patterns of various Ti-based materials. (TNTs: titanate nanotubes synthesized via hydrothermally treatment of  $\text{TiO}_2$ ; Pt(IV)-TNTs-600: Pt(IV)-deposited TNTs calcined at 600 °C; Pt(0)-TNTs-600: Pt(0) -deposited TNTs calcined at 600 °C).

**Figure 5-4** displays the FTIR spectra of four Ti-based nanomaterials. The observed absorption bands of  $\text{TiO}_2$  at 652, 1634, and 3406  $\text{cm}^{-1}$  are assigned to Ti–O, H–O–H (bound water molecule), and O–H bonding vibrations (Park and Kang 2005). For TNTs, the bands at 474 and 904  $\text{cm}^{-1}$  are attributed to the  $[\text{TiO}_6]$  octahedron and four-coordinate Ti–O stretching vibrations of titanate (Liu et al. 2013a, Liu et al. 2013c, Xiong et al. 2011). The FTIR spectra of Pt(0)-TNTs-600 and Pt(IV)-TNTs-600 are similar to that of TNTs but the Ti–O band is shifted from 904 to 897  $\text{cm}^{-1}$  for Pt(0)-



TNTs-600, due to interaction of Pt with Ti–O band and formation of Ti–O–Pt (Zhao et al. 2016). Moreover, the calcination shifted the  $[\text{TiO}_6]$  octahedron band from 474 to 545  $\text{cm}^{-1}$  for both materials, which is attributed to the conversion of tri-titanate to anatase or hexa-titanate (Zhao et al. 2016).

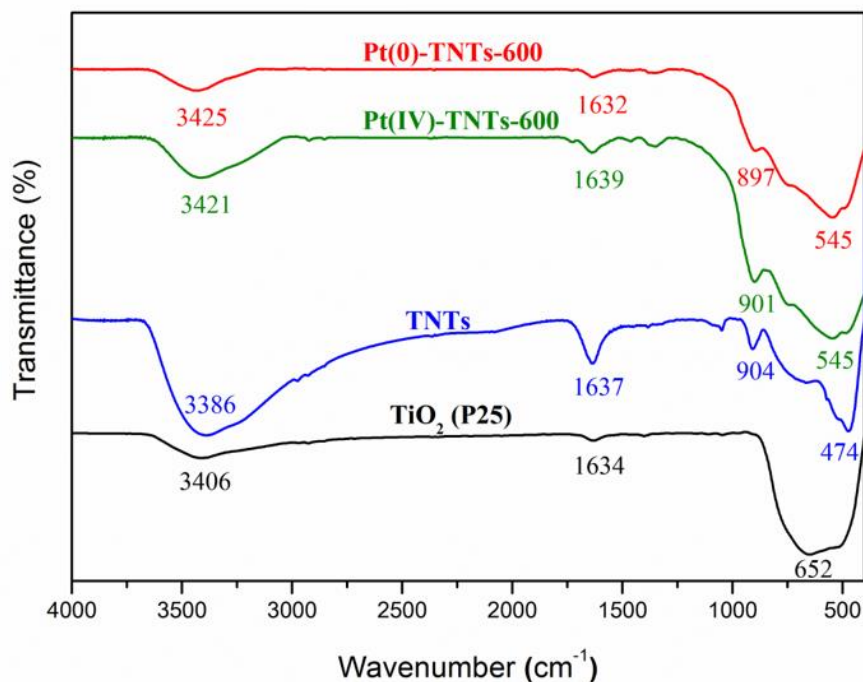


**Figure 5-4.** FTIR spectra of various Ti-based materials.

XPS survey spectra (**Figure 5-5a**) indicate that the main elements for the both Pt-TNTs are Na, Ti, O, Pt and Cl (**Table 5-2**). The calculated surface Pt loading based on the XPS results is 0.11 wt.% for Pt(0)-TNTs-600 and 0.14 wt.% for Pt(IV)-TNTs-600, which is consistent with the designed Pt content (0.1 wt.%). In the high resolution spectra for Pt(0)-TNTs-600 (**Figure 5-5b**), the peaks at 70.6 (Pt  $4f_{7/2}$ ) and 74.1 eV (Pt  $4f_{5/2}$ ) are assigned to Pt(0) (Kuribayashi and Kitamura 2001, Wang et al. 2005). For Pt(IV)-TNTs-600, two new peaks at 71.7 and 75.4 eV, which are

attributed to Pt(II) from PtO, were observed in addition to the Pt(0) peaks (Kuribayashi and Kitamura 2001, Wang et al. 2005); yet, no peaks for Pt(IV) were observed (Jin et al. 2003), indicating that Pt(IV) was converted to Pt(II) and Pt(0) during the calcination process (Ghita et al. 2012, Jin et al. 2003). The following reactions may describe the thermal decomposition of Pt(IV)-TNTs at 600 °C:



where “Ti≡” represents the TNTs which support the deposited Pt.

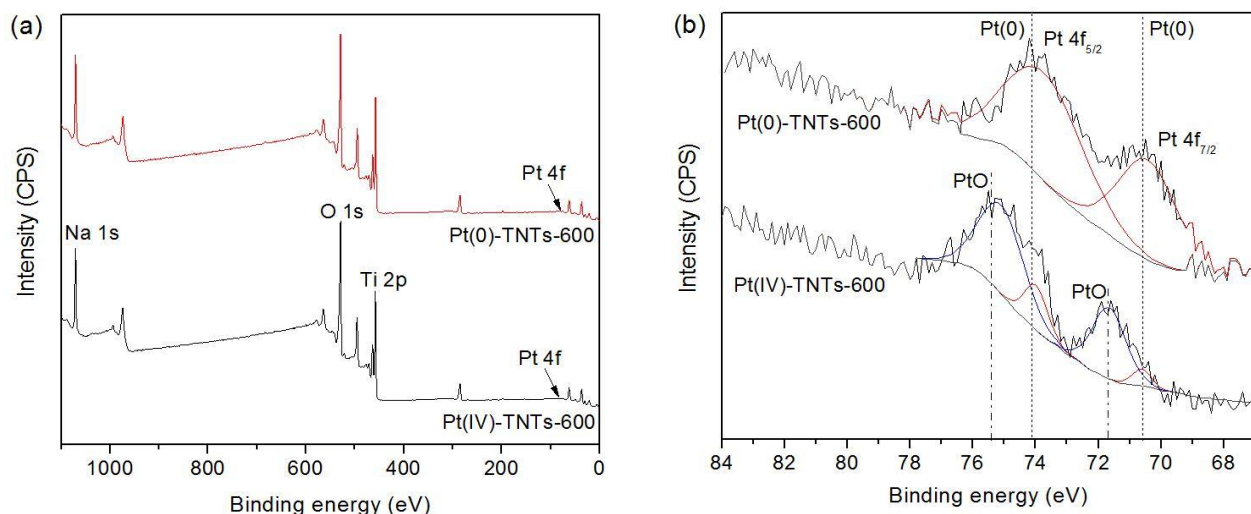


**Figure 5-5.** XPS survey spectra (a) and high resolution of Pt 4f (b) for Pt(0)-TNTs-600 and Pt(IV)-TNTs-600.

**Table 5-2.** Elemental weight percentages in Pt(0)-TNTs-600 and Pt(IV)-TNTs-600.

Material	Element atomic ratio (wt.%)				
	Na	O	Ti	Pt	Cl
Pt(0)-TNTs-600	9.6	45.3	43.2	0.11	1.8
Pt(IV)-TNTs-600	13.1	44.8	39.9	0.14	2.0

### 5.3.3. Photocatalytic degradation of phenanthrene by various Ti-based materials

**Figure 5-6** shows the photocatalytic degradation of phenanthrene by various Ti-based nanomaterials, including the precursor TiO<sub>2</sub>, neat TNTs, Pt(0)-TNTs, TNTs calcined at 600 °C without Pt (TNTs-600), Pt(0)-TNTs-600 and Pt(IV)-TNTs-600. **Table 5-3** gives the best-fitted first-order kinetic model parameters. Pristine TiO<sub>2</sub> is a well-known photocatalyst under UV light, but insensitive to visible light. As a result, only 30% phenanthrene at 10 h ( $k_1 = 0.04 \text{ h}^{-1}$ ) was degraded under solar light, which contains ~5% UV. Neat TNTs showed the lowest photocatalytic activity ( $k_1 = 0.02 \text{ h}^{-1}$ ) due to rapid recombination of the electron-hole pairs (Kim et al. 2012, Lee et al. 2007a, Yu et al. 2006a, Zhao et al. 2016). The uncalcined Pt(0)-TNTs showed little improvement of the photo-activity. Calcined TNTs without Pt (TNTs-600) displayed a 50% greater photocatalytic activity than TNTs ( $k_1 = 0.03 \text{ h}^{-1}$ ), due to formation of anatase/hexa-titanate (Lee et al. 2007b, Yu et al. 2006b, Zhao et al. 2016). Pt(0)-TNTs-600 showed the highest activity, with a  $k_1$  value being 3 times of that for TiO<sub>2</sub> and 6 times of TNTs under solar light. Pt(IV)-TNTs-600 also exhibited high photo-activity, though the  $k_1$  value was only half that for Pt(0)-TNTs-600, suggesting that Pt(0) is more effective than Pt(II).



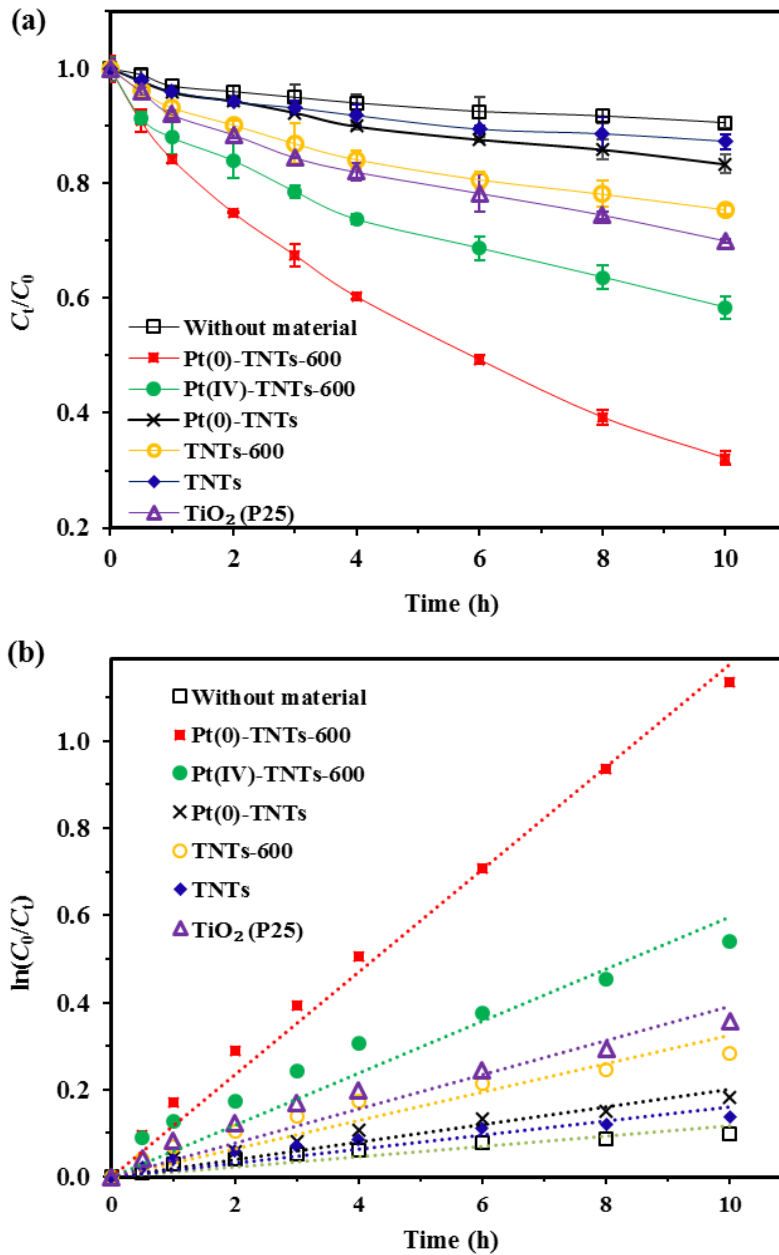


**Figure 5-6.** Photocatalytic degradation of phenanthrene by various Ti-based materials (a), and linearized first-order model fittings of the kinetic data (b). Experimental conditions: initial phenanthrene = 200  $\mu\text{g/L}$ , material dosage = 0.2 g/L, pH =  $7.0 \pm 0.2$ , temperature =  $25 \pm 0.2$   $^\circ\text{C}$ .

**Table 5-3.** Best-fitted first-order kinetic model parameters for photocatalytic degradation of phenanthrene by various Pt-based nanomaterials.

Material	$k_1$ (h <sup>-1</sup> )	$R^2$
Without material	0.01	0.83
Pt(0)-TNTs-600	0.12	0.99
Pt(IV)-TNTs-600	0.06	0.90
Pt(0)-TNTs	0.02	0.91
TNTs-600	0.03	0.87
TNTs	0.02	0.81
TiO <sub>2</sub> (P25)	0.04	0.91

### 5.3.4. Mechanisms for enhanced photocatalytic activity of Pt-deposited TNTs

**Figure 5-7** presents the DRS UV-vis spectra of TNTs, Pt(0)-TNTs-600 and Pt(IV)-TNTs-600. The optical energy gaps ( $E_g$ ) of the tested materials were calculated following the Kubelka-Munk method (Feng et al. 2015, Zhao et al. 2016). The absorption edges of both Pt(0)-TNTs-600 and Pt(IV)-TNTs-600 show a red shift to the visible light region compared to neat TNTs. A narrowed  $E_g$  was found for Pt(0)-TNTs-600 (3.1 eV) and Pt(IV)-TNTs-600 (3.3 eV), as compared to 3.4 eV for TNTs. In addition, Pt(0)-TNTs-600 exhibited the highest absorbance in the visible region, suggesting the good photocatalytic activity under visible light. The absorbance peak at 401 nm for Pt(0)-TNTs-600 can be attributed to the deposited Pt(0) in the band gap of TiO<sub>2</sub>, which derives a new electronic state below the band gap (Driessen and Grassian 1998). Therefore, incorporation

of Pt in TNTs altered the  $e$ -donor levels, which facilitates the transfer of the photo-generated electrons and inhibit recombination of electron-hole pairs (Zhao et al. 2016).

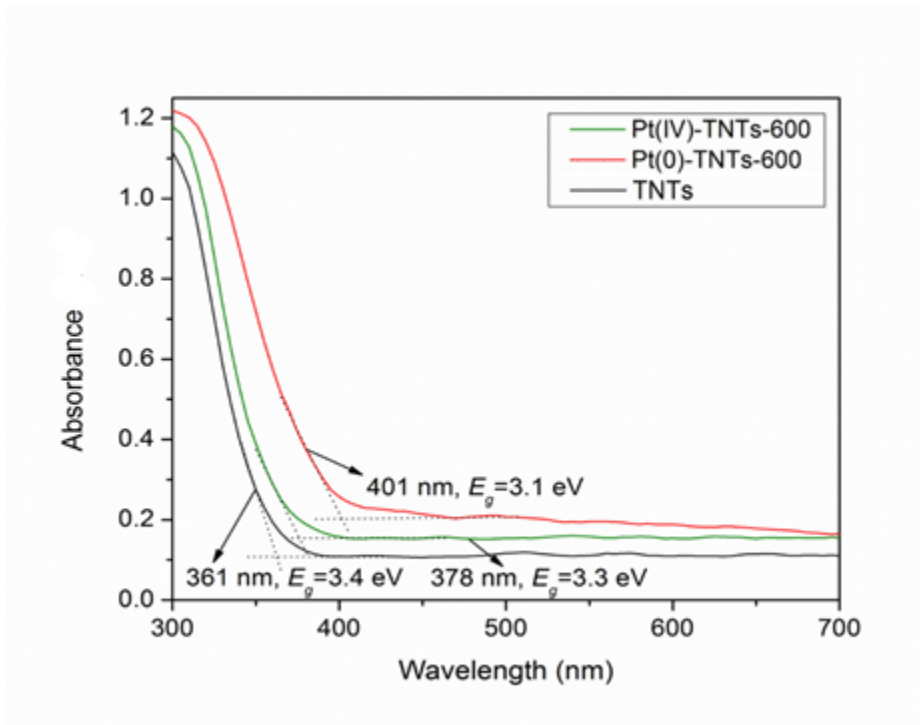


**Figure 5-7.** DRS UV-vis spectra of TNTs, Pt(0)-TNTs-600 and Pt(IV)-TNTs-600.

To verify the enhanced photocatalytic activity of the new catalysts under visible light, the degradation of phenanthrene under visible irradiation was compared with that under solar irradiation. **Figure 5-8** shows that that the total phenanthrene degradation at 10 h under solar light was 24.6%, 41.7% and 68.1% in the presence of TNTs-600, Pt(IV)-TNTs-600 and Pt(0)-TNTs-600, respectively. Under the visible light only, almost no photodegradation of phenanthrene (<3%) was observed with TNTs-600; however, the visible radiation contributed 68.1% and 48.9% to the total phenanthrene degraded in the presence of Pt(IV)-TNTs-600 and Pt(0)-TNTs-600,

respectively. The much higher contribution of UV light for Pt(0)-TNTs-600 can be attributed to the more efficient utilization of UV by the anatase phase. For both cases, the Pt deposition dramatically enhanced the visible light activity of the nanomaterials, which agrees with the observed shift of DRS UV-vis spectra.

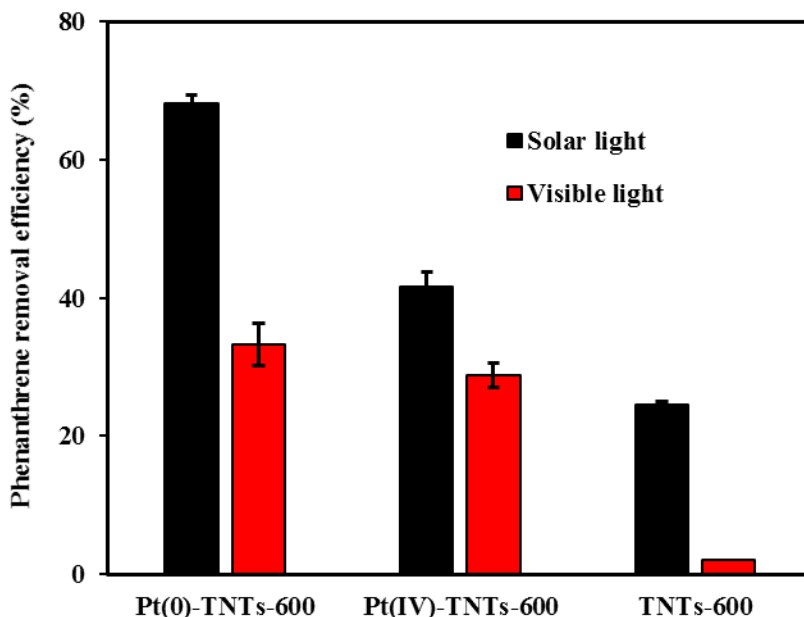
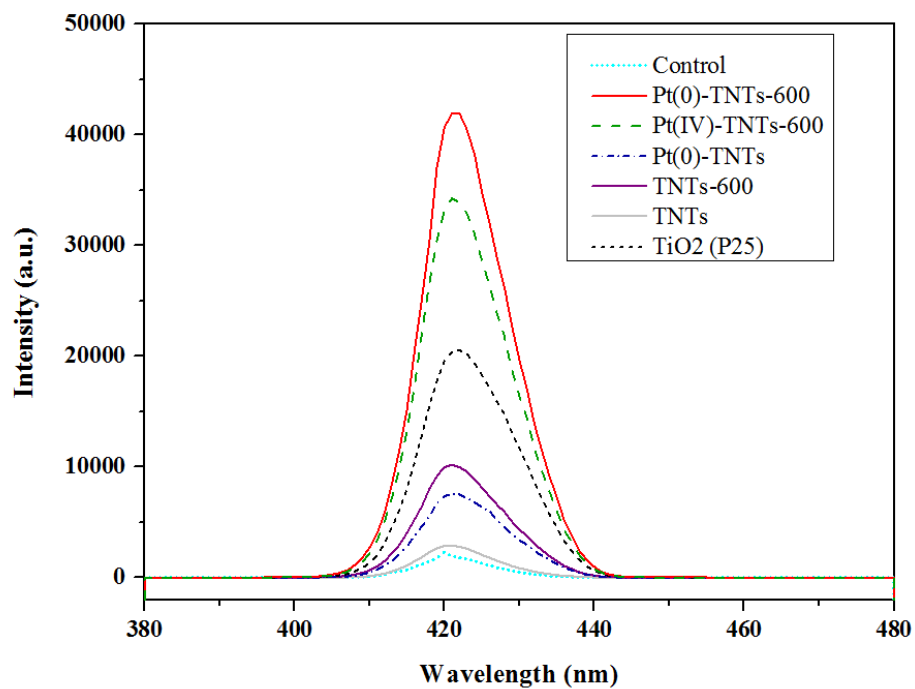


**Figure 5-8.** Contributions of UV and visible irradiation toward photocatalytic degradation of phenanthrene by different Ti-based materials. Experimental conditions: initial phenanthrene = 200  $\mu\text{g/L}$ , material dosage = 0.2 g/L, pH =  $7.0 \pm 0.2$ , temperature =  $25 \pm 0.2$   $^{\circ}\text{C}$ , reaction time = 10 h.

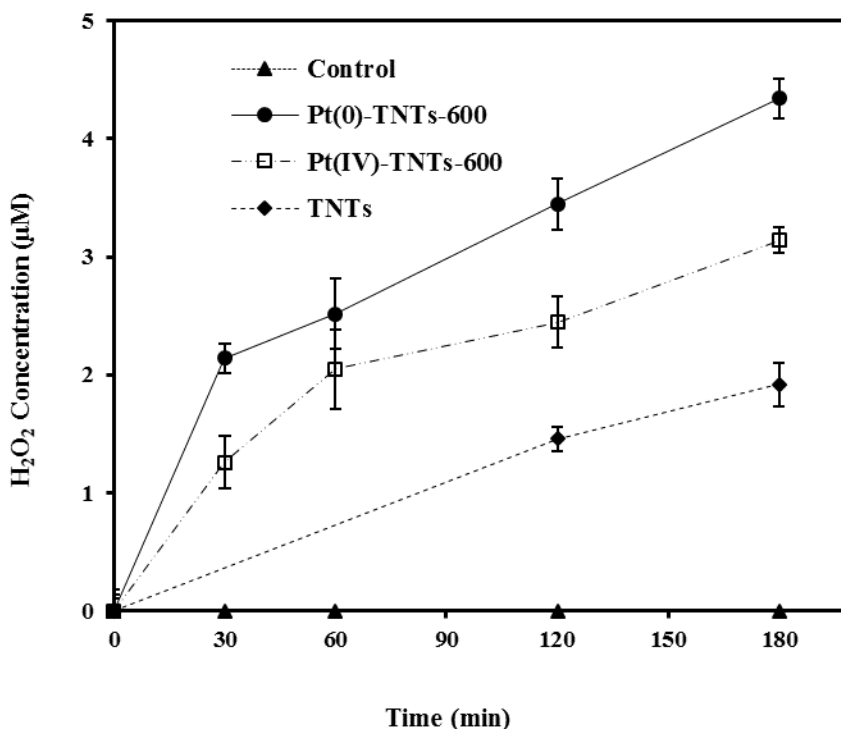
Pt(0)-TNTs-600 far outperformed Pt(IV)-TNTs-600 in the phenanthrene photodegradation, which can be attributed to some fundamental differences in their functional compositions. First, Pt(0)-TNTs-600 contains both anatase and hexa-titanate, while Pt(IV)-TNTs-600 has only hexa-

titanate. Anatase from tri-titanate promotes the production of more electron-hole pairs than hexa-titanate, resulting in greater quantum yield for Pt(0)-TNTs-600. Second, Pt(0) is an excellent conductor, which can more efficiently transfer photo-generated electrons than PtO. It is noteworthy that hexa-titanate has higher photocatalytic activity than tri-titanate due to the tunnel structures of [TiO<sub>6</sub>] octahedra, but weaker than TiO<sub>2</sub> (Inoue et al, 1994).

Production of ROS, i.e. •OH and H<sub>2</sub>O<sub>2</sub>, was determined to further elucidate the underlying mechanisms. **Figure 5-9** shows the PL spectra of terephthalic acid in the presence of various nanomaterials under solar irradiation, which indirectly shows the amount of •OH produced with the photocatalysts. The fluorescence intensity follows the order of: Pt(0)-TNTs-600 >Pt(IV)-TNTs-600 >TiO<sub>2</sub> (P25) >TNTs-600 >Pt(0)-TNTs >TNTs, which is consistent with the phenanthrene degradation rate. Evidently, •OH radicals play an important role in facilitating the photocatalytic degradation of phenanthrene for both Pt(0)-TNTs-600 and Pt(IV)-TNTs-600. In addition, production of H<sub>2</sub>O<sub>2</sub> under solar light follows the sequence of: Pt(0)-TNTs-600 >Pt(IV)-TNTs-600 >TNTs (shown in **Figure 5-10**), confirmed the higher photocatalytic activity of TNTs after Pt deposition.



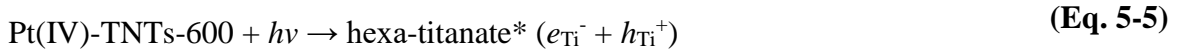
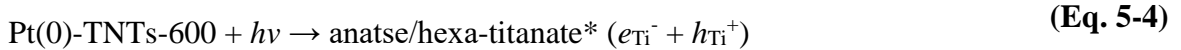
**Figure 5-9.** PL spectra of various Ti-based materials under solar irradiation. Experimental conditions: material dosage = 0.2 g/L, pH =  $7.0 \pm 0.2$ , temperature =  $25 \pm 0.2$  °C, no phenanthrene was added.



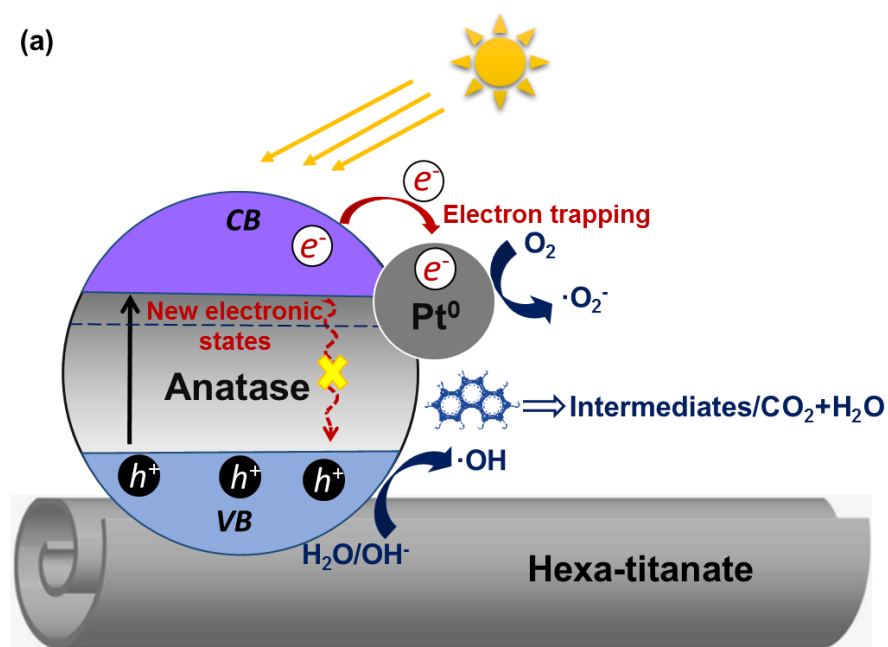
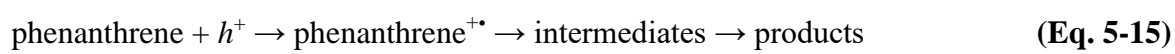
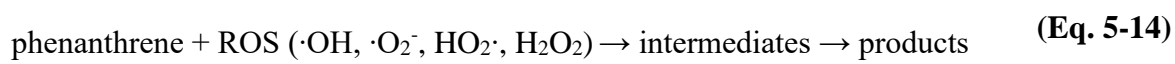
**Figure 5-10.** Formation of  $\text{H}_2\text{O}_2$  in various nanomaterial suspensions under solar irradiation. Experimental conditions: material dosage = 0.2 g/L, pH =  $7.0 \pm 0.2$ , temperature =  $25 \pm 0.2$  °C, no phenanthrene was added.

**Figure 5-11** depicts the key mechanisms for the enhanced photocatalytic activity of Pt(0)-TNTs-600 and Pt(IV)-TNTs-600. Under solar irradiation, both  $\text{TiO}_2$  (anatase) and TNTs (mainly hexa-titanate) can generate a conduction band ( $e^-$ , electrons) and a valence band ( $h^+$ , holes) (**Eq. 5-4** and **5-5**). However, the pristine  $\text{TiO}_2$  and titanate are not active under visible light due to their relatively high band gaps (Veldurthi et al. 2015, Zhao et al. 2016). Moreover, the photo-generated electron-hole pairs on titanate are susceptible to recombination, resulting in a low quantum yield (Li et al. 2015). In contrast, for Pt(0)-TNTs-600, the electrons can be immediately transferred to

the deposited Pt metal upon excitation (**Eq. 5-6**), thus inhibiting the electron-hole recombination; for Pt(IV)-TNTs-600, besides the Pt(0)-facilitated electron transfer, Pt in PtO can act as a photocatalysis center (**Eq. 5-7**) (Hu et al. 2015), where electrons excited on the conduction band of PtO migrate to the conduction band of TiO<sub>2</sub> due to their conduction band offset (**Eq. 5-7** and **5-8**), thus electron-hole recombination for both PtO and TiO<sub>2</sub> is suppressed due to electrons trapping on TiO<sub>2</sub> and holes on PtO (**Eq. 5-8** and **5-9**) (Hu et al. 2015), resulting in enhanced photocatalytic activity. In addition, for both Pt(0)-TNTs-600 and Pt(IV)-TNTs-600, the deposited Pt lies in their band gaps, which may derive new electronic states below the band gaps (Driessen and Grassian 1998, Schierbaum et al. 1996), and thus extends the absorbance to the visible region. The electrons can react with electron acceptors, e.g., O<sub>2</sub>, to form superoxide radicals ( $\bullet\text{O}_2^-$ ), and further to HOO $\bullet$  (**Eq. 5-10** and **5-11**) (Driessen and Grassian 1998). The holes can oxidize water molecules and oxygen into ROS (e.g.,  $\bullet\text{OH}$  and H<sub>2</sub>O<sub>2</sub>) (**Eq. 5-12** and **5-13**), which are responsible for degradation of phenanthrene (**Eq. 5-14**). Meanwhile, phenanthrene can also be directly attacked by holes to produce phenanthrene<sup>+</sup>, which is further degraded via **Eq. 5-15**) (Kou et al. 2009).







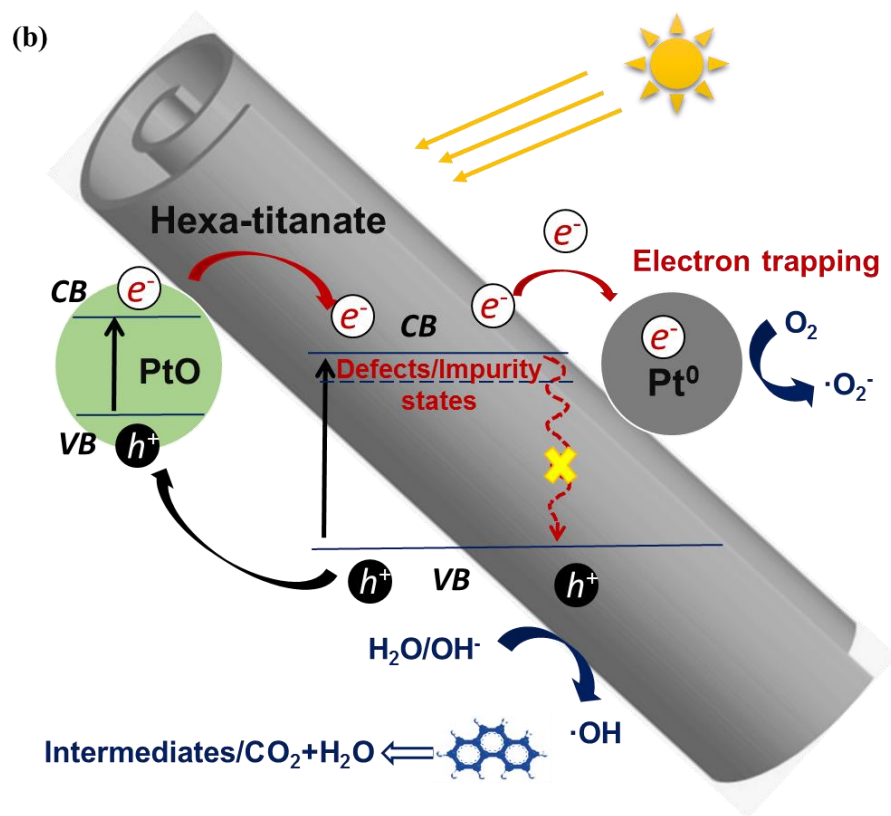


**Figure 5-11.** Schematic illustration of enhanced photocatalytic activity of Pt(0)-TNTs-600 (a) and Pt(IV)-TNTs-600 (b).

### 5.3.5. Reusability of Pt doped TNTs

Reusability of photocatalysts is crucial for cost-effective application of the technology in water treatment. **Figure 5-12** shows that Pt(0)-TNTs-600 can be more easily separated from water. For instance, after gravitational settling for 8 h, 91.5% of Pt(0)-TNTs-600 was removed, compared to 79.5% for TNTs, and only 4.4% for the commercial  $TiO_2$ . The good sedimentation performance

is attributed to the tubular structure, higher density, and large aggregated particle size (Liu et al. 2013a, Zhao et al. 2016).

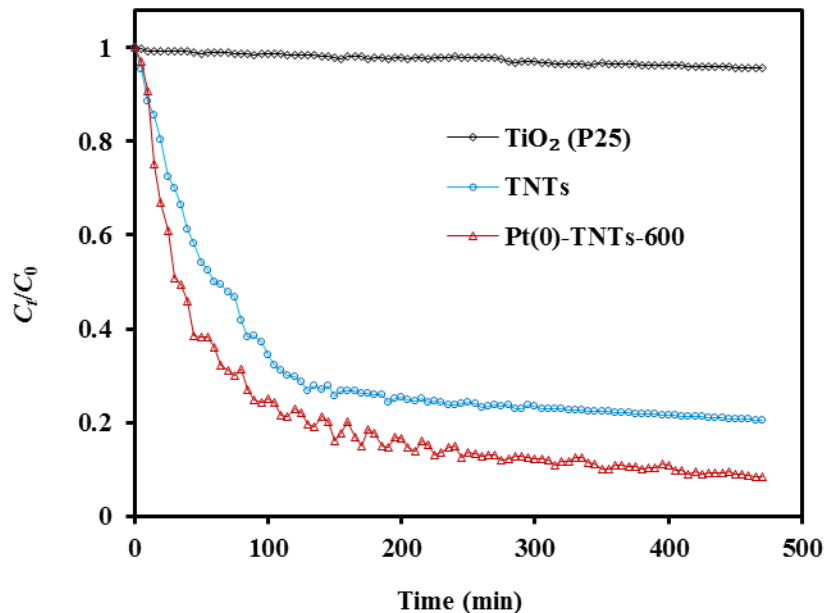


**Figure 5-12.** Sedimentation kinetics of TiO<sub>2</sub>, TNTs and Pt(0)-TNTs-600 under gravity settling. Experimental conditions: material concentration = 0.2 g/L, pH = 7.0, temperature = 25 ± 0.2 °C.

**Figure 5-13** presents phenanthrene photodegradation kinetics over 6 cycles of repeated uses of the same Pt(0)-TNTs-600. The 24-h phenanthrene degradation showed only a slight drop (~3.7%) in the second cycle, remained identical thereafter (**Table 5-4**). The observation indicates that the photodegradation process also completely regenerates the catalyst, granting it long-lasting photocatalytic activity. In addition, no Pt leaching was detected over the 6 cycles of operations, indicating high physico-chemical stability of the catalyst.

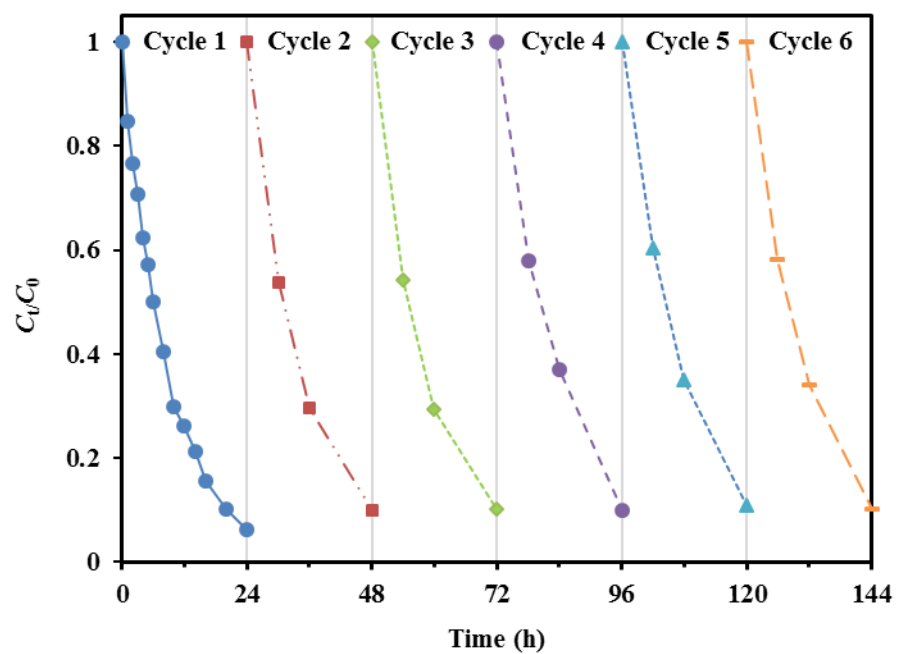


**Figure 5-13.** Photocatalytic degradation of phenanthrene using the same Pt(0)-TNTs-600 over 6 consecutive runs. Experimental conditions: initial phenanthrene concentration in each cycle = 200  $\mu\text{g/L}$ , material dosage = 0.2 g/L, pH =  $7.0 \pm 0.2$ , temperature =  $25 \pm 0.2$  °C.

**Table 5-4.** Apparent rate constants ( $k_1$ ) and phenanthrene removal efficiency ( $R$ ) by Pt(0)-TNTs-600 over 6 cycles of consecutive runs.

Cycles	$k_1$ (h <sup>-1</sup> )	$R$ (%)
1	0.11	93.8
2	0.10	90.1
3	0.10	89.8
4	0.09	90.0
5	0.09	89.1
6	0.10	91.7

**Table 5-5.** Materials costs of Ti-based nanomaterials.

		TiO <sub>2</sub> (P25)	H <sub>2</sub> Cl <sub>6</sub> Pt	NaBH <sub>4</sub>	NaOH	Total cost (\$)
<b>Unit price (\$/kg)</b>		30	3600	5	0.37	
<b>Consumption (kg)</b>	TiO <sub>2</sub> (P25)	1	0	0	0	
	TNTs	1	0	0	24.17	
	Pt(IV)-TNTs-600	1	0.0025	0	24.17	
	Pt(0)-TNTs-600	1	0.0025	0.00388	24.17	
<b>Cost (\$)</b>	TiO <sub>2</sub> (P25)	30	0	0	0	<b>30</b>
	TNTs	30	0	0	8.95	<b>38.95</b>
	Pt(IV)-TNTs-600	30	9	0	8.95	<b>47.95</b>
	Pt(0)-TNTs-600	30	9	1.5	8.95	<b>49.45</b>

The material costs of the Pt(IV)-TNTs-600 and Pt(0)-TNTs-600 are only about 60% and 65% higher than the commercial TiO<sub>2</sub> (P25) based on the wholesale price on the market (shown in Error! Not a valid bookmark self-reference.), but their phenanthrene removal rates increased by the factors of 150% and 300%, respectively. Therefore, the Pt(0)-TNTs-600 is a promising photocatalyst for the degradation of PAHs.

#### 5.4. Conclusions

This work synthesized, characterized and tested a new class of Pt-deposited TNTs photocatalysts for highly efficient photocatalytic degradation of phenanthrene under solar light. The key findings and conclusions are summarized as follows:

- (1) A new class of Pt-deposited TNTs were successfully synthesized via a simple three-step process: hydrothermal treatment of TiO<sub>2</sub>, deposition of Pt, and calcination at 600 °C. The optimum Pt dosage was 0.1 wt.%, and calcination temperature was 600 °C.
- (2) Both Pt(0)-TNTs-600 and Pt(IV)-TNTs-600 exhibited high photocatalytic activity for degradation of phenanthrene under solar light, with a first-order rate constant ( $k_1$ ) being 3 and 1.5 times of that of the parent TiO<sub>2</sub>.
- (3) Pt(0)-TNTs-600 outperformed Pt(IV)-TNTs-600 in catalyzing phenanthrene degradation. During the calcination process, tri-titanate was converted to anatase and hexa-titanate in Pt(0)-TNTs-600, but only hexa-titanate in Pt(IV)-TNTs-600. The extra anatase is photo-catalytically more active than hexa-titanate. Moreover, the calcination also converted Pt(IV) in Pt(IV)-TNTs-600 into PtO (majority) and Pt(0) (minority). For both materials, Pt(0) transfers the excited electrons, thereby inhibiting the electron-hole recombination; for Pt(IV)-TNTs-600,

PtO acts as an electron-hole trap, which also inhibits the recombination of electron-hole pairs though less effective than Pt(0).

- (4) DRS UV-vis spectra revealed that Pt(0)-TNTs-600 and Pt(IV)-TNTs-600 give a narrower optical energy gap of 3.1 and 3.3 eV, respectively, compared to 3.4 eV of TNTs, resulting in the much enhanced photocatalytic activity under visible light of these nanomaterials.
- (5) Pt(0)-TNTs-600 can be separated through gravity-sedimentation, and reused in multiple cycles of operations without loss in the photocatalytic activity.

Overall, Pt(0)-TNTs-600 represents a significant step forward in development of novel photocatalysts for environmental cleanup uses, and the new material appears promising for more cost-effective photocatalytic degradation of persistent organic pollutants under solar light.

## Chapter 6. Conclusions and Recommendations for Future Research

### 6.1. Summary and conclusions

Oil and associated pollutants have frequently been released into marine environments through oil spills and via discharge of wastewater by the oil industry. Dispersant has regularly been applied to mitigate the adverse effects of oil spills. In this study, a new method was proposed to measure the dispersant concentration in seawater, and the effects of dispersants on the sediment-facilitated transport of oil, as well as on the photodegradation of oil-related pollutants that have been emulated. Moreover, a new class of catalysts was synthesized and tested for photocatalytic degradation of phenanthrene in the water phase. The results of the research are summarized below:

A new method was developed to determine concentration of Corexit EC9500A, and other likely oil dispersants, in seawater. The method can accurately analyze Corexit EC9500A in the concentration range of 0.5–23.5 mg/L. Minor changes in solution salinity (<0.3%), pH (7.9–9.0), and dissolved organic matter (<2.0 mg/L as TOC) had negligible effects on the measurements. Moreover, effects of extracts from marine sediments were negligible, and thus, the method may be directly applied to seawater-sediment systems. The method accuracy was confirmed by comparison with direct TOC analysis. This simple, fast, economical method offers a convenient



analytical tool for quantifying complex oil dispersants in water/seawater, which has been desired by the oil spill research community and industries.

The effects of three model oil dispersants (Corexit EC9527A, Corexit EC9500A and SPC1000) on settling of fine sediment particles as well as particle-facilitated distribution and transport of oil components in sediment-seawater systems were investigated. All three dispersants enhanced settling of sediment particles. The nonionic surfactants (Tween 80 and Tween 85) play key roles in promoting particle aggregation, yet the effects varied with environmental factors (pH, salinity, DOM, and temperature). The strongest dispersant effect was observed at neutral or alkaline pH and in a salinity range of 0–3.5 wt.%. The presence of water accommodated oil and dispersed oil accelerated settling of the particles. Total petroleum hydrocarbons in the sediment phase were increased from 6.9% to 90.1% in the presence of Corexit EC9527A, and from 11.4% to 86.7% for PAHs. This information is useful for understanding roles of oil dispersants in the formation of oil-sediment aggregates and in the sediment-facilitated transport of oil and PAHs in marine eco-systems.

The effects of oil dispersants on photodegradation of anthracene and 9,10-DMA in marine environment were studied. All three dispersants, i.e. Corexit EC9500A, Corexit EC9527A and SPC1000, promoted the photolysis rate of 9,10-DMA, following the order: Corexit EC9500A >Corexit EC9527A >SPC 1000. Span 80, Tween 85 and kerosene were found the key dispersant components, which enhance the photodegradation by boosting absorbance of solar radiation and/or dispersing more PAHs in the upper layer of the water column. The DO decreased the photodegradation rate of anthracene, indicating that the O<sub>2</sub> may act as quencher for the excited

state of anthracene or organic matters. Conversely, the DO increased the photolysis rate of 9,10-DMA, indicating that the  $O_2$  is involved in the 9,10-DMA degradation, and experiments also showed that the  $^1O_2$  contributed to the 9,10-DMA degradation. The photolysis pathway of anthracene and 9,10-DMA showed no difference in the presence or absence of dispersant. Meanwhile, the dispersants have been found to undergo photodegradation under solar light. The results provide useful information for understanding the roles of oil dispersants on the environmental weathering and fate of persistent oil components in a marine environment, as well as the fate of oil dispersants.

A new type of photocatalyst, referred to as Pt-deposited anatase/hexa-titanate nanotubes, was prepared through a two-step process: hydrothermal treatment and subsequent calcination. The composite material was thoroughly characterized and tested for photocatalytic degradation of phenanthrene (a prototype polycyclic aromatic hydrocarbon) under simulated solar light. The material (Pt(0)-TNTs-600) prepared with a Pt(0) dosage of 0.1 wt.%) and a calcination temperature of 600 °C showed the highest photocatalytic activity for degrading phenanthrene. The apparent rate constant ( $k_1$ ) was determined to be  $0.12\text{ h}^{-1}$ , which was ca. 3 times higher than that for the standard  $TiO_2$  (P25). TEM, XRD, FTIR and XPS analyses indicate that Pt(0)-TNTs-600 is a composite of anatase, hexa-titanate and deposited metallic Pt, where the deposited Pt facilitates the transport of photo-generated electrons, thus inhibiting recombination of the hole-electron pairs. Moreover, DRS UV-vis analysis revealed a narrower optical energy gap of 3.1 eV for Pt(0)-TNTs-600 compared to 3.4 eV for the pristine TNTs, resulting in enhanced absorbance in the visible light region. The new photocatalyst could also produce more reactive oxygen species (mainly  $\bullet OH$  and

H<sub>2</sub>O<sub>2</sub>) than P25 and pristine TNTs. The material can be reused in multiple cycles of water treatment operations (almost no activity loss after 6 consecutive cycles). The new photocatalyst appears promising for efficiently photodegrading a host of important organic pollutants in water under solar light.

## **6.2. Contributions and limitations**

The contributions of the research are summarized below:

- (1) The new surface-tension based method developed in this study is a convenient and useful alternative tool for researchers and practitioners for quantitative analysis of complex oil dispersants in aquatic systems.
- (2) The effects of oil dispersants on the photolysis and sediment-associated transport of oil contaminants are quantified, which provide useful information for understanding the roles of oil dispersants on the fate of persistent oil components in the marine environment.
- (3) Pt(0)-TNTs-600 represents a significant step forward in development of novel photocatalysts for waste treatment, and the new material appears to be a promising and cost-effective technology for photocatalytic degradation of persistent organic pollutants.

However, the research has some limitations:

- (1) The dispersants or dispersants components concentration used in the research, i.e. 18 mg/L, is much higher than the value observed in marine systems. For example, the dispersant detected near the well head of *DwH* site are in the range of 10–100 µg/L (Kujawinski et al. 2011).

(2) This study only focused on the physical and chemical process of oil transport in marine environment. However, the biological processes, e.g. formation of marine snow, can alter the oil transport.

(3) The suspended sediment particles concentration (12 g/L) that used in experiment is much higher than the values frequently observed in marine systems. The concentration of suspended particles in deep ocean is almost negligible, and typical shoreline suspended particles concentration measured in this study were in the range of 0.5 to 32 mg/L.

(4) Further characterization methods are needed to investigate the enhanced visible light activity of the new photocatalyst.

### **6.3. Recommendations for future work**

This study investigated the effects of oil dispersants on transport and photolysis of oil contaminants, and a new class of catalysts on the enhanced photocatalytic degradation of PAHs under solar radiation. There are still a number of scientific issues that require further investigations, and the specific recommendations for future work are made as follows:

(1) The surface tension method that was used for determining Corexit EC9500A concentration in seawater may be extended for measuring other dispersants' or surfactants' concentrations in seawater and fresh water. Further effort is needed to verify the effectiveness of this method for measuring the concentration of other dispersants or surfactants in both seawater and fresh water.

(2) Some bio-related particles in marine system, e.g. marine snow, are responsible for the transport of related contaminants. Therefore, the effects of oil dispersants on their formation and settling performance may need to be studied.

(3) The intermediates that are produced from the photocatalytic degradation of PAHs can be more toxic than PAHs themselves. The extent of PAHs photodegradation, e.g. complete mineralization, needs to be considered, and the toxicity of treated effluent needs to be assessed.

(4) The high cost of new photocatalysts always restricts their practical application. The catalyst preparation method could be further optimized to cut back the energy and material cost. For instances, the hydrothermal temperature may be elevated to decrease the reaction time, the NaOH solution can be recycled, etc.

(5) Many nanomaterials, e.g. carbon nanotubes, carbon nanofibers, carbon nanoparticles (Magrez et al. 2006), quantum dots, gold and silver nanoparticles (Srivastava et al. 2015), are reported to be toxic to microorganisms. However, to the best of our knowledge, there is no published study that reveals the fate, transport and toxicity of TNTs in the environment. Therefore, studies are needed for evaluating the ecological risk of the TNTs.

## Appendix

### **Reduction of Nitrobenzene in the Aqueous and Soil Phases Using Carboxyl Methyl Cellulose -Stabilized Zero-Valent Iron Nanoparticles**

Zhengqing Cai, Dongye Zhao\*

*Environmental Engineering Program, Department of Civil Engineering, Auburn University,  
Auburn, AL 36849, USA*

\***Corresponding author.** Tel: 1-334 844 6277; Fax: 1-334 844 6290; E-mail:  
[zhaodon@auburn.edu](mailto:zhaodon@auburn.edu).

## Abstract

Zero valent iron (ZVI) nanoparticles have been extensively studied for reductive degradation of nitrobenzene (NB) in water phase. However, little is known about the effectiveness of polymer-stabilized ZVI nanoparticles on NB degradation. In this study, a food-grade and low-cost polysugar, carboxyl methyl cellulose (CMC), was used to stabilize ZVI nanoparticles through a pre-aggregation method. The feasibility and efficiency of NB reduction by the CMC-stabilized ZVI nanoparticles in water and soil phase were investigated. The results showed the CMC-stabilized ZVI nanoparticles could overcome the rate-limiting step of surface mass transfer, which greatly limit the efficiency of non-stabilized ZVI. CMC-stabilized ZVI nanoparticles showed a high NB reduction rate ( $k_{app} = 0.643 \text{ min}^{-1}$ ), which was approximately 3.7 times faster than the non-stabilized ZVI nanoparticles. That the presence of DOM decreased NB reduction rate was mainly due to inhibition of the mass transfer of NB to ZVI nanoparticles surface and competitive reaction with target NB. Higher pH (>8) is favorable for NB reduction because more  $\text{Fe}(\text{OH})^+$  was formed. A rarely detected but important compound (phenylhydroxylamine) was identified in the NB reductive degradation process, and the primary rate-limiting step for NB reduction was the conversion of nitrosobenzene to phenylhydroxylamine. Sorption isotherm of NB on the tested potting soil can be well fitted by a dual-mode model, and the desorption of NB showed significant hysteresis. The CMC-stabilized ZVI nanoparticles could completely reduce the soil-sorbed NB at ZVI dosage of 0.6 g/L. The findings in this work indicate that the CMC-stabilized ZVI nanoparticles display a high efficiency for NB reduction in both aqueous and soil phases, and hold the potential to facilitate *in-situ* remediation of NB-contaminated soil and groundwater.

## Keywords

Zero-valent iron; Nanoparticles; Reductive degradation; Nitrobenzene; Soil remediation; Groundwater contamination

## 1. Introduction

Nitrobenzene (NB) has been widely used in herbicides, insecticides, explosives, pharmaceuticals, and dyes (Rodriguez et al. 2002, Wang et al. 2011). NB is prone to contaminate surface and groundwater by improper disposal or accidents (Kuscu and Sponza 2009, Tong et al. 2011). According to the U.S. Environmental Protection Agency (EPA) released data, about 416 tons of NB were released to the environment in 1992, of which approximate 94.32% was introduced into underground injection sites (USEPA 1995). In 2005, an explosion of petrochemical plant in Jilin, China discharged approximately 100 tons of toxic chemicals (NB as the main component) into the Songhua River (Wang et al. 2012, Zhu et al. 2007), and the NB concentration was found as high as 0.581 mg/L in the river even after dilution (Zhu et al. 2007). The U.S. EPA conducted a survey on NB levels in the effluents from 4000 publicly owned treatment works and industrial sites. The survey revealed that the NB contamination is associated with wastewaters from organic chemicals and plastics industries, with NB concentrations as high as 190 mg/L (Jameson et al. 2002, World Health Organization (WHO) 2003). NB is of moderate to low toxicity to aquatic and terrestrial organisms, the LC<sub>50</sub> (50% lethal concentration) for freshwater organisms range from 2 to 156 mg/L (Kuscu and Sponza 2009). This chemical is classified as *a likely human*



*carcinogen by any route of human exposure* according to a carcinogenicity test conducted by U.S. EPA (USEPA 1998). NB has been listed as a priority pollutant by U.S. EPA (USEPA 2014), and strict limitations in environment have been introduced, e.g. the maximum allowable concentration is 1 mg/L in wastewater in the U.S. (USEPA 1980), and 17 µg/L in drinking water in both U.S. (National Toxicology Program 2011, USEPA 2004) and China (Zhang and Chen 2009).

To mitigate human exposure, researchers have tested numerous engineered technologies to degrade NB in water, such as photocatalysis (Jo et al. 2014), supercritical oxidation (Arslan-Alaton and Ferry 2002, Jo et al. 2014), combined Fenton and photochemical oxidation (Rodriguez et al. 2000), and ultrasound-enhanced zero-valent iron (ZVI) reduction (Hung et al. 2000). Although NB can be either oxidized or reduced, reductive degradation is much more favorable than the oxidation process either biotically or abiotically due to the electron-deficient character of the nitro-group ( $\text{NO}_2^-$ ) (Zhang et al. 2007). When subjected to reduction, e.g. by ZVI (Zhang et al. 2013) or photocatalytic reduction (Roy et al. 2013), the primary product, aniline, is more prone to further biodegradation (Wang et al. 2011).

Reductive degradation of NB using ZVI powder or synthesized ZVI particles has been extensively investigated for more than 70 years (Chen et al. 2011, Hazlet and Dornfeld 1944). In 1944, Hazlet and Dornfeld (1944) used a HCl activated granulate iron (40 mesh) to reduce NB and other aromatic nitro compounds dissolved in benzene, the aniline hydrochloride was identified as the final product of NB reduction by means of melting point. Mu et al. (2004) studied the degradation of NB by iron particles (diameter <0.85 mm) at various pH values, and found that formation of aniline followed zero-order kinetics with a maximum aniline formation rate of 0.016

mM/min at the optimum pH (3.0). Agrawal and Tratnyek (1996) used an 18–20 mesh acid-washed iron (33.3 g/L) to reductively degrade NB under anaerobic condition, and found that the reduction of both NB and nitrosobenzene (an intermediate) followed first order law (with pseudo-first-order rate constant of  $k_{app} = 0.035$  and  $0.034 \text{ min}^{-1}$ , respectively). Their study also showed that the reduction rate increased linearly with iron surface area concentration, giving a specific reaction rate constant of  $3.9 \times 10^{-2} \text{ min}^{-1} \text{ m}^{-2} \text{ L}$  (Agrawal and Tratnyek 1996). Huang and Zhang (2006) found that a stratified iron corrosion coating (lepidocrocite) was formed on the ZVI particle during the reduction of NB, which blocked active surface sites and thus limited further reduction of NB. Therefore, the reduction rate of NB by ZVI powder is primarily limited by the effective surface area of iron, so the application of ZVI nanoparticles may provide faster degradation kinetics due to the larger surface area and higher reactivity.

ZVI nanoparticles were extensively studied for the reductive degradation of NB in the aqueous phase (Dong et al. 2015, Ling et al. 2012, Sun et al. 2010). However, due to the strong van der Waals and magnetic interactions, synthetic non-stabilized ZVI nanoparticles tend to aggregate rapidly into micro-millimeter scale aggregates, which not only reduces their specific surface area, but also soil deliverability. As a result, non-stabilized ZVI particles cannot be directly delivered into contaminated aquifers to facilitate *in situ* remediation of contaminated soil and groundwater. To prevent particle aggregation and maximize the reactivity, various stabilization techniques have been developed. For instances, Tong et al. (2011) immobilized ZVI nanoparticles on a nylon membrane to treat NB in groundwater, where the ZVI nanoparticles exhibited a high reactivity ( $k_{app} = 2.28 \text{ h}^{-1}$ ) toward NB at the iron dosage of 32.5 mg/L. They found that both ZVI nanoparticles

and  $\text{Fe}^{2+}$  were responsible for the reduction. Likewise, Ling et al. (2012) loaded ZVI nanoparticles on an ordered mesoporous carbon (OMC) to remove NB in water, the composite material showed enhanced removal efficiency due to synergistic adsorption and reduction effects.

Supporting of ZVI nanoparticles on templates, e.g. on PVA microspheres (Bai et al. 2009), organobentonite (Ren et al. 2014) and montmorillonite (Jia and Wang 2013), are reported to mitigate aggregation. This results in higher reactivity of NB degradation in the aqueous phase, but the supported particles cannot be delivered into contaminated aquifers. To facilitate soil delivery of ZVI nanoparticles for *in situ* degradation, He et al. (2007) developed stabilization techniques using water soluble starch or carboxymethyl cellulose (CMC) as a “green” and low-cost stabilizer. CMC is a modified polysaccharide carrying dense carboxymethyl groups with a  $\text{p}K_a$  value of 4.3. Due to its strong interactions with the ZVI surface and high negative charges, CMC can effectively stabilize ZVI nanoparticles through concurrent steric and electrostatic repulsion interactions. Many bench- and field-scale studies have demonstrated that CMC-stabilized ZVI nanoparticles are not only more reactive than their non-stabilized counterparts, but also more deliverable in soil. For instance, the TCE degradation rate by CMC-stabilized ZVI nanoparticles (doped with palladium) was reported to be 17 times faster than the non-stabilized counterparts in aqueous phase, and column tests showed that the CMC-stabilized nanoparticles can be readily transported in a loamy sand soil (He et al. 2007). Moreover, a single well push-pull test in the field confirmed that the CMC-stabilized ZVI nanoparticles were mobile in saturated sediments, but appeared to lose mobility with time due to the interactions with sediments (Bennett et al. 2010). In a pilot-scale field experiment (He et al. 2010), CMC-stabilized ZVI nanoparticles were tested for *in situ*

destruction of various chlorinated solvents in the subsurface. The results showed that CMC-stabilized ZVI can be delivered into contaminated source zone under gravity (<5 psi), and the nanoparticles showed nearly the same transport pattern as the tracer when monitored at ~3 m down-stream. While the most abiotic reduction was observed during the first two weeks of particle injection, a lingering biological dechlorination process was boosted after one month, which lasted for nearly 600 days (until the end of the monitoring).

Since the *in situ* remediation of organic contaminants, such as 1,1-dichloroethane (Varadhi et al. 2005) and trichloroethene (TCE) (He et al. 2010, Quinn et al. 2005), in groundwater by stabilized ZVI nanoparticles has been reported, only a few studies reported the reduction of NB using soil phase deliverable ZVI nanoparticles. Dong et al. (2015) prepared ZVI nanoparticles by coating an emulsified vegetable oil membrane on the surface for NB degradation. Although the as-prepared materials were well dispersed and claimed as oil phase deliverable, the reactivity was dramatically decreased as compared with the non-stabilized material ( $k_{app}$  is 0.0942 and 0.276 min<sup>-1</sup> for emulsified and non-stabilized ZVI nanoparticles) (Dong et al. 2015).

Environmental factors, such as dissolved organic matter (DOM) and pH, can affect the effectiveness of ZVI nanoparticles. For instance, Tong et al. (2011) observed that the NB reduction by ZVI nanoparticles immobilized in PEG/nylon membranes was more effective at lower pH (pH = 3) as higher pH favored formation of iron hydroxide precipitates on the reactive sites. DOM is known to interact with ZVI particles and then inhibit their reactivity (Zhang et al. 2011). While such environmental effects are expected to be lower for dispersed (CMC-stabilized) ZVI nanoparticles, however, the relevant tests have not been performed.

NB exhibits a moderate adsorption potential and is relative mobile in the soil phase (Ruiping et al. 2008). Hence, soil-sorbed NB can be slowly released back into groundwater, rendering NB a long-term threat to the environment and human health. The desorption and diffusion of soil-sorbed NB may limit their availability for ZVI nanoparticles, and the soil can hinder the deliverability of ZVI nanoparticles to the target contaminants. In addition, the water chemistry condition, e.g. pH, dissolved anions, DOM, *etc.*, in the water-sediment system can also affect the effectiveness of ZVI (Yin et al. 2012). There has been no information available on the reduction of soil-sorbed NB by ZVI, and lacking of this critical information can render results from various field tests inconclusive.

The overall goal of this present work was to test the feasibility of applying CMC-stabilized ZVI nanoparticles for *in situ* remediation of NB-contaminated soil and groundwater. The specific objectives were to: 1) test the reactivity of CMC-stabilized ZVI for reductive degradation of dissolved and soil-sorbed NB; 2) investigate effects of environmental factors, such as pH and DOM, on NB reduction; 3) study effects of soil adsorption of NB on the degradation effectiveness; and 4) identify the reaction products and pathway of NB degradation. The results may lead to a new alternative technology for *in situ* remediation of NB-contaminated aquifers.

## 2. Materials and methods

### 2.1. Chemicals

The following chemicals (analytical grade or higher) were used as received:  $\text{FeSO}_4 \cdot 7\text{H}_2\text{O}$  and  $\text{Na}_2\text{SO}_4$  (Fisher, Rochester, NJ, USA),  $\text{NaBH}_4$  and nitrosobenzene (MP Biomedicals, Solon, OH, USA), sodium carboxymethyl cellulose (Na-CMC or CMC, M.W. = 90,000, Acros Organics), humic acid (Fluka Chemie, Switzerland), NB, aniline and methanol (Alfa Aesar, Ward Hill, MA, USA), acetonitrile (EMD chemicals Inc. Gibbstown, NJ, USA), dichloromethane (BDH, Radnor, PA, USA). Ultra-pure water ( $18.2 \text{ M}\Omega \cdot \text{cm}$ ) was used to prepare all solutions.

A potting soil (Marysville, OH, USA) purchased from a local Wal-Mart store (Auburn, AL, USA) was used to study degradation of soil-sorbed NB and the soil adsorption effects. The soil was sieved using a standard sieve of 2-mm openings, and then washed using tap water to remove fine suspended particles that are hard to separate from water by simple centrifugation. Finally, the soil was dried at  $60 \text{ }^\circ\text{C}$  for 12 h and stored in the dark at  $4 \text{ }^\circ\text{C}$ . The soil analysis was performed by the Soil Testing Laboratory at Auburn University, the analytical methods are described by Gong et al. (2012). **Table A-1** gives salient properties of the soil. The organic matter (OM) content of this soil is 27%, which gives high NB adsorption capacity.

**Table A-1.** Physicochemical characteristics of the potting soil used in this work.

<b>pH</b>	<b>OM*</b>	<b>CEC**</b>	<b>Ca</b>	<b>K</b>	<b>Mg</b>
	%	meq/100g	mg/kg	mg/kg	mg/kg
6	27	2.08	155.0	68.0	119.0
<b>Zn</b>	<b>Al</b>	<b>Fe</b>	<b>Mn</b>	<b>Na</b>	<b>P</b>
mg/kg	mg/kg	mg/kg	mg/kg	mg/kg	mg/kg
0.3	1.3	1.1	1.1	29.0	36.0

OM\* : Organic matter content,

CEC\*\* : Cation exchange capacity.

## 2.2. Preparation of stabilized ZVI nanoparticles

Stabilized ZVI nanoparticles were prepared using a pre-aggregation method described by He and Zhao (2007). First, the following solutions were prepared using N<sub>2</sub>-purged DI water: 0.1 wt.% CMC, 6.77 g/L NaBH<sub>4</sub>, and 6 g/L FeSO<sub>4</sub>·7H<sub>2</sub>O. Then, 20 mL of the FeSO<sub>4</sub>·7H<sub>2</sub>O stock solution, 48 mL of the CMC solution, and 402 mL DI water were added into a flask of 1 L volume, and the mixture was bubbled with N<sub>2</sub> for 20 min to ensure formation of the Fe<sup>2+</sup>-CMC complex (He and Zhao 2007). Then, 10 mL of the fresh NaBH<sub>4</sub> solution was added into the flask dropwise within 4 min (BH<sub>4</sub><sup>-</sup>/Fe<sup>2+</sup> molar ratio = 2) under vacuum and 200 rpm shaking on a flat-top shaker. After the NaBH<sub>4</sub> addition, the reactor was kept shaking for 5 min, and let still for another 10 more min. The obtained ZVI nanoparticle suspension was then used for subsequent characterizations or tests within 1 h. The resulting suspension contained 0.05 g/L (as Fe) of ZVI and 0.1 wt.% CMC, which was used for degrading NB in the aqueous phase. Later, the same procedure was followed to prepare nanoparticles at 1 g/L and with 0.8 wt.% CMC for treating soil-sorbed NB. For

comparison, non-stabilized ZVI particles were synthesized in a similar manner except no CMC stabilizer was used.

### **2.3. Reduction of aqueous NB**

Batch kinetic tests were carried out in 43-mL amber glass vials with PTFE-lined screw caps. NB degradation was initiated by injecting 21.5  $\mu\text{L}$  of a NB stock solution (0.8 mol/L in methanol) into the vials filled with 43 mL ZVI suspension (0.05 g/L), which resulted in an initial NB concentration of 0.4 mmol/L. The vials were then mixed on a rotator (50 rpm) placed in an incubator at 22 °C. At predetermined times, duplicate vials were sacrificially sampled by filtering the suspensions using a 0.2  $\mu\text{m}$  syringe filter (Whatman® Anotop 10, Germany) for further analysis. To detect the degradation intermediates of NB, selected samples (40 mL) at 5 and 60 min were extracted consecutively twice using dichloromethane (5 mL each time). Then the moisture in these extracts was removed by addition of sodium sulfate anhydrous ( $\text{Na}_2\text{SO}_4$ ), then filtered through a 0.2  $\mu\text{m}$  syringe filter, and analyzed by gas chromatography-mass spectrometry (GC/MS). To compare the performances of stabilized and non-stabilized ZVI, the same kinetic tests were carried out in parallel using bare ZVI. To probe the film mass transfer effect, 0.5 g glass beads (with a diameter of 2 mm) were added in selected cases.

To test the effects of DOM, humic acid was chosen as the representative DOM and a working solutions of 200 mg/L (as total organic carbon (TOC)) was prepared. The NB degradation kinetic tests were carried out in the presence of 10 and 50 mg/L HA as TOC. Upon deoxygenation, 21.5 mL of diluted HA stock solution was mixed with 21.5 mL of 0.1 g/L CMC-ZVI in the 43 mL vials. To test the pH effect, the NB reduction tests were conducted at initial pH values of 4–10 adjusted



by diluted NaOH or HCl solutions (0.5 mol/L), and the effects were assessed by comparing the NB remaining after 30 min of reaction.

#### **2.4. Soil sorption/desorption of NB**

Sorption of NB by the potting soil was tested using the same 43-mL amber glass vials, each containing 2 g of the soil and 41.5 mL of DI water. To inhibit any biological degradation, 0.2 g/L of NaN<sub>3</sub> was included in the solution. The sorption tests were initiated by adding a known volume of NB stock solutions into the vials to yield an initial NB concentration of 0.8 mmol/L, which were then mixed on a rotator (50 rpm) in an incubator at 22 °C. At predetermined times, duplicate vials were centrifuged at 3000 rpm (1359 × g force), and 2 mL of supernatant was sampled and filtered for NB analysis.

Desorption kinetic tests were conducted with the soil pre-equilibrated with NB at the initial concentration of 0.8 mmol/L. Upon centrifugation, approximately 40 mL supernatant was replaced with the same volume of a soil-amended solution. The soil-amended solution was prepared by mixing the soil with DI water at the same soil/solution ratio as in the kinetic tests, and thus, it has identical background compositions as in the sorption experiments. At predetermined times, the vials were sampled and analyzed as in the sorption tests.

The NB sorption isotherm tests were conducted in the same manner at initial NB concentrations of 0.2–5.8 mmol/L. According to the sorption kinetic tests, the isotherm tests were followed for 7 days to ensure equilibrium. Following the sorption isotherm tests, desorption isotherm tests were initiated by replacing the supernatant with the same volume of the soil-

amended water, and then re-equilibrating for another 7 d. The amount of soil-sorbed NB was calculated from the difference between the initial and final NB concentrations (**Eq. A-1**).

$$S_t = (C_0 - C_t)(V/m) \quad (\text{Eq. A-1})$$

where  $C_0$  and  $C_t$  (mmol/L) are the initial and final NB concentrations in the solution phase, respectively,  $V$  is the solution volume (L), and  $m$  is the soil mass (g).

To evaluate the mass balance of NB in water and soil phase, soil-sorbed NB was also extracted by ultrasonic extraction using 10 mL acetonitrile for 20 min (Wang et al. 2014). Upon centrifugation ( $1359 \times g$  force), the supernatant was collected. The extraction was conducted consecutively for three times, and the supernatant was merged and filtered using a 0.2  $\mu\text{m}$  syringe filter for NB analysis. Control tests indicated that NB recovery was >95% for all cases.

## 2.5. Degradation of soil-sorbed NB

NB was first loaded on the potting soil following the same procedure as in the sorption kinetic tests in the 43 ml vials at an initial solution NB concentration of 0.8 mmol/L. Upon equilibrium, 40 mL of the supernatant was replaced with the same volume of CMC-stabilized ZVI suspension with ZVI dosage varying from 0.1 to 0.9 g/L. The vials were then mixed at 50 rpm on a rotator at 22 °C for 7 d, and sampled in duplicate for NB concentration measurements. Based on the screening test results, further kinetic experiments were conducted at the ZVI dosage of 0.2 g/L. Control tests indicated no significant mass loss of NB due to other mechanisms such as biodegradation.

## 2.6. Analytical methods

Zeta potential and size of the ZVI nanoparticles were obtained through dynamic light scattering (DLS) measurement on a Malvern Nano-ZS Zetasizer (Malvern Instruments Ltd, UK), and the data was processed by the Malvern Zetasizer Software (Version 7.11) to yield volume-weighted particle size distributions. Solution viscosities were measured to correct their influence on the DLS measurements.

NB, nitrosobenzene, and aniline were determined by high-performance liquid chromatography (HPLC) (Hewlett-Packard) with a Hypersil BDS-C18 column at 40 °C and a UV detector. The mobile phase consisted of a mixture of acetonitrile and water (40:60 of v:v) and the flow rate was 1 mL/min, and the injection volume was 80 µL. The optimal wavelength was found to be 280 nm, which afforded NB and nitrosobenzene detection limit of 0.2 mg/L, aniline detection limit of 0.5 mg/L.

The degradation intermediates were identified by means of an Agilent gas chromatograph (7890A) coupled with a 5975C Series mass spectrometer (GC-MS). A HP-5MS 5% phenyl methyl siloxane capillary column was used. Sample injection (2 µL) was performed in the splitless mode at 250 °C. The oven temperature was ramped from 70 °C to 280 °C at 10 °C/min, and then kept constant at 280 °C for 6 min. The scan range was from 35 to 550 m/z (mass to charge ratio).

DOM concentration was quantified as TOC and analyzed by a TOC Analyzer (Tekmar Dohrmann Phoenix 8000, USA) with a detection limit of 0.2 mg/L.

### 3. Results and Discussion

#### 3.1. Reduction of aqueous NB

The effectiveness of ZVI nanoparticles for NB degradation in aqueous phase was tested in batch kinetic experiments. **Figure A-1** shows that the reduction of NB by CMC-stabilized ZVI nanoparticles proceeded through a very fast step, as >95% NB was removed within 5 min (**Figure A-1a**). Complete conversion of NB to aniline was achieved within 7 hours. In comparison, the non-stabilized ZVI material exhibited a much lower NB reduction rate, and 95% of NB removal was achieved at 180 min (**Figure A-1b**). More than 16 h were needed to completely convert NB to aniline. Nitrosobenzene was the most abundant intermediate, which reached a peak concentration during the initial stage (5 min for CMC-stabilized ZVI while 20 min for non-stabilized ZVI), then gradually decreased. The mass balance, which is the sum of HPLC detected NB, nitrosobenzene and aniline, was not 100% at the initial stage (5 min), then gradually reached full recovery, indicating the presents of unidentified intermediates in the system.

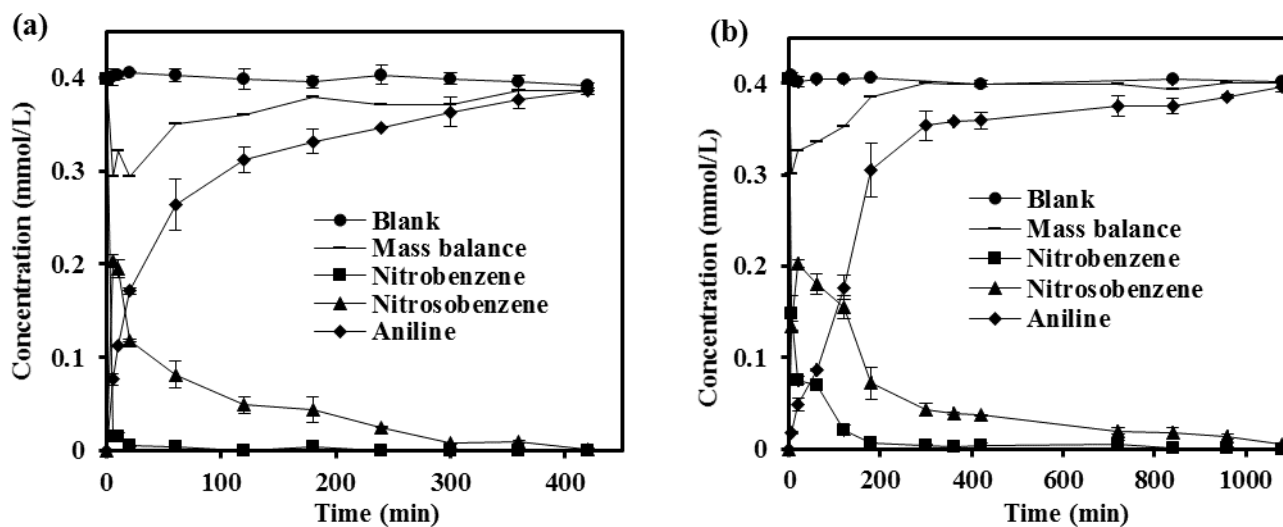


**Figure A-1.** NB reduction kinetics by CMC-stabilized ZVI nanoparticles (a), and non-stabilized ZVI (b). Experimental conditions: initial NB = 0.4 mmol/L, ZVI dosage = 0.05 g/L, pH = 8.1 ± 0.2, and temperature = 22 ± 0.5 °C.

Considering that the NB reduction by ZVI is a surface-mediated reaction, the degradation rate can be described by pseudo first-order reaction kinetic (**Eq. A-2**) (Bai et al. 2009, Scherer et al. 2001).

$$\frac{-dC_t}{dt} = k_{app}C_t \quad (\text{Eq. A-2})$$

where  $C_t$  is NB concentration (mmol/L) at time  $t$  (min),  $k_{app}$  is the pseudo first-order rate constant.

**Table A-2.** Apparent pseudo-first-order rate constants of NB reduction by ZVI nanoparticles under various experimental conditions.

Type of ZVI	$k_{app}$	$R^2$
Non-stabilized	0.175	0.912
CMC-stabilized	0.643	0.998

**Table A-2** lists the fitted parameters of the pseudo first-order kinetic model. The  $k_{app}$  for NB reduction by CMC-stabilized ZVI nanoparticles was  $0.643 \text{ min}^{-1}$ , which was ca. 3.7 times the value for non-stabilized ZVI ( $0.175 \text{ min}^{-1}$ ). The larger  $k_{app}$  of stabilized ZVI nanoparticles suggests that the CMC-stabilized ZVI nanoparticles exhibited higher reactivity. The  $k_{app}$  value of stabilized ZVI nanoparticles is much higher than the reported rate constant for ZVI nanoparticles. For instance, Bai et al. (2009) studied NB reduction using poly(vinyl alcohol) (PVA) microsphere immobilized ZVI nanoparticles at an Fe dosage of 200 mg/L and initial NB concentration of 1 mol/L. The resulting  $k_{app}$  values were determined in the range of  $0.0051$  to  $0.0072 \text{ min}^{-1}$ , which are ca. 100 times lower than in our study. Another study reported the reduction of NB ( $C_0 = 2.44 \text{ mmol/L}$ ) by an emulsified vegetable oil membrane coated with ZVI nanoparticles (3 690 mg/L as Fe) and obtained a  $k_{app}$  value of  $0.0942 \text{ min}^{-1}$  (Dong et al. 2015). It is noteworthy that the CMC-stabilized ZVI nanoparticles synthesized in our work exhibit approximately 7–90 times higher NB degradation rates ( $k_{app}$ ) as compared with the previously reported ZVI nanoparticles. The  $k_{app}$  is correlated to the iron loading or surface area (Sun et al. 2010). The non-stabilized nanoparticles tend to aggregate owing to their large surface energy, leading to a decrease of activated sites for

NB degradation. However, the CMC-stabilized ZVI nanoparticles exhibited much smaller particle sizes and were well dispersed in the solution, thus behaving in a much more reactive way.

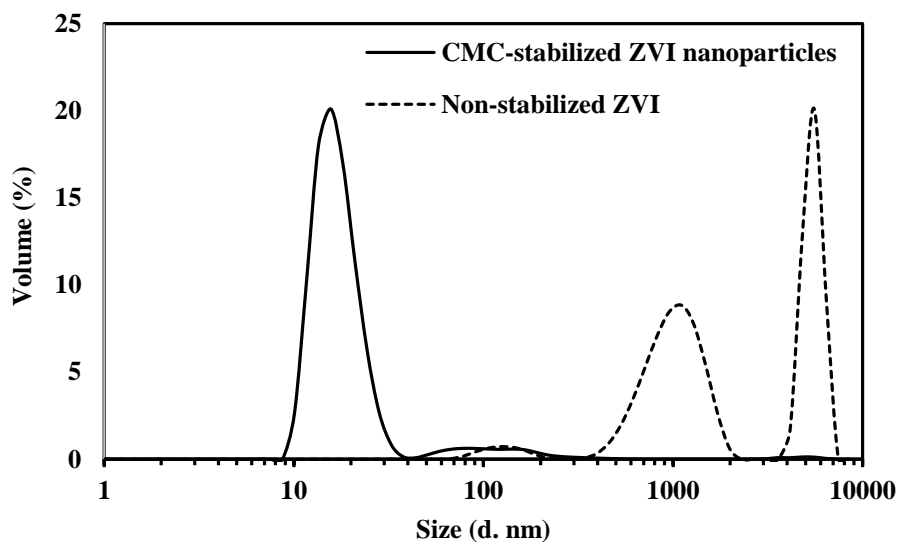


**Figure A-2.** Hydrodynamic size distribution (by volume) of CMC-stabilized ZVI nanoparticles and non-stabilized ZVI.

**Figure A-2** compares the hydrodynamic diameter (size) distribution of CMC-stabilized and non-stabilized ZVI nanoparticles. It can be seen that the volume distribution of stabilized ZVI nanoparticles consisted primarily (88.8%) of particles with diameter of 17 nm, followed by diameter around 85 nm (3.7%) and 190 nm (2.8%). However, the non-stabilized ZVI sample shows a primary large cluster with the diameter of 1857 nm (64.8%), followed by particle diameters of 4840 nm (31.4%) and 82.58 nm (3.7%). Therefore, the smaller average hydrodynamic diameter of the CMC-stabilized ZVI nanoparticles resulted in materials with a higher reactivity. It should be noted that the large particle size of non-stabilized ZVI is due to aggregation of nanoparticles, which

can be dispersed using external forces (e.g., sonication and shearing), and the hindered reactivity of non-stabilized ZVI may be due to limitations in the mass transfer events of such particles.

To clarify whether mass transfer is a rate limiting step for the NB reduction by ZVI nanoparticles, a test was conducted via enhancing the mixing of ZVI and NB suspension (by adding glass beads). **Figure A-3** shows the reduction of NB by CMC-stabilized and non-stabilized ZVI nanoparticles in the presence of glass beads at a reaction time of 60 min. The results show that glass beads dramatically improved the NB reduction efficiency from 77% to 99% by non-stabilized ZVI (**Figure A-3b**). Moreover, the formed aniline is 3 times compared to the case without glass beads. However, glass beads had no significant effect ( $p > 0.05$ ) on the NB reduction and nitrosobenzene formation for the stabilized ZVI nanoparticles. It is evident that the mass transfer is a rate limiting process for the NB degradation by non-stabilized ZVI, but not for CMC-stabilized ZVI nanoparticles. The results well agree with the measured ZVI particle size by DLS, where the CMC-stabilized ZVI nanoparticles show much smaller particle size than non-stabilized ZVI, and thus the larger surface area of stabilized ZVI makes the interface mass transfer be a negligible parameter for limiting the reaction rate. The mass transfer of ZVI is frequently reported as rate limiting factor for NB degradation, for example, the mass transport coefficient of the iron particle (e.g. diameter of 1.0 mm) is reported to be approximately 10 times slower than the first-order heterogeneous rate coefficient for surface reaction of NB reduction (Scherer et al. 2001). This is the first time that the mass transfer is found as a negligible parameter for the iron materials on NB reduction.



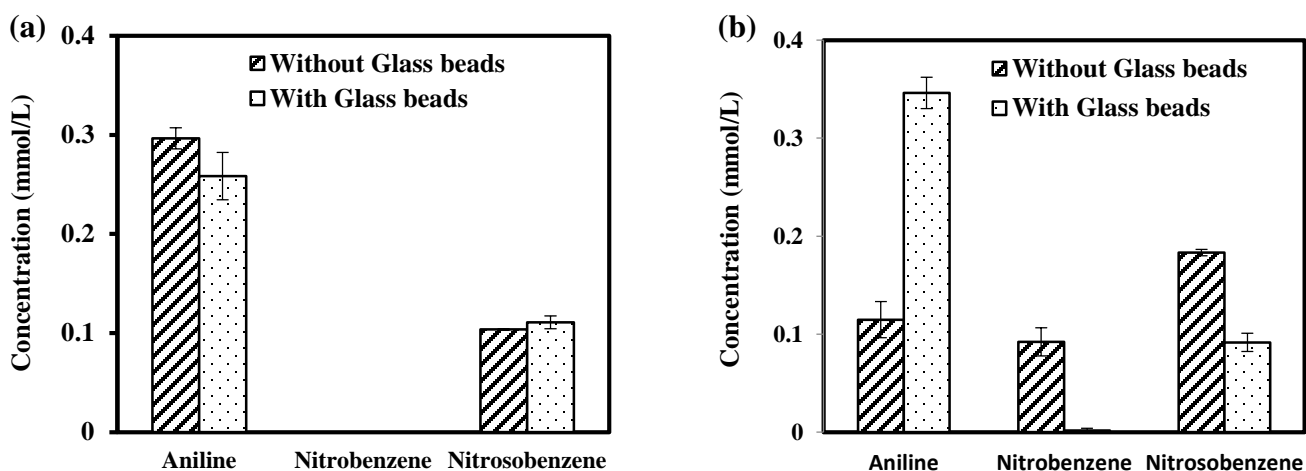


**Figure A-3.** NB reduction by CMC-stabilized ZVI nanoparticles (a) and non-stabilized ZVI (b) in the presence of glass beads. Experimental conditions: initial NB concentration = 0.4 mmol/L, ZVI dosage = 0.05 g/L, pH =  $8.1 \pm 0.2$ , and temperature =  $22 \pm 0.5$  °C, reaction time = 60 min.

To identify the intermediates and pathway of NB reduction by CMC-stabilized ZVI particles, samples at different reaction times were selected and analyzed by GC/MS. **Table A-3** and **Figure A-4** present the retention time and  $m/z$  values of the detected intermediates. Nitrosobenzene, phenylhydroxylamine, and azobenzene are identified as major intermediates in the NB reduction process, and aniline is determined to be the final degradation product. The unrecovered mass in **Figure A-1** can be, or partially, due to the formation of phenylhydroxylamine and azobenzene which are not detectable by HPLC. The intermediates formed during the NB reduction by CMC-stabilized and non-stabilized ZVI are the same, indicating that the CMC-stabilized ZVI nanoparticles only accelerated the degradation kinetics without changing the degradation mechanism.

**Table A-3.** Identified intermediates and products during NB reduction process by ZVI nanoparticles.

Name	Retention time (min)	<i>m/z</i>
Nitrosobenzene	3.410	77, 107, 51
Aniline	4.093	93, 66, 52
NB	5.534	77, 123, 51
Phenylhydroxylamine	6.534	93, 65, 109
Azobenzene	14.680	77, 182, 105

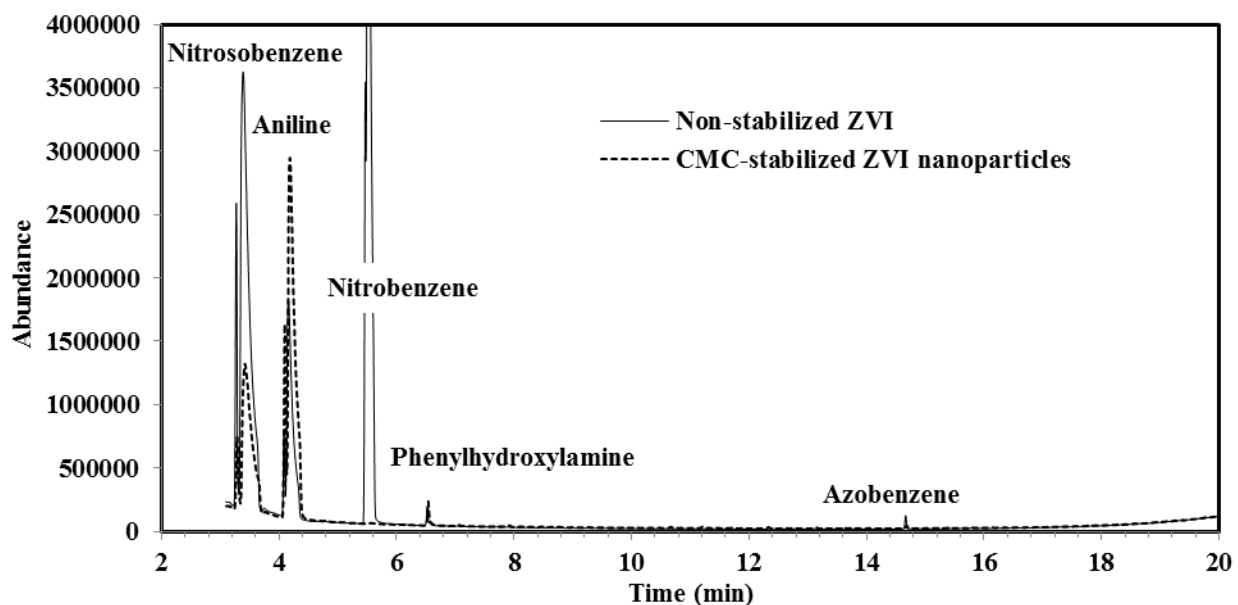


**Figure A-4.** GC spectra of the reductive products of NB by CMC-stabilized ZVI nanoparticles and non-stabilized ZVI. Experimental conditions: initial NB concentration = 0.4 mmol/L, ZVI dosage = 0.05 g/L, pH = 8.1 ± 0.2, and temperature = 22 ± 0.5 °C, reaction time = 30 min.

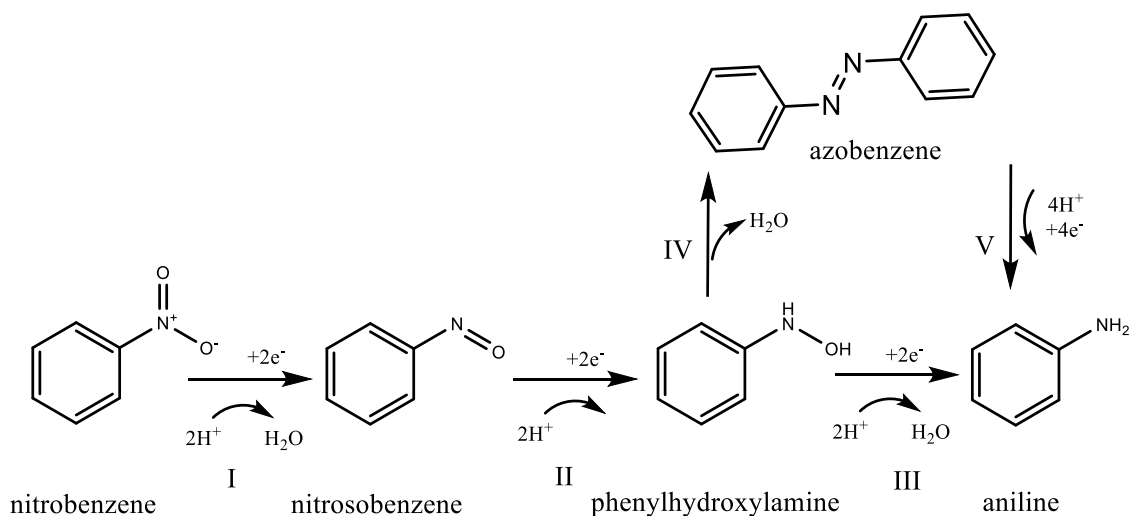


**Figure A-5.** Proposed reduction pathway of NB by ZVI nanoparticles.

The NB reduction pathway by ZVI nanoparticles is proposed in **Figure A-5**. The reaction I–III were the dominant pathway (Agrawal and Tratnyek 1996, Mu et al. 2004), in which each consists of a two electron addition. The condensation reaction (IV) for the formation of azobenzene and further to aniline (reaction V) occur in parallel with reaction III.

The phenylhydroxylamine that was detected in this study, is a rarely reported intermediate during the NB reduction process using iron metal (powder) (1996, Lee et al. 2015, Mu et al. 2004), which may due to the slow kinetics of reaction II or a fast reaction III. The reduction potentials ( $E_m$ ) of NB and aniline are -0.485 and 1.030 V (Heijman et al. 1995, Wardman 1989), and the standard Gibbs free energy ( $\Delta_f G^\circ$ ) of NB, nitrosobenzene, phenylhydroxylamine, aniline, and water are 146.2, 201.3, 303.33, 149.1 and -237.1 kJ/mol respectively (Choo et al. 1975, MetaCyc 2015, Stevens et al. 2010). The standard redox potential change ( $\Delta_r G^\circ$ ) for the reactions in **Figure**

**A-5** were calculated based on Gibbs free energy (**Eq. A-3**), then the redox potentials ( $E$ ) were calculated based on Nernst equation (**Eq. A-4**) at the experimental pH (Wardman 1989).

$$\Delta_r G^\circ = - n F E^\circ \quad (\text{Eq. A-3})$$

where  $n$  is number of electrons involved in the reaction; and  $F$  is the Faraday number (96485 C/mol).

$$E = E^\circ - RT/(nF) \times \ln Q \quad (\text{Eq. A-4})$$

where  $R$  is gas constant (8.314 J/(mol K)),  $T$  is absolute temperature (K),  $Q$  is the reaction quotient. The experimental pH is ca. 8 in the reaction, so  $[H^+]$  is assumed to be  $10^{-8}$  M.

The changes of redox potential were calculated as 0.47 V for reduction of NB to nitrosobenzene (Reaction I), -1.00 V for nitrosobenzene to phenylhydroxylamine (Reaction II), and 1.54 V for phenylhydroxylamine to aniline (Reaction III). Therefore, the reduction of nitrosobenzene to phenylhydroxylamine is unfavorable. However, the increase of nitrosobenzene concentration decreases the  $Q$  value of the Reaction II, which results in the increase of  $E$  value and makes the reaction be possible but still at relatively low rates.

The theoretical reactivity of each step agree well with the nitrosobenzene conversion and aniline formation rates in our experiments (**Figure A-1**), which explains the accumulation of nitrosobenzene during the early stage of reaction (**Figure A-1**). The GC/MS peak in **Figure A-4** showed that the phenylhydroxylamine concentration is much lower than nitrosobenzene,

supporting the idea that the rate-limiting step of the NB reduction is the conversion of nitrosobenzene to phenylhydroxylamine (Reaction II).

**Figure A-4** shows that the complete reduction of NB to aniline needs 6 electrons. In our experiments, 0.05 g/L ZVI nanoparticles were capable to completely reduce the NB (initial concentration = 0.4 mmol/L) to aniline, indicating that nearly 90% of the electrons donated by iron were used in the NB reduction process. The high electron transfer efficiency, high reactivity and quick kinetic make the CMC-stabilized ZVI a promising material for environmental application

### 3.2. Effects of DOM and pH on NB reduction

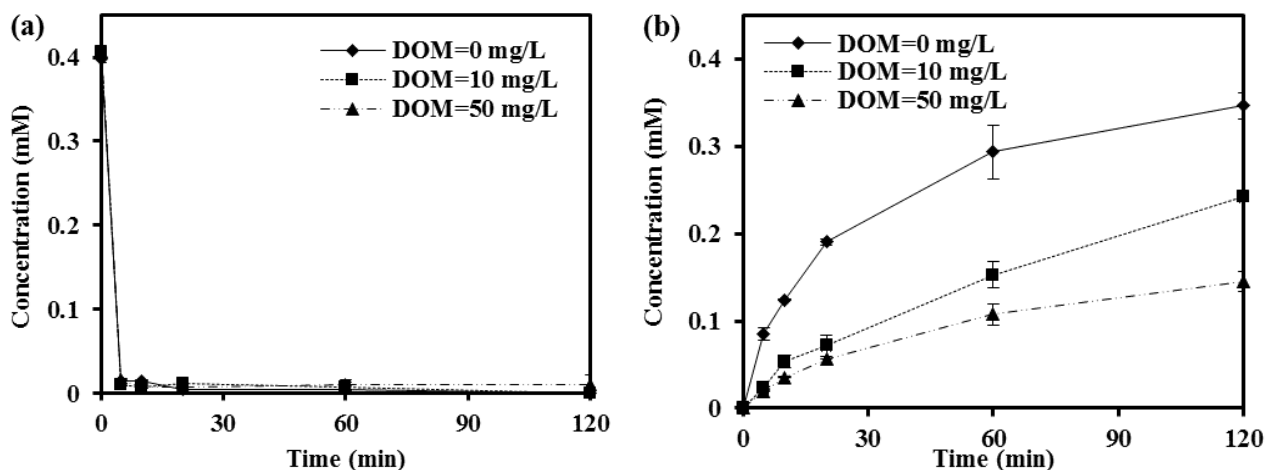


**Figure A-6.** Effect of DOM on NB reduction (a) and aniline production (b) by CMC-stabilized ZVI nanoparticles. Experimental conditions: initial NB = 0.4 mmol/L, ZVI dosage = 0.05 g/L, pH =  $8.1 \pm 0.2$ , and temperature =  $22 \pm 0.5$  °C.

**Figure A-6** shows kinetic data of the NB reduction and aniline formation in the presence of 0, 10 and 50 mg/L DOM (as TOC). The NB reduction reached >95% completion within 5 min regardless of DOM, but the formation of aniline was retarded by DOM. The results indicate that the DOM could compete with reaction intermediates for electron, thus decrease the reaction rate. **Figure A-7** compares the NB and intermediates concentrations in the suspension after 30 min reaction with DOM (ranging from 0 to 100 mg/L). Increasing DOM concentration did not significantly change the NB removal efficiency, though decreased the formed aniline concentration. Moreover, more nitrosobenzene was accumulated in the suspension with higher DOM concentration.

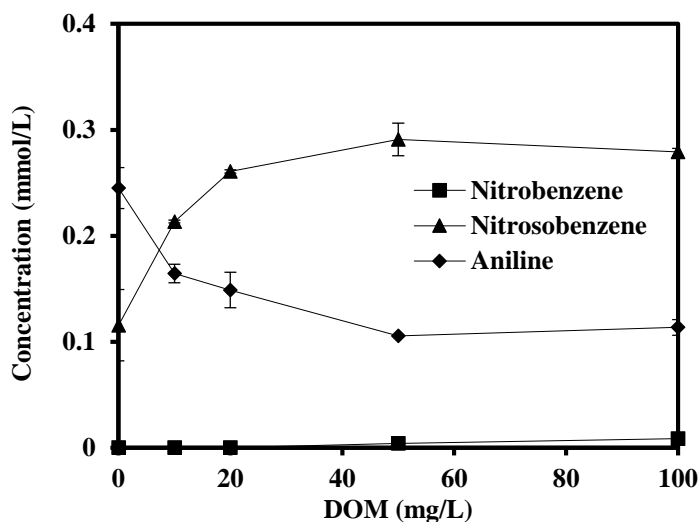


**Figure A-7.** NB degradation by CMC-stabilized ZVI nanoparticles at various DOM concentrations at the reaction time of 30 min.

The inhibition effect of DOM on the reduction of NB by CMC-stabilized ZVI nanoparticles can be due to: 1) destabilizing of CMC-stabilized ZVI. Humic acid and fulvic acid, as main

components in DOM, are likely to chelate with the iron oxides shell of the ZVI (Giasuddin et al. 2007), which compete with CMC molecules on the ZVI nanoparticles surface and decrease the stabilizing effectiveness of CMC, resulting in elevated particle agglomeration. A previous study showed that the presence of soil organic matter (SOM) changed the zeta potential of CMC-stabilized ZVI nanoparticles from -160 mV to -111 mV, which resulted in the increase of ZVI particle size (Zhang et al. 2011). 2) Binding of DOM molecules to the surface of ZVI nanoparticles would hinder both the mass transfer of NB and electron transfer, resulting in a lower reaction rate. Studies revealed that the ZVI nanoparticles were stabilized by concurrent steric exclusion and electrostatic repulsion in the presence of CMC (He and Zhao 2007, He et al. 2007). Also, the sorbed CMC on the iron surface was loosely structured due to the large CMC molecular structure (M.W. = 90 000). This structure is favorable for the transfer of NB to the ZVI nanoparticles surface. Upon adsorption of low molecular weight DOM, the loose ZVI surface structure becomes tight, which slowed down mass transfer and inhibited the reaction. 3) DOM may compete with NB for the reactive sites of ZVI nanoparticles.

**Figure A-8** shows the effect of pH on the reduction of NB by CMC-stabilized ZVI nanoparticles, as well as the formed nitrosobenzene and aniline concentration at reaction time of 30 min. It is demonstrated that high pH is favorable for the NB reduction and aniline formation. For instance, at acidic condition (pH 4), the NB removal efficiency was only 4%, with low formed nitrosobenzene concentration (0.017 mmol/L) and no aniline. Increasing pH promoted the reductive degradation of NB, and >99% of NB could be removed within 30 min at  $\text{pH} \geq 8$ . In addition, it is noteworthy that the formed aniline increased from 0.14 to 0.36 mmol/L when pH

increased from 8 to 11, though there was no difference for NB removal. The low NB reduction efficiency at lower pH can be primarily due to the corrosion of iron at acidic condition (Giasuddin et al. 2007), which left limited irons for NB reduction. The rapid dissolving of CMC-stabilized ZVI nanoparticles was observed in the solution at  $\text{pH} \leq 5$  (the visible ZVI particles disappeared within 10 min), and faster dissolving rate at lower pH. The iron was probably consumed by reacting with  $\text{H}_2\text{O}$  for  $\text{H}_2$  production (Liu and Lowry 2006). Secondly, NB shows partial negative atomic charge because of the nitro group's electron-withdrawing property (Yan and Bailey 2001), which makes it easy to be attacked by positively charged  $\text{Fe}^{2+}$ . The reduction potential of  $\text{Fe}^{2+}$  is highly dependent on the solution pH, the  $\text{Fe}^{2+}$  forms  $\text{FeOH}^+$  at high pH and which behave high NB reduction rate (Huang and Zhang 2006). Huang et al. (2006) found that no reduction of  $\text{Fe}^{2+}$  by NB occurred at pH of 5 and 6, but exhibited high rate at pH of 7.5 and 9. Thirdly, the formed aniline is a well-known corrosion inhibitor (Hung et al. 2000). At low pH, the protonation of the formed aniline ( $\text{p}K_a = 4.6$ ) prevented its desorption from iron surface (Mantha et al. 2001), which may retard the mass transfer.



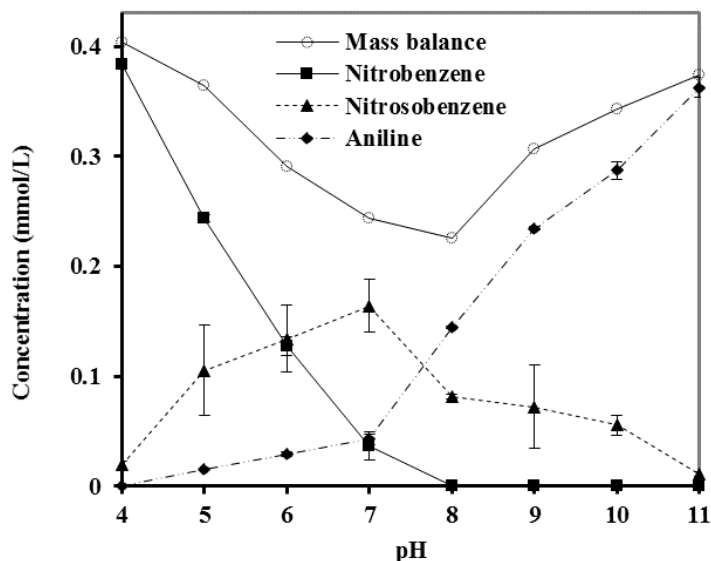


**Figure A-8.** Effect of pH on NB reduction by CMC-stabilized ZVI nanoparticles. Experimental conditions: initial NB = 0.4 mmol/L, ZVI dosage = 0.05 g/L, and temperature =  $22 \pm 0.5$  °C.

The effect of pH on NB reduction by CMC-stabilized ZVI nanoparticles is greatly different from that by bulk iron particles (Dong et al. 2010, Mu et al. 2004). Both Dong et al. (2010) and Mu et al. (2004) found the NB reduction and aniline production rates dropped with increasing pH when ZVI grains were used. For the bulk ZVI grains, the low pH increased the reduction potential of the reaction ( $\text{Fe}^0 - 2\text{e}^- \rightarrow \text{Fe}^{2+}$ ), and accelerates the corrosion of ZVI, which favors the reduction of NB. However, high pH slows down the corrosion of iron, but favors the formation of iron hydroxide precipitates on the iron surface, which inhibit the electron transfer from  $\text{Fe}^0$  to the contaminants. Therefore, the ZVI with different particle sizes can exhibit different physiochemical properties at various environmental conditions. The effects of the environmental factors on reaction should be clearly studied before the field application of different types of ZVI materials.

### 3.3. Sorption and desorption of NB by soils

The NB sorption and desorption kinetic tests showed that the sorption on the potting soil phase reached equilibrium within 6 h, but the desorption process was slower, which reached equilibrium at 12 h.

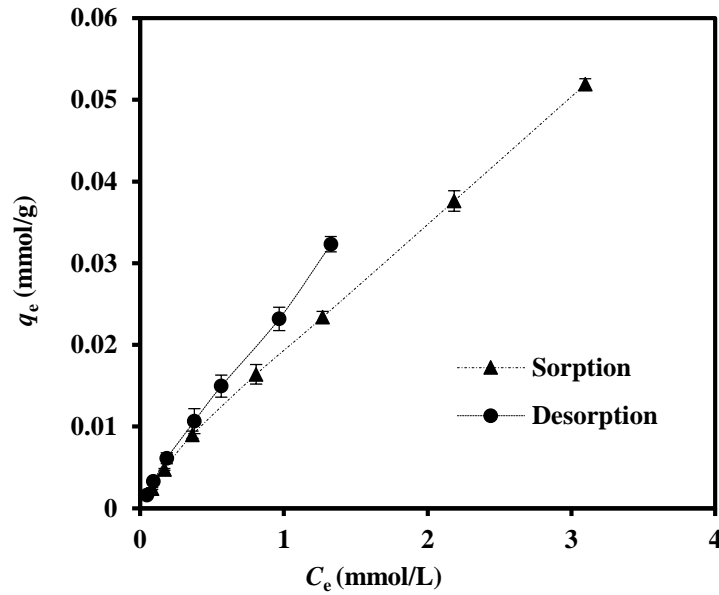


**Figure A-9.** NB sorption and desorption isotherm on the potting soil. Experimental conditions: soil to water ratio = 2 g: 41.5 mL, temperature = 22 °C, pH = 6.4 ± 0.2.

**Figure A-9** shows the NB sorption and desorption isotherms on the potting soil. The Freundlich (**Eq. A-5**) and dual-mode isotherm model (**Eq. A-6**) are applied to interpret the adsorption isotherm data (Qin et al. 2007, Zhao et al. 2001):

$$\text{Freundlich model: } q_e = K_F C_e^{1/n} \quad (\text{Eq. A-5})$$

where  $q_e$  is the uptake of NB at equilibrium (mmol/g),  $C_e$  is the equilibrium aqueous NB concentration (mmol/L),  $K_F$  is Freundlich capacity coefficient constant ((mmol/g)(L/mmol)<sup>1/n</sup>), and  $n$  is the Freundlich exponent which reflecting the nonlinearity of the sorption isotherm.

$$\text{Dual-mode model: } q_e = K_D C_e + \frac{Q K_L C_e}{1 + K_L C_e} \quad (\text{Eq. A-6})$$

where  $K_D$  is the lumped partition coefficient between aqueous phase and the dissolution domains of rubbery and glassy solid (L/g),  $K_L$  and  $Q$  are the Langmuir affinity (L/mmol) and capacity coefficients (mmol/g) for hole-filling domain. The holes are suggested to be semipermanent, and hydrophobic cavities of subnanometer scale may exist within the folds of individual macromolecules, between macromolecules, or between the organic phase and a mineral surface (Zhao et al. 2001).

**Table A-4.** Parameters of isotherms models for NB adsorption onto the potting soil.

Freundlich model			Dual-mode model			
$K_F$	$1/n$	$R^2$	$K_D$ (L/g)	$Q_0$	$K_L$	$R^2$
(mmol/g(L/mmol) <sup>1/n</sup> )				(mmol/g)	(L/mmol)	
0.0196	0.8536	0.98	0.0152	0.0051	4.496	1.00

**Table A-4** lists the fitted parameters for the two sorption isotherm models. Both of the two models can adequately describe the adsorption, with high  $R^2$  value of 0.98 for Freundlich model, and 1.00 for dual-mode model. Freundlich model is an empirical equation assuming an exponential site energy distribution (Kah et al. 2011), which is often used for adsorption isotherm with greater

complexity. The dual-mode model assumes the rubbery state sorbs by a solid phase dissolution mechanism and the glassy state sorbs by concurrent dissolution and hole-filling mechanisms. It combines linear partitioning and Langmuir modes sorption, thus can well describe the nonideal sorbent behavior of SOM to its existence in rubbery and glassy states (Vieth and Sladek 1965, Zhao et al. 2001). In **Figure A-9**, the adsorption (on surface) dominated the process at low NB concentration, while at higher NB concentration, the NB molecules in the hole of soil with reduced mobility and retarded diffusion through the solid, which lowered the sorption capacity and the distribution process dominated. Therefore, the adsorption capacity increased linearly with the NB concentration at the higher equilibrium NB concentration (e.g. >1 mmol/L). The octanol/water partition coefficient ( $\log K_{ow}$ ) of NB is 1.85, which indicates that NB behaves moderate adsorption potential in soils, so NB is relatively mobile in soil. **Figure A-9** showed relatively high NB adsorbability of potting soil, which was due to the high organic matter content (27%) of the potting soil. Zhao et al. (2003) studied the sorption behaviors of NB on the H<sub>2</sub>O<sub>2</sub> treated marine sediments, and found the adsorption isotherm can be well fitted by Langmuir isotherm ( $R^2 = 0.90-0.99$ ), but the untreated sediment showed linearly adsorption isotherm ( $R^2 = 0.91-0.96$ ). It indicated that the NB partitioning process to SOM is dominant in the non-treated sediment.

Significant NB sorption-desorption hysteresis on the soil was observed in **Figure A-9**, which can be related to sorbate-sorbent interactions and the structural properties of sorbent. On one hand, the NB concentration gradient promotes deep NB penetration into the particle micropores, which can deform the micropores and lower the amount of desorbed NB (Oren and Chefetz 2005). On the other hand, sorption-desorption hysteresis may be due to non-Fickian diffusion of sorbed NB

within condensed glassy SOM domains. The aqueous phase NB concentration decreased abruptly in the early desorption stage, then the desorption rate become slower and potentially show apparent rate-related desorption hysteresis over long observation term (Huang and Weber 1997). The hysteresis makes the solute less mobile in soil phase, thus it is unfavorable for the reduction of soil-sorbed NB by ZVI nanoparticles.

### **3.4. Reduction of soil-sorbed NB by CMC-stabilized ZVI nanoparticles**

**Figure A-10** compares kinetics of NB desorption without ZVI and soil-leached NB with 0.2 g/L CMC-stabilized ZVI nanoparticles. The potting soil exhibited a rapid desorption rate in the initial 20 min, followed by a slow desorption rate and reached equilibrium within 24 h. About 33% of pre-loaded NB was desorbed into aqueous phase, with a concentration of 0.18 mg/L at equilibrium. The CMC-stabilized ZVI nanoparticles dramatically eliminated the released NB concentration in aqueous phase (to 0.019 mmol/L). The soil extraction experiment showed that 81% of total pre-loaded NB was removed by CMC-stabilized ZVI nanoparticles. The removal of pre-loaded NB can be due to the reduction of both soil-sorbed NB and desorbed NB in aqueous phase by ZVI. The NB in the aqueous phase is more vulnerable to ZVI reduction, and the removal of NB in aqueous phase further enhanced the desorption of NB from soil.

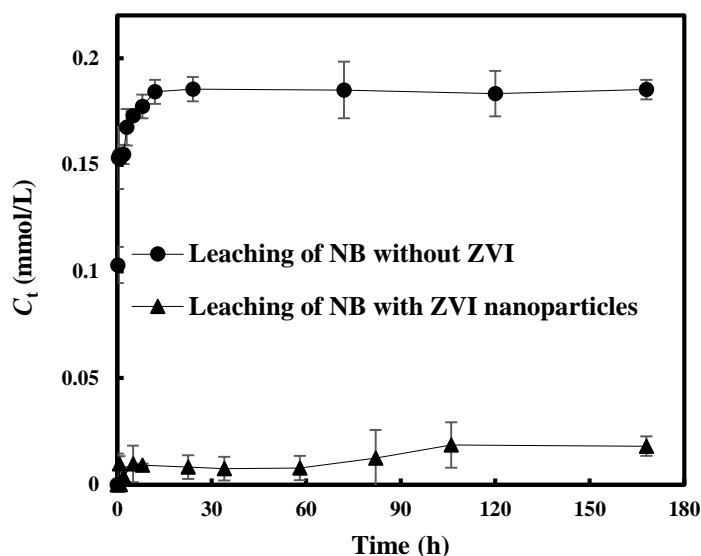


**Figure A-10.** Aqueous phase NB concentration during desorption/reduction process of pre-sorbed NB in the potting soil. Experimental conditions: soil to water ratio = 2 g: 41.5 mL, initial sorbed NB on soil = 0.01 mmol/g, CMC-stabilized ZVI nanoparticles dosage = 0.2 g/L as Fe, temperature = 22 °C, pH = 6.4 ± 0.2.

The reduction of soil-sorbed NB at various CMC-stabilized ZVI nanoparticles dosages were tested by measuring the concentration of leached NB into the aqueous phase after a reaction time of 7 d. **Figure A-11** shows that the leached NB was decreased by 98% and 99% at the ZVI dosage of 0.1 and 0.2 g/L, respectively, compared with the batch without ZVI. Further increasing ZVI dosage to 0.4, 0.6 and 0.9 g/L could completely remove the leached NB in the aqueous phase. The NB in the soil phase was determined as low as 0.06 μmol/g at a ZVI dosage of 0.4 g/L, or undetectable at higher ZVI dosages.

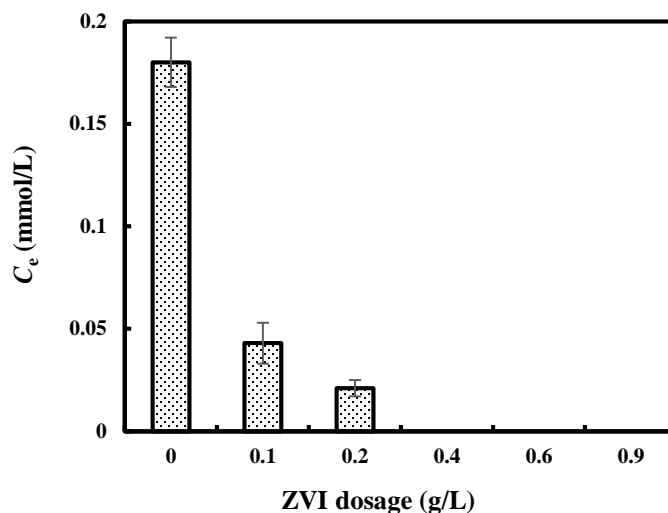


**Figure A-11.** Leaching of pre-sorbed NB from the potting soil in the presence of CMC-stabilized ZVI nanoparticles of various dosages. Experimental conditions: soil to liquid ratio = 2 g: 41.5 mL, temperature = 22 °C, pH = 6.4 ± 0.5, reaction time = 7 d.

Comparing with the completely NB reduction in aqueous phase, the reduction rate and extent in soil phase was strongly suppressed. In aqueous phase, both the released SOM from soil and the relatively low solution pH inhibited the reduction power of stabilized ZVI nanoparticles (**Figure A-7 and A-8**). The inhibition effect of SOM in soil could be much more prominent. The mass transfer of NB in soil phase is much slower than in aqueous phase, which greatly limited the NB reduction. Meanwhile, the soil exhibits strong uptake capacity for the CMC-stabilized ZVI nanoparticles (Zhang et al. 2011), which retard the transfer of ZVI in soil phase.

Nevertheless, the CMC-stabilized ZVI nanoparticles still showed high efficiency for NB reduction in soil. Meanwhile, according to stoichiometric calculation, less than 7 times of the required iron (as electron donor) was applied to reduce NB, which completely avoided the NB leaching into the aqueous phase. These results indicate that the CMC-stabilized ZVI nanoparticles are potentially useful for treating soil-sorbed NB.

#### 4. Conclusions

This study investigated the feasibility and efficiency of CMC-stabilized ZVI nanoparticles for NB reduction in aqueous and soil phase, and the primary findings and conclusions are summarized as bellow:

- (1) Stabilized ZVI nanoparticles showed high efficiency for NB reduction. The NB reduction rate constant ( $k_{app}$ ) derived by pseudo first-order reaction kinetic model was  $0.643 \text{ min}^{-1}$ , which was 3.7 times the value for non-stabilized ZVI, and ca. 7–90 times faster than the reduction previously reported for ZVI nanoparticles. According to the stoichiometry, nearly 90% of the electrons donated by iron were used for the NB reduction.
- (2) A rarely detected intermediate (phenylhydroxylamine) was identified during the NB reductive degradation process. The primary rate-limiting step for NB reduction is the conversion of nitrosobenzene to phenylhydroxylamine.
- (3) The presence of DOM decreased the NB reduction rate due to inhibition of the mass transfer of NB to the surface of the ZVI nanoparticles and reaction with target NB. Higher pH (>8) is favorable for the NB reduction because more  $\text{Fe}(\text{OH})^+$  is formed.



- (4) Sorption isotherm of NB by the tested potting soil is well described by a dual-mode model ( $R^2 = 1$ ), suggesting that sorption of NB in soil are due to both solid phase dissolution and hole-filling mechanisms. Desorption of NB shows significant hysteresis because part of NB is strongly bonded to the sorption sites of soil, indicating less favorable reduction of soil-sorbed NB by ZVI nanoparticles.
- (5) The CMC-stabilized ZVI nanoparticles can rapidly reduce the soil-sorbed NB (reduction rate was higher than desorption rate from soil), and exhibit a reduction efficiency (only 7 times of ZVI (as electron donor) are needed to completely avoid NB leaching).

The findings in this work provide compelling evidence that the CMC-stabilized ZVI nanoparticles may be used for *in situ* reductive remediation of NB polluted soil or groundwater.

## References

- Abdel-Shafi, A.A. and Wilkinson, F. (2000) Charge transfer effects on the efficiency of singlet oxygen production following oxygen quenching of excited singlet and triplet states of aromatic hydrocarbons in acetonitrile. *Journal of Physical Chemistry A* 104(24), 5747-5757.
- Abdelwahab, O., Amin, N. and El-Ashtoukhy, E.Z. (2009) Electrochemical removal of phenol from oil refinery wastewater. *Journal of Hazardous Materials* 163(2), 711-716.
- Adamson, A.W. (2001) The physical chemistry of surfaces. Abstracts of Papers of the American Chemical Society 221, U320-U320.
- Afzal, S., Daoud, W.A. and Langford, S.J. (2013) Photostable self-cleaning cotton by a Copper(II) porphyrin/TiO<sub>2</sub> visible-light photocatalytic system. *ACS Applied Materials & Interfaces* 5(11), 4753-4759.
- Agrawal, A. and Tratnyek, P.G. (1996) Reduction of nitro aromatic compounds by zero-valent iron metal. *Environmental Science & Technology* 30(1), 153-160.
- Ahmadun, F.R., Pendashteh, A., Abdullah, L.C., Biak, D.R.A., Madaeni, S.S. and Abidin, Z.Z. (2009) Review of technologies for oil and gas produced water treatment. *Journal of Hazardous Materials* 170(2-3), 530-551.
- Ahn, C.K., Woo, S.H. and Park, J.M. (2010) Selective adsorption of phenanthrene in nonionic–anionic surfactant mixtures using activated carbon. *Chemical Engineering Journal* 158(2), 115-119.

- Al-Ekabi, H. and Serpone, N. (1988) Kinetics studies in heterogeneous photocatalysis. I. Photocatalytic degradation of chlorinated phenols in aerated aqueous solutions over titania supported on a glass matrix. *The Journal of Physical Chemistry* 92(20), 5726-5731.
- Allan, S.E., Smith, B.W. and Anderson, K.A. (2012) Impact of the Deepwater Horizon oil spill on bioavailable polycyclic aromatic hydrocarbons in Gulf of Mexico coastal waters. *Environmental Science & Technology* 46(4), 2033-2039.
- Andrews, S.S., Caron, S., Zafiriou, O.C., (2000) Photochemical oxygen consumption in marine waters: A major sink for colored dissolved organic matter? *Limnol Oceanogr* 45, 267-277.
- Almeda, R., Bona, S., Foster, C.R. and Burskey, E.J. (2014) Dispersant Corexit 9500A and chemically dispersed crude oil decreases the growth rates of meroplanktonic barnacle nauplii (*Amphibalanus improvisus*) and tornaria larvae (*Schizocardium* sp.). *Marine Environmental Research* 99, 212-217.
- An, Y.J. (2001) Photochemical treatment of a mixed PAH/Surfactant solution for surfactant recovery and reuse. *Environmental Progress* 20(4), 240-246.
- Anderson, J.A. (2011) Assessment of the toxicity of oil spill dispersant Corexit 9500 on Juvenile and Larval blue crabs, *Callinectes sapidus*. *Journal of Shellfish Research* 30(2), 482-482.
- Anpo, M. and Takeuchi, M. (2003) The design and development of highly reactive titanium oxide photocatalysts operating under visible light irradiation. *Journal of Catalysis* 216(1-2), 505-516.
- Antony, R.P., Mathews, T., Ramesh, C., Murugesan, N., Dasgupta, A., Dhara, S., Dash, S. and Tyagi, A.K. (2012) Efficient photocatalytic hydrogen generation by Pt modified TiO<sub>2</sub> nanotubes fabricated by rapid breakdown anodization. *International Journal of Hydrogen Energy* 37(10), 8268-8276.

- Apergis, N. and Payne, J.E. (2010) Structural breaks and petroleum consumption in US states: are shocks transitory or permanent? *Energy Policy* 38(10), 6375-6378.
- Arslan-Alaton, I. and Ferry, J.L. (2002)  $\text{H}_4\text{SiW}_{12}\text{O}_{40}$ -catalyzed oxidation of nitrobenzene in supercritical water: kinetic and mechanistic aspects. *Applied Catalysis B: Environmental* 38(4), 283-293.
- Asatekin, A. and Mayes, A.M. (2009) Oil industry wastewater treatment with fouling resistant membranes containing amphiphilic comb copolymers. *Environmental Science & Technology* 43(12), 4487-4492.
- Aumann, E., Hildemann, L.M. and Tabazadeh, A. (2010) Measuring and modeling the composition and temperature-dependence of surface tension for organic solutions. *Atmospheric Environment* 44(3), 329-337.
- Bai, X., Ye, Z.F., Qu, Y.Z., Li, Y.F. and Wang, Z.Y. (2009) Immobilization of nanoscale Fe-0 in and on PVA microspheres for nitrobenzene reduction. *Journal of Hazardous Materials* 172(2-3), 1357-1364.
- Bandara, U.C., Yapa, P.D. and Xie, H. (2011) Fate and transport of oil in sediment laden marine waters. *Journal of Hydro-Environment Research* 5(3), 145-156.
- Barbetta, A. and Cameron, N.R. (2004) Morphology and surface area of emulsion-derived (PolyHIPE) solid foams prepared with oil-phase soluble porogenic solvents: Span 80 as surfactant. *Macromolecules* 37(9), 3188-3201.
- Batchu, S.R., Ramirez, C.E. and Gardinali, P.R. (2014) Stability of dioctyl sulfosuccinate (DOSS) towards hydrolysis and photodegradation under simulated solar conditions. *Science of the Total Environment* 481(0), 260-265.

- Bavykin, D.V., Friedrich, J.M. and Walsh, F.C. (2006) Protonated titanates and TiO<sub>2</sub> nanostructured materials: synthesis, properties, and applications. *Advanced Materials* 18(21), 2807-2824.
- Bennett, P., He, F., Zhao, D.Y., Aiken, B. and Feldman, L. (2010) In situ testing of metallic iron nanoparticle mobility and reactivity in a shallow granular aquifer. *Journal of Contaminant Hydrology* 116(1-4), 35-46.
- Board, M. and Board, O.S. (2003) *Oil in the sea III: inputs, fates, and effects*, national academies Press.
- Bouloubassi, I., Mejanelle, L., Pete, R., Fillaux, J., Lorre, A. and Point, V. (2006) PAH transport by sinking particles in the open Mediterranean Sea: a 1 year sediment trap study. *Marine Pollution Bulletin* 52(5), 560-571.
- Bouyoucos, G.J. (1962) Hydrometer method improved for making particle size analyses of soils. *Agronomy Journal* 54(5), 464-465.
- Bragg, J.R., Prince, R.C., Harner, E.J. and Atlas, R.M. (1994) Effectiveness of bioremediation for the Exxon-Valdez oil-spill. *Nature* 368(6470), 413-418.
- Brandt, C.A., Becker, J.M. and Porta, A. (2002) Distribution of polycyclic aromatic hydrocarbons in soils and terrestrial biota after a spill of crude oil in Trecate, Italy. *Environmental Toxicology and Chemistry* 21(8), 1638-1643.
- Braun, A.M., Maurette, M.-T. and Oliveros, E. (1991) *Photochemical technology*, John Wiley & Son Ltd.

- Bruheim, P., Bredholt, H. and Eimhjellen, K. (1999) Effects of surfactant mixtures, including Corexit 9527, on bacterial oxidation of acetate and alkanes in crude oil. *Applied and Environmental Microbiology* 65(4), 1658-1661.
- Burgeth, G. and Kisch, H. (2002) Photocatalytic and photoelectrochemical properties of titania-chloroplatinate(IV). *Coordination Chemistry Reviews* 230(1-2), 41-47.
- Cai, J.M., Zhu, Y.M., Liu, D.S., Meng, M., Hu, Z.P. and Jiang, Z. (2015) Synergistic effect of titanate-anatase heterostructure and hydrogenation-induced surface disorder on photocatalytic water splitting. *ACS Catalysis* 5(3), 1708-1716.
- Carls, M.G., Rice, S.D. and Hose, J.E. (1999) Sensitivity of fish embryos to weathered crude oil: part I. Low-level exposure during incubation causes malformations, genetic damage, and mortality in larval Pacific herring (*Clupea pallasii*). *Environmental Toxicology and Chemistry* 18(3), 481-493.
- Chen, H.W., Ku, Y. and Kuo, Y.L. (2007) Effect Of Pt/TiO<sub>2</sub> characteristics on temporal behavior of o-cresol decomposition by visible light-induced photocatalysis. *Water Research* 41(10), 2069-2078.
- Chen, J.W., Xiu, Z.M., Lowry, G.V. and Alvarez, P.J.J. (2011) Effect of natural organic matter on toxicity and reactivity of nano-scale zero-valent iron. *Water Research* 45(5), 1995-2001.
- Chen, Q., Zhou, W., Du, G. and Peng, L.-M. (2002) Trititanate nanotubes made via a single alkali treatment. *Advanced Materials* 14(17), 1208-1211.
- Choo, K.Y., Golden, D.M. and Benson, S.W. (1975) Very-low-pressure pyrolysis of nitroso-and pentafluoronitrosobenzene C-NO bond dissociation energies. *International Journal of Chemical Kinetics* 7(5), 713-724.

- Christiansen, A., Backensfeld, T., Kuhn, S. and Weitschies, W. (2011) Stability of the non-ionic surfactant polysorbate 80 investigated by HPLC-MS and charged aerosol detector. *Pharmazie* 66(9), 666-671.
- Chu, W. and Kwan, C.Y. (2002) The direct and indirect photolysis of 4,4'-dichlorobiphenyl in various surfactant/solvent-aided systems. *Water Research* 36(9), 2187-2194.
- Cirin, D.M., Posa, M.M., Krstonosic, V.S. and Milanovic, M.L. (2012) Conductometric study of sodium dodecyl sulfate-nonionic surfactant (Triton X-100, Tween 20, Tween 60, Tween 80 or Tween 85) mixed micelles in aqueous solution. *Hemijaska Industrija* 66(1), 21-28.
- Clayton, J.R., Payne, James R., Farlow, John S. (1993) Oil spill dispersants: mechanisms of action and laboratory tests, CRC Press, Boca Raton, Florida, USA.
- Coleman, J.M., Baker, J., Cooper, C., Fingas, M., Hunt, G.L., Kvenvolden, K.A., McDowell, J.E., Michel, J., Michel, R.K., Phinney, J., Pond, R., Rabalais, N.N., Roesner, L.A. and Spies, R.B. (2002) Oil in the sea: inputs, fates, and effects. *Spill Science & Technology Bulletin* 7(5-6), 197-199.
- Cornwall, W. (2015) Critics question plans to spray dispersant in future deep spills. *Science* 348(6230), 27-27.
- D'Auria, M., Racioppi, R. and Velluzzi, V. (2008) Photodegradation of crude oil: liquid injection and headspace solid-phase microextraction for crude oil analysis by gas chromatography with mass spectrometer detector. *Journal of Chromatographic Science* 46(4), 339-344.
- Dabestani, R. and Ivanov, I.N. (1999) A compilation of physical, spectroscopic and photophysical properties of polycyclic aromatic hydrocarbons. *Photochemistry and Photobiology* 70(1), 10-34.

- Davies, B.E. (1974) Loss-on-ignition as an estimate of soil organic-matter. *Soil Science Society of America Journal* 38(1), 150-151.
- Diaz, M., Luiz, M., Bertolotti, S., Miskoski, S. and Garcia, N.A. (2004) Scavenging of photogenerated singlet molecular oxygen and superoxide radical anion by sulphur drugs - Kinetics and mechanism. *Canadian Journal of Chemistry-Revue Canadienne De Chimie* 82(12), 1752-1759.
- Diercks, A.R., Highsmith, R.C., Asper, V.L., Joung, D.J., Zhou, Z.Z., Guo, L.D., Shiller, A.M., Joye, S.B., Teske, A.P., Guinasso, N., Wade, T.L. and Lohrenz, S.E. (2010) Characterization of subsurface polycyclic aromatic hydrocarbons at the Deepwater Horizon site. *Geophysical Research Letters* 37.
- Díez, S., Jover, E., Bayona, J.M. and Albaigés, J. (2007) Prestige oil spill. III. Fate of a heavy oil in the marine environment. *Environmental Science & Technology* 41(9), 3075-3082.
- Dong, J., Wen, C.Y., Liu, D.F., Zhang, W.J., Li, J.T., Jiang, H.J., Qin, C.W. and Hong, M. (2015) Study on degradation of nitrobenzene in groundwater using emulsified nano-zero-valent iron. *Journal of Nanoparticle Research* 17(1).
- Dong, J., Zhao, Y.S., Zhao, R. and Zhou, R. (2010) Effects of pH and particle size on kinetics of nitrobenzene reduction by zero-valent iron. *Journal of Environmental Sciences-China* 22(11), 1741-1747.
- Dong, M.M. and Rosario-Ortiz, F.L. (2012) Photochemical formation of hydroxyl radical from effluent organic matter. *Environmental Science & Technology* 46(7), 3788-3794.
- Doong, R.A., Chang, S.M. and Tsai, C.W. (2013) Enhanced photoactivity of Cu-deposited titanate nanotubes for removal of bisphenol A. *Applied Catalysis B: Environmental* 129, 48-55.



- Driessen, M.D. and Grassian, V.H. (1998) Photooxidation of trichloroethylene on Pt/TiO<sub>2</sub>. *Journal of Physical Chemistry B* 102(8), 1418-1423.
- Eastoe, J. and Dalton, J.S. (2000) Dynamic surface tension and adsorption mechanisms of surfactants at the air-water interface. *Advances in Colloid and Interface Science* 85(2-3), 103-144.
- Erdem, N.S., Alawani, N. and Wesdemiotis, C. (2014) Characterization of polysorbate 85, a nonionic surfactant, by liquid chromatography vs. ion mobility separation coupled with tandem mass spectrometry. *Analytica Chimica Acta* 808, 83-93.
- Fasnacht, M.P. and Blough, N.V. (2002) Aqueous photodegradation of polycyclic aromatic hydrocarbons. *Environmental Science & Technology* 36(20), 4364-4369.
- Fasnacht, M.P. and Blough, N.V. (2003) Mechanisms of the aqueous photodegradation of polycyclic aromatic hydrocarbons. *Environmental Science & Technology* 37(24), 5767-5772.
- Feng, C., Teng, F., Liu, Z., Chang, C., Zhao, Y., Wang, S., Chen, M., Yao, W. and Zhu, Y. (2015) A newly discovered BiF<sub>3</sub> photocatalyst with a high positive valence band. *Journal of Molecular Catalysis A: Chemical* 401(0), 35-40.
- Foote, C.S. and Wexler, S. (1964) Singlet oxygen. A probable intermediate in photosensitized autoxidations. *Journal of the American Chemical Society* 86(18), 3880-3881.
- Fu, J., Cai, Z.Q., Gong, Y.Y., O'Reilly, S.E., Hao, X.D. and Zhao, D.Y. (2015) A new technique for determining critical micelle concentrations of surfactants and oil dispersants via UV absorbance of pyrene. *Colloids and Surfaces A: Physicochemical and Engineering Aspects* 484, 1-8.

- Fu, J., Gong, Y., Zhao, X., O'Reilly, S.E. and Zhao, D. (2014) Effects of oil and dispersant on formation of marine oil snow and transport of oil hydrocarbons. *Environmental Science & Technology* 48(24), 14392-14399.
- Fuerstenau, D.W. (2002) Equilibrium and nonequilibrium phenomena associated with the adsorption of ionic surfactants at solid-water interfaces. *Journal of Colloid and Interface Science* 256(1), 79-90.
- Fujishima, A. and Honda, K. (1972) TiO<sub>2</sub> photoelectrochemistry and photocatalysis. *Nature* 238(5358), 37-38.
- Furukawa, Y., Watkins, J.L., Kim, J., Curry, K.J. and Bennett, R.H. (2009) Aggregation of montmorillonite and organic matter in aqueous media containing artificial seawater. *Geochemical Transactions* 10(2), 1-11.
- Gandra, N., Chiu, P.L., Li, W.B., Anderson, Y.R., Mitra, S., He, H.X. and Gao, R.M. (2009) Photosensitized singlet oxygen production upon two-photon excitation of single-walled carbon nanotubes and their functionalized analogues. *Journal of Physical Chemistry C* 113(13), 5182-5185.
- Gauthier, T.D., Shane, E.C., Guerin, W.F., Seitz, W.R. and Grant, C.L. (1986) Fluorescence quenching method for determining equilibrium constants for polycyclic aromatic hydrocarbons binding to dissolved humic materials. *Environmental Science & Technology* 20(11), 1162-1166.
- Gesteira, J.L.G. and Dauvin, J.C. (2000) Amphipods are good bioindicators of the impact of oil spills on soft-bottom macrobenthic communities. *Marine Pollution Bulletin* 40(11), 1017-1027.

- Ghita, D., Rosca, P. and Ezeanu, D.S. (2012) Synthesis and characterization of Pt catalysts supported on mesoporous matters. *Revista De Chimie* 63(10), 1056-1061.
- Giasuddin, A.B.M., Kanel, S.R. and Choi, H. (2007) Adsorption of humic acid onto nanoscale zerovalent iron and its effect on arsenic removal. *Environmental Science & Technology* 41(6), 2022-2027.
- Glover, C.M., Mezyk, S.P., Linden, K.G. and Rosario-Ortiz, F.L. (2014) Photochemical degradation of Corexit components in ocean water. *Chemosphere* 111, 596-602.
- Gong, Y.Y., Fu, J., O'Reilly, S.E. and Zhao, D.Y. (2015) Effects of oil dispersants on photodegradation of pyrene in marine water. *Journal of Hazardous Materials* 287, 142-150.
- Gong, Y.Y., Liu, Y.Y., Xiong, Z., Kaback, D. and Zhao, D.Y. (2012) Immobilization of mercury in field soil and sediment using carboxymethyl cellulose stabilized iron sulfide nanoparticles. *Nanotechnology* 23(29), 1-13.
- Gong, Y.Y., Zhao, X., Cai, Z.Q., O'Reilly, S.E., Hao, X.D. and Zhao, D.Y. (2014a) A review of oil, dispersed oil and sediment interactions in the aquatic environment: influence on the fate, transport and remediation of oil spills. *Marine Pollution Bulletin* 79(1-2), 16-33.
- Gong, Y.Y., Zhao, X., O'Reilly, S.E., Qian, T.W. and Zhao, D.Y. (2014b) Effects of oil dispersant and oil on sorption and desorption of phenanthrene with Gulf Coast marine sediments. *Environmental Pollution* 185, 240-249.
- González, J., Viñas, L., Franco, M., Fumega, J., Soriano, J., Grueiro, G., Muniategui, S., López-Mahía, P., Prada, D. and Bayona, J. (2006) Spatial and temporal distribution of dissolved/dispersed aromatic hydrocarbons in seawater in the area affected by the Prestige oil spill. *Marine Pollution Bulletin* 53(5), 250-259.

- Goodbody-Gringley, G., Wetzel, D.L., Gillon, D., Pulster, E., Miller, A. and Ritchie, K.B. (2013) Toxicity of Deepwater Horizon source oil and the chemical dispersant, Corexit 9500, to Coral Larvae. *Plos One* 8(1), e45574.
- Gordon, D.C. (1970) A microscopic study of organic particles in the North Atlantic Ocean, pp. 175-185, Elsevier.
- Griffiths, S.K. (2012) Oil Release from Macondo Well MC252 following the Deepwater Horizon accident. *Environmental Science & Technology* 46(10), 5616-5622.
- Guo, W., He, M.C., Yang, Z.F., Lin, C.Y., Quan, X.C. and Wang, H.Z. (2007) Distribution of polycyclic aromatic hydrocarbons in water, suspended particulate matter and sediment from Daliao River watershed, China. *Chemosphere* 68(1), 93-104.
- Gupta, A., Sender, M., Fields, S. and Bothun, G.D. (2014) Phase and sedimentation behavior of oil (octane) dispersions in the presence of model mineral aggregates. *Marine Pollution Bulletin* 87(1-2), 164-170.
- Guyomarch, J., Merlin, F.X. and Bernanose, P. (1999) Oil interaction with mineral fines and chemical dispersion: behaviour of the dispersed oil in coastal or estuarine conditions, pp. 137-150, Minister of Supply and Services, Canada.
- Harayama, S., Kishira, H., Kasai, Y. and Shutsubo, K. (1999) Petroleum biodegradation in marine environments. *Journal of Molecular Microbiology and Biotechnology* 1(1), 63-70.
- Harris, D.C. (2010) *Quantitative chemical analysis*, Macmillan.
- Harvey, R.G. (1991) *Polycyclic aromatic hydrocarbons: chemistry and carcinogenicity*, CUP Archive.

- Hayworth, J.S. and Clement, T.P. (2012) Provenance of Corexit-related chemical constituents found in nearshore and inland Gulf Coast waters. *Marine Pollution Bulletin* 64(10), 2005-2014.
- Hazen, T.C., Dubinsky, E.A., DeSantis, T.Z., Andersen, G.L., Piceno, Y.M., Singh, N., Jansson, J.K., Probst, A., Borglin, S.E., Fortney, J.L., Stringfellow, W.T., Bill, M., Conrad, M.E., Tom, L.M., Chavarria, K.L., Alusi, T.R., Lamendella, R., Joyner, D.C., Spier, C., Baelum, J., Auer, M., Zemla, M.L., Chakraborty, R., Sonnenthal, E.L., D'haeseleer, P., Holman, H.Y.N., Osman, S., Lu, Z.M., Van Nostrand, J.D., Deng, Y., Zhou, J.Z. and Mason, O.U. (2010) Deep-sea oil plume enriches indigenous oil-degrading bacteria. *Science* 330(6001), 204-208.
- Hazlet, S.E. and Dornfeld, C.A. (1944) The reduction of aromatic nitro compounds with activated iron. *Journal of the American Chemical Society* 66(10), 1781-1782.
- He, F. and Zhao, D.Y. (2007) Manipulating the size and dispersibility of zerovalent iron nanoparticles by use of carboxymethyl cellulose stabilizers. *Environmental Science & Technology* 41(17), 6216-6221.
- He, F., Zhao, D.Y., Liu, J.C. and Roberts, C.B. (2007) Stabilization of Fe-Pd nanoparticles with sodium carboxymethyl cellulose for enhanced transport and dechlorination of trichloroethylene in soil and groundwater. *Industrial & Engineering Chemistry Research* 46(1), 29-34.
- He, F., Zhao, D.Y. and Paul, C. (2010) Field assessment of carboxymethyl cellulose stabilized iron nanoparticles for in situ destruction of chlorinated solvents in source zones. *Water Research* 44(7), 2360-2370.

- Heijman, C.G., Grieder, E., Holliger, C. and Schwarzenbach, R.P. (1995) Reduction of nitroaromatic - compounds coupled to microbial iron reduction in laboratory aquifer columns. *Environmental Science & Technology* 29(3), 775-783.
- Heil, D. and Sposito, G. (1993a) Organic-matter role in illitic soil colloids flocculation. 1. Counter ions and pH. *Soil Science Society of America Journal* 57(5), 1241-1246.
- Heil, D. and Sposito, G. (1993b) Organic-matter role in illitic soil colloids flocculation. 2. Surface-charge. *Soil Science Society of America Journal* 57(5), 1246-1253.
- Hickenbottom, K.L., Hancock, N.T., Hutchings, N.R., Appleton, E.W., Beaudry, E.G., Xu, P. and Cath, T.Y. (2013) Forward osmosis treatment of drilling mud and fracturing wastewater from oil and gas operations. *Desalination* 312, 60-66.
- Hoffmann, M.R., Martin, S.T., Choi, W.Y. and Bahnemann, D.W. (1995) Environmental applications of semiconductor photocatalysis. *Chemical Reviews* 95(1), 69-96.
- Hu, Y., Song, X., Jiang, S. and Wei, C. (2015) Enhanced photocatalytic activity of Pt-doped TiO<sub>2</sub> for NO<sub>x</sub> oxidation both under UV and visible light irradiation: a synergistic effect of lattice Pt<sup>4+</sup> and surface PtO. *Chemical Engineering Journal* 274, 102-112.
- Huang, K.C. and Chien, S.H. (2013) Improved visible-light-driven photocatalytic activity of rutile/titania-nanotube composites prepared by microwave-assisted hydrothermal process. *Applied Catalysis B: Environmental* 140, 283-288.
- Huang, W.L. and Weber, W.J. (1997) A distributed reactivity model for sorption by soils and sediments. 10. Relationships between desorption, hysteresis, and the chemical characteristics of organic domains. *Environmental Science & Technology* 31(9), 2562-2569.

- Huang, Y.H. and Zhang, T.C. (2006) Reduction of nitrobenzene and formation of corrosion coatings in zerovalent iron systems. *Water Research* 40(16), 3075-3082.
- Hung, H.M., Ling, F.H. and Hoffmann, M.R. (2000) Kinetics and mechanism of the enhanced reductive degradation of nitrobenzene by elemental iron in the presence of ultrasound. *Environmental Science & Technology* 34(9), 1758-1763.
- Hunter, R.J. (2013) *Zeta potential in colloid science: principles and applications*, Academic press.
- Im, S.H., Jeong, Y.H. and Ryoo, J.J. (2008) Simultaneous analysis of anionic, amphoteric, nonionic and cationic surfactant mixtures in shampoo and hair conditioner by RP-HPLC/ELSD and LC/MS. *Analytica Chimica Acta* 619(1), 129-136.
- Incardona, J.P., Swarts, T.L., Edmunds, R.C., Linbo, T.L., Aquilina-Beck, A., Sloan, C.A., Gardner, L.D., Block, B.A. and Scholz, N.L. (2013) Exxon Valdez to deepwater horizon: comparable toxicity of both crude oils to fish early life stages. *Aquatic Toxicology* 142, 303-316.
- Inoue, Y., Kubokawa, T. and Sato, K. (1991) Photocatalytic activity of alkali-metal titanates combined with Ru in the decomposition of water. *Journal of Physical Chemistry* 95(10), 4059-4063.
- Inoue, Y., Niiyama, T. and Sato, K. (1994) Photocatalysts using hexa- and octa-titanates with different tunnel space for water decomposition. *Topics in Catalysis* 1(1-2), 137-144.
- Ireland, J.C., Davila, B., Moreno, H., Fink, S.K. and Tassos, S. (1995) Heterogeneous photocatalytic decomposition of polyaromatic hydrocarbons over titanium-dioxide. *Chemosphere* 30(5), 965-984.

- Jameson, C., Lunn, R., Jeter, S. and Sabella, A. (2002) Final report on carcinogens background document for nitrobenzene. US Department of Health and Human Services, Public Health Service, National Toxicology Program Research, Triangle Park, NC 27709.
- Jacob, S. M., Bergman, R. E. Water based oil dispersant. In Google Patents: 2001.
- Jia, H.Z. and Wang, C.Y. (2013) Comparative studies on montmorillonite-supported zero-valent iron nanoparticles produced by different methods: reactivity and stability. *Environmental Technology* 34(1), 25-33.
- Jin, Z.S., Xi, C.J., Zeng, Q.M., Yin, F., Zhao, J.Z. and Xue, J.Z. (2003) Catalytic behavior of nanoparticle  $\alpha$ -PtO<sub>2</sub> for ethanol oxidation. *Journal of Molecular Catalysis A: Chemical* 191(1), 61-66.
- Jo, W.K., Won, Y.S., Hwang, I. And Tayade, R.J. (2014) Enhanced photocatalytic degradation of aqueous nitrobenzene using graphitic carbon–TiO<sub>2</sub> composites. *Industrial & Engineering Chemistry Research* 53(9), 3455-3461.
- Jones-Hughes, T. and Turner, A. (2005) Sorption of ionic surfactants to estuarine sediment and their influence on the sequestration of phenanthrene. *Environmental Science & Technology* 39(6), 1688-1697.
- Joshi, O., McGuire, J. and Wang, D.Q. (2008) Adsorption and function of recombinant factor VIII at solid-water interfaces in the presence of Tween-80. *Journal of Pharmaceutical Sciences* 97(11), 4741-4755.
- Joye, S.B. (2015) Deepwater Horizon, 5 years on. *Science* 349(6248), 592-593.



- Jung, Y.H., Yoon, K.T., Shim, W.J. and Park, H.S. (2015) Short-term variation of the macrobenthic fauna structure on rocky shores after the Hebei spirit oil spill, west coast of Korea. *Journal of Coastal Research* 31(1), 177-183.
- Kah, M., Zhang, X.R., Jonker, M.T.O. and Hofmann, T. (2011) Measuring and modelling adsorption of PAHs to carbon nanotubes over a six order of magnitude wide concentration range. *Environmental Science & Technology* 45(14), 6011-6017.
- Kahan, T.F. and Donaldson, D.J. (2007) Photolysis of polycyclic aromatic hydrocarbons on water and ice surfaces. *Journal of Physical Chemistry A* 111(7), 1277-1285.
- Kasahara, I., Hashimoto, K., Kawabe, T., Kunita, A., Magawa, K., Hata, N., Taguchi, S. and Goto, K. (1995) Spectrophotometric determination of anionic surfactants in sea-water based on ion-pair extraction with Bis[2-(5-Trifluoromethyl-2-Pyridylazo)-5-Diethylaminophenolato] Cobalt(III) as counter ion. *Analyst* 120(6), 1803-1807.
- Kester, D.R., Duedall, I.W., Connors, D.N. and Pytkowic.Rm (1967) Preparation of artificial seawater. *Limnology and Oceanography* 12(1), 176-179.
- Khelifa, A. and Hill, P.S. (2006) Models for effective density and settling velocity of flocs. *Journal of Hydraulic Research* 44(3), 390-401.
- Kim, K.H., Jahan, S.A., Kabir, E. and Brown, R.J.C. (2013a) A review of airborne polycyclic aromatic hydrocarbons (PAHs) and their human health effects. *Environment International* 60, 71-80.
- Kim, M., Hong, S.H., Won, J., Yim, U.H., Jung, J.H., Ha, S.Y., An, J.G., Joo, C., Kim, E., Han, G.M., Baek, S., Choi, H.W. and Shim, W.J. (2013b) Petroleum hydrocarbon contaminations in the intertidal seawater after the Hebei Spirit oil spill-Effect of tidal cycle on the TPH

- concentrations and the chromatographic characterization of seawater extracts. *Water Research* 47(2), 758-768.
- Kim, S., Kim, M., Hwang, S.-H. and Lim, S.K. (2012) Enhancement of photocatalytic activity of titania–titanate nanotubes by surface modification. *Applied Catalysis B: Environmental* 123, 391-397.
- Kiruri, L.W., Dellinger, B. and Lomnicki, S. (2013) Tar balls from Deep Water Horizon oil spill: Environmentally persistent free radicals (EPFR) formation during crude weathering. *Environmental Science & Technology* 47(9), 4220-4226.
- Klassen, N.V., Marchington, D. and McGowan, H.C.E. (1994) H<sub>2</sub>O<sub>2</sub> determination by the I<sub>3</sub><sup>-</sup> method and by KMnO<sub>4</sub> titration. *Analytical Chemistry* 66(18), 2921-2925.
- Kleindienst, S., Paul, J.H. and Joye, S.B. (2015a) Using dispersants after oil spills: impacts on the composition and activity of microbial communities. *Nature Reviews Microbiology* 13(6), 388-396.
- Kleindienst, S., Seidel, M., Ziervogel, K., Grim, S., Loftis, K., Harrison, S., Malkin, S.Y., Perkins, M.J., Field, J., Sogin, M.L., Dittmar, T., Passow, U., Medeiros, P.M. and Joye, S.B. (2015b) Chemical dispersants can suppress the activity of natural oil-degrading microorganisms. *Proceedings of the National Academy of Sciences of the United States of America* 112(48), 14900-14905.
- Kline, S.R. and Kaler, E.W. (1994) Colloidal interactions in water/2-butoxyethanol solvents. *Langmuir* 10(2), 412-417.

- Kohtani, S., Tomohiro, M., Tokumura, K. and Nakagaki, R. (2005) Photooxidation reactions of polycyclic aromatic hydrocarbons over pure and Ag-loaded BiVO<sub>4</sub> photocatalysts. *Applied Catalysis B: Environmental* 58(3-4), 265-272.
- Kou, J., Li, Z., Yuan, Y., Zhang, H., Wang, Y. and Zou, Z. (2009) Visible-light-induced photocatalytic oxidation of polycyclic aromatic hydrocarbons over tantalum oxynitride photocatalysts. *Environmental Science & Technology* 43(8), 2919-2924.
- Kover, S.C., Rosario-Ortiz, F.L. and Linden, K.G. (2014) Photochemical fate of solvent constituents of Corexit oil dispersants. *Water Research* 52(0), 101-111.
- Kretzschmar, R., Hesterberg, D. and Sticher, H. (1997) Effects of adsorbed humic acid on surface charge and flocculation of kaolinite. *Soil Science Society of America Journal* 61(1), 101-108.
- Kretzschmar, R., Holthoff, H. and Sticher, H. (1998) Influence of pH and humic acid on coagulation kinetics of kaolinite: a dynamic light scattering study. *Journal of Colloid and Interface Science* 202(1), 95-103.
- Kretzschmar, R., Robarge, W.P. and Weed, S.B. (1993) Flocculation of kaolinitic soil clays-effects of humic substances and iron-oxides. *Soil Science Society of America Journal* 57(5), 1277-1283.
- Kujawinski, E.B., Soule, M.C.K., Valentine, D.L., Boysen, A.K., Longnecker, K. and Redmond, M.C. (2011) Fate of dispersants associated with the Deepwater Horizon oil spill. *Environmental Science & Technology* 45(4), 1298-1306.
- Kujawski, D. (2009) New trends in oil refinery wastewater reclamation <<http://www.waterworld.com/articles/2009/04/new-trends-in-oil-refinery-wastewater-reclamation.html>>.

- Kuribayashi, K. and Kitamura, S. (2001) Preparation of Pt-PtO<sub>x</sub> thin films as electrode for memory capacitors. *Thin Solid Films* 400(1-2), 160-164.
- Kuscu, O.S. and Sponza, D.T. (2009) Effect of increasing nitrobenzene loading rates on the performance of anaerobic migrating blanket reactor and sequential anaerobic migrating blanket reactor/completely stirred tank reactor system. *Journal of Hazardous Materials* 168(1), 390-399.
- Lam, M.W., Tantuco, K. and Mabury, S.A. (2003) Photofate: a new approach in accounting for the contribution of indirect photolysis of pesticides and pharmaceuticals in surface waters. *Environmental Science & Technology* 37(5), 899-907.
- Latch, D.E., McNeill, K. (2006) Microheterogeneity of singlet oxygen distributions in irradiated humic acid solutions. *Science* 311(5768), 1743-1747.
- Lee, C.K., Wang, C.C., Lyu, M.D., Juang, L.C., Liu, S.S. and Hung, S.H. (2007) Effects of sodium content and calcination temperature on the morphology, structure and photocatalytic activity of nanotubular titanates. *Journal of Colloid and Interface Science* 316(2), 562-569.
- Lee, H., Kim, B.H., Park, Y.K., Kim, S.J. and Jung, S.C. (2015) Application of recycled zero-valent iron nanoparticle to the treatment of wastewater containing nitrobenzene. *Journal of Nanomaterials* 2015.
- Lee, J.Y. and Hildemann, L.M. (2013) Surface tension of solutions containing dicarboxylic acids with ammonium sulfate, D-glucose, or humic acid. *Journal of Aerosol Science* 64, 94-102.
- Lehto, K.M., Vuorimaa, E. and Lemmetyinen, H. (2000) Photolysis of polycyclic aromatic hydrocarbons (PAHs) in dilute aqueous solutions detected by fluorescence. *Journal of Photochemistry and Photobiology A: Chemistry* 136(1-2), 53-60.

- Lessard, R.R. and Demarco, G. (2000) The significance of oil spill dispersants. *Spill Science & Technology Bulletin* 6(1), 59-68.
- Li, F.B. and Li, X.Z. (2002) The enhancement of photodegradation efficiency using Pt-TiO<sub>2</sub> catalyst. *Chemosphere* 48(10), 1103-1111.
- Li, P.X., Li, Z.X., Shen, H.H., Thomas, R.K., Penfold, J. and Lu, J.R. (2013) Application of the gibbs equation to the adsorption of nonionic surfactants and polymers at the air-water interface: comparison with surface excesses determined directly using neutron reflectivity. *Langmuir* 29(30), 9324-9334.
- Li, R.M., Dong, G.J. and Chen, G.M. (2015) Synthesis, characterization and performance of ternary doped Cu-Ce-B/TiO<sub>2</sub> nanotubes on the photocatalytic removal of nitrogen oxides. *New Journal of Chemistry* 39(9), 6854-6863.
- Lin, Q.X. and Mendelssohn, I.A. (2012) Impacts and recovery of the Deepwater Horizon oil spill on vegetation structure and function of coastal salt marshes in the Northern Gulf of Mexico. *Environmental Science & Technology* 46(7), 3737-3743.
- Ling, X.F., Li, J.S., Zhu, W., Zhu, Y.Y., Sun, X.Y., Shen, J.Y., Han, W.Q. and Wang, L.J. (2012) Synthesis of nanoscale zero-valent iron/ordered mesoporous carbon for adsorption and synergistic reduction of nitrobenzene. *Chemosphere* 87(6), 655-660.
- Liu, W., Ni, J.R. and Yin, X.C. (2014) Synergy of photocatalysis and adsorption for simultaneous removal of Cr(VI) and Cr(III) with TiO<sub>2</sub> and titanate nanotubes. *Water research* 53, 12-25.
- Liu, W., Sun, W., Borthwick, A.G.L. and Ni, J. (2013a) Comparison on aggregation and sedimentation of titanium dioxide, titanate nanotubes and titanate nanotubes-TiO<sub>2</sub>: influence

of pH, ionic strength and natural organic matter. *Colloids and Surfaces A: Physicochemical and Engineering Aspects* 434(0), 319-328.

Liu, W., Wang, T., Borthwick, A.G., Wang, Y., Yin, X., Li, X. and Ni, J. (2013c) Adsorption of  $Pb^{2+}$ ,  $Cd^{2+}$ ,  $Cu^{2+}$  and  $Cr^{3+}$  onto titanate nanotubes: competition and effect of inorganic ions. *Science of the Total Environment* 456, 171-180.

Liu, W., Zhao, X., Borthwick, A.G., Wang, Y. and Ni, J. (2015a) Dual-enhanced photocatalytic activity of Fe-deposited titanate nanotubes used for simultaneous removal of As(III) and As (V). *ACS Applied Materials & Interfaces* 7(35), 19726-19735.

Liu, W., Zhao, X., Wang, T., Fu, J. and Ni, J. (2015b) Selective and irreversible adsorption of Mercury (II) from aqueous solution by a flower-like titanate nanomaterial. *Journal of Materials Chemistry A* 3(34), 17676-17684.

Liu, Y.L., Zhong, L., Peng, Z.Y., Cai, Y., Song, Y.B. and Chen, W. (2011) Self-assembly of Pt nanocrystals/one-dimensional titanate nanobelts heterojunctions and their great enhancement of photocatalytic activities. *Crystengcomm* 13(17), 5467-5473.

Liu, Y.Q. and Lowry, G.V. (2006) Effect of particle age (FeO content) and solution pH on NZVI reactivity:  $H_2$  evolution and TCE dechlorination. *Environmental Science & Technology* 40(19), 6085-6090.

Liu, Z., Liu, J., Zhu, Q. and Wu, W. (2012a) The weathering of oil after the Deepwater Horizon oil spill: insights from the chemical composition of the oil from the sea surface, salt marshes and sediments. *Environmental Research Letters* 7(3), 035302.

- Liu, Z.F., Liu, J.Q., Zhu, Q.Z. and Wu, W. (2012b) The weathering of oil after the Deepwater Horizon oil spill: insights from the chemical composition of the oil from the sea surface, salt marshes and sediments. *Environmental Research Letters* 7(3), 1-14.
- Lopez-Cervantes, J.L., Gracia-Fadrique, J., Calvo, E. and Amigo, A. (2013) Surface tensions, densities, and speeds of sound for aqueous solutions of lauryl ether ethoxylates. *Fluid Phase Equilibria* 356, 193-200.
- Lunkenheimer, K. and Wantke, K.D. (1981) Determination of the surface-tension of surfactant solutions applying the method of lecomte-du-nouy (ring tensiometer). *Colloid and Polymer Science* 259(3), 354-366.
- Luo, X.J., Chen, S.J., Mai, B.X., Sheng, G.Y., Fu, J.M. and Zeng, E.Y. (2008) Distribution, source apportionment, and transport of PAHs in sediments from the Pearl River Delta and the northern South China Sea. *Archives of Environmental Contamination and Toxicology* 55(1), 11-20.
- MacDonald, I. (2010) Deepwater disaster: how the oil spill estimates got it wrong. *Significance* 7(4), 149-154.
- Mackay, D. and Hickie, B. (2000) Mass balance model of source apportionment, transport and fate of PAHs in Lac Saint Louis, Quebec. *Chemosphere* 41(5), 681-692.
- Magrez, A., Kasas, S., Salicio, V., Pasquier, N., Seo, J.W., Celio, M., Catsicas, S., Schwaller, B. and Forro, L. (2006) Cellular toxicity of carbon-based nanomaterials. *Nano Letters* 6(6), 1121-1125.
- Mahdi, E.S., Sakeena, M.H.F., Abdulkarim, M.F., Abdullah, G.Z., Sattar, M.A. and Noor, A.M. (2011) Effect of surfactant and surfactant blends on pseudoternary phase diagram behavior of newly synthesized palm kernel oil esters. *Drug Design Development and Therapy* 5, 311-323.

- Malakoff, D. and Pegau, W.S. (2014) 25 years after the Exxon Valdez, where are the herring?  
Science 343(6178), 1416-1416.
- Malato, S., Fernandez-Ibanez, P., Maldonado, M.I., Blanco, J. and Gernjak, W. (2009)  
Decontamination and disinfection of water by solar photocatalysis: recent overview and trends.  
Catalysis Today 147(1), 1-59.
- Mallakin, A., Dixon, D.G. and Greenberg, B.M. (2000) Pathway of anthracene modification under  
simulated solar radiation. Chemosphere 40(12), 1435-1441.
- Mantha, R., Taylor, K.E., Biswas, N. and Bewtra, J.K. (2001) A continuous system for Fe<sup>0</sup>  
reduction of nitrobenzene in synthetic wastewater. Environmental Science & Technology  
35(15), 3231-3236.
- McCormack, P., Jones, P., Hetheridge, M. and Rowland, S. (2001) Analysis of oilfield produced  
waters and production chemicals by electrospray ionisation multi-stage mass spectrometry.  
Water Research 35(15), 3567-3578.
- McNutt, M.K., Camilli, R., Crone, T.J., Guthrie, G.D., Hsieh, P.A., Ryerson, T.B., Savas, O. and  
Shaffer, F. (2012) Review of flow rate estimates of the Deepwater Horizon oil spill.  
Proceedings of the National Academy of Sciences of the United States of America 109(50),  
20260-20267.
- Menger, F.M., Shi, L. and Rizvi, S.A.A. (2009) Re-evaluating the gibbs analysis of surface tension  
at the air/water interface. Journal of the American Chemical Society 131(30), 10380-10381.
- MetaCyc (2015) MetaCyc Compound: hydroxyaminobenzene.
- Mill, T., Mabey, W.R., Lan, B.Y. and Baraze, A. (1981) Photolysis of polycyclic aromatic-  
hydrocarbons in water. Chemosphere 10(11-1), 1281-1290.



- Miller, J.S. and Olejnik, D. (2001) Photolysis of polycyclic aromatic hydrocarbons in water. *Water Research* 35(1), 233-243.
- Minella, M., Laurentiis, E.D., Buhvestova, O., Haldna, M., Kangur, K., Maurino, V., Minero, C. and Vione, D. (2013) Modelling lake-water photochemistry: Three-decade assessment of the steady-state concentration of photoreactive transients (radical  $\bullet\text{OH}$ ,  $\text{CO}_3^{\cdot-}$  and  $^3\text{CDOM}^*$ ) in the surface water of polymictic Lake Peipsi (Estonia/Russia). *Chemosphere* 90(10), 2589-2596.
- Mitchell, F.M. and Holdway, D.A. (2000) The acute and chronic toxicity of the dispersants Corexit 9527 and 9500, water accommodated fraction (WAF) of crude oil, and dispersant enhanced WAF (DEWAF) to *Hydra viridissima* (green hydra). *Water Research* 34(1), 343-348.
- Moles, A., Holland, L. and Short, J. (2002) Effectiveness in the laboratory of Corexit 9527 and 9500 in dispersing fresh, weathered, and emulsion of Alaska North Slope crude oil under subarctic conditions. *Spill Science & Technology Bulletin* 7(5-6), 241-247.
- Mu, Y., Yu, H.Q., Zheng, J.C., Zhang, S.J. and Sheng, G.P. (2004) Reductive degradation of nitrobenzene in aqueous solution by zero-valent iron. *Chemosphere* 54(7), 789-794.
- Murov, S. and Carmichael, I. (1993) *Handbook of photochemistry*, Marcel Dekker, New York.
- Myers, D. (1999) *Surfaces, Interfaces, and Colloids*, Wiley, New York, NY, USA.
- National Toxicology Program (2011) Report on carcinogens, US Dept. of Health and Human Services, Public Health Service, National Toxicology Program.
- Nicodem, D.E., Guedes, C.L.B., Fernandes, M.C.Z., Severino, D., Correa, R.J., Coutinho, M.C. and Silva, J. (2001) Photochemistry of petroleum. *Progress in Reaction Kinetics and Mechanism* 26(2-3), 219-238.

- Noüy, P.L.D. (1925) An interfacial tensiometer for universal use. *The Journal of general physiology* 7(5), 625-631.
- NRC (2005) national Research Council: understanding oil spill dispersant: efficacy and effects, National Academies Press, Washington, DC.
- O'Sullivan, A. and Richardson, A.J. (1967) The Torrey Canyon disaster and intertidal marine life. *Nature* 214, 448-542.
- Oren, A. and Chefetz, B. (2005) Sorption-desorption behavior of polycyclic aromatic hydrocarbons in upstream and downstream river sediments. *Chemosphere* 61(1), 19-29.
- Ou, H.H. and Lo, S.L. (2007a) Review of titania nanotubes synthesized via the hydrothermal treatment: fabrication, modification, and application. *Separation and Purification Technology* 58(1), 179-191.
- Ou, H.H. and Lo, S.L. (2007b) Effect of Pt/Pd-doped TiO<sub>2</sub> on the photocatalytic degradation of trichloroethylene. *Journal of Molecular Catalysis A: Chemical* 275(1-2), 200-205.
- Pal, B. and Sharon, M. (2000) Photodegradation of polyaromatic hydrocarbons over thin film of TiO<sub>2</sub> nanoparticles; a study of intermediate photoproducts. *Journal of Molecular Catalysis A: Chemical* 160(2), 453-460.
- Pan, X.Y., Chen, X.X. and Yi, Z.G. (2016) Defective, porous TiO<sub>2</sub> nanosheets with Pt decoration as an efficient photocatalyst for ethylene oxidation synthesized by a C<sub>3</sub>N<sub>4</sub> templating method. *ACS Applied Materials & Interfaces* 8(16), 10104-10108.
- Paria, S. and Khilar, K.C. (2004) A review on experimental studies of surfactant adsorption at the hydrophilic solid-water interface. *Advances in Colloid and Interface Science* 110(3), 75-95.

- Paris, C.B., Le Henaff, M., Aman, Z.M., Subramaniam, A., Helgers, J., Wang, D.P., Kourafalou, V.H. and Srinivasan, A. (2012) Evolution of the Macondo well blowout: simulating the effects of the circulation and synthetic dispersants on the subsea oil transport. *Environmental Science & Technology* 46(24), 13293-13302.
- Park, O.K. and Kang, Y.S. (2005) Preparation and characterization of silica-coated TiO<sub>2</sub> nanoparticle. *Colloids and Surfaces A: Physicochemical and Engineering Aspects* 257-58, 261-265.
- Patton, J.S., Rigler, M.W., Boehm, P.D. and Fiest, D.L. (1981) Ixtoc-1 oil-spill: flaking of surface mousse in the Gulf of Mexico. *Nature* 290(5803), 235-238.
- Payne, J.R., Clayton, J.R., McNabb, G.D., Kirstein, B.E., Clary, C.L., Redding, R.T., Evans, J.S., Reimnitz, E. and Kempema, E.W. (1989) Oil-ice sediment interactions during freeze-up and break-up: final report, pp. 1-382, US Department of Commerce, NOAA.
- Perez, L., Pinazo, A., Rosen, M.J. and Infante, M.R. (1998) Surface activity properties at equilibrium of novel gemini cationic amphiphilic compounds from arginine, Bis(Arg). *Langmuir* 14(9), 2307-2315.
- Persson, C.M., Jonsson, A.P., Bergstrom, M. and Eriksson, J.C. (2003) Testing the Gouy-Chapman theory by means of surface tension measurements for SDS-NaCl-H<sub>2</sub>O mixtures. *Journal of Colloid and Interface Science* 267(1), 151-154.
- Place, B., Anderson, B., Mekebri, A., Furlong, E.T., Gray, J.L., Tjeerdema, R. and Field, J. (2010) A role for analytical chemistry in advancing our understanding of the occurrence, fate, and effects of corexit oil dispersants. *Environmental Science & Technology* 44(16), 6016-6018.

- Prince, R.C., Coolbaugh, T.S. and Parkerton, T.F. (2016) Oil dispersants do facilitate biodegradation of spilled oil. *Proceedings of the National Academy of Sciences of the United States of America* 113(11), E1421-E1421.
- Prince, R.C., Garrett, R.M., Bare, R.E., Grossman, M.J., Townsend, T., Suflita, J.M., Lee, K., Owens, E.H., Sergy, G.A., Braddock, J.F., Lindstrom, J.E. and Lessard, R.R. (2003) The roles of photooxidation and biodegradation in long-term weathering of crude and heavy fuel oils. *Spill Science & Technology Bulletin* 8(2), 145-156.
- Prosser, A.J. and Franses, E.I. (2001) Adsorption and surface tension of ionic surfactants at the air-water interface: review and evaluation of equilibrium models. *Colloids and Surfaces A: Physicochemical and Engineering Aspects* 178(1-3), 1-40.
- Qin, Q.D., Ma, J. and Liu, K. (2007) Adsorption of nitrobenzene from aqueous solution by MCM-41. *Journal of Colloid and Interface Science* 315(1), 80-86.
- Quinn, J., Geiger, C., Clausen, C., Brooks, K., Coon, C., O'Hara, S., Krug, T., Major, D., Yoon, W.S., Gavaskar, A. and Holdsworth, T. (2005) Field demonstration of DNAPL dehalogenation using emulsified zero-valent iron. *Environmental Science & Technology* 39(5), 1309-1318.
- Raber, B., Kogel-Knabner, I., Stein, C. and Klem, D. (1998) Partitioning of polycyclic aromatic hydrocarbons to dissolved organic matter from different soils. *Chemosphere* 36(1), 79-97.
- Radding, S.B., Mill, T., Gould, C., Liw, D. and Johnson, H. (1976) The environmental fate of selected poly-nuclear aromatic hydrocarbons. Available from the National Technical Information Service, Springfield VA.
- Rahsepar, S., Smit, M.P., Murk, A.J., Rijnaarts, H.H. and Langenhoff, A.A. (2016) Chemical dispersants: oil biodegradation friend or foe? *Marine Pollution Bulletin* 108(1-2), 113-119.

- Reddy, C.M., Arey, J.S., Seewald, J.S., Sylva, S.P., Lemkau, K.L., Nelson, R.K., Carmichael, C.A., McIntyre, C.P., Fenwick, J., Ventura, G.T., Van Mooy, B.A.S. and Camilli, R. (2012) Composition and fate of gas and oil released to the water column during the Deepwater Horizon oil spill. *Proceedings of the National Academy of Sciences of the United States of America* 109(50), 20229-20234.
- Redman, J.A., Walker, S.L. and Elimelech, M. (2004) Bacterial adhesion and transport in porous media: role of the secondary energy minimum. *Environmental Science & Technology* 38(6), 1777-1785.
- Reichert, M.D. and Walker, L.M. (2013) Interfacial tension dynamics, interfacial mechanics, and response to rapid dilution of bulk surfactant of a model oil-water-dispersant system. *Langmuir* 29(6), 1857-1867.
- Ren, C.X., Li, Y.M., Li, J.F., Sheng, G.D., Hu, L.J. and Zheng, X.M. (2014) Immobilization of nanoscale zero valent iron on organobentonite for accelerated reduction of nitrobenzene. *Journal of Chemical Technology and Biotechnology* 89(12), 1961-1966.
- Rodriguez-Gonzalez, V., Ruiz-Gomez, M.A., Torres-Martinez, L.M., Zanella, R. and Gomez, R. (2009) Sol-gel silver hexatitanates as photocatalysts for the 4-chlorophenol decomposition. *Catalysis Today* 148(1-2), 109-114.
- Rodriguez, M., Kirchner, A., Contreras, S., Chamarro, E. and Esplugas, S. (2000) Influence of H<sub>2</sub>O<sub>2</sub> and Fe(III) in the photodegradation of nitrobenzene. *Journal of Photochemistry and Photobiology A: Chemistry* 133(1-2), 123-127.

- Rodriguez, M., Timokhin, V., Michl, F., Contreras, S., Gimenez, J. and Esplugas, S. (2002) The influence of different irradiation sources on the treatment of nitrobenzene. *Catalysis Today* 76(2-4), 291-300.
- Ross, S. and Olivier, J.P. (1959) A new method for the determination of critical micelle concentrations of un-ionized associations colloids in aqueous or in non-aqueous solution. *The Journal of Physical Chemistry* 63(10), 1671-1674.
- Roy, P., Periasamy, A.P., Liang, C.T. and Chang, H.T. (2013) Synthesis of graphene-ZnO-Au nanocomposites for efficient photocatalytic reduction of nitrobenzene. *Environmental Science & Technology* 47(12), 6688-6695.
- Ruckmani, K., Jayakar, B. and Ghosal, S.K. (2000) Nonionic surfactant vesicles (niosomes) of cytarabine hydrochloride for effective treatment of leukemias: encapsulation, storage, and in vitro release. *Drug Development and Industrial Pharmacy* 26(2), 217-222.
- Rufier, C., Collet, A., Viguiier, M., Oberdisse, J. and Mora, S. (2011) Influence of surfactants on hydrophobically end-capped poly(ethylene oxide) self-assembled aggregates studied by SANS. *Macromolecules* 44(18), 7451-7459.
- Ruiping, L., Huijuan, L., Dongjin, W. and Min, Y. (2008) Characterization of the Songhua River sediments and evaluation of their adsorption behavior for nitrobenzene. *Journal of Environmental Sciences* 20(7), 796-802.
- Ryu, J. and Choi, W. (2004) Effects of TiO<sub>2</sub> surface modifications on photocatalytic oxidation of arsenite: the role of superoxides. *Environmental Science & Technology* 38(10), 2928-2933.
- Saeed, T., Ali, L.N., Al-Bloushi, A., Al-Hashash, H., Al-Bahloul, M., Al-Khabbaz, A. and Al-Khayat, A. (2011) Effect of environmental factors on photodegradation of polycyclic aromatic

- hydrocarbons (PAHs) in the water-soluble fraction of Kuwait crude oil in seawater. *Marine Environmental Research* 72(3), 143-150.
- Scelfo, G.M. and Tjeerdema, R.S. (1991) A simple method for determination of Corexit 9527 in natural-waters. *Marine Environmental Research* 31(1), 69-78.
- Scherer, M.M., Johnson, K.M., Westall, J.C. and Tratnyek, P.G. (2001) Mass transport effects on the kinetics of nitrobenzene reduction by iron metal. *Environmental Science & Technology* 35(13), 2804-2811.
- Schierbaum, K.D., Fischer, S., Torquemada, M.C., deSegovia, J.L., Roman, E. and MartinGago, J.A. (1996) The interaction of Pt with TiO<sub>2</sub>(110) surfaces: a comparative XPS, UPS, ISS, and ESD study. *Surface Science* 345(3), 261-273.
- Schwarzenbach, R.P., Gschwend, P.M. and Imboden, D.M. (2003) *Environmental organic chemistry*, Wiley, Hoboken, N.J.
- Semlali, S., Pigot, T., Flahaut, D., Allouche, J., Lacombe, S. and Nicole, L. (2014) Mesoporous Pt-TiO<sub>2</sub> thin films: photocatalytic efficiency under UV and visible light. *Applied Catalysis B: Environmental* 150, 656-662.
- Shankar, R., Shim, W.J., An, J.G. and Yim, U.H. (2015) A practical review on photooxidation of crude oil: laboratory lamp setup and factors affecting it. *Water Research* 68, 304-315.
- Shannon, M.A., Bohn, P.W., Elimelech, M., Georgiadis, J.G., Mariñas, B.J. and Mayes, A.M. (2008) Science and technology for water purification in the coming decades. *Nature* 452(7185), 301-310.

- Shen, C., Li, B., Huang, Y. and Jin, Y. (2007) Kinetics of coupled primary- and secondary-minimum deposition of colloids under unfavorable chemical conditions. *Environmental Science & Technology* 41(20), 6976-6982.
- Shen, L., Guo, A. and Zhu, X.Y. (2011) Tween surfactants: adsorption, self-organization, and protein resistance. *Surface Science* 605(5-6), 494-499.
- Simanzhenkov, V. and Idem, R. (2003) *Crude oil chemistry*, CRC Press.
- Simister, E.A., Thomas, R.K., Penfold, J., Aveyard, R., Binks, B.P., Cooper, P., Fletcher, P.D.I., Lu, J.R. and Sokolowski, A. (1992) Comparison of neutron reflection and surface-tension measurements of the surface excess of tetradecyltrimethylammonium bromide layers at the air-water-interface. *Journal of Physical Chemistry* 96(3), 1383-1388.
- Singer, M.M., Aurand, D., Bragin, G.E., Clark, J.R., Coelho, G.M., Sowby, M.L. and Tjeerdema, R.S. (2000) Standardization of the preparation and quantitation of water-accommodated fractions of petroleum for toxicity testing. *Marine Pollution Bulletin* 40(11), 1007-1016.
- Singer, M.M., George, S., Jacobson, S., Lee, I., Weetman, L.L., Tjeerdema, R.S. and Sowby, M.L. (1996) Comparison of acute aquatic effects of the oil dispersant Corexit 9500 with those of other Corexit series dispersants. *Ecotoxicology and Environmental Safety* 35(2), 183-189.
- Sires, I. and Brillas, E. (2012) Remediation of water pollution caused by pharmaceutical residues based on electrochemical separation and degradation technologies: a review. *Environment International* 40, 212-229.
- Skadsheim, A., Sanni, S., Cova, C. and Gaudebert, B. (2000) Bioavailability to fish of hydrocarbons contained in oil droplets or dissolved in water, Society of Petroleum Engineers.



- Slaga, T., Gleason, G., Mills, G., Ewald, L., Fu, P., Lee, H. and Harvey, R. (1980) Comparison of the skin tumor-initiating activities of dihydrodiols and diol-epoxides of various polycyclic aromatic hydrocarbons. *Cancer research* 40(6), 1981-1984.
- Sorial, G., Chandrasekar, S. and Weaver, J.W. (2004) Characteristics of spilled oils, fuels, and petroleum products: 2a. dispersant effectiveness data for a suite of environmental conditions – the effects of temperature, volatilization, and energy U.S. Environmental Protection Agency, Athens, Georgia.
- Southward, A.J., Southward, Eve C. (1978) Recolonization of rocky shores in Cornwall after use of toxic dispersants to clean up the Torrey Canyon spill. *Journal of the Fisheries Research Board of Canada* 35(5), 682-706.
- Srivastava, V., Gusain, D. and Sharma, Y.C. (2015) Critical review on the toxicity of some widely used engineered nanoparticles. *Industrial & Engineering Chemistry Research* 54(24), 6209-6233.
- Stepnowski, P., Siedlecka, E., Behrend, P. and Jastorff, B. (2002) Enhanced photo-degradation of contaminants in petroleum refinery wastewater. *Water Research* 36(9), 2167-2172.
- Stevens, W.R., Ruscic, B. and Baer, T. (2010) Heats of formation of  $C_6H_5$ ,  $C_6H_5^+$ , and  $C_6H_5NO$  by threshold photoelectron photoion coincidence and active thermochemical tables analysis. *Journal of Physical Chemistry A* 114(50), 13134-13145.
- Sun, H.W., Xu, X.Y., Gao, G.D., Zhang, Z.Z. and Yin, P.J. (2010) A novel integrated active capping technique for the remediation of nitrobenzene-contaminated sediment. *Journal of Hazardous Materials* 182(1-3), 184-190.

- Sun, X.M. and Li, Y.D. (2003) Synthesis and characterization of ion-exchangeable titanate nanotubes. *Chemistry-A European Journal* 9(10), 2229-2238.
- Sung-Suh, H.M., Choi, J.R., Hah, H.J., Koo, S.M. and Bae, Y.C. (2004) Comparison of Ag deposition effects on the photocatalytic activity of nanoparticulate TiO<sub>2</sub> under visible and UV light irradiation. *Journal of Photochemistry and Photobiology A: Chemistry* 163(1), 37-44.
- Takeda, K., Takedoi, H., Yamaji, S., Ohta, K. and Sakugawa, H. (2004) Determination of hydroxyl radical photoproduction rates in natural waters. *Analytical Sciences* 20(1), 153-158.
- Theron, J., Walker, J.A. and Cloete, T.E. (2008) Nanotechnology and water treatment: applications and emerging opportunities. *Critical Reviews in Microbiology* 34(1), 43-69.
- Theurich, J., Bahnemann, D., Vogel, R., Ehamed, F., Alhakimi, G., Rajab, I. (1997) Photocatalytic degradation of naphthalene and anthracene: GC-MS analysis of the degradation pathway. *Research on Chemical Intermediates* 23, 247-274.
- Tombacz, E., Libor, Z., Illes, E., Majzik, A. and Klumpp, E. (2004) The role of reactive surface sites and complexation by humic acids in the interaction of clay mineral and iron oxide particles. *Organic Geochemistry* 35(3), 257-267.
- Tong, M., Yuan, S.H., Long, H.Y., Zheng, M.M., Wang, L.L. and Chen, J. (2011) Reduction of nitrobenzene in groundwater by iron nanoparticles immobilized in PEG/nylon membrane. *Journal of Contaminant Hydrology* 122(1-4), 16-25.
- Tremblay, L., Kohl, S.D., Rice, J.A. and Gagne, J.P. (2005) Effects of temperature, salinity, and dissolved humic substances on the sorption of polycyclic aromatic hydrocarbons to estuarine particles. *Marine Chemistry* 96(1-2), 21-34.

- Tuckermann, R. (2007) Surface tension of aqueous solutions of water-soluble organic and inorganic compounds. *Atmospheric Environment* 41(29), 6265-6275.
- Turcotte, D., Headley, J.V., Abudulai, N.L., Hodson, P.V. and Brown, R.S. (2011) Identification of phase II in vivo metabolites of alkyl-anthracenes in rainbow trout (*Oncorhynchus mykiss*). *Chemosphere* 85(10), 1585-1591.
- UGA (1983) Reference soil test methods for the southern region of the United States, Southern Cooperative Series Bulletin 289, 1983, University of Georgia College of Agriculture Experiment Stations, Athens, GA, 30602.
- Underberg, W.J.M. and Lingeman, H. (1983) Aspects of the chemical-stability of mitomycin and porfiromycin in acidic solution. *Journal of Pharmaceutical Sciences* 72(5), 549-553.
- US EPA (2014) Toxic and priority pollutants under the clean water act: priority pollutant list, Washington, DC.
- US EPA (1980) Ambient water quality criteria, Washington, DC.
- US EPA (1995) Nitrobenzene fact sheet: support document; OPPT chemical fact sheets, Washington, DC.
- US EPA (1998) Nitrobenzene carcinogenicity (EPA/600/R-95/100), National Center for Environmental Assessment–Washington Office, Washington, DC.
- US EPA (2004) National recommended water quality criteria, Washington, DC.
- US EPA (2010) Methods for detecting dispersants in water, Washington, DC.
- US EPA (2011) Questions and Answers on Dispersants.  
<http://archive.epa.gov/bpspill/web/html/dispersants-qanda.html>.
- US EPA (2014) Priority pollutant list, Washington, DC.

- Vader, F.V. (1960) Adsorption of detergents at the liquid-liquid interface. 1. Transactions of the Faraday Society 56(7), 1067-1077.
- Varadhi, S., Gill, H., Apoldo, L.J., Liao, K., Blackman, R. and Wittman, W.K. (2005) Full-scale nanoiron injection for treatment of groundwater contaminated with chlorinated hydrocarbons. The Natural Gas Technologies 2005 Conference.
- Vela, N., Martinez-Menchon, M., Navarro, G., Perez-Lucas, G. and Navarro, S. (2012) Removal of polycyclic aromatic hydrocarbons (PAHs) from groundwater by heterogeneous photocatalysis under natural sunlight. Journal of Photochemistry and Photobiology A: Chemistry 232, 32-40.
- Veldurthi, N.K., Velchuri, R., Pola, S., Prasad, G., Muniratnam, N.R. and Vithal, M. (2015) Synthesis, characterization and silver/copper-nitrogen substitutional effect on visible light driven photocatalytic performance of sodium hexatitanate nanostructures. Journal of Chemical Technology and Biotechnology 90(8), 1507-1514.
- Vieth, W.R. and Sladek, K.J. (1965) A model for diffusion in a glassy polymer. Journal of Colloid Science 20(9), 1014-1033.
- Vione, D., Falletti, G., Maurino, V., Minero, C., Pelizzetti, E., Malandrino, E., Ajassa, R., Olariu, R.I. and Arsene, A. (2006) Sources and sinks of hydroxyl radicals upon irradiation of natural water samples. Environmental Science & Technology 40(12), 3775-3781.
- von Szyszkowski, B. (1908) Experimental studies on capillary properties of aqueous solutions of fatty acids. Zeitschrift für Physikalische Chemie 64, 385-414.
- Wan, L.S.C. and Lee, P.F.S. (1974) CMC of polysorbates. Journal of Pharmaceutical Sciences 63(1), 136-137.

- Wang, A.J., Cheng, H.Y., Liang, B., Ren, N.Q., Cui, D., Lin, N., Kim, B.H. and Rabaey, K. (2011) Efficient reduction of nitrobenzene to aniline with a biocatalyzed cathode. *Environmental Science & Technology* 45(23), 10186-10193.
- Wang, C., Feng, Y.J., Zhao, S.S. and Li, B.L. (2012) A dynamic contaminant fate model of organic compound: a case study of nitrobenzene pollution in Songhua river, China. *Chemosphere* 88(1), 69-76.
- Wang, Q., Li, Y., Wang, C., Wu, Y. and Wang, P.F. (2014) Development of a novel multi-functional active membrane capping barrier for the remediation of nitrobenzene-contaminated sediment. *Journal of Hazardous Materials* 276, 415-421.
- Wang, W.Z., Zheng, Y. and Lee, K. (2013) Role of the hydrophobicity of mineral fines in the formation of oil-mineral aggregates. *Canadian Journal of Chemical Engineering* 91(4), 698-703.
- Wang, X.C., Yu, J.C., Yip, H.Y., Wu, L., Wong, P.K. and Lai, S.Y. (2005) A mesoporous Pt/TiO<sub>2</sub> nanoarchitecture with catalytic and photocatalytic functions. *Chemistry-A European Journal* 11(10), 2997-3004.
- Wardman, P. (1989) Reduction potentials of one-electron couples involving free-radicals in aqueous-solution. *Journal of Physical and Chemical Reference Data* 18(4), 1637-1755.
- Wenk, J., von Gunten, U. and Canonica, S. (2011) Effect of Dissolved organic matter on the transformation of contaminants induced by excited triplet states and the hydroxyl radical. *Environmental Science & Technology* 45(4), 1334-1340.
- White, H.K., Hsing, P.Y., Cho, W., Shank, T.M., Cordes, E.E., Quattrini, A.M., Nelson, R.K., Camilli, R., Demopoulos, A.W.J., German, C.R., Brooks, J.M., Roberts, H.H., Shedd, W.,

- Reddy, C.M. and Fisher, C.R. (2012) Impact of the Deepwater Horizon oil spill on a deep-water coral community in the Gulf of Mexico. *Proceedings of the National Academy of Sciences of the United States of America* 109(50), 20303-20308.
- World Health Organization (WHO) (2003) *Environmental Health Criteria* 230, United Nations Environment Programme, the International Labour Organization or the World Health Organization, Geneva, Switzerland.
- Wu, D.M., Wang, Z.D., Hollebone, B., McIntosh, S., King, T. and Hodson, P.V. (2012) Comparative toxicity of four chemically dispersed and undispersed crude oils to rainbow trout embryos. *Environmental Toxicology and Chemistry* 31(4), 754-765.
- Xiong, L., Chen, C., Chen, Q. and Ni, J. (2011) Adsorption of Pb(II) and Cd(II) from aqueous solutions using titanate nanotubes prepared via hydrothermal method. *Journal of Hazardous Materials* 189(3), 741-748.
- Xiong, L., Yang, Y., Mai, J., Sun, W., Zhang, C., Wei, D., Chen, Q. and Ni, J. (2010) Adsorption behavior of methylene blue onto titanate nanotubes. *Chemical Engineering Journal* 156(2), 313-320.
- Xu, H., Li, P.X., Ma, K., Thomas, R.K., Penfold, J. and Lu, J.R. (2013) Limitations in the application of the gibbs equation to anionic surfactants at the air/water surface: sodium dodecylsulfate and sodium dodecylmonooxyethylenesulfate above and below the CMC. *Langmuir* 29(30), 9335-9351.
- Xu, Z.H., Jing, C.Y., Li, F.S. and Meng, X.G. (2008) Mechanisms of photocatalytical degradation of monomethylarsonic and dimethylarsinic acids using nanocrystalline titanium dioxide. *Environmental Science & Technology* 42(7), 2349-2354.

- Xue, J.L., Yu, Y., Bai, Y., Wang, L.P. and Wu, Y.N. (2015) Marine oil-degrading microorganisms and biodegradation process of petroleum hydrocarbon in marine environments: a review. *Current Microbiology* 71(2), 220-228.
- Yan, L.B. and Bailey, G.W. (2001) Sorption and abiotic redox transformation of nitrobenzene at the smectite-water interface. *Journal of Colloid and Interface Science* 241(1), 142-153.
- Yang, D., Sarina, S., Zhu, H., Liu, H., Zheng, Z., Xie, M., Smith, S.V. and Komarneni, S. (2011) Capture of radioactive cesium and iodide ions from water by using titanate nanofibers and nanotubes. *Angewandte Chemie International Edition* 50(45), 10594-10598.
- Yates, L.M. and von Wandruszka, R. (1999) Effects of pH and metals on the surface tension of aqueous humic materials. *Soil Science Society of America Journal* 63(6), 1645-1649.
- Yehia, A. (1992) Adsorption of dioctyl sodium sulphosuccinate on some synthetic carbonate apatites. *Minerals Engineering* 5, 707-714.
- Yeom, I.T., Ghosh, M.M., Cox, C.D. and Robinson, K.G. (1995) Micellar solubilization of polynuclear aromatic hydrocarbons in coal tar-contaminated soils. *Environmental Science & Technology* 29(12), 3015-3021.
- Yin, W.Z., Wu, J.H., Li, P., Wang, X.D., Zhu, N.W., Wu, P.X. and Yang, B. (2012) Experimental study of zero-valent iron induced nitrobenzene reduction in groundwater: the effects of pH, iron dosage, oxygen and common dissolved anions. *Chemical Engineering Journal* 184, 198-204.
- Yu, H., Yu, J., Cheng, B. and Zhou, M. (2006a) Effects of hydrothermal post-treatment on microstructures and morphology of titanate nanoribbons. *Journal of Solid State Chemistry* 179(2), 349-354.

- Yu, J.G., Xiang, Q.J. and Zhou, M.H. (2009) Preparation, characterization and visible-light-driven photocatalytic activity of Fe-doped titania nanorods and first-principles study for electronic structures. *Applied Catalysis B: Environmental* 90(3-4), 595-602.
- Yu, J.G., Yu, H.G., Cheng, B. and Trapalis, C. (2006b) Effects of calcination temperature on the microstructures and photocatalytic activity of titanate nanotubes. *Journal of Molecular Catalysis A: Chemical* 249(1-2), 135-142.
- Yukselen, Y. and Kaya, A. (2003) Zeta potential of kaolinite in the presence of alkali, alkaline earth and hydrolyzable metal ions. *Water Air and Soil Pollution* 145(1), 155-168.
- Zepp, R.G. and Cline, D.M. (1977) Rates of direct photolysis in aquatic environment. *Environmental Science & Technology* 11(4), 359-366.
- Zepp, R.G., Schlotzhauer, P.F. (1979) Polynuclear aromatic hydrocarbons, Ann Arbor, MI.
- Zhang, H.P., Khatibi, M., Zheng, Y., Lee, K., Li, Z.K. and Mullin, J.V. (2010) Investigation of OMA formation and the effect of minerals. *Marine Pollution Bulletin* 60(9), 1433-1441.
- Zhang, M., He, F., Zhao, D.Y. and Hao, X.D. (2011) Degradation of soil-sorbed trichloroethylene by stabilized zero valent iron nanoparticles: effects of sorption, surfactants, and natural organic matter. *Water Research* 45(7), 2401-2414.
- Zhang, Q.H., Gao, L. and Guo, J.K. (2000) Effects of calcination on the photocatalytic properties of nanosized TiO<sub>2</sub> powders prepared by TiCl<sub>4</sub> hydrolysis. *Applied Catalysis B: Environmental* 26(3), 207-215.
- Zhang, R., Li, J., Liu, C., Shen, J., Sun, X., Han, W. and Wang, L. (2013) Reduction of nitrobenzene using nanoscale zero-valent iron confined in channels of ordered mesoporous silica. *Colloids and Surfaces A: Physicochemical and Engineering Aspects* 425, 108-114.



- Zhang, W., Chen, L., Chen, H. and Xia, S.Q. (2007) The effect of  $\text{Fe}^0/\text{Fe}^{2+}/\text{Fe}^{3+}$  on nitrobenzene degradation in the anaerobic sludge. *Journal of Hazardous Materials* 143(1-2), 57-64.
- Zhang, X.J. and Chen, C. (2009) Emergency drinking water treatment in source water pollution incident-technology and practice in China. *Frontiers of Environmental Science & Engineering in China* 3(3), 364-368.
- Zhao, D.Y., Pignatello, J.J., White, J.C., Braida, W. and Ferrandino, F. (2001) Dual-mode modeling of competitive and concentration-dependent sorption and desorption kinetics of polycyclic aromatic hydrocarbons in soils. *Water Resources Research* 37(8), 2205-2212.
- Zhao, X., Cai, Z., Wang, T., O'Reilly, S., Liu, W. and Zhao, D. (2016) A new type of cobalt-deposited titanate nanotubes for enhanced photocatalytic degradation of phenanthrene. *Applied Catalysis B: Environmental* 187(15), 134-143.
- Zhao, X., Gong, Y.Y., O'Reilly, S.E. and Zhao, D.Y. (2015) Effects of oil dispersant on solubilization, sorption and desorption of polycyclic aromatic hydrocarbons in sediment-seawater systems. *Marine Pollution Bulletin* 92(1-2), 160-169.
- Zhao, X.K., Yang, G.P. and Gao, X.C. (2003) Studies on the sorption behaviors of nitrobenzene on marine sediments. *Chemosphere* 52(5), 917-925.
- Zhou, W.Q., Li, J., Wei, W., Su, Z.G. and Ma, G.H. (2011) Effect of solubilization of surfactant aggregates on pore structure in gigaporous polymeric particles. *Colloids and Surfaces A: Physicochemical and Engineering Aspects* 384(1-3), 549-554.
- Zhu, L.Y., Ma, B., Zhang, L. and Zhang, L. (2007) The study of distribution and fate of nitrobenzene in a water/sediment microcosm. *Chemosphere* 69(10), 1579-1585.

Zhuang, H.F., Lin, C.J., Lai, Y.K., Sun, L. and Li, J. (2007) Some critical structure factors of titanium oxide nanotube array in its photocatalytic activity. *Environmental Science & Technology* 41(13), 4735-4740.

Zhuang, M.B., Abulikemu, G., Campo, P., Platten, W.E., Suidan, M.T., Venosa, A.D. and Conmy, R.N. (2016) Effect of dispersants on the biodegradation of South Louisiana crude oil at 5 and 25 degrees. *Chemosphere* 144, 767-774.

Zuijdgheest, A. and Huettel, M. (2012) Dispersants as used in response to the MC252-spill lead to higher mobility of polycyclic aromatic hydrocarbons in oil-contaminated Gulf of Mexico sand. *Plos One* 7(11), e54549.